DIGITAL ACCESS TO SCHOLARSHIP AT HARVARD
DASH.HARVARD.EDU

HARVARD LIBRARY
Office for Scholarly Communication

Properties of Dark Matter Halos and Novel Signatures of Baryons in Them

Citation
Rubin, Douglas Seth. 2014. Properties of Dark Matter Halos and Novel Signatures of Baryons in Them. Doctoral dissertation, Harvard University.

Permanent link
http://nrs.harvard.edu/urn-3:HUL.InstRepos:12274129

Terms of Use
This article was downloaded from Harvard University's DASH repository, and is made available under the terms and conditions applicable to Other Posted Material, as set forth at http://nrs.harvard.edu/urn-3:HUL.InstRepos:dash.current.terms-of-use#LAA

Share Your Story

The Harvard community has made this article openly available.
Please share how this access benefits you. Submit a story .

Accessibility

© 2014 — Douglas Seth Rubin

All rights reserved.

Dissertation Advisor: Professor Abraham Loeb Douglas Seth Rubin

Properties of Dark Matter Halos and Novel Signatures of Baryons in Them

Abstract

This thesis investigates the properties of dark matter halos and places constraints on the baryons within them by utilizing observational data. In Chapter 2, we use spherical collapse dynamics to calculate the non-linear over-density of a dark matter halo at virialization given realistic initial and final density profiles in an Einstein-de Sitter cosmology and cosmologies with matter, dark energy and possible curvature. We find that the non-linear over-density at virialization can be reduced by as much as a factor of 10 as compared to the standard value.

In Chapter 3 we present novel analytic solutions to the non-linear dynamics of dark matter structures. We use the spherical collapse model to consider collapsing over-dense regions, over-dense regions which never collapse (due to the cosmological constant) and under-dense voids. These calculations can be applied to studies about the formation and abundance of cosmic structure.

In Chapter 4 we use a novel method to constrain the initial mass function (IMF) of stars in the Galactic center. We calculate the mass loss rate in the Galactic center due to stellar collisions given a present-day mass function (PDMF) of stars. We model the total x-ray luminosity due to the ejected mass and utilize x-ray observations of the Galactic center to constrain the PDMF. By considering several star formation histories, we are able to constrain the IMF of stars in the Galactic center.

In the final chapter, we calculate the expected kinetic Sunyaev-Zel'dovich (kSZ) signal from the diffuse gas associated with the Local Group (LG) halo. By modeling the distribution of gas in the LG we find that the kSZ sky map is dominated by a hot spot in the direction of M31. By performing a correlation analysis with the CMB temperature map measured by the Planck satellite, we find no statistical evidence that the LG kSZ signal is embedded in the Planck map. We constrain the total mass of the LG halo by limiting the kSZ temperature shift around the hot spot to be less than what is observed.

Contents

Acknowledgments

Many people deserve my thanks for their part in helping me complete this thesis. Firstly, I would like to thank my family for their love and support over the years. I also want to thank my girlfriend Rachel for her love, understanding and companionship.

I am extremely grateful to have had Avi Loeb as my Ph.D. advisor. Avi has many wonderful qualities that have made his mentorship such a pleasure. I'll briefly name a few. His optimism and passion for science. His insight and uncanny ability to quickly identify the crux of a problem. His truly amazing breadth of knowledge in Astrophysics. It's been a privilege to work by your side and to learn from you.

I would also like to thank some of my past advisors and collaborators, who, over the years, have steered me in the right direction and have shaped me into a scientist: Debra Elmegreen, Greg Voth, Suzanne Madden and Sacha Hony.

I must say, graduate school truly was a journey. For me, it's been a time of personal growth and reflection, intellectual growth, occasional frustration, and above all, friendship. I'd like to express my appreciation for all my graduate school friends at Harvard for sharing this experience with me: Tarek Anous, Jon Bittner, Clinton Hansen, Neil Jhaveri, Greg Kestin, Maxim Lavrentovich, Kevin Mercurio, Dick Nug, Liz Petrik, Nick Van Meter, Eli Visbal and Ben and Katy Woodring. Clinton: "Nerd God's here!" Greg: "Let's sconify." Kevin: "360 s." Nick: "Sometimes the beefcake carries through." We made some remarkable memories. Thank you.

Chapter 1

Introduction

The formation and evolution of cosmic structure is a problem that can, in principle, be solved completely by using the laws of physics to evolve the initial physical conditions of the universe. It turns out that a full statistical description of the initial conditions of the entire universe can be summarized by a surprisingly small number of parameters. These parameters describe the cosmology of our universe, quantifying such things as its composition, geometry and distribution of density fluctuations (the most recent measurement of some of these parameters is presented in Table 1.1). Within the last two decades the cosmological parameters have been measured to high precision by observations of the power spectrum of temperature fluctuations of the cosmic microwave background (CMB) radiation (e.g. Komatsu et al. 2011; Planck Collaboration et al. 2013a). The CMB measurements, and a number of other independent observations, such as the clustering of galaxies and high redshift supernovae have lead to a standard, ΛCDM, model of cosmology.

With the initial conditions of the universe now measured to high precision, we

Table 1.1:: The most recent determination of several cosmological parameters from the CMB temperature fluctuation power spectrum measured by the Planck satellite (Planck Collaboration et al. 2013a).

Parameter	Value	Description
$\Omega_b h^2$	0.02205 ± 0.00028	The baryon density today
$\Omega_c h^2$	0.1199 ± 0.0027	The cold dark matter density today
Ω_Λ	$0.685^{+0.018}_{-0.016}$	The dark energy density today
n_s	0.9603 ± 0.0073	The spectral index of primordial fluctuations
H_o	(67.3 ± 1.2)km s^{-1} Mpc^{-1}	The expansion rate of the universe today
σ_8	0.829 ± 0.012	The cosmic variance at a scale of $8h^{-1}$Mpc

may attempt to describe in detail the formation of dark matter halos, inside of which, galaxies, stars, planets and ultimately life have formed. Our current understanding of the formation of dark structure in the universe goes something like this: a scale-invairant power spectrum of matter density fluctuations is laid down by inflation. Some regions of the universe are slightly more dense than the average, and some less dense. Initially, when densities are small, the dark matter within these perturbations moves with the expansion of the universe. But, owing to gravity, the density perturbations eventually decouple from the Hubble flow. Matter is drained from low density regions to become voids and funneled into regions of high density, further enhancing density contrast in the universe. Density perturbations become increasingly non-linear, and, under the influence of gravity begin to collapse where densities are the greatest. As shown in computer simulations, and as predicted by the Sunyaev-Zel'dovich approximation, collapse first

occurs along one axis, forming a two-dimensional sheet, then along a second axis forming a one-dimensional filament. A snapshot of the universe at one point in time will show an assortment of these inter-connected structures, resulting in the so-called "cosmic web." At the intersection of filaments, collapse in the third dimension finally occurs, until halted by a process of virialization, resulting in a roughly spherical, self-supporting concentration of dark matter, called a dark matter halo.

As seen from Table 1.1, dark matter is about five times more abundant in mass than ordinary matter (also called "baryons"). Ordinary matter, however, is still of prime concern to astrophysicists since only it is directly observable through the light it gives off, and since it is this matter from which galaxies, stars and people are made of. Whereas the dynamics of dark matter is relatively simple (since it is solely determined by gravity) the dynamics of baryons is far more complicated since they have a non-negligible temperature and exert pressure, interact with light and can be heated or cooled through radiative processes (or even become coupled to light) and can form molecules through chemistry. Still, much effort has been put in to simulations and semi-analytic models to understand how gas was accreted into dark matter halos to form stars and galaxies (for a review see Loeb & Furlanetto 2013). To create the first generation of stars, gas first fell into the potential wells of halos. Accretion, however, onto the shallowest wells was impeded due to pressure forces and the coherent motion of gas relative to dark matter (Tseliakhovich & Hirata 2010). The gas that *was* able to be accreted shocked and heated to the so-called "virial temperature" of the halo. For stars to form within the halo, the gas had to cool and condense in order to lower the Jean's mass[1] to the mass

[1]The Jean's mass determines whether or not a cloud of gas of mass M is supported against gravitational collapse. Pressure waves in the gas tend to smooth out increases in density due to compression from

scale of a star. The first protostars cooled via molecular hydrogen (forming "Pop III stars"), and subsequent generations were able to cool from atomic hydrogen and heavier elements created inside stars from earlier stellar generations and dispersed throughout the interstellar medium through supernovae explosions.

This thesis is concerned with the structure and formation of dark matter halos and signatures of baryons in them. We use simple, analytic models to calculate properties of dark matter halos in cosmologies with dark energy and possible curvature. Although highly simplified, these models provide fast and easy results and allow for physical insight which can be missed when N-body simulations are used to consider structure formation. We also constrain properties of baryons in dark matter halos, such as the stellar mass function in the Galactic center and the amount of gas in the Local Group, by limiting these properties through observations.

---

gravity. The timescale associated with this process is $t_{press} \sim R/c_s$, where R is the size of the cloud and c_s is the speed of sound in the cloud. The relevant timescale for the competing process of gravitational collapse is the free-fall time, given by $t_{ff} \sim 1/\sqrt{G\rho}$, where ρ is the density of the cloud (assumed to be constant). Gravitational collapse can only occur when $t_{ff} < t_{press}$, so that collapse occurs faster than the time it takes pressure to dissipate density increases due to collapse. Thus, to order of magnitude, clouds with $R > \lambda_J \equiv c_s/\sqrt{G\rho}$ (where λ_J is called the "Jean's length"), or equivalently with mass $M > M_J \equiv (4\pi/3)\rho\lambda_J^3$ (where M_J is called the "Jean's mass"), are able to collapse until halted by rotational (angular momentum) support, or some other mechanism.

1.1 The Virialization Density of Dark Matter Halos

The abundance of cosmological dark matter halos is a problem that has been studied theoretically for several decades through analytic models and numerical simulations. The Press-Schecter mass function (Press & Schechter 1974) was the first of these models, and is perhaps the most well known. It uses the linearized density at the virialization time (as predicted from the spherical collapse model) as a density threshold above which a halo is defined. The halo mass function can be found from the initial cosmic density field by determining at which redshift regions of a certain mass surpass the density threshold. Since the Press-Schecter model was introduced, more sophisticated models have been proposed. Under the excursion set formalism (Bond et al. 1991; Sheth et al. 2001; Sheth & Tormen 2002), the halo mass function can be predicted by determining the fraction of particular trajectories in a diffusion process. The Sheth-Tormen mass function (Sheth et al. 2001) incorporates the more realistic ellipsoidal collapse scenario of a dark matter halo. The success of these models is often determined by their agreement with the halo mass function as measured from numerical simulations. This, in turn, depends on the algorithm for identifying halos. One such algorithm, the spherical over-density algorithm (Lacey & Cole 1994) , identifies halos through a predetermined non-linear over-density threshold, Δ_c, often taken to be $\Delta_c \approx 178$, calculated from the spherical collapse model.

In Chapter 2, we present a more realistic calculation of Δ_c using the spherical collapse model. The standard calculation assumes an initial top-hat density profile as well as a final, virialized top-hat density profile. This initial density profile significantly simplifies the calculation as it results in a collapsing dark matter sphere where each shell has a self-similar trajectory. This means that all shells turn-around at the same time (so

that the kinetic energy at this time is zero) and that the sphere maintains its top-hat shape throughout collapse (so that the potential energy is always that of a uniform sphere). Using realistic density profiles, we employ the equations of spherical collapse to calculate the kinetic and potential energy at turn around in order to determine Δ_c at virialization. We derive the formalism for this calculation in an Einstein-de Sitter (E-dS) universe as well as in cosmologies including a cosmological constant and possible curvature. We present results in both E-dS and ΛCDM cosmologies using power-law initial profiles as well as highly realistic profiles calculated from the statistics of a Gaussian random field. The value of Δ_c can be reduced by as much as a factor of 10 as compared to the standard calculation. This may significantly affect the halo mass function measured from simulations when the spherical over-density algorithm is employed to identify halos. We attempt to quantify this effect, and find that the halo mass function can be enhanced by a factor of a few at the highest mass scales.

1.2 Analytic Properties of Dark Matter Dynamics

Early in the universe, when density perturbations are small, the dynamics of dark matter is determined by a linearized theory of fluid flow in an expanding background. Both Newtonian and relativistic solutions of the linearized theory have been fully worked out for some time (e.g. Lifshitz 1946; Silk 1968; Peebles & Yu 1970; Satō 1971; Weinberg 1971). The dynamics of dark matter when its density becomes increasingly non-linear, however, is far less certain. Generally, our understanding of the non-linear dynamics of dark matter has progressed through the implementation of numerical simulations and through simple analytic models. Simulations have the advantage that very few

simplifying assumptions need be employed. The disadvantages are resolution effects (both spatial and temporal) and the sheer amount of computational power and time needed to perform the simulation at hand. The main drawback of analytic models, on the other hand, is that they rely on broad simplifications of the actual physical problem. These models, however, are typically quick to solve and can provide insight into the underlying physics of the non-linear dynamics.

In Chapter 3, we utilize the spherical collapse model to compute several novel analytic properties of the non-linear dynamics of dark matter. We consider three distinct regimes: over-dense regions which eventually collapse to form dark matter halos, over-dense regions for which collapse is indefinitely halted due to the cosmological constant and under-dense voids. For the first category, we present an analytic solution of the turn-around radius of a dark matter sphere in a cosmology with matter, a cosmological constant and possible curvature. We also calculate several properties of dark matter halos in various cosmologies, such as the non-linear density at collapse, the virial radius, virial temperature, circular velocity and the binding energy. For the second category, we work out formalism that allows us to identify a critical over-density at any redshift, below which the perturbation will never collapse. We also derive a formula in a cosmology with matter, a cosmological constant and possible curvature for the critical value of the initial density seed below which the perturbation will never turn around and virialize. For the third category, we compute the shell crossing redshift and associated linear and non-linear under-densities in a cosmology with matter, a cosmological constant and possible curvature. We provide fitting formulae to this quantities as a function of the matter density of the universe at the shell-crossing redshift. This calculation has only previously been done for an Einstein-de Sitter cosmology, and is used to compute

the so-called void mass function. The new calculations presented in this chapter can be applied to a variety of problems regarding dark matter structure and formation.

1.3 Mass Loss due to Stellar Collisions in the Galactic Center

The initial mass function (IMF) of stars gives the number of stars per unit stellar mass for a recently born stellar population. Described by Salpeter (Salpeter 1955) more than 50 years ago, the canonical IMF is an empirical mass function which has been found to be universal (Kroupa 2001), with perhaps the sole exception the stellar population near the Galactic center. By specifying an IMF and assuming realistic star formation histories, many studies have attempted to derive an IMF near the Galactic center consistent with present observations (e.g. Maness et al. 2007; Paumard et al. 2006; Bartko et al. 2010; Löckmann et al. 2010).

In Chapter 4, we use a novel method to investigate the IMF in the Galactic center. We calculate the mass loss rate in the Galactic center due to direct and indirect stellar collisions given a certain present-day mass function (PDMF) of stars. Given the high stellar densities and large velocity dispersions in the Galactic center, stellar collisions frequently occur. In fact, several studies have attempted to explain anomalies in the observed population of stars through stellar collisions (e.g. Genzel et al. 1996; Davies et al. 1998; Alexander 1999; Bailey & Davies 1999; Dale et al. 2009). By modeling the thermal emission from the mass loss rates that we calculate, we derive the total x-ray luminosity in the Galactic center and are thus able to constrain the PDMF of stars

by limiting our calculations against x-ray observations from the Chandra satellite. By assuming reasonable star formation histories in the Galactic center, we work backwards to constrain the power-law slope of the IMF in the Galactic center. Consistent with (Maness et al. 2007; Bartko et al. 2010), we find evidence for a top-heavy to canonical IMF in the Galactic center.

1.4 The kSZ Effect from Gas in the Local Group

Measuring the power spectrum of the CMB radiation temperature fluctuations is now a precision science (Komatsu et al. 2011; Planck Collaboration et al. 2013a), allowing us to put tight constraints on the cosmological parameters of our universe. The increase in the sensitivity and angular resolution of the CMB sky maps has motivated a thorough understanding of all foreground contaminants to the primordial signal. Attempts to understand these contaminants is all the more interesting given that they may explain well known large-scale anomalies in the CMB maps, such as the observed hemispherical asymmetry (Planck Collaboration et al. 2013b; Eriksen et al. 2004). One possible contaminant is the temperature shift due to the kinetic Sunyaev-Zel'dovich (kSZ) effect from local sources, which, because of their proximity, produce large-scale temperature shifts on the sky.

Recently, kSZ studies of the diffuse gas in the Milky Way (MW) (Hajian et al. 2007), the MW halo (Birnboim & Loeb 2009; Peiris & Smith 2010) and local superclusters (Dolag et al. 2005) have found associated temperature shifts of order a few μK. They have not, however, found compelling statistical evidence that these signals actually contaminate the observed CMB maps (Birnboim & Loeb 2009), nor that they can

induce strong enough asymmetries to contribute significantly to the CMB anomalies (Peiris & Smith 2010). In Chapter 5, we investigate the kSZ signal from the diffuse gas associated with the Local Group (LG) halo, which because it has a baryonic mass several times larger than that of the MW halo (Rubin & Loeb 2013b), may produce larger kSZ temperature shifts. We model the distribution of gas in the LG halo, calculate the expected kSZ signal, and find that it is dominated by a hot spot several degrees in size in the direction of M31. Although the kSZ signal is far subdominant to that of the primordial signal, the hot spot produces kSZ temperature shifts several times greater than in the studies mentioned above. By performing a cross correlation analysis, we find no statistical evidence that the kSZ signal from the LG is embedded in the CMB temperature shift map measured by the Planck Satellite. By limiting the temperature around the hot spot to be less than that observed by Planck, we are able to constrain the total mass in the LG halo.

Chapter 2

The Virialization Density of Peaks with General Density Profiles Under Spherical Collapse

D. Rubin & A. Loeb, *Journal of Cosmology and Astroparticle Physics*, Issue 12, ID 019, 2013

Abstract

We calculate the non-linear virialization density, Δ_c, of halos under spherical collapse from peaks with an arbitrary initial and final density profile. This is in contrast to the standard calculation of Δ_c which assumes top-hat profiles. Given our formalism, the non-linear halo density can be calculated once the shape of the initial peak's density profile and the shape of the virialized halo's profile are provided. We solve for Δ_c

for halos in an Einstein-de Sitter and a ΛCDM universe. As examples, we consider power-law initial profiles as well as spherically averaged peak profiles calculated from the statistics of a Gaussian random field.

We find that, depending on the profiles used, Δ_c is smaller by a factor of a few to as much as a factor of 10 as compared to the density given by the standard calculation (≈ 200). Using our results, we show that, for halo finding algorithms that identify halos through an over-density threshold, the halo mass function measured from cosmological simulations can be enhanced at all halo masses by a factor of a few. This difference could be important when using numerical simulations to assess the validity of analytic models of the halo mass function.

2.1 Introduction

The physics underlying the abundance of cosmological dark matter halos has received considerable attention for several decades. The problem has been studied both with analytic models such as the excursion set formalism and with high resolution numerical simulations. In the excursion set formalism, the abundance of halos can be predicted by setting a linearized density barrier, used to calculate the fraction of particular "trajectories" in a diffusion process (Bond et al. 1991; Sheth et al. 2001; Sheth & Tormen 2002). In numerical simulations, the halo mass function is directly measured by searching the cosmological density field for halos identified by halo finding algorithms, (e.g. Sheth & Tormen 1999; Jenkins et al. 2001; Springel et al. 2005; Warren et al. 2006; Reed et al. 2007; Tinker et al. 2008; Crocce et al. 2010; Angulo et al. 2012). The success of an analytic model is often based on its agreement with the halo mass function as measured

from simulations. The measured mass function, however, is dependent on the method used to identify halos. A commonly used method is the friends-of-friends algorithm (Davis et al. 1985) which assigns particles to a particular halo when they are separated by less than a linking length. Another method is the spherical over-density algorithm (Lacey & Cole 1994) which identifies halos through a predetermined non-linear density threshold. The halo mass function measured with this method of course depends on the threshold used (Watson et al. 2013). In order to compare these mass functions to the predictions of analytic models, it is therefore necessary to provide an appropriate value for the expected non-linear density of a halo.

The non-linear density of a halo is also useful in estimating physical properties of dark matter halos such as the virial radius, virial temperature and circular velocity (see for example Loeb & Furlanetto 2013). It is also frequently used to normalize formulas for the density profiles of halos. For example, the normalization constant for a Navarro, Frenk & White (NFW) profile, $\rho = \rho_o/[cw(1+cw)^2]$ (where w is the radial position scaled by halo radius), (Navarro et al. 1996) is given by

$$\rho_o = \frac{\rho_c(z_{vir})\Delta_c(z_{vir})}{3}\frac{c^3}{\ln(1+c) - \frac{c}{1+c}}, \tag{2.1}$$

where $\rho_c(z_{vir})$ is the critical density of the universe at the time of halo virialization, c is the concentration parameter, and $\Delta_c(z_{vir})$ is the volume-averaged, non-linear density of the halo at virialization in units of the critical density of the universe.

The value of Δ_c is typically taken to be ≈ 200, derived by considering the dynamics of spherical collapse (Gunn & Gott 1972). It is calculated by assuming that at an early time, the initial density profile of the nascent halo is uniform out to its edge (also known as a "top-hat"). According to the spherical collapse model, for this profile, all shells

within the density perturbation will have self-similar trajectories, and will therefore turn-around at the same time. At turn-around, therefore, the kinetic energy of the system is zero. One then assumes that the energy of the system is conserved between the turn-around time and the time it takes the system to reach virial equilibrium. To calculate the halo's potential energy at virialization it is customary to assume a top-hat density profile. By employing the virial thereom and setting the energies at these times equal to each other, it is possible to solve for the ratio of the halo's virial radius to its turn-around radius. This value cubed gives the collapsing sphere's fractional change in volume. To calculate Δ_c, it is left to multiply by the ratio of the turn-around mean density to the critical density of the universe at virialization. This ratio is found with the spherical collapse solution, assuming that virialization occurs at twice the turn-around time.

For an Einstein-de Sitter universe (E-dS), $R_{vir}/R_{ta} = 1/2$ and $\Delta_c = 18\pi^2 \approx 178$ (Gunn & Gott 1972). For cosmologies including a cosmological constant, the calculation is slightly more complex since the cosmological constant contributes gravitational energy and must be included in the virial thereom (Lahav et al. 1991). Further, the equations for spherical collapse are more complicated and must be solved numerically. This calculation has been done for various cosmologies by Eke et al. (1996); Lacey & Cole (1993); Bryan & Norman (1998) and for general cosmologies by Rubin & Loeb (2013a); Lokas & Hoffman (2001). They find that, depending on the cosmology, the value of Δ_c can be larger or smaller than the E-dS value by about a factor of 2.

The assumptions of top-hat density profiles at the initial time and at virialization lead to several simplifications which make the calculation relatively easy. Since the assumption of an initial top-hat results in zero kinetic energy at turn-around, the total

kinetic energy of the system at this time need not be calculated. Moreover, for this initial density profile, the sphere maintains its top-hat shape during collapse, so that the calculation of its potential energy at turn-around (due to gravity and the cosmological constant for cosmologies with $\Lambda \neq 0$) is simply that of a homogenous sphere. Finally, for an initial top-hat profile, since the shells are on self-similiar trajectories, they do not cross before turn-around. This simplifies the spherical collapse problem since the mass within each shell remains constant in time. By assuming a top-hat density profile at virialization, the calculation of the halo's potential energy due to gravity and Λ is also simplified to that of a homogenous sphere.

To calculate more realistic values of the non-linear over-density of a halo at virialization, we repeat this calculation, generalized for any density profiles. We re-derive the formulas for R_{vir}/R_{ta} and Δ_c to allow for non-zero kinetic energy at turn-around as well potential energies for an arbitrary density profile sphere. Given an initial, realistic density profile, we use the spherical collapse equations to analytically calculate the velocity and density profiles at turn-around (and thus the total kinetic energy and potential energies due to gravity and Λ). For initial density profiles which result in shell crossings before turn-around, we employ a one dimensional code to numerically solve the equations of spherical collapse. By specifying realistic density profiles for the virialized halo, we are able to calculate realistic potential energies due to gravity and Λ at virialization. We non-dimensionalize our equations in such a way that, as with the standard calculation, R_{vir}/R_{ta} and Δ_c are independent of halo mass and only depend on the redshift of virialization.

Our calculation still relies on an idealized spherical geometry in the Newtonian limit. However, the formalism we derive allows us to utilize realistic density profiles and

thus calculate more representative estimates of the non-linear over-density of a virialized halo. This is favorable when using the halo mass function measured from numerical simulations with the spherical over-density algorithm to compare to analytic models. It also provides us with better estimates of the physical parameters of virialized halos as mentioned above. Moreover, our calculation allows us to normalize halo density profiles in a self consistent manner. For example, to normalize an NFW profile with Eqn. 2.1, we can calculate $\Delta_c(z_{vir})$ using an actual NFW profile at virialization, rather than a top-hat as in the standard calculation. We can do this because, in deriving our formalism, we non-dimensionalize all equations such that we do not require the normalized density, but only its shape.

In § 2.2, we present relevant equations from the spherical collapse model which are used for derivations in the rest of this paper. In § 2.3, we consider an E-dS cosmology and derive the formula for the non-linear halo over-density for any initial and final density profiles (§ 2.3.1). Using spherical collapse dynamics in an E-dS universe, we solve for the velocity and density profiles at turn-around and use these to calculate the total kinetic and potential energies in § 2.3.2. We present our E-dS results for several density profiles in § 2.3.4. In § 2.4 we perform the same derivations as in the E-dS case, but keep our equations general to allow for a cosmological constant and curvature. In § 2.4.4, we show results for a ΛCDM cosmology with highly realistic initial density profiles as calculated from peak statistics in a Gaussian random field.

2.2 Relevant Results from the Spherical Collapse Model

In this section, we summarize a few key results from the spherical collapse model that will be of use later in this paper. For a more detailed treatment of spherical collapse, we refer the reader to Gunn & Gott (1972); Peebles (1980); Rubin & Loeb (2013a); Loeb (2006); Peebles & Yu (1970); Bertschinger (1985a,b); Lokas & Hoffman (2001); Sheth & van de Weygaert (2004). According to the spherical collapse model, the evolution of a spherical perturbation in the cosmic density field is understood as a series of thin, concentric shells of mass whose positions vary with time. Solving for the evolution of the perturbation is then simply reduced to a problem of kinematics. In the Newtonian limit, the evolution of a shell is governed by the following partial differential equation, found by integrating the shell's equation of motion and assuming an initial velocity given by linear theory (Loeb 2006):

$$\frac{1}{H_o^2}\left(\frac{\partial \varkappa}{\partial t}\right)^2 = \frac{\Omega_m}{\varkappa} + \Omega_\Lambda \varkappa^2 + \Omega_k - \frac{5}{3}\frac{\bar{\delta}_i(r_i)}{a_i}\Omega_m, \tag{2.2}$$

where the radius of the shell, $r(t, r_i)$, is non-dimensionalized with

$$\varkappa \equiv \frac{r a_i}{r_i}. \tag{2.3}$$

Here, r_i is the initial position of the shell when the scale factor is a_i, H_o is the present-day Hubble parameter, and Ω_m, Ω_Λ and Ω_k $(= 1 - \Omega_m - \Omega_\Lambda)$ are the present-day matter, vacuum and curvature energy densities respectively. The initial density profile of the perturbation is parameterized by $\delta_i(r_i)$, defined as $\rho_i(r_i)/\bar{\rho}_m(a_i) - 1$, where $\bar{\rho}_m(a_i)$ is the mean matter density of the universe at a_i. The "bar" over the delta denotes a volume

average:

$$\bar{\delta}(r) = \frac{3}{r^3}\int_0^r \delta(r')r'^2 dr'. \tag{2.4}$$

Notice that for a top-hat profile, $\bar{\delta}_i(r_i) = const$ and Eqn. 3.3 is independent of initial position so that the trajectories of each shell are self-similar. Equation 3.3 is strictly valid only if the mass within r is constant in time (i.e. there are no shell crossings for the shell in question). In a perturbation consisting of dark matter, shell crossing is a legitimate concern since the matter is collisionless, and shells can therefore slide past each other unencumbered. It should also be noted that the equation was derived assuming that both $|\bar{\delta}_i|$ and a_i are $\ll 1$. Indeed, we make this assumption in our derivations throughout the rest of this paper.

Eqn. 3.3 can be further integrated to find the time, tH_o, at which a shell has reached a position $\chi(t)$ (Rubin & Loeb 2013a),

$$tH_o = \begin{cases} \mathcal{I}\left[0, \chi(t), \frac{\bar{\delta}_i(r_i)}{a_i}\right] & \text{for} \quad tH_o \leq t_{\mathscr{TA}}H_o \\ \mathcal{I}\left[0, \chi_{\mathscr{TA}}, \frac{\bar{\delta}_i(r_i)}{a_i}\right] + \mathcal{I}\left[\chi(t), \chi_{\mathscr{TA}}, \frac{\bar{\delta}_i(r_i)}{a_i}\right] & \text{for} \quad tH_o > t_{\mathscr{TA}}H_o \end{cases}, \tag{2.5}$$

with

$$\mathcal{I}(l,u,d) \equiv \int_l^u d\lambda \left[1 + \Omega_m\left(\frac{1}{\lambda} - 1 - \frac{5}{3}d\right) + \Omega_\Lambda\left(\lambda^2 - 1\right)\right]^{-1/2}. \tag{2.6}$$

The first line of Eqn. 2.5 applies to shells which have yet to turn-around (denoted by $_{\mathscr{TA}}$), and the second applies to shells which have already turned around. The first integral in the second line represents the amount of time that it takes for a shell to reach turn-around, and the second integral represents the amount of time between turn-around and t. Of course if the energy of the shell is greater than zero, it will be on an unbound orbit and will never collapse[1]. In this paper, however, we only concern ourselves with

[1]This is neglecting the effect of shells crossing from its exterior to its interior.

shells with bound trajectories.

For an E-dS universe the trajectory can be written in parametric form. This is obtained by first integrating Eqn. 3.3 with $\Omega_k = \Omega_\Lambda = 0$ and $\Omega_m = 1$ to find

$$t = \frac{1}{H_o}\int_0^{\chi} \frac{\sqrt{\chi'}d\chi'}{\sqrt{1 \pm \frac{5}{3}\frac{|\bar{\delta}_i|}{a_i}\chi'}}, \tag{2.7}$$

where the plus and minus sign correspond to open ($\bar{\delta}_i < 0$) and closed ($\bar{\delta}_i > 0$) trajectories respectively. Since in this paper we are considing collapsing halos, we derive the parametric trajectory for only the closed (although the derivation for the open case is almost exactly same, using hyperbolic geometry). By defining, $\sin^2(\Theta/2) \equiv (5/3)(\bar{\delta}_i/a_i)\chi$, we can take advantage of the Pythagorean trigonometric identity in the denominator, so that the integral may be computed analytically[2]. Switching the variable of integration to Θ results in

$$\begin{aligned} t &= \frac{1}{H_o}\left[\frac{5}{3}\frac{\bar{\delta}_i(r_i)}{a_i}\right]^{-3/2}\int_0^{\Theta}\sin^2\left(\frac{\Theta'}{2}\right)d\Theta' \\ &= \frac{1}{2H_o}\left[\frac{5}{3}\frac{\bar{\delta}_i(r_i)}{a_i}\right]^{-3/2}\left[\Theta(r_i) - \sin\Theta(r_i)\right]. \end{aligned} \tag{2.8}$$

The solution for χ as a function of Θ may also be simplified with the double-angle formula,

$$\begin{aligned} \chi &= \left[\frac{5}{3}\frac{\bar{\delta}_i(r_i)}{a_i}\right]^{-1}\sin^2\frac{\Theta}{2} \\ &= \frac{1}{2}\left[\frac{5}{3}\frac{\bar{\delta}_i(r_i)}{a_i}\right]^{-1}\left[1 - \cos\Theta(r_i)\right]. \end{aligned} \tag{2.9}$$

We have written the so-called "development angle", Θ, as a function of r_i to make explicit that each shell in the perturbation moves independently of one another, and so

[2]We may use this definition since $\chi \in [0, (3/5)(a_i/\bar{\delta}_i)]$, where the maximal value of χ can quickly be verified by solving for the extremum of Eqn. 3.3.

has its own development angle parameterizing its motion. The values of $\Theta = 0$, π and 2π correspond to the the initial, turn-around and collapse times for a shell respectively. This parametric solution is valid until shell crossing, which, for a top-hat initial perturbation, occurs at $\Theta = 2\pi$, when the shells have collapse to a singularity, cross each other, and then re-expand (of course the Newtonian approximation will break down at this point). Evaluating Eqn. 2.8 at $\Theta = \pi$, we find that $t_{ta}H_o = \pi/2[(5/3)(\bar{\delta}_i/a_i)]^{-3/2}$, and thus, the turn-around time decreases monotonically with $\bar{\delta}_i$. In fact, one can show that t_{ta} decreases monotonically with $\bar{\delta}_i$ for a general cosmology by evaluating $\mathcal{I}[0, \chi_{\mathscr{TA}}(\bar{\delta}_i/a_i), \bar{\delta}_i/a_i]$ $(= t_{ta}H_o)$, with $\chi_{\mathscr{TA}}(\bar{\delta}_i/a_i)$ found by solving Eqn. 3.7, and plotting $t_{ta}H_o$ vs. $\bar{\delta}_i/a_i$. Thus, for a perturbation with a monotonically decreasing $\bar{\delta}_i$ profile, collapse proceeds from the inside out, and we do not have to worry about shell crossing until the innermost shell reaches the center of the sphere and crosses itself.

The value of χ for a shell at turn-around, $\chi_{\mathscr{TA}}$, can be found by setting the velocity in Eqn. 3.3 to 0, resulting in the following cubic:

$$\Omega_\Lambda \chi_{\mathscr{TA}}^3 + \left[\Omega_k - \frac{5}{3}\frac{\bar{\delta}_i(r_i)}{a_i}\Omega_m\right]\chi_{\mathscr{TA}} + \Omega_m = 0. \tag{2.10}$$

For a general cosmology, $\chi_{\mathscr{TA}}$ must either be solved numerically by taking the smallest, positive, pure real root (if one exists)[3] or by using the closed form solution of $\chi_{\mathscr{TA}}$ presented in Rubin & Loeb (2013a) (their Eqns. 2.13-2.15). For an E-dS universe,

[3]The proper solution is the *smallest* positive, pure real root since for the case of two pure real, positive roots, an expanding sphere first reaches the smaller root, turns around and collapses to zero. Any turn-around solution after this time is spurious since Eqn. 3.3 is no longer valid because shell crossing at the origin has occurred.

Eqn. 3.7 simplifies to

$$\chi_{\mathscr{TA}} = \left[\frac{5}{3}\frac{\bar{\delta}_i(r_i)}{a_i}\right]^{-1}, \tag{2.11}$$

which is the same turn-around solution obtained by setting $\Theta = \pi$ in Eqn. 2.9. Throughout this paper, we will refer to two turn-around times: the turn-around time of a particular shell (which we denote with a script font, "$\mathscr{TA}$", subscript as in the previous two equations), and the turn-around time of the outermost shell of a spherical perturbation (which we denote with a, "ta", subscript). For example, for a particular shell with radius χ the value, $\chi_{\mathscr{TA}}$, refers to the radius at the time that this shell turns around, and the value χ_{ta} refers to the radius at the time that the outermost shell turns around. Unless we explicitly state otherwise, from this point on, whenever we refer to "turn-around" in the text, we are referring to the time at which the outermost shell turns around.

2.3 Einstein-de Sitter Universe

In this section we re-derive the equations for calculating the over-density of a halo at collapse for an E-dS universe with $\Omega = 1$, leaving the initial and virialized density profiles completely general. We then use this formalism to calculate Δ_c for several examples of reasonable initial and virialized density profiles.

2.3.1 R_{vir}/R_{ta} and Δ_c

The gravitational potential energy of a spherically symmetric object of mass M, radius R, and density profile $\rho(r)$ is

$$U = -\int_0^R GM(r)4\pi r\rho(r)dr, \tag{2.12}$$

where $M(r) = 4\pi\int_0^R r^2\rho(r)dr$. Note that throughout this paper, we reserve upper case "R"s to denote the edge of the sphere, and lower case "r"s to denote the position variable. For a uniform sphere, Eqn. 2.12 can be integrated to show that its potential energy is $U = -(3/5)GM^2/R$. For a sphere with an arbitrary density profile, we re-write Eqn. 2.12 as

$$U = -\frac{3}{5}\frac{GM^2}{R}\mathscr{U}. \tag{2.13}$$

The factor, $\mathscr{U}$, is a geometric correction factor accounting for the deviation of the sphere from complete homogeneity (and can also be viewed as the non-dimensionalized binding energy of the sphere), and is given by

$$\mathscr{U} = 5\int_0^1 \mathscr{M}(r)\varrho(r)rdr, \tag{2.14}$$

with $r \equiv r/R$,

$$\mathscr{M} = \frac{M(r)}{M}, \tag{2.15}$$

and

$$\varrho \equiv \frac{\rho(r)}{M/(\frac{4}{3}\pi R^3)}. \tag{2.16}$$

For a dark matter sphere, the energy at turn-around can be related to the potential energy at virialization by employing the virial theorem and assuming energy conservation: $KE_{ta} + U_{ta} = E_{vir} = U_{vir}/2$ (for a universe with no cosmological constant). Replacing

the potential energies with Eqn. 2.13 results in

$$KE_{ta} - \frac{3}{5}\frac{GM^2}{R_{ta}}\mathscr{U}_{ta} = -\frac{3}{10}\frac{GM^2}{R_{vir}}\mathscr{U}_{vir}, \tag{2.17}$$

which when solved for R_{vir}/R_{ta} yields

$$\frac{R_{vir}}{R_{ta}} = \frac{1}{2}\left(\frac{\mathscr{U}_{vir}}{\mathscr{U}_{ta} - \mathscr{K}_{ta}}\right). \tag{2.18}$$

Here,

$$\mathscr{K}_{ta} \equiv \frac{KE_{ta}}{3GM^2/(5R_{ta})}, \tag{2.19}$$

which represents the non-dimensionalized kinetic energy at turn-around.

As mentioned in the introduction, the density of a halo at virialization is typically parameterized by Δ_c, the volume averaged density of the halo at virialization in units of the critical density of the universe at virialization: $\Delta_c = \bar{\rho}_{vir}/\rho_c(z_{vir})$. It is customary to assume that a halo virializes at its collapse time, defined as twice the turn-around time of the edge of the halo. In an E-dS universe, we can use the parametric solution in conjunction with the formula $a(t) = (3H_o t/2)^{2/3}$ (valid for an E-dS cosmology) to find that

$$\begin{aligned}\Delta_c &= \left(\frac{3\pi}{2}\right)^2\left(\frac{R_{ta}}{R_{vir}}\right)^3 \\ &= 18\pi^2\left(\frac{\mathscr{U}_{ta} - \mathscr{K}_{ta}}{\mathscr{U}_{vir}}\right)^3.\end{aligned} \tag{2.20}$$

Notice that in the limit of a homogenous sphere, $\mathscr{U}_{vir}$ and $\mathscr{U}_{ta} \to 1$, $\mathscr{K}_{ta} \to 0$, and Eqns. 2.18 and 2.20 reduce to the familiar results that $R_{vir}/R_{ta} = 1/2$ and $\Delta_c = 18\pi^2$ in an E-dS universe. Since Δ_c depends on the cube of $(\mathscr{U}_{ta} - \mathscr{K}_{ta})/\mathscr{U}_{vir}$, it is possible that the even slight deviations from homogeneity cause significant deviation from the standard value of $18\pi^2$.

2.3.2 Conditions at Turn-around

According to the spherical collapse model, once the initial density and velocity profile of a perturbation is specified, the complete kinematics of each shell within the perturbation is known at any time up until shell crossing. In this section we express the density and velocity profiles (and hence potential and kinetic energies) at turn-around as a simple mapping of position from the initial time, to the turn-around time. We then use the shell kinematics of the spherical collapse model to solve for the mapping, so that, given an initial density profile, the physical conditions of the sphere at turn-around are completely specified.

Density and Potential Energy

Assuming that the mass within each shell is conserved (i.e., no shell crossings) from the initial time to the turn-around time,

$$4\pi \int_0^{r_{ta}} r'^2_{ta} \rho_{ta}(r'_{ta}) dr'_{ta} = 4\pi \int_0^{r_i} r'^2_i \rho_i(r'_i) dr'_i, \tag{2.21}$$

from which $\rho_{ta}(r_{ta})$ may be solved by taking a derivative with respect to r_{ta}:

$$\rho_{ta}(r_{ta}) = \rho_i(r_i) \frac{r_i^2}{r_{ta}^2} \frac{dr_i}{dr_{ta}}. \tag{2.22}$$

We re-write this as

$$\varrho_{ta}(y) = \frac{x^2}{y^2} \frac{dx}{dy}, \tag{2.23}$$

where ϱ is defined by Eqn. 2.16, and where

$$y \equiv \frac{r_{ta}}{R_{ta}}, \tag{2.24}$$

and

$$x \equiv \frac{r_i}{R_i}, \tag{2.25}$$

with both y and $x \in [0,1]$. In Eqn. 2.23, we have set ϱ_i to unity since

$$\begin{aligned}\varrho_i &= \rho_i \frac{4/3\pi R_i^3}{M} \\ &= \frac{\bar{\rho}_m(a_i)[1+\delta_i(r_i)]4/3\pi R_i^3}{4/3\pi\bar{\rho}_m(a_i)R_i^3[1+\bar{\delta}_i(R_i)]} \\ &\cong 1. \end{aligned} \tag{2.26}$$

Using these expressions, $\mathscr{U}_{ta}$ (Eqn. 4.26) can be re-written as

$$\mathscr{U}_{ta} = 5\int_0^1 \mathscr{M}(y)\frac{x^2(y)}{y}\frac{dx}{dy}(y)dy \tag{2.27}$$

with

$$\mathscr{M}_{ta}(y) = 3\int_0^y x^2(y')\frac{dx}{dy'}(y')dy'. \tag{2.28}$$

Notice that we have just expressed the density and potential energy at turn-around as a simple mapping from the initial shell positions, x, to the positions at turn-around, y.

Velocity and Kinetic Energy

We now solve for the non-dimensionalized kinetic energy at turn-around, $\mathscr{K}_{ta}$. Since,

$$\begin{aligned} M &= \frac{4}{3}\pi R_i^3\bar{\rho}_m(a_i)\left[1+\bar{\delta}_i(R_i)\right] \\ &\cong \frac{R_i^3 H_o^2\Omega_m}{2a_i^3 G}, \end{aligned} \tag{2.29}$$

we get rid of one power of M in Eqn. 2.19, resulting in

$$\mathscr{K}_{ta} = \frac{10}{3}\frac{\mathscr{X}_{ta}{}^3\frac{1}{2}\int_0^{R_{ta}} 4\pi r_{ta}^2\rho_{ta}(r_{ta})v_{ta}^2(r_{ta})dr_{ta}}{MH_o^2R_{ta}^2\Omega_m}, \tag{2.30}$$

where

$$\mathcal{X}_{ta} \equiv \frac{R_{ta} a_i}{R_i}, \tag{2.31}$$

(the non-dimensionalized turn-around radius of the outermost shell) and where we have computed the total kinetic energy at turn-around by integrating throughout the sphere. Using Eqns. 2.16, 2.24 and 2.23, this can be rewritten as

$$\begin{aligned} \mathscr{K}_{ta} &= 5 \int_0^1 y^2 \varrho_{ta}(y) {v_{ta}}^2(y) dy \\ &= 5 \int_0^1 x^2(y) \frac{dx}{dy}(y) {v_{ta}}^2(y) dy, \end{aligned} \tag{2.32}$$

where the non-dimensionalized velocity (squared) profile is:

$$v_{ta}^2(y) \equiv \frac{v_{ta}^2(y) \mathcal{X}_{ta}^3}{R_{ta}^2 H_o^2 \Omega_m}. \tag{2.33}$$

In an E-dS universe, this velocity profile can be found from the spherical collapse model by setting $\Omega_m = 1$ and $\Omega_\Lambda = 0$ in Eqn. 3.3. Using the definitions given by Eqns. 2.24, 2.25, 2.31 and 2.33, and after a bit of algebra, this equation becomes:

$$v_{ta}^2(y) = \frac{x^3}{y} - \frac{5}{3} \frac{\bar{\delta}_i(x)}{a_i} x^2 \mathcal{X}_{ta}. \tag{2.34}$$

Since in an E-dS universe

$$\mathcal{X}_{ta} = \left[\frac{5}{3} \frac{\bar{\delta}_i(R_i)}{a_i} \right]^{-1}, \tag{2.35}$$

(see Eqn. 2.11) the non-dimensionalized kinetic energy can finally be written as:

$$\mathscr{K}_{ta} = 5 \int_0^1 x^2(y) \frac{dx}{dy}(y) \left[\frac{x^3(y)}{y} - x^2(y) \frac{\bar{\delta}_i(x)}{\bar{\delta}_i(R_i)} \right] dy. \tag{2.36}$$

We have just expressed the velocity profile and kinetic energy at turn-around in terms of the shape of the initial density profile ($\bar{\delta}_i(x)/\bar{\delta}_i(R_i)$), and in terms of the mapping from x to y.

Solving the Mapping Using Spherical Collapse

In this section, we use the spherical collapse model to solve for the mapping from the initial to turn-around positions: x to y. This then allows us to solve for the density profile, potential energy, velocity profile and kinetic energy at turn-around. The relationship between x and y is given by

$$y = x\frac{\chi_{ta}(x)}{\mathcal{X}_{ta}}, \tag{2.37}$$

where this equality can be shown by writing out $\chi_{ta}(x)$ and $\mathcal{X}_{ta}$ explicitly with Eqns 2.3 and 2.31. Using Eqns. 2.9 and 2.35, this equation becomes:

$$y = x\frac{1}{2}\left[\frac{\bar{\delta}_i(x)}{\bar{\delta}_i(R_i)}\right]^{-1}\left[1-\cos\Theta_{ta}(x)\right], \tag{2.38}$$

where $\Theta_{ta}(x)$ is the development angle for a shell initially at x at the time when the outermost shell turns around.

We solve for $\Theta_{ta}(x)$ by matching the parametric solution for the turn-around time of the outermost shell (Eqn. 2.8 with $\Theta(R_i)=\pi$) with the parametric solution for the time of a shell starting at position x ($\Theta=\Theta_{ta}(x)$):

$$\frac{1}{2H_o}\left[\frac{5}{3}\frac{\bar{\delta}_i(R_i)}{a_i}\right]^{-3/2}\pi = \frac{1}{2H_o}\left[\frac{5}{3}\frac{\bar{\delta}_i(x)}{a_i}\right]^{-3/2}\left[\Theta_{ta}(x)-\sin\Theta_{ta}(x)\right]. \tag{2.39}$$

Simplifying this expression leads to a transcendental equation:

$$\Theta_{ta}(x)-\sin\Theta_{ta}(x) = \pi\left[\frac{\bar{\delta}_i(x)}{\bar{\delta}_i(R_i)}\right]^{3/2}, \tag{2.40}$$

which, when $\bar{\delta}_i(x)/\bar{\delta}_i(R_i)$ is specified, must be solved numerically. The mapping, $y(x)$, is then found by plugging $\Theta_{ta}(x)$ into Eqn. 2.38.

Equation 3.68 places a constraint on the steepness of the initial density profile that we can use before our model fails. For the sake of realism, and to avoid shell crossing

before turn-around within the bulk of the sphere, we only consider monotonically decreasing initial density profiles. Therefore, the first shell to undergo crossing will be the innermost shell when it crosses itself at the origin and re-expands to cross incoming shells. Since our goal is to calculate the total kinetic and potential energies at turn-around with the formalism we have just presented, and since this formalism fails at shell crossing, the maximum that $\Theta_{ta}(x = 0)$ can be is 2π. Evaluating Eqn. 3.68 at $x = 0$, the maximum that the left hand side of this equation can be for $0 \leq \Theta_{ta}(0) \leq 2\pi$ is 2π, and therefore $[\bar{\delta}_i(0)/\bar{\delta}_i(R_i)]_{max} = 2^{2/3} \cong 1.587$. The amplitude of the initial density profiles that we utilize at the origin is therefore constrained by $1 \leq \bar{\delta}_i(0)/\bar{\delta}_i(R_i) \leq 1.587$.

2.3.3 Procedure

Once a $\bar{\delta}_i(x)/\bar{\delta}_i(R_i)$ profile is specified, R_{vir}/R_{ta} and Δ_c can be found in the following manner. The function $\Theta_{ta}(x)$ can be built up by solving Eqn. 3.68 for values of x from 0 to 1. The function $y(x)$ can then be found by plugging $\Theta_{ta}(x)$ into Eqn. 2.38, and $dy/dx(x)$ can then by found by taking the derivative numerically. Eqns. 2.27, 2.28 and 2.36 can then be numerically integrated to solve for $\mathscr{U}_{ta}$, $\mathscr{M}_{ta}$ and $\mathscr{K}_{ta}$. Once a density profile at virialization is specified, Eqn. 4.26 can be integrated to solve for $\mathscr{U}_{vir}$. The quantities R_{vir}/R_{ta} and Δ_c can be found by plugging $\mathscr{U}_{ta}$, $\mathscr{K}_{ta}$ and $\mathscr{U}_{vir}$ into Eqns. 2.18 and 2.20 respectively. Note that the only dependence of R_{vir}/R_{ta} and Δ_c is on the initial, normalized density profile, $\bar{\delta}_i(x)/\bar{\delta}_i(R_i)$, and on the final, virialized density profile.

2.3.4 E-dS Results

We now present our results in an E-dS universe by adopting reasonable density profiles at the initial time and at virialization. We use a power-law initial density profile of the form,

$$\frac{\bar{\delta}_i(x)}{\bar{\delta}_i(R_i)} = \frac{\delta_i(0)}{\bar{\delta}_i(R_i)}\left(1 - Ax^\beta\right), \tag{2.41}$$

since it both decreases monotonically and is quite pliable depending on the value of β. We set A such that $\bar{\delta}_i(x=1)/\bar{\delta}_i(R_i) = 1$ ($A = 1 - [\delta_i(0)/\bar{\delta}_i(R_i)]^{-1}$). The local (not volume averaged) density profile, $\delta_i(x)/\bar{\delta}_i(R_i)$, is given by the same function with $A \to A(\beta+3)/3$. This can be found with the formula, $\delta(r) = (r/3)d\bar{\delta}/dr + \bar{\delta}$, derived by taking the derivative with respect to r of Eqn. 2.4. To maximize the effects that a non-uniform initial density profile has in our calculations, we use $\bar{\delta}_i(0)/\bar{\delta}_i(R_i) = 2^{2/3}$. We show several examples of the volume averaged initial density profile in Fig. 2.1, along with the corresponding local density profiles for comparison. In Fig. 2.2 we show the x to y mapping for the same initial density profiles following the procedures outlined in the previous section. As a practical matter, the mapping becomes very difficult to solve numerically for small x at large values of β ($\gtrsim 5$), as explained in Appendix 2.6. In this regime, we use a highly accurate analytic approximation formula to calculate y as a function of x, which we derive in the same appendix. We show the physical conditions within the dark matter sphere at turn-around by plotting the non-dimensionalized velocity, density and interior mass profiles as given by Eqns. 2.34, 2.23 and 2.28. The panels show that, in contrast to the case of an initially uniform sphere, the velocity profile within the sphere at turn-around is non-zero, and the density is profile can be far from uniform.

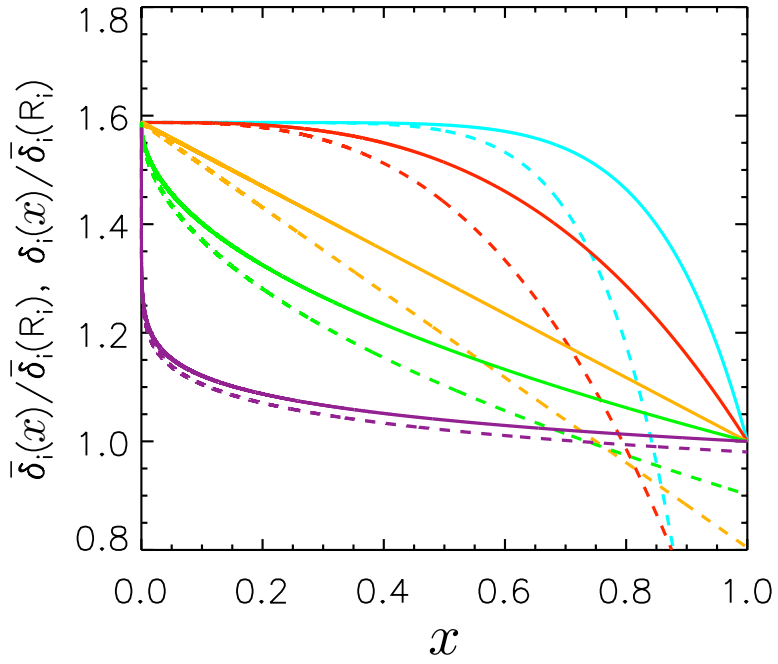

Figure 2.1.—: Examples of the volume averaged, $\bar{\delta}_i(x)/\bar{\delta}_i(R_i)$, (solid lines) and local, $\delta_i(x)/\bar{\delta}_i(R_i)$, initial density profiles that we use in our calculations. The turquoise, red, orange, light green and purple lines (top line to bottom line) correspond to $\beta = 7$, 3, 1, 0.5 and 0.1 respectively, with β defined by Eqn. 2.41.

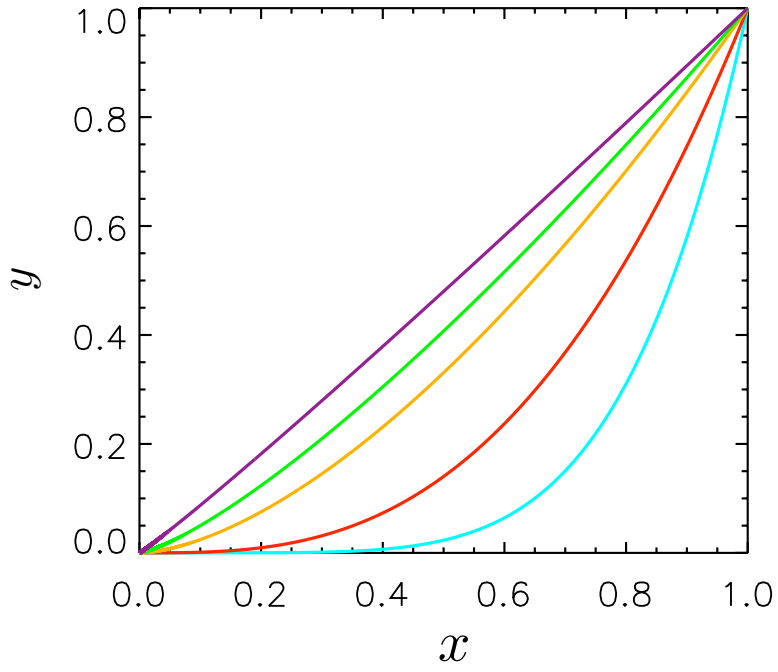

Figure 2.2.—: The normalized position at turn-around, y as a function of the initial normalized position, x for the same density profiles as in Fig. 2.1 (from bottom line to top line: $\beta = 7$, 3, 1, 0.5 and 0.1).

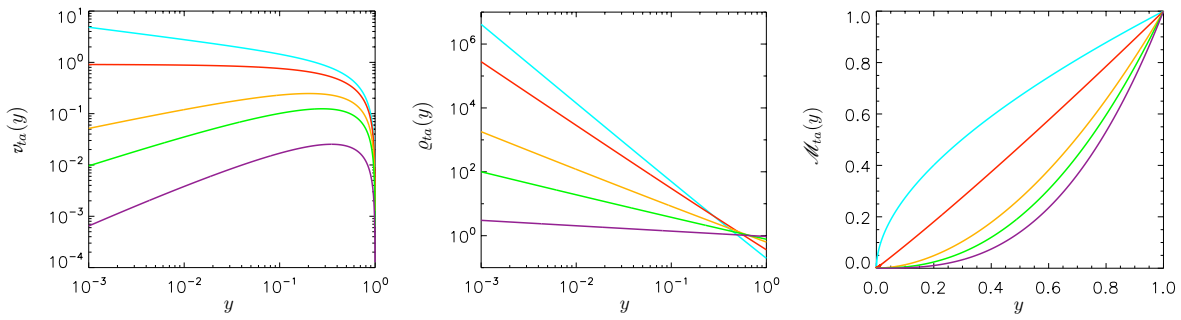

Figure 2.3.—: The normalized velocity, density and interior mass profiles (defined by Eqns. 2.33, 2.16, 2.15 respectively) within a dark matter sphere at turn-around for the same density profiles as in Fig. 2.1 (for all panels, from top line to bottom line: $\beta = 7$, 3, 1, 0.5 and 0.1).

To calculate the non-dimensionalized binding energy of the dark matter halo at virialization, we use an NFW density profile (Navarro et al. 1996). For an NFW profile,

$$\varrho(w) = \frac{1}{3}\frac{c^2}{w(1+cw)^2}\frac{1}{\ln(1+c) - \frac{c}{1+c}} \tag{2.42}$$

and

$$\mathscr{M}(w) = \frac{\ln(1+cw) - \frac{cw}{1+cw}}{\ln(1+c) - \frac{c}{1+c}}, \tag{2.43}$$

where $w \equiv r_{vir}/R_{vir}$, and where c, the concentration parameter, depends on the recent merger history of the halo. Using these expressions we calculate the non-dimsionalized binding energy at virialization with Eqn. 4.26, where the integral can be evaluated analytically:

$$\begin{aligned}\mathscr{U}_{vir} &= \frac{5}{3}\frac{c^2}{\left[\ln(1+c) - \frac{c}{1+c}\right]^2}\int_0^1 \frac{\ln(1+cw) - \frac{cw}{1+cw}}{(1+cw)^2}dw \\ &= \frac{5}{6}\frac{c[c(2+c) - 2(1+c)\ln(1+c)]}{(1+c)^2\left[\ln(1+c) - \frac{c}{1+c}\right]^2}.\end{aligned} \tag{2.44}$$

In Fig. 2.4 we show $\mathscr{U}_{vir}$ as a function of the concentration parameter, as well as $\mathscr{K}_{ta}$ and $\mathscr{U}_{ta}$ as a function of β, calculated with Eqns. 2.36 and 2.27 respectively. For comparison,

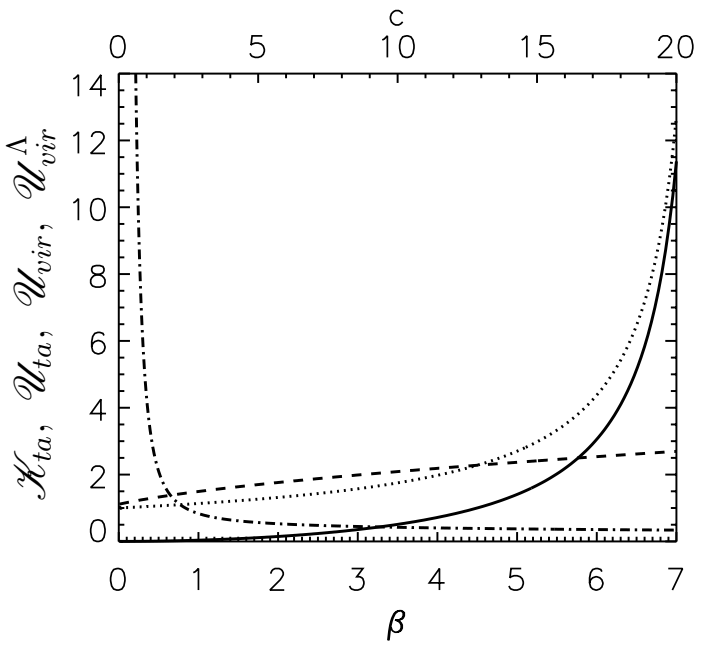

Figure 2.4.—: The non-dimensionalized kinetic (solid line) and potential energy (dotted line) at turn-around as a function of β for an E-dS cosmology (bottom x-axis), as well as the non-dimensionalized potential energy at virialization due to gravity (dashed line) and dark energy (dot-dashed line) for an NFW density profile as a function of concentration parameter, c (top x-axis). The former two quantities are independent of cosmology since they are computed directly from the NFW profile. The non-dimensionalized potential energy at virialization due dark energy, $\mathscr{U}_{vir}^{\Lambda}$, is defined in § 2.4.4.

we note that for an initially uniform sphere, $\mathscr{K}_{ta} = 0$ and $\mathscr{U}_{ta} = 1$ and for a uniform sphere at virialization $\mathscr{U}_{vir} = 1$.

Having calculated $\mathscr{K}_{ta}$, $\mathscr{U}_{ta}$ and $\mathscr{U}_{vir}$, we may now calculate R_{vir}/R_{ta} and Δ_c with Eqns. 2.18 and 2.20. We show R_{vir}/R_{ta} and Δ_c as a function of β for several values of c in Fig. 2.5. For comparison, we also show the results for the standard uniform sphere calculation in an E-dS cosmology ($R_{vir}/R_{ta} = 1/2$ and $\Delta_c = 18\pi^2$) with the black dashed line. Since, for an NFW profile, $\mathscr{U}_{vir}$ never equals unity (regardless of the value of c used) we also plot a curve with $\mathscr{U}_{vir}$ set to unity (blue dotted line) to show that in the limit that β goes to zero, our results reduce to the uniform sphere calculation. The figure shows that R_{vir}/R_{ta} and Δ_c can deviate significantly from the standard values, with a slightly stronger dependence on the density profile at virialization than on the initial density profile (i.e., a stronger dependence on c than on β). By taking into account non-uniform density profiles, the non-linear density at virialization is typically smaller by a factor of a few to more than a factor of 10 for halos with the highest concentration parameter. We note, however, that for the highest concentration parameters shown, these halos can be quite rare. In fact, when considering Fig. 2.5 (as well as Figs. 2.9 and 2.11) one should note that the concentration parameter for recently formed halos is typically $c \approx 4$ (Zhao et al. 2009). It is interesting note that for the highest values of c (the steepest NFW profiles), the virial radius can be bigger than the turn-around radius.

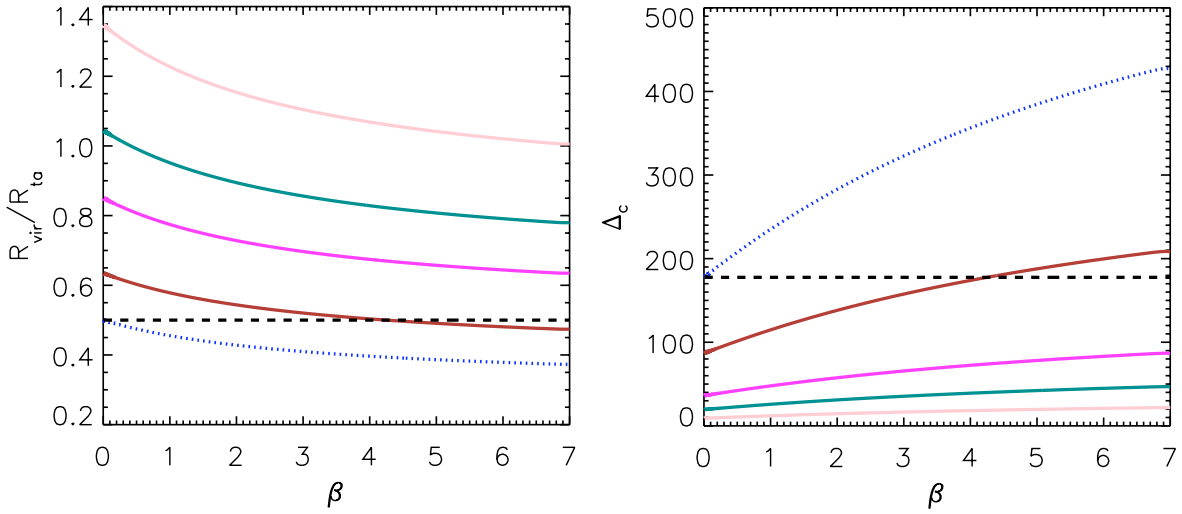

Figure 2.5.—: R_{vir}/R_{ta} and Δ_c as a function of β for different values of c. The brown, magenta, teal and pink lines (bottom line to top line in the left panel and top line to bottom line in the right panel) correspond to $c = 1$, 5, 10 and 20 respectively. The blue dotted line has $\mathscr{U}_{vir}$ set to unity (corresponding to a uniform sphere). The black dashed lines show that standard results for an initially uniform density profile.

2.4 Cosmologies with a Cosmological Constant and Curvature

The universe in which we live has a non-zero dark energy component which significantly affects the formation of cosmological structure at low redshifts. To accurately describe the non-linear collapse of halos at low redshift, we repeat our calculation of Δ_c, but include the dynamical effects of a cosmological constant. Since the derivations are not any more difficult when curvature is included, we leave our equations general to allow for any cosmology with matter, curvature and vacuum energy components.

2.4.1 R_{vir}/R_{ta} and Δ_c

To solve for R_{vir}/R_{ta} and Δ_c in a cosmology with a cosmological constant, one must include the effective gravitational potential energy due to dark energy. The gravitational density associated with dark energy is $\rho_\Lambda + 3P/c^2 = -2\rho_\Lambda = -3H_o^2\Omega_\Lambda/(4\pi G)$, from which it can be found that the contribution to the potential energy of a sphere from dark energy is:

$$U_\Lambda = -\frac{1}{2}\Omega_\Lambda H_o^2 \int_0^R 4\pi r^4 \rho(r) dr. \tag{2.45}$$

For a uniform sphere, $U_\Lambda = (-3/10)\Omega_\Lambda H_o^2 M R^2$, motivating our re-expression of the previous equation,

$$U_\Lambda = -\frac{3}{10}\Omega_\Lambda H_o^2 M R^2 \mathscr{U}^\Lambda, \tag{2.46}$$

where,

$$\mathscr{U}^\Lambda = 5\int_0^1 \varrho(r) r^4 dr. \tag{2.47}$$

Analogous to the case of $\mathscr{U}$ introduced in Eqn. 2.13, $\mathscr{U}^\Lambda$ can either be viewed as a geometric correction factor accounting for the deviation of a sphere from complete homogeneity, or as the non-dimensionalized binding energy of a sphere due to dark energy.

According to the virial theorem, for potential energies of the form $U \propto R^n$, $KE = (n/2)U$, where the energies are time averaged. Since $U_\Lambda \propto R^2$ and $U \propto R^{-1}$ (see Eqns. 2.13 and 2.46), for a dark matter halo at virialization, $KE_{vir} = -U_{vir}/2 + U^\Lambda_{vir}$, and the total energy is therefore $E_{vir} = KE_{vir} + U_{vir} + U^\Lambda_{vir} = U_{vir}/2 + 2U^\Lambda_{vir}$. If energy is conserved between turn-around virialization then $KE_{ta} + U_{ta} + U^\Lambda_{ta} = U_{vir}/2 + 2U^\Lambda_{vir}$.

Replacing the potential energies in this equation with Eqns. 2.13 and 2.46 results in:

$$KE_{ta} - \frac{3}{5}\frac{GM^2}{R_{ta}}\mathscr{U}_{ta} - \frac{3}{10}\Omega_\Lambda H_o^2 M R_{ta}^2 \mathscr{U}_{ta}^\Lambda = -\frac{3}{10}\frac{GM^2}{R_{vir}}\mathscr{U}_{vir} - \frac{3}{5}\Omega_\Lambda H_o^2 M R_{vir}^2 \mathscr{U}_{vir}^\Lambda. \quad (2.48)$$

Using Eqns. 2.29 and 2.31, and after a bit of algebra, one finds the following cubic in R_{vir}/R_{ta}:

$$4\zeta\mathscr{U}_{vir}^\Lambda \left(\frac{R_{vir}}{R_{ta}}\right)^3 - 2\left[\mathscr{U}_{ta} - \mathscr{K}_{ta} + \zeta\mathscr{U}_{ta}^\Lambda\right]\frac{R_{vir}}{R_{ta}} + \mathscr{U}_{vir} = 0, \quad (2.49)$$

with

$$\zeta[\bar{\delta}_i(R_i)/a_i] \equiv \frac{\Omega_\Lambda}{\Omega_m}\mathcal{X}_{ta}^3[\bar{\delta}_i(R_i)/a_i], \quad (2.50)$$

and where $\mathscr{K}_{ta}$ is still defined by Eqn. 2.19. The proper solution of R_{vir}/R_{ta} is the smallest, positive, pure real root of the cubic (if a positive, pure real root exists). A physical solution will not exist if the initial seed of the perturbation, $\bar{\delta}_i/a_i$, is less than a critical value, given by Rubin & Loeb (2013a):

$$\left(\frac{\bar{\delta}_i}{a_i}\right)_{cr} = \frac{3}{10\Omega_m}\left[2\Omega_k + 3\left(2\Omega_\Lambda\Omega_m^2\right)^{1/3}\right]. \quad (2.51)$$

The equation implies that the presence of curvature and/or a cosmological constant can prevent a perturbation from ever turning around to eventually form a virialized halo even if $\bar{\delta}_i/a_i > 0$.

Having solved for R_{vir}/R_{ta}, we may now solve for Δ_c. This parameter can be written as

$$\Delta_c(z_c) = \left(\frac{R_{vir}}{R_{ta}}\right)^{-3}\frac{a_c^3\Omega_m(z_c)}{\mathcal{X}_{ta}^3}, \quad (2.52)$$

where we have used Eqns. 2.29, 2.31 and

$$\rho_c(z_c) = \frac{3H_o^2\Omega_m}{8\pi G\Omega_m(z_c)a_c^3}, \quad (2.53)$$

and where

$$\Omega_m(z) = \frac{\Omega_m(1+z)^3}{\Omega_m(1+z)^3 + \Omega_\Lambda + \Omega_k(1+z)^2}. \quad (2.54)$$

In the limit of a homogenous sphere, $\mathscr{U}_{vir}$ and $\mathscr{U}_{ta} \rightarrow 1$ and $\mathscr{K}_{ta} \rightarrow 0$, Eqns. 2.49 and 2.52 reduce to the equations for R_{vir}/R_{ta} and Δ_c derived assuming an initially uniform sphere (for example, see Eqns. 2.18 and 2.23 of Rubin & Loeb 2013a).

Equations. 2.49 and 2.52 show that one of the main differences between the calculation of R_{vir}/R_{ta} and Δ_c in an E-dS cosmology and in a general cosmology is that in the former case, these quantities are constant, while in the latter case, they are functions of the collapse redshift of the halo. This is because these parameters depend on $\mathcal{X}_{ta}$ (through Eqn. 2.50), which is a function of the initial seed, $\bar{\delta}_i(R_i)/a_i$, which uniquely determines the collapse redshift of a halo. Once a value of $\bar{\delta}_i(R_i)/a_i$ is specified, the halo collapse time (defined as twice the turn-around time) can be found by integrating Eqn. 3.3:

$$H_o t_c = 2\,\mathcal{I}\left[0, \mathcal{X}_{ta}, \frac{\bar{\delta}_i(R_i)}{a_i}\right], \tag{2.55}$$

where $\mathcal{X}_{ta}$ is also solely a function of $\bar{\delta}_i(R_i)/a_i$ (see Eqn. 3.7), and where $\mathcal{I}$ is defined by Eqn. 2.6. The collapse time can then be converted to a collapse redshift by integrating the Friedmann equation:

$$H_o t_c = \int_0^{a_c} da' \left[1 + \Omega_m\left(\frac{1}{a'} - 1\right) + \Omega_\Lambda(a'^2 - 1)\right]^{-1/2}, \tag{2.56}$$

where $a_c = (1 + z_c)^{-1}$, and matching the times. Thus, by setting the previous two equations equal to each other, one may numerically build up $\bar{\delta}_i(R_i)/a_i$ as a function of z_c.

A very accurate fitting formula for $\bar{\delta}_i(R_i)/a_i$ given a collapse redshift, z_c, is given by Rubin & Loeb (2013a):

$$\frac{\bar{\delta}_i(R_i)}{a_i} = \frac{0.674588(1 + z_c)}{\Omega_m^{0.9945}(z_c)}\left\{\Omega_m^{4/7}(z_c) + \Omega_\Lambda(z_c) + \left[1 + \frac{\Omega_m(z_c)}{2}\right]\left[1 + \frac{\Omega_\Lambda(z_c)}{70}\right]\right\}, \tag{2.57}$$

where this expression is strictly valid for a flat cosmology. This formula was found by inserting a fitting formula for the linear theory growth factor (Carroll et al. 1992) and

a fitting formula for the linear theory over-density at collapse (Mo et al. 2010) into the linear theory relation, $\bar{\delta}_i/a_i = \bar{\delta}_c(z_c)/D(z_c)$ (where it is assumed that $a_i << 1$ so that $D(a_i) \rightarrow a_i$).

2.4.2 Conditions at Turn-around

As we have done for the E-dS calculation, we now express the conditions at turn-around in terms of the mapping, x to y. We then solve for the mapping using the shell kinematics as given by the spherical collapse model.

Density and Potential Energy

In the case of a general cosmology, the non-dimesionalized density, binding energy and interior mass profile is still given by Eqns. 2.23, 2.27 and 2.28 respectively, with the caveat that the function $x(y)$ must be re-solved to include curvature and a cosmological constant (we cover this in § 2.4.2). The non-dimensionalized binding energy at turn-around associated with dark energy is found simply by inserting Eqn. 2.23 into Eqn. 2.47:

$$\mathscr{U}_{ta}^{\Lambda} = 5 \int_0^1 y^2 \frac{dx}{dy}(y) x^2(y) dy. \tag{2.58}$$

Velocity and Kinetic Energy

The non-dimensionalized velocity profile at turn-around (defined in Eqn. 2.33) for a dark matter sphere in a general cosmology can be found by rearranging Eqn. 3.3,

$$v_{ta}^2(y) = \frac{x^3}{y} + \zeta y^2 + x^2 \mathcal{X}_{ta} \left[\frac{\Omega_k}{\Omega_m} - \frac{5}{3} \left(\frac{\bar{\delta}_i(x)}{\bar{\delta}_i(R_i)} \right) \left(\frac{\bar{\delta}_i(R_i)}{a_i} \right) \right]. \tag{2.59}$$

Inserting this expression into Eqn. 2.32, we find the non-dimensionalized kinetic energy of the sphere at turn-around:

$$\mathscr{K}_{ta} = 5\int_0^1 x^2(y)\frac{dx}{dy}(y)\left\{\frac{x^3(y)}{y} + \zeta y^2 + x^2(y)\mathcal{X}_{ta}\left[\frac{\Omega_k}{\Omega_m} - \frac{5}{3}\left(\frac{\bar{\delta}_i(x)}{\bar{\delta}_i(R_i)}\right)\left(\frac{\bar{\delta}_i(R_i)}{a_i}\right)\right]\right\}dy, \tag{2.60}$$

which reduces to Eqn. 2.36 in the limit that $\Omega_k, \Omega_\Lambda \to 0$ and $\Omega_m \to 1$.

Solving the Mapping Using Spherical Collapse

To solve for the x to y mapping in a general cosmology, we must first specify the halo collapse redshift of interest, z_c. The corresponding $\bar{\delta}_i(R_i)/a_i$ value can then be calculated as explained in § 2.4.1. The non-dimensionalized turn-around radius of the outermost shell, $\mathcal{X}_{ta}$, is then found by solving Eqn. 3.7, and the turn-around time is found by evaluating the following integral:

$$t_{ta}H_o = \mathcal{I}\left[0, \mathcal{X}_{ta}\left(\frac{\bar{\delta}_i(R_i)}{a_i}\right), \frac{\bar{\delta}_i(R_i)}{a_i}\right]. \tag{2.61}$$

To solve for the position of a shell at time $t_{ta}H_o$ which starts at x, we re-write Eqn. 3.3 as

$$\frac{d\chi}{d(tH_o)} = \pm\sqrt{\frac{\Omega_m}{\chi} + \Omega_\Lambda\chi^2 + \Omega_k - \frac{5}{3}\left(\frac{\bar{\delta}_i(x)}{\bar{\delta}_i(R_i)}\right)\left(\frac{\bar{\delta}_i(R_i)}{a_i}\right)\Omega_m}, \tag{2.62}$$

where the velocity is taken to be positive if $tH_o < t_{\mathscr{TA}}H_o$, and negative if $tH_o > t_{\mathscr{TA}}H_o$ (keeping in mind that $t_{\mathscr{TA}}$ corresponds to the turn-around time of a shell starting at x). Thus, if the initial normalized density profile, $\bar{\delta}_i(x)/\bar{\delta}_i(R_i)$, is known, a value of x is specified and the differential equation is integrated numerically with $\chi(t=0) = 0$ until $tH_o = t_{ta}H_o$ to find $\chi_{ta}(x)$. The corresponding y value is then found with Eqn. 2.37. By repeating this procedure for values of $x \in [0,1]$, we build up the function $x(y)$.

As noted in § 2.3.2, there is a maximum value of $\bar{\delta}_i(0)/\bar{\delta}_i(R_i)$ for which our analysis is valid due to the innermost shell undergoing shell crossing at the origin before the outermost shell turns around. We can solve for this value numerically by matching the time it takes for the innermost shell to reach the origin with with the time it takes for the outermost shell to turn-around (Eqn. 2.61):

$$2\,\mathcal{I}\left[0, \chi_{\mathscr{TA}}\left(\frac{\bar{\delta}_i(0)}{a_i}\right), \left(\frac{\bar{\delta}_i(0)}{\bar{\delta}_i(R_i)}\right)_{max}\left(\frac{\bar{\delta}_i(R_i)}{a_i}\right)\right] = \mathcal{I}\left[0, \chi_{ta}\left(\frac{\bar{\delta}_i(R_i)}{a_i}\right), \frac{\bar{\delta}_i(R_i)}{a_i}\right]. \quad (2.63)$$

The parameter $\chi_{\mathscr{TA}}(\bar{\delta}_i(0)/a_i)$ is found from Eqn. 3.7 with the substitution $\bar{\delta}_i(0)/a_i \rightarrow [\bar{\delta}_i(0)/\bar{\delta}_i(R_i)][\bar{\delta}_i(R_i)/a_i]$. We solve for $(\bar{\delta}_i(0)/\bar{\delta}_i(R_i))_{max}$ as a function of z_c for a cosmology with $\Omega_m = 0.27$ and $\Omega_\Lambda = 0.73$, shown in Fig. 2.6. At high redshift, when the cosmology approaches an E-dS cosmology, $(\bar{\delta}_i(0)/\bar{\delta}_i(R_i))_{max}$ approaches the E-dS value of $2^{2/3}$.

2.4.3 Procedure

The values of R_{vir}/R_{ta} and Δ_c as functions of the collapse redshift for a specified cosmology are found in the following manner. First, we specify a collapse redshift, z_c, and normalized initial density profile, $\bar{\delta}_i(x)/\bar{\delta}_i(R_i)$. The value of $\bar{\delta}_i(R_i)/a_i$ corresponding to z_c is then found either by equating Eqns. 2.55 and 3.8 and solving for $\bar{\delta}_i(R_i)/a_i$ numerically, or by simply using Eqn. 2.57 (for a flat cosmology). We then solve for the x to y mapping as explained in § 2.4.2. Once the $x(y)$ function is found, the non-dimensionalized kinetic energy, interior mass profile and potential energies associated with gravity and dark energy at turn-around are found by integrating Eqns. 2.60, 2.28, 2.27 and 2.58, respectively. By specifying a density profile at virialization, the non-dimensionalized potential energies associated with gravity and dark energy at virialization can be found by integrating Eqns. 4.26 and 2.47, respectively. The ratio R_{vir}/R_{ta} is then found

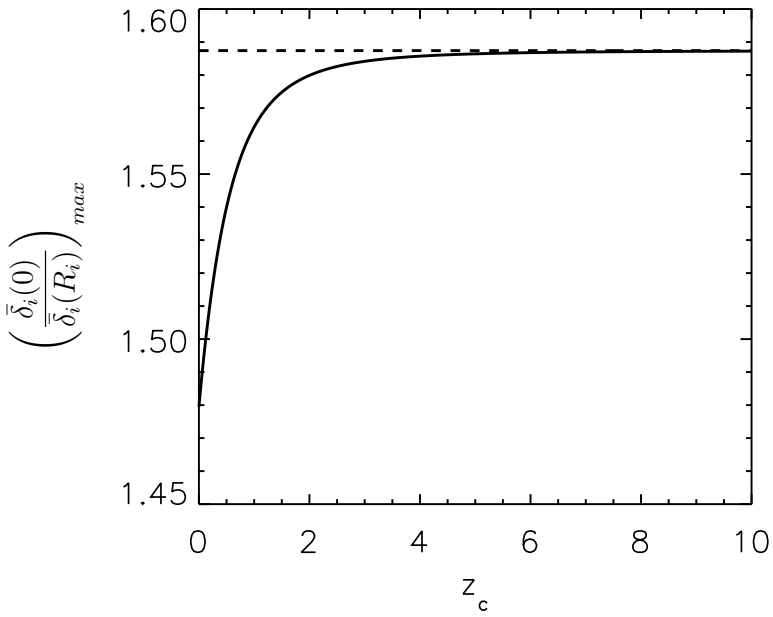

Figure 2.6.—: The maximum value of $\bar{\delta}_i(0)/\bar{\delta}_i(R_i)$ allowed for a monotonically decreasing density profile before our model breaks down due to shell crossing. The solid line is for a cosmology with $\Omega_m = 0.27$ and $\Omega_\Lambda = 0.73$, and the dashed line is for an E-dS cosmology $(\bar{\delta}_i(0)/\bar{\delta}_i(R_i))_{max} = 2^{2/3}$.

by numerically solving the cubic in Eqn. 2.49, and Δ_c is found with Eqn. 2.52. This entire procedure is then repeated for different values of z_c so that we may build up the functions, $R_{vir}/R_{ta}(z_c)$ and $\Delta_c(z_c)$.

2.4.4 ΛCDM Results

In this section we present results for a ΛCDM cosmology with $(\Omega_m, \Omega_\Lambda) = (0.27, 0.73)$, consistent with the WMAP7+BAO+H_o cosmological parameters of Komatsu et al. (2011). We note that although these parameters may differ slightly from those as measured by the Planck satellite, slight differences in $(\Omega_m, \Omega_\Lambda)$ do not produce any

appreciable differences in our results. We consider two different prescriptions to define the initial density profile. As a simple example, we use the same initial density profile as in § 2.3.4 (Eqn. 2.41), with the normalization at $z = 0$ chosen to avoid shell crossing before $z_c = 0$ in a ΛCDM cosmology. We also calculate results for more realistic initial density profiles, derived from the statistics of peaks in an initial density field characterized by the linear theory matter power spectrum. In either case, we assume an NFW profile as the final halo density profile, so that $\mathscr{U}_{vir}$ is still given by Eqn. 2.44. The non-dimensionalized binding energy associated with dark energy, $\mathscr{U}^{\Lambda}_{vir}$, is found by integrating Eqn. 2.47, with $\varrho(r)$ given by Eqn. 2.42. The integral can be computed analytically, and is

$$\begin{aligned}\mathscr{U}^{\Lambda}_{vir} &= \frac{5}{3}\frac{c^2}{\ln(1+c) - \frac{c}{1+c}}\int_0^1 \frac{w^3}{(1+cw)^2}dw \\ &= \frac{5}{6}\frac{c[c(c-3)-6] + 6(1+c)\ln(1+c)}{c^2(1+c)\left[\ln(1+c) - \frac{c}{1+c}\right]},\end{aligned} \tag{2.64}$$

which is plotted as a function of c in Fig. 2.4.

Power-law Initial Density Profile

For an initial density profile given by Eqn. 2.41, as with the E-dS case, we choose the value of $\bar{\delta}_i(0)/\bar{\delta}_i(R_i)$ to avoid shell crossing before the outermost shell turns around. The maximum that $\bar{\delta}_i(0)/\bar{\delta}_i(R_i)$ can be in order to avoid shell crossing before t_{ta} for a ΛCDM cosmology, given a halo collapse redshift, is shown in Fig. 2.6. The value of $(\bar{\delta}_i(0)/\bar{\delta}_i(R_i))_{max}$ at $z_c = 0$ is about 1.479450. Since $(\bar{\delta}_i(0)/\bar{\delta}_i(R_i))_{max}$ increases monotonically with z_c, we can avoid shell crossing at all values of z_c by choosing $\bar{\delta}_i(0)/\bar{\delta}_i(R_i)$ just below this value. We therefore use a constant value of $\bar{\delta}_i(0)/\bar{\delta}_i(R_i) = 1.479$. By using a constant value of $\bar{\delta}_i(0)/\bar{\delta}_i(R_i)$, rather than using the

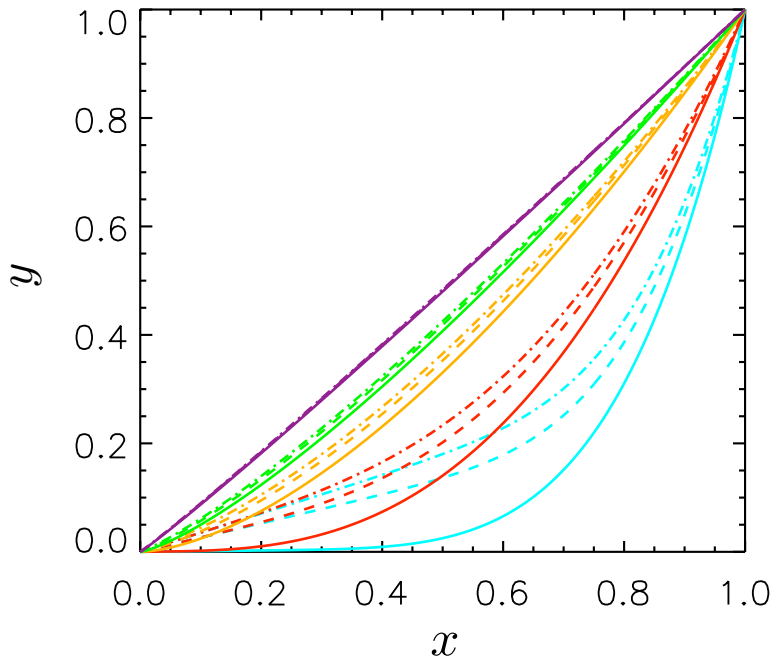

Figure 2.7.—: The x - y mapping for a ΛCDM cosmology with an initial density profile given by Eqn. 2.41 with $\bar{\delta}_i(0)/\bar{\delta}_i(R_i) = 1.479$. The different colors correspond to the same β values as in Fig. 2.1 (from bottom lines to top lines: $\beta = 7$, 3, 1, 0.5 and 0.1). The solid, dashed, and dot-dashed lines correspond to collapse redshifts of 0, 0.5 and 3 respectively.

$(\bar{\delta}_i(0)/\bar{\delta}_i(R_i))_{max}$ value for the z_c under consideration, we keep interpretation of our results simple. That is, we keep the initial density profile constant so that we may be able to clearly see how our results vary with only z_c.

In Fig. 2.7, we show the x - y mapping for several values of β (where β is defined in Eqn. 2.41) for halos collapsing at different redshifts. The redshift of collapse clearly affects the mapping, especially at high values of β. In Fig. 2.8 we show the non-dimensionalized kinetic and binding energies at turn-around as a function of collapse redshift for the same values of β. For comparison, for a top-hat, the non-dimensionalized kinetic and binding energies at turn-around should be 0 and unity respectively. We note

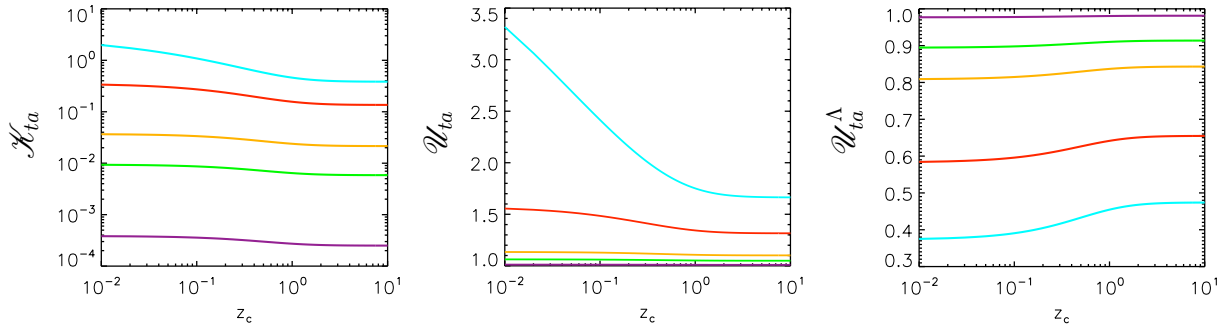

Figure 2.8.—: The non-dimensionalized kinetic and potential energies associated with gravity and dark energy at turn-around as a function of collapse time for a ΛCDM cosmology. In each panel, the different color lines correspond to the same β values as in Fig. 2.1 ($\beta = 7$, 3, 1, 0.5 and 0.1 from top line to the bottom line for the left two panels and from bottom line to top line for the rightmost panel).

that we do not run into the same numerical issues for high values of β as with the E-dS case (see App. 2.6), so that we do not need to resort to an approximation formula. This is because our value of $\bar{\delta}_i(0)/\bar{\delta}_i(R_i) = 1.479$ is sufficiently below $(\bar{\delta}_i(0)/\bar{\delta}_i(R_i))_{max}$ at $z_c = 0$ (about 1.479450) that we avoid having to resolve prohibitively small differences in our calculations.

We show our results for R_{vir}/R_{ta} and Δ_c as functions of z_c for the same values of β, and for $c = 1$, 5, and 10 in Fig. 2.9. For comparison, we show the standard initial top-hat results for a ΛCDM cosmology (solid black lines in both panels). We see that Δ_c is typically lower than the top-hat case by a factor of a few to as much a factor of about 10. As with the E-dS results, non-uniformity can allow the virial radius to be bigger than the turn-around radius.

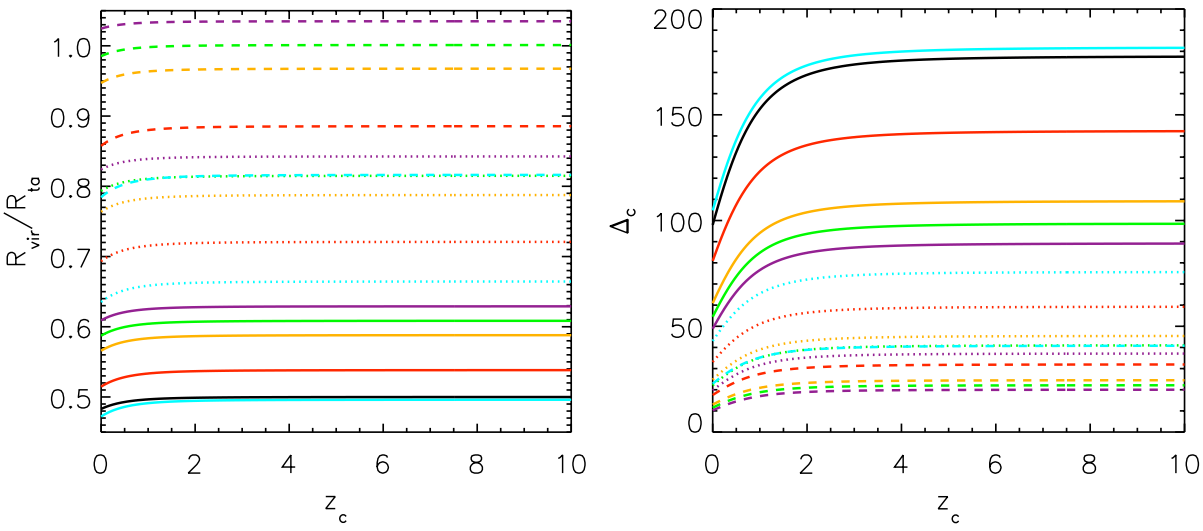

Figure 2.9.—: R_{vir}/R_{ta} and Δ_c as functions of the collapse redshift for different values of β and concentration parameter. In each panel, the different color lines correspond to the same β values as in Fig. 2.1. The solid, dotted, and dashed lines correspond to $c = 1$, 5 and 10 respectively. The solid black line corresponds to the standard initial top-hat result.

Peak Statistics Initial Density Profiles

In this section we consider the collapse of halos initially seeded by highly realistic density profiles calculated from the statistics of a Gaussian random field. With a given linear theory matter power spectrum, one may calculate average halo density profiles while still in the linear regime (Bardeen et al. 1986). In App. 2.7 we summarize this formalism, and cover how we use it to calculate the initial, normalized, volume averaged density profiles, $\bar{\delta}_i(x)/\bar{\delta}_i(R_i)$, needed for our calculations. The profiles are parameterized by halo mass, M, collapse redshift, z_c, and a co-moving smoothing scale, M_f. In Fig. 2.10 we show examples of these profiles along with the local (non-volume averaged) profiles for several combinations of halo mass, collapse redshift and smoothing scale.

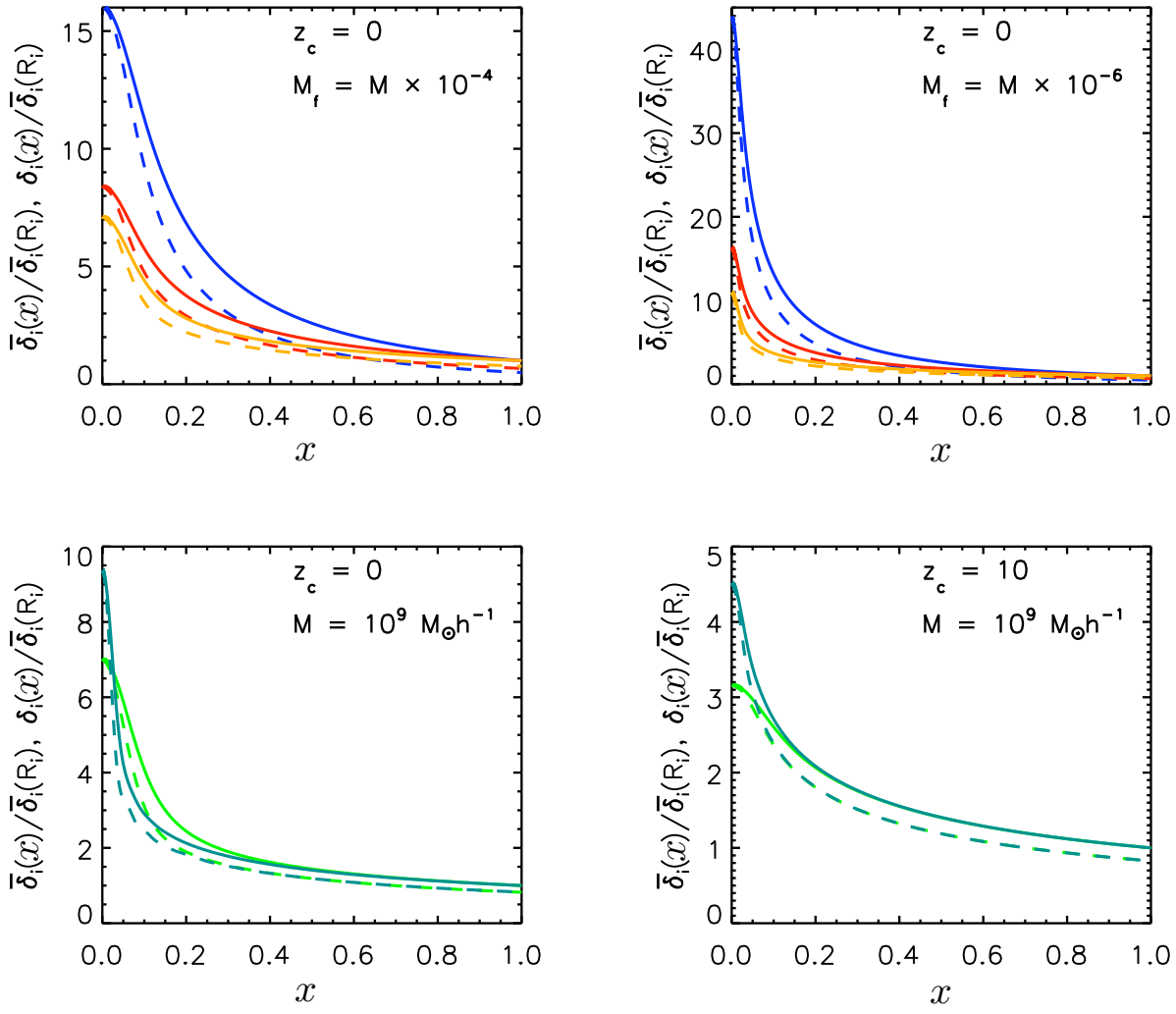

Figure 2.10.—: Examples of the volume averaged $\bar{\delta}_i(x)/\bar{\delta}_i(R_i)$ (solid lines) and local $\delta_i(x)/\bar{\delta}_i(R_i)$ (dashed lines) initial density profiles calculated from the peak statistics formalism presented in App. 2.7. The top two panels show profiles with halo masses of $M = 10^{15}$ (blue), 10^{13} (red) and $10^{11}\mathrm{M}_\odot h^{-1}$ (orange) (top set of lines to bottom set of lines) for $z_c = 0$ and $M_f = 10^{-4}$ and 10^{-6} times the halo mass. The bottom two panels show profiles for a $10^9\mathrm{M}_\odot h^{-1}$ halo with M_f=10^5 (teal) and $M_f = 10^3\mathrm{M}_\odot h^{-1}$ (light green) (top set of lines to bottom set of lines) collapsing at $z_c = 0$ and $z_c = 10$.

From Fig. 2.10 it is clearly evident that for these density profiles, shell crossing within the halo will occur before the outermost shell turns around since the density of the innermost shell can far exceed ~ 1.48 (as previously discussed). We therefore may not use the shell kinematic formalism derived in § 2.4.2 to calculate the physical conditions at turn-around (i.e., $\mathscr{K}_{ta}$, $\mathscr{U}_{ta}$ and $\mathscr{U}_{ta}^{\Lambda}$). To calculate these quantities, we employ a one dimensional Lagrangian simulation (described in detail in App. 2.8) up until the outermost shell turns around. These quantities are then found by summing across all shells at the end of the simulation using Eqns. 2.104-2.106 (where the symbols in these equations are defined throughout App. 2.8).

To calculate R_{vir}/R_{ta} and Δ_c we may still use Eqns. 2.49 and 2.52 since these equations only assume global conservation of energy (not energy conservation for each particular shell). We calculate these quantities for halo masses ranging from $M = 10^9$ to $M = 10^{15}\mathrm{M}_{\odot}h^{-1}$. This range in mass corresponds roughly to the halo mass of a small galaxy up to a large galaxy cluster. To calculate $\mathscr{U}_{vir}^{\Lambda}$ and $\mathscr{U}_{vir}$ we again use an NFW profile at virialization (Eqns. 2.64 and 2.44) with $c = 4$. We show R_{vir}/R_{ta} and Δ_c as functions of collapse redshift for different halo masses in Fig. 2.11. For $M = 10^9\mathrm{M}_{\odot}h^{-1}$ we show the results for two different smoothing scales (teal and light green lines). It is seen that R_{vir}/R_{ta} and Δ_c have little dependance on smoothing scale. For halos of larger mass, these quantities have even less dependance on smoothing scale. We do not plot Δ_c from the standard calculation since it goes significantly above 120. It should be kept in mind that, as see in Fig. 2.9, this function starts at about 100 and rises gradually to about 180 at the highest redshifts. By using these density profiles, Δ_c is typically smaller by a factor of a few as compared to the standard calculation.

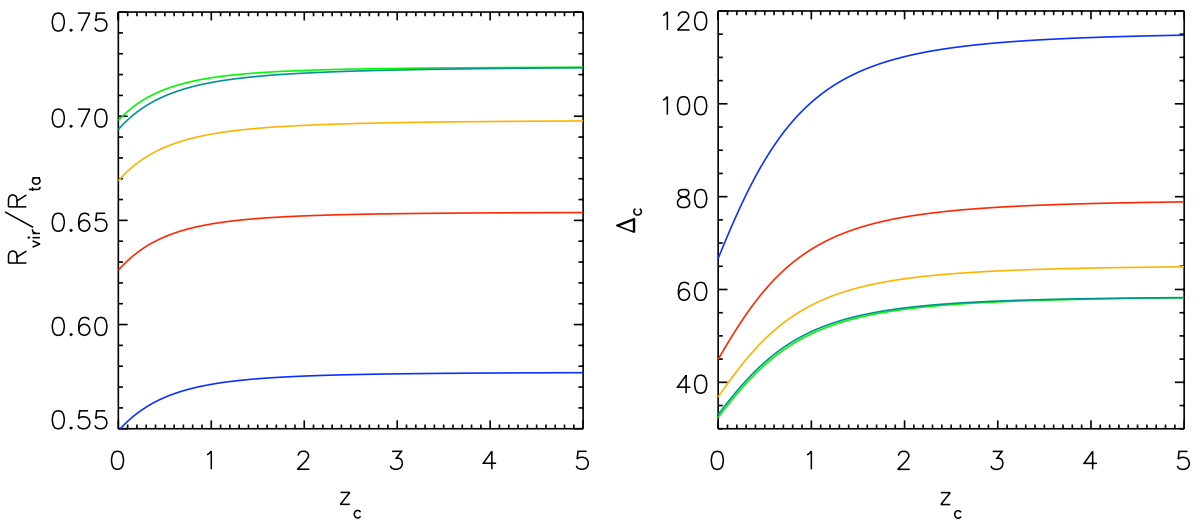

Figure 2.11.—: R_{vir}/R_{ta} and Δ_c as functions of the collapse redshift for halos initialized with density profiles calculated from the peak statistics formalism. The blue, red, orange, teal and light green lines (bottom line to top line in the left panel and top line to bottom line in the right panel) correspond to $(M, M_f)/\mathrm{M}_\odot h^{-1} = (10^{15}, 10^{10})$, $(10^{13}, 10^{8})$, $(10^{11}, 10^{7})$, $(10^{9}, 10^{5})$ and $(10^{9}, 10^{3})$, respectively.

2.5 Discussion and Conclusions

We have calculated the non-linear density of a halo at virialization based on the spherical collapse of a density peak with arbitrary initial and final density profiles. This is an improvement over the standard result which assumes top-hat profiles in order to simplify the calculation. For collapsing halos in an E-dS universe, we have used the parametric solution of spherical collapse to solve for the density and velocity profiles at turn-around. We are thus able to calculate the total potential and kinetic energy at turn-around. By assuming a density profile at virialization, we are able to employ the virial theorem to calculate the non-linear over-density at the time of collapse. Using power-law profiles for the initial density and an NFW profile for the virialized density, we find that the

over-density at collapse can be lower by a factor of 10 relative to the standard value of 178.

We extend our calculation to cosmologies which can include curvature and a cosmological constant. For moderately peaked initial density profiles, we numerically solve the equations of spherical collapse till turn-around. For initial profiles which result in shell crossing before turn-around, we implement a one dimensional numerical simulation. We calculate the over-density for halos in a ΛCDM cosmology using power-law initial density profiles and profiles calculated from the statistics of a Gaussian random field characterized by a ΛCDM linear theory matter power spectrum. For all cases, we find that the non-linear halo density at collapse is significantly smaller by as much as a factor of about 20 (depending on the density profiles used) than that as predicted by the standard top-hat calculation. We note that for regions in our universe with large-scale over-densities (such as superclusters) or large-scale under-densities (such as voids) the over-density of newly formed halos is the same, regardless of environment. Even though the dynamics of these regions are effectively governed by a cosmology that includes curvature, Rubin & Loeb (2013a) show that, regardless of the large-scale over/under-density, halos collapsing at the same time must have the same non-linear density.

While our calculation is an improvement over the standard one, it is still based on a highly simplified model of the dynamics of halo collapse. We have assumed that halos evolve in isolation, so that the gravitational potential of nearby matter can be ignored. In reality, nearby matter exerts torques on a collapsing halo, inducing angular momentum and breaking the spherical symmetry. In fact, numerical simulations show that halo collapse is in general ellipsoidal rather than spherical. The assumption of

isolation also ignores the accretion of matter and mergers during collapse. Additionally, by only considering the final, virialized state of the system, we have swept under the rug all the uncertain physics that occurs during virialization.

It is interesting to ask how our results may affect analytic halo mass functions when implemented in them. One such function, the Press-Schechter (PS) (Press & Schechter 1974) mass function, requires a linearized density threshold above which a halo is defined. This threshold is typically found by using the spherical collapse model to determine the collapse time (defined as twice the turn-around time) of a top-hat density perturbation in the cosmic density field. Linear theory is then used to calculate the linear over-density at the time of collapse, δ_c, which, for an E-dS universe equals 1.686. Our results, however, will not affect the PS mass function since our definition of the halo collapse time (twice the turn-around time of the outermost shell) is equivalent to the collapse time of a top-hat perturbation since we do not consider halos whose outermost shell undergoes shell crossing before turn around. Another mass function which compares better to numerical simulations is the Sheth-Tormen (ST) mass function (Sheth et al. 2001), the form of which is motivated by ellipsoidal collapse. Our results have no effect on the ST mass function either since its shape is determined by several free parameters which are calibrated with numerical simulations.

An important implication of our results is how they affect the halo mass function measured from simulations which use halo finders that search for an over-density threshold in the cosmological density field (the spherical over-density method). For example, Watson et al. (2013) have studied this problem by implementing cosmological simulations and by measuring the halo mass function using different over-density thresholds. They find that the halo mass function measured with an arbitrary over-density criterion is

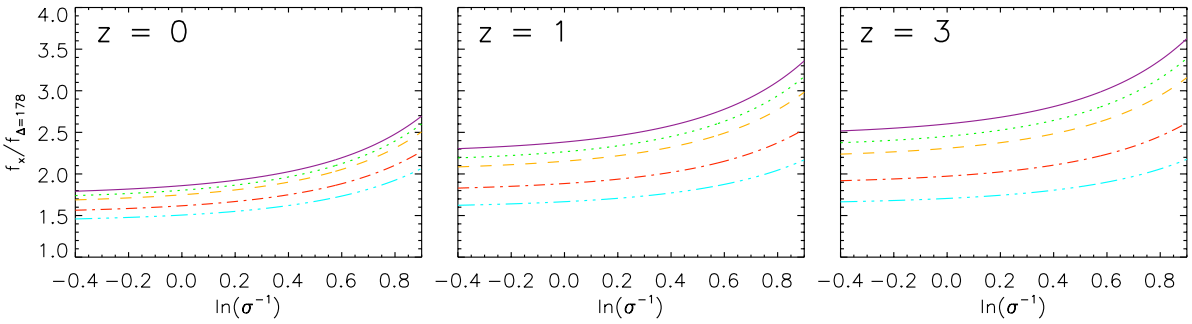

Figure 2.12.—: The halo mass function using an over-density criterion given by our calculations relative to the halo mass function with the standard 178 over-density criterion. We use power-law initial density profiles with $\beta = 7$, 3, 1, 0.5, 0.1 (dot-dot-dot dashed turquoise, dot-dashed red, dashed orange, dotted green and solid purple lines respectively). Here, $f \equiv dN/d\ln\sigma^{-1}$, where N is the halo mass function and σ is the cosmic variance. To make these figures, we use the fitting functions provided by Watson et al. (2013).

related to the halo mass function measured with the 178 criterion by a simple scaling relation. Defining f to be $dN/d\ln\sigma^{-1}$, where N is the halo mass function and σ is the cosmic variance of different sized regions, they provide an accurate fitting formula (as a function of over-density criterion, z and σ) for the scaling relation $f_x/f_{\Delta=178}$. Using this fitting formula, we show how our results may affect the measured halo mass function in a ΛCDM cosmology. Given collapse redshifts of 0, 1 and 3, we calculate the appropriate over-density criterion, Δ_c, assuming power-law initial density profiles with $\beta = 0.1$, 0.5, 1, 3 and 7 and an NFW profile with $c = 5$ at virialization[4]. Fig. 2.12 shows that the mass

[4]We should note that the fitting function for $f_x/f_{\Delta=178}$ at a particular redshift represents the cumulative effect of halo collapse (and halo mergers) at all earlier times. It is thus not strictly valid to use a single over-density criterion to calculate $f_x/f_{\Delta=178}$ at z. For simplicity, however, we use $\Delta_c(z_c = z)$.

function measured with our over-density criterion can be several times higher relative to the standard 178 criterion mass function. The discrepancy is most significant at the highest halo masses. The overall enhancement of the halo mass function when using our over-density threshold makes qualitative sense since it is easier for density peaks to meet the halo criterion when it is lowered. This discrepancy is important when analytic models of the halo mass function are assessed by their agreement with the results from numerical simulations.

2.6 Appendix A: Approximation Formula for x - y Mapping in an E-dS Universe

Numerically calculating the mapping from x to y as given by the formalism in § 2.3.2 becomes impossible for small x at the largest values of β. This is because, as seen in Fig. 2.1, $\bar{\delta}_i(x)/\bar{\delta}_i(R_i)$ comes very close $2^{2/3}$ for small x when β is large (for example, see the turquoise line which corresponds to $\beta = 7$). Thus, when the outermost shell turns around, the inner shells have a value of $\Theta_{ta}(x)$ extremely close to 2π (i.e., these shells are almost fully collapsed). Even when using double-precision, the difference between $\Theta_{ta}(x)$ and 2π ($\equiv \Delta_\Theta$) for these shells becomes impossible to resolve numerically. Since $y \propto 1 - \cos\Theta_{ta}(x) \propto \Delta_\Theta^2/2 + \mathcal{O}(\Delta_\Theta^4)$ (see Eqn. 2.38) when expanded around 2π, y is also impossible to resolve. This is a problem in our analysis, because even though y is very small in this regime, these shells still contribute non-negligibly to the integrals used to compute $\mathscr{M}_{ta}$, $\mathscr{U}_{ta}$ and $\mathscr{K}_{ta}$.

In this appendix, we derive a highly accurate approximation formula used to

calculate the mapping in this regime. We start by setting equal the solution for the time of the outermost shell at turn-around to the solution at this time for a shell starting at x, found by integrating Eqn. 3.3 in an E-dS universe:

$$\int_0^{\mathcal{X}_{ta}} \frac{dx}{\sqrt{\frac{1}{x}-\frac{5}{3}\frac{\bar{\delta}_i(R_i)}{a_i}}} = \int_0^{\mathcal{X}_{\mathscr{TA}}} \frac{dx}{\sqrt{\frac{1}{x}-\frac{5}{3}\frac{\bar{\delta}_i(r_i)}{a_i}}} + \int_{\frac{y}{x}\mathcal{X}_{ta}}^{\mathcal{X}_{\mathscr{TA}}} \frac{dx}{\sqrt{\frac{1}{x}-\frac{5}{3}\frac{\bar{\delta}_i(r_i)}{a_i}}}. \tag{2.65}$$

On the right hand side of this equation, the first integral represents the amount of time that it takes for a shell starting at x to turn-around, and the second the time between this shell's turn-around and the outermost shell's turn-around. The lower bound on the second integral $(y/x)\mathcal{X}_{ta}$ is equal to $\mathcal{X}_{ta}$ (the normalized position of the shell when the outermost shell turns around), as found with Eqn. 2.37.

We change the variable of integration on the left hand side of the equation with $x' \equiv x(5/3)\bar{\delta}_i(R_i)/a_i = x\mathcal{X}_{ta}^{-1}$ and $x' \equiv x = x(5/3)\bar{\delta}_i(r_i)/a_i = x\mathcal{X}_{\mathscr{TA}}^{-1}$ on the right hand side of the equation:

$$\begin{aligned}\int_0^1 \frac{dx'}{\sqrt{\frac{1}{x'}-1}} &= \left[\frac{\bar{\delta}_i(r_i)}{\bar{\delta}_i(R_i)}\right]^{-3/2}\left[\int_0^1 \frac{dx'}{\sqrt{\frac{1}{x'}-1}} + \int_{\frac{y}{x}\frac{\bar{\delta}_i(r_i)}{\bar{\delta}_i(R_i)}}^1 \frac{dx'}{\sqrt{\frac{1}{x'}-1}}\right] \\ &= \left[\frac{\bar{\delta}_i(r_i)}{\bar{\delta}_i(R_i)}\right]^{-3/2}\left[2\int_0^1 \frac{dx'}{\sqrt{\frac{1}{x'}-1}} - \int_0^{\frac{y}{x}\frac{\bar{\delta}_i(r_i)}{\bar{\delta}_i(R_i)}} \left[x^{1/2}+\mathcal{O}(x^{3/2})\right]dx\right]. \end{aligned} \tag{2.66}$$

In going from the first line to the second line, we have re-written the second integral on the right hand side as the integral going from 0 to 1 minus the integral going from 0 to $(y/x)(\bar{\delta}_i(r_i)/\bar{\delta}_i(R_i))$. We taylor expand the integrand of the second integral in the second line because its upper bound is much smaller than unity for shells starting at small x ($y \ll x$ for these shells). The integral $\int_0^1 dx/\sqrt{1/x-1}$ is equal to $\pi/2$, so that integrating all terms and soving for $(y/x)^{3/2}$, we find

$$\left(\frac{y}{x}\right)^{3/2} = \frac{3\pi}{2}\left\{\frac{1}{\left[\bar{\delta}_i(r_i)/\bar{\delta}_i(R_i)\right]^{3/2}} - \frac{1}{2}\right\} + \mathcal{O}\left(\left(\frac{y}{x}\right)^{5/2}\right). \tag{2.67}$$

Since $1/[\bar{\delta}_i(0)/\bar{\delta}_i(R_i)]^{3/2} = 1/2$, and since $1/[\bar{\delta}_i(r_i)/\bar{\delta}_i(R_i)]^{3/2}$ gets very close to this value at small r_i for large β, the subtraction within the curly brackets becomes impossible to resolve (even with double-precision). To avoid computing this subtraction, we work instead with the difference between the density at the origin and the density profile,

$$\Delta \equiv \frac{\bar{\delta}_i(0)}{\bar{\delta}_i(R_i)} - \frac{\bar{\delta}_i(r_i)}{\bar{\delta}_i(R_i)}, \tag{2.68}$$

and for our adopted initial density profile $\Delta = x^\beta(2^{2/3} - 1)$ (see Eqn. 2.41). Substituting Eqn. 2.68 in Eqn. 2.67, and taylor expanding in $\Delta/2^{2/3}$ we find that

$$\left(\frac{y}{x}\right)^{3/2} = \frac{3\pi}{2}\left\{\frac{1}{2} + \frac{3}{4}\frac{\Delta}{2^{2/3}} + \frac{15}{16}\frac{\Delta^2}{2^{4/3}} + \mathcal{O}(\Delta^3) - \frac{1}{2}\right\} + \mathcal{O}\left(\left(\frac{y}{x}\right)^{5/2}\right), \tag{2.69}$$

so that the 1/2 cancels out (and thus the problem of resolving the difference from 1/2 goes away). We keep terms to second order in $\Delta/2^{2/3}$ since we find that this results in very high accuracy when comparing to our numerical calculation for y as a function of x in the regime in which both the analytic and numerical approaches are valid. Solving for y, our approximation formula is

$$y \cong \left\{\frac{9\pi}{8}\frac{\Delta}{2^{2/3}}\left[1 + \frac{5}{4}\frac{\Delta}{2^{2/3}}\right]\right\}^{2/3} x. \tag{2.70}$$

Our numerical approach is not an issue for $\beta \lesssim 1$ because the integrals used to compute $\mathscr{M}_{ta}$, $\mathscr{U}_{ta}$ and $\mathscr{K}_{ta}$ converge in x before y becomes too small to calculate numerically. For $\beta \approx 1$ we find that the approximation formula is accurate to $\sim 0.01\%$ for $y \sim 10^{-6}$, and increases in accuracy by several magnitudes for decreasing y, and higher values of β. Since our numerical mapping fails at $y \sim 10^{-10}$ to $y \sim 10^{-13}$ for $\beta \approx 7$ to $\beta \approx 1$ respectively, we therefore switch to the approximation formula for $y < 10^{-9}$, a regime in which the formula's accuracy is excellent.

2.7 Appendix B: Initial Density Profile of a Spherical Perturbation

The formalism to calculate average density profiles around peaks in a Gaussian random field has been derived by Bardeen et al. (1986). Subsequent authors have used these equations to initialize realistic density profiles of collapsing dark matter halos (e.g. Lilje & Lahav 1991; Eisenstein & Loeb 1995; Cupani et al. 2008, 2011), as well as expanding voids (Sheth & van de Weygaert 2004). We now present this formalism, and our prescription to normalize the initial density profile given a halo mass M, and collapse redshift, z_c.

The $(l+1)$-th even moment of a density field smoothed on a comoving scale, R_f, and described by a linear theory matter power spectrum today, $P(k)$, is given by

$$\sigma_l^2 \equiv \frac{1}{2\pi^2}\int_0^\infty P(k)|\widetilde{W}(kR_f)|^2 k^{2(l+1)}dk. \tag{2.71}$$

Consistent with the works mentioned above, we use a Gaussian window function (in real space) so that, that in k space:

$$\widetilde{W}(u) = \exp\left(-\frac{1}{2}u^2\right). \tag{2.72}$$

The choice of a Gaussian window function was originally made by Bardeen et al. (1986) since a top-hat leads to divergence issues in some of their integrals. [5] According to linear

[5]We note that the calculations of σ_l^2 and $\bar{\delta}_i$ (which also involves a factor of $|\widetilde{W}(x)|^2$) in both Cupani et al. (2008) and Cupani et al. (2011) contain a factor of 1/2 mistake. Their mistake is due to not squaring the fourier transform of the window function (Eqn. 2.72), which cancels out the factor of 1/2 in the exponential.

theory, the mass contained within the smoothing scale, R_f, is given by

$$\begin{aligned} M_f &= (2\pi)^{3/2}\bar{\rho}_m(0)R_f^3 \\ &= 4.37\times10^{12}\mathrm{M}_\odot h^{-1}\Omega_m\left(\frac{R_f}{\mathrm{Mpc}\ h^{-1}}\right)^3, \end{aligned} \tag{2.73}$$

where $\bar{\rho}_m(0)$ is the co-moving average (matter) density of the universe, and where the pre-factor of $(2\pi)^{3/2}$ is due to the use of the Gaussian window function.

We use a linear theory matter power spectrum calculated with the CAMB web interface with cosmological parameters consistent with the WMAP7+BAO+H_0 parameters of Komatsu et al. (2011): $(\Omega_m,\ \Omega_b,\ \Omega_\Lambda,\ \sigma_8,\ n,\ h) = (0.27,\ 0.046,\ 0.73,\ 0.81,\ 0.97,\ 0.7)$. Note that, for consistency, the values $\Omega_m = 0.27$ and $\Omega_\Lambda = 0.73$ are the same as those used in § 2.4.4 to calculate the spherical collapse dynamics to solve for the conditions at turn-around in a ΛCDM cosmology.

Lilje and Lahav 1991 show that the spherically (and peak ensemble) averaged density profile associated with a $\nu\sigma_0$ peak in a Gaussian random field, smoothed on a scale R_f and linearly extrapolated to a time, a_i, is[6].

$$\delta_i(\mathscr{r}, a_i, R_f) = \frac{1}{2\pi^2\sigma_0(R_f)}\frac{D(a_i)}{D(0)}\int_0^\infty k^2P(k)e^{-(R_fk)^2}\frac{\sin k\mathscr{r}}{k\ r}\left[\frac{\nu-\gamma^2\nu-\gamma\theta}{1-\gamma^2}+\frac{\theta r_\star^2}{3\gamma(1-\gamma^2)}k^2\right]dk. \tag{2.74}$$

The density profile, when volume averaged with Eqn. 2.4, is given by:

$$\bar{\delta}_i(\mathscr{r}, a_i, R_f) = \frac{3}{2\pi^2\sigma_0(R_f)\mathscr{r}}\frac{D(a_i)}{D(0)}\int_0^\infty kj_1(k\mathscr{r})P(k)e^{-(R_fk)^2}\left[\frac{\nu-\gamma^2\nu-\gamma\theta}{1-\gamma^2}+\frac{\theta r_\star^2}{3\gamma(1-\gamma^2)}k^2\right]dk, \tag{2.75}$$

where j_1 is the 1st order Bessel function.

[6]Since we have hitherto been using the letter, r, to denote the radial variable in physical coordinates, in the following equations we use the script, $\mathscr{r}$ to denote the co-moving radial position.

The quantities $r_\star$ and γ are calculated from the moments of the power spectrum,

$$r_\star \equiv \sqrt{3}\frac{\sigma_1(R_f)}{\sigma_2(R_f)} \quad \text{and} \quad \gamma \equiv \frac{\sigma_1^2(R_f)}{\sigma_2(R_f)\sigma_0(R_f)}, \tag{2.76}$$

$\theta = \theta(\gamma\nu, \gamma)$ and D is the growing mode of the linear theory growth factor. For a flat cosmology with a cosmological constant, the growth factor is well approximated (to within $\sim 2\%$ for $\Omega_m > 0.1$ Loeb & Furlanetto 2013) by Carroll et al. (1992):

$$D = \frac{5}{2}\frac{\Omega_m(z)}{(1+z)}\left\{\Omega_m^{4/7}(z) - \Omega_\Lambda(z) + \left[1 + \frac{\Omega_m(z)}{2}\right]\left[1 + \frac{\Omega_\Lambda(z)}{70}\right]\right\}^{-1}, \tag{2.77}$$

with

$$\Omega_m(z) = \frac{\Omega_m(1+z)^3}{\Omega_m(1+z)^3 + \Omega_\Lambda}, \tag{2.78}$$

and

$$\Omega_\Lambda(z) = \frac{\Omega_\Lambda}{\Omega_m(1+z)^3 + \Omega_\Lambda}. \tag{2.79}$$

This expression for the growth factor is normalized so that $D = a$ as $\Omega_m(z) \to 1$ at high redshift. For the use of the reader, we tabulate values of $r_\star$, γ and σ_0 for our power spectrum for various smoothing scales in Tab. 2.1.

Since the function, $\theta(\gamma\nu, \gamma)$ is not straightforward to calculate, most authors have used the fitting function for θ provided by Bardeen et al. (1986), which they quote to be accurate to within 1% in the ranges $0.4 < \gamma < 0.7$ and $1 < \gamma\nu < 3$. For the calculations presented in this paper, we do not necessarily stay within this range, and therefore calculate $\theta(\gamma\nu, \gamma)$ explicitly. The function θ is found by evaluating (Bardeen et al. 1986):

$$\theta(\gamma\nu, \gamma) = \frac{\int_0^\infty \exp\left[\frac{-(x-\gamma\nu)^2}{2(1-\gamma^2)}\right] x f(x) dx}{\int_0^\infty \exp\left[\frac{-(x-\gamma\nu)^2}{2(1-\gamma^2)}\right] f(x) dx} - \gamma\nu, \tag{2.80}$$

Table 2.1:: $r_\star$, γ and σ_0 for various smoothing scales

M_f [$\mathrm{M}_\odot h^{-1}$]	$r_\star$ [coMpc h^{-1}]	γ	σ_0
10^4	0.00373710	0.381189	8.99722
10^5	0.00745276	0.400130	8.02269
10^6	0.0155689	0.419671	6.97921
10^7	0.0330506	0.440261	5.94865
10^8	0.0704251	0.463409	4.96486
10^9	0.149908	0.489483	4.04212
10^{10}	0.318194	0.518820	3.19087
10^{11}	0.672599	0.551657	2.42195
10^{12}	1.41376	0.587942	1.74736
10^{13}	2.95001	0.627038	1.17972
10^{14}	6.10172	0.667419	0.730102
10^{15}	12.5073	0.706831	0.403660

with

$$f(x) \equiv \frac{x^3 - 3x}{2}\left\{\mathrm{erf}\left[\left(\frac{5}{2}\right)^{1/2} x\right] + \mathrm{erf}\left[\left(\frac{5}{2}\right)^{1/2}\frac{x}{2}\right]\right\} + \left(\frac{2}{5\pi}\right)^{1/2}\left[\left(\frac{31x^2}{4} + \frac{8}{5}\right)e^{-5x^2/8} + \left(\frac{x^2}{2} - \frac{8}{5}\right)e^{-5x^2/2}\right]. \quad (2.81)$$

For the purposes of this paper, we wish to specify the initial density profile of a halo, normalized by its value at the edge at which the halo is identified, $\bar{\delta}_i(r_i)/\bar{\delta}_i(R_i)$. To solve for this profile, we first specify a smoothing scale of interest, M_f, so that σ_0, $r_\star$ and γ may be calculated for a given power spectrum. We then find the initial seed of a

halo, $\bar{\delta}_i(R_i)/a_i$, given a collapse redshift, z_c, utilizing the formalism presented in § 2.4.1 (Eqn. 2.57 for a flat universe). Finally, given a halo mass, M, the initial co-moving radius of a sphere enclosing this mass can be calculated by noting that

$$\begin{aligned} M &= \frac{4\pi}{3}\bar{\rho}_m(0)R_{i,co}^3[1+\bar{\delta}_i(R_i)] \\ &\cong 1.16\times10^{12}M_\odot h^{-1}\Omega_m\left(\frac{R_{i,co}}{\text{Mpc } h^{-1}}\right)^3. \end{aligned} \tag{2.82}$$

We evaluate Eqn. 2.75 at $r = R_{i,co}$, divide by $D(a_i)$ and take $a_i \to 0$ ($D(a_i) \to 1$) so that the left hand side of this equation becomes $\bar{\delta}_i(R_i)/a_i$. Inserting the calculated quantities addressed in the previous paragraph (R_f, σ_0, $r_\star$, γ, $R_{i,co}$, $\bar{\delta}_i(R_i)/a_i$) leads to a non-linear equation with a single, unknown variable, ν, for which we solve numerically (the parameter θ is a function of ν given a value γ). We tabulate ν and θ calculated under this prescription for several values of z_c, M and M_f in Tab. 2.2. With ν and θ known, the profile $\bar{\delta}_i(r_i)/\bar{\delta}_i(R_i)$ can be found using

$$\frac{\bar{\delta}_i(x)}{\bar{\delta}_i(R_i)} = \frac{1}{x}\frac{\int_0^\infty kj_1(kxR_{i,co})P(k)e^{-(R_fk)^2}\left[\frac{\nu-\gamma^2\nu-\gamma\theta}{1-\gamma^2}+\frac{\theta r_\star^2}{3\gamma(1-\gamma^2)}k^2\right]dk}{\int_0^\infty kj_1(kR_{i,co})P(k)e^{-(R_fk)^2}\left[\frac{\nu-\gamma^2\nu-\gamma\theta}{1-\gamma^2}+\frac{\theta r_\star^2}{3\gamma(1-\gamma^2)}k^2\right]dk}, \tag{2.83}$$

easily derived from Eqn. 2.75. A similar formula can be derived from Eqn. 2.74 to solve for the (non-volume averaged) normalized initial density profile, $\delta_i(r_i)/\bar{\delta}_i(R_i)$. We show examples of these profiles for several halo masses, smoothing scales, and collapse redshifts in Fig. 2.10.

We should note that, as seen by the ν values in Tab. 2.2, halos with certain combinations of z_c, M and M_f (according to the prescription above) originate from unrealistically high peaks in the initial cosmic density field. Specifically, the largest halos collapsing at the earliest times must be spawned from density perturbations with prohibitively large values of ν. This facet of structure formation, that the largest halos

Table 2.2:: ν and θ for different halos

z_c	M [$\mathrm{M}_\odot h^{-1}$]	ν^{a}			θ^{a}		
0	10^{15}	11.0716	14.4091	18.1462	0.347416	0.296147	0.258404
	10^{13}	3.47730	4.00833	4.59198	1.20029	1.16248	1.11979
	10^{11}	1.99916	2.14021	2.28591	1.62999	1.63876	1.64644
	10^{9}	1.46096	1.49284	1.61482	1.82373	1.84741	1.75778
0.5	10^{15}	14.0725	18.3877	23.2059	0.271592	0.231193	0.201581
	10^{13}	4.16247	4.86503	5.63470	1.07048	1.01764	0.963021
	10^{11}	2.28085	2.47430	2.67408	1.56644	1.56723	1.56752
	10^{9}	1.61455	1.66656	1.79871	1.78976	1.81067	1.71615
1	10^{15}	17.6053	23.0571	29.1345	0.216289	0.183973	0.160342
	10^{13}	4.97424	5.88034	6.87037	0.936227	0.872630	0.811449
	10^{11}	2.61115	2.86608	3.12927	1.49436	1.48646	1.47880
	10^{9}	1.79424	1.86980	2.01397	1.75057	1.76832	1.66831
2	10^{15}	25.3402	33.2571	42.0693	0.149763	0.127298	0.110906
	10^{13}	6.78250	8.14031	9.61633	0.707607	0.640391	0.582862
	10^{11}	3.33495	3.72473	4.12687	1.34587	1.32154	1.29918
	10^{9}	2.18643	2.31334	2.48431	1.66713	1.67834	1.56720
3	10^{15}	33.3940	43.8634	55.5100	0.113493	0.0964424	0.0840119
	10^{13}	8.70946	10.5399	12.5203	0.548857	0.491082	0.444443
	10^{11}	4.09315	4.62437	5.17210	1.20463	1.16702	1.13338
	10^{9}	2.59483	2.77521	2.97478	1.58339	1.58827	1.46689
4	10^{15}	41.5547	54.6043	69.1171	0.0911469	0.0774432	0.0674569
	10^{13}	10.6947	13.0009	15.4878	0.443557	0.395722	0.357683
	10^{11}	4.86788	5.54379	6.24018	1.07563	1.02855	0.987555
	10^{9}	3.00952	3.24413	3.47361	1.50173	1.50073	1.37039
5	10^{15}	49.7604	65.4011	82.7929	0.0760898	0.0646453	0.0563071
	10^{13}	12.7109	15.4920	18.4851	0.371276	0.330910	0.298932
	10^{11}	5.65413	6.47686	7.32380	0.960358	0.907584	0.862900
	10^{9}	3.42773	3.71698	3.97751	1.42290	1.41653	1.27868
10	10^{15}	90.9825	119.622	151.461	0.0415916	0.0353319	0.0307728
	10^{13}	22.9564	28.0998	33.6178	0.203789	0.181370	0.163696
	10^{11}	9.70684	11.2775	12.8858	0.577297	0.530356	0.494605
	10^{9}	5.55144	6.11736	6.54909	1.07889	1.05418	0.901541

[a]Each of the three sub-columns corresponds to a smoothing scale of 10^{-4}, 10^{-5}, 10^{-6} times the halo mass, M, from left to right respectively.

generally form at later cosmic times is well known, and is reflected in such simple models as the Press-Schecter halo mass function. For perspective when considering the different halos presented in Tab. 2.2, we here calculate averages and standard deviations of ν and θ given z_c, M and M_f from the formalism in Bardeen et al. (1986).

A natural way to average these quantities is to weight by peak number. According to Bardeen et al. (1986), the co-moving number density of peaks in a smoothed Gaussian random field in the range ν to $\nu + d\nu$ is

$$\mathcal{N}_{pk}(\nu)d\nu = \frac{1}{(2\pi)^2 r_\star^3} e^{-\nu^2/2} G(\gamma, \gamma\nu) d\nu, \tag{2.84}$$

with

$$G(\gamma, y) = \frac{1}{\sqrt{2\pi(1-\gamma^2)}} \int_0^\infty \exp\left[\frac{-(x-y)^2}{2(1-\gamma^2)}\right] f(x) dx, \tag{2.85}$$

so that the averages are:

$$\bar{\nu} = \frac{\int_{\nu_{th}}^\infty \nu \mathcal{N}_{pk}(\nu) d\nu}{\int_{\nu_{th}}^\infty \mathcal{N}_{pk}(\nu) d\nu}, \quad \text{and} \quad \bar{\theta} = \frac{\int_{\nu_{th}}^\infty \theta(\nu) \mathcal{N}_{pk}(\nu) d\nu}{\int_{\nu_{th}}^\infty \mathcal{N}_{pk}(\nu) d\nu}. \tag{2.86}$$

The corresponding variances are given by:

$$\sigma_\nu^2 = \frac{\int_{\nu_{th}}^\infty (\nu - \bar{\nu})^2 \mathcal{N}_{pk}(\nu) d\nu}{\int_{\nu_{th}}^\infty \mathcal{N}_{pk}(\nu) d\nu}, \quad \text{and} \quad \sigma_\theta^2 = \frac{\int_{\nu_{th}}^\infty [\theta(\nu) - \bar{\theta}]^2 \mathcal{N}_{pk}(\nu) d\nu}{\int_{\nu_{th}}^\infty \mathcal{N}_{pk}(\nu) d\nu}. \tag{2.87}$$

As we did for the function θ, we calculate $\mathcal{N}_{pk}(\nu)$ exactly with Eqns. 2.84 and 2.85, rather than using the fitting function for $\mathcal{N}_{pk}(\nu)$ provided by Bardeen et al. (1986). In this way, we need not worry about the range of validity of the fitting function. The paramter, ν_{th}, is a physically motivated peak height threshold to isolate peaks which will eventually turn into the class of objects under consideration (i.e., halos of a certain mass collapsing at a certain redshift z_c). Bardeen *et al* 1986 provide a simple prescription for estimating this value. They state that, a halo associated with an initial peak height,

$\nu < \nu_{th}(z_c)$, will not have collapsed by a redshift z_c if ν is less than the linear theory over-density at collapse (extrapolated to the present day) in units of σ_0 today, filtered at the mass scale of interest:

$$\nu_{th}(z_c) \approx \frac{\bar{\delta}_{lin}(z=0|z_c)}{\sigma_0(R_f)}. \tag{2.88}$$

For a flat universe with a cosmological constant, the linear theory over-density of a halo at collapse is well approximated by $1.686[\Omega_m(z_c)]^{0.0055}$ (Mo et al. 2010), so that the linear theory over-density today, given a collapse redshift z_c, is:

$$\bar{\delta}_{lin}(z=0|z_c) = \frac{D(0)}{D(z_c)} 1.686[\Omega_m(z_c)]^{0.0055}. \tag{2.89}$$

Under this prescription, the threshold peak height may therefore be calculated when the halo collapse redshift is specified.

To illustrate how probable it is to find a halo associated with an initial peak height ν (and corresponding θ value) given a collapse redshift z_c and smoothing scale M_f, we plot $\bar{\nu}$ and $\bar{\theta}$ in Figs. 2.13a and b respectively. We show $\bar{\nu}$ and $\bar{\theta}$ as a function of M_f for several values of z_c (lines). The shaded area around each line corresponds to the 1-σ value for ν and θ, calculated with Eqn. 2.87. The lines with the dotted, light grey, dark grey and line-filled 1-σ areas correspond to $z_c = 0$, 1, 5 and 10, respectively. For clarity of presentation, the $z_c = 0$ line is dotted. These plots show which halos in Tab. 2.2 are relatively common (i.e., which halos have ν and θ close to the mean) and which are rare (i.e. which halos have ν and θ several sigma away from the mean).

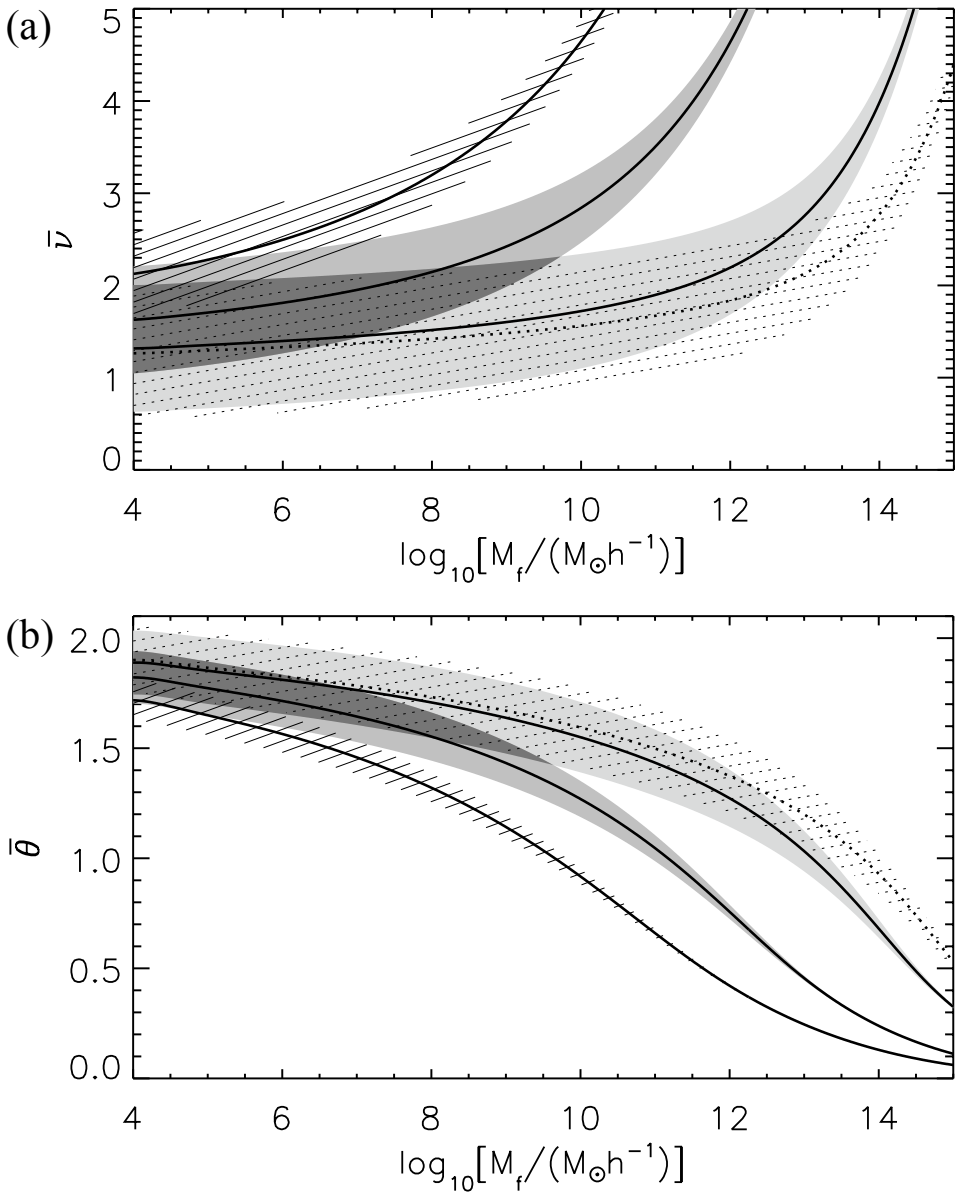

Figure 2.13.—: The peak number averaged ν (a) and θ (b) values for halos collapsing at different redshifts (different lines) as a function of smoothing scale. The shaded areas around each line correspond to the 1-σ values (σ_ν, σ_θ). The lines with the dotted, light grey, dark grey and line-filled 1-σ areas correspond to $z_c = 0$, 1, 5 and 10, respectively. For clarity of presentation, the $z_c = 0$ line is dotted.

2.8 Appendix C: Spherical Collapse After Shell Crossing

To follow the dynamics of shells under spherical collapse beyond shell crossing we, employ a one dimensional, Lagrangian shell code with $N_{shells} = 10^4$ similar to that used by Thoul & Weinberg (1995), Lu & Mo (2007) and Rubin & Loeb (2013a). The code discretizes the density field into a set of concentric, equal mass, shells whose equations of motion must be solved simultaneously since they are coupled via their mutual gravitational attraction. The equation of motion for an individual shell, labelled as shell "j ", can be written as two coupled first order differential equations:

$$\frac{dv_j}{dt} = -\frac{Gm_j(t)}{r_j^2} + H_o^2\Omega_\Lambda r_j \tag{2.90}$$

and

$$\frac{dr_j}{dt} = v_j, \tag{2.91}$$

where

$$m_j(t) = \sum_{j'} \Delta m. \tag{2.92}$$

The symbol, Δm represents the mass of an individual shell, and j' is the subset of shells that satisfy $r_{j'}(t) \leq r_j(t)$. Equation 2.90 could also include an r^{-3} outwardly directed force term due to angular momentum, however, for consistency with the rest of this paper, we choose not to include it.

2.8.1 Integration Scheme

We employ the following definitions to non-dimensionalize our code: $\tilde{r} \equiv r/R_0$, $\tilde{v} \equiv v/(R_0 H_o \Omega_m/2)$, $\tilde{a} \equiv a/(R_0 H_o^2 \Omega_m/2)$, $\tilde{m} \equiv m/M_0$ and $\tilde{t} \equiv t/(H_o^{-1})$. The variables R_0 and M_0 refer to the position of the outermost shell, and the mass contained within it at the start time our simulation, t_0. Similar to Eqn. 2.29, M_0 can be written as

$$M_0 = R_0^3 H_o^2 \Omega_m [1 + \bar{\delta}_0(R_0)]/(2G a_0^3), \tag{2.93}$$

where the factor, $1 + \bar{\delta}_0(R_0)$ is given by

$$1 + \bar{\delta}_0(R_0) = \mathcal{X}_0^{-3} a_0^3. \tag{2.94}$$

In the previous equation we have assumed a time when the outermost shell has yet to undergo shell crossing. The factor, $\mathcal{X}_0$ ($\equiv R_0 a_i/R_i$), is found by solving Eqn. 2.110 when $\tilde{t}_0$ is specified (as explained in the next section).

To integrate each shell's equation of motion, we use the (locally) second order accurate kick-drift-kick leap-frog integration scheme with adaptive time-steps. Using the units adopted for this calculation, and Eqn. 2.93, the non-dimensionalized update equations are written as:

$$\tilde{v}_j^{n+1/2} = \tilde{v}_j^n + \tilde{a}_j^n \frac{\widetilde{\Delta t}}{2}, \tag{2.95}$$

$$\tilde{r}_j^{n+1} = \tilde{r}_j^n + \tilde{v}_j^{n+1/2} \widetilde{\Delta t} \frac{\Omega_m}{2}, \tag{2.96}$$

$$\tilde{a}_j^{n+1} = -\frac{\tilde{m}_j^{n+1}}{(\tilde{r}^{n+1})^2} \left(\frac{1 + \bar{\delta}_0(R_0)}{a_0^3} \right) + 2 \frac{\Omega_\Lambda}{\Omega_m} \tilde{r}_j^{n+1}, \tag{2.97}$$

and

$$\tilde{v}_j^{n+1} = \tilde{v}_j^{n+1/2} + \tilde{a}_j^{n+1}\frac{\widetilde{\Delta t}}{2}, \tag{2.98}$$

where the superscript, "n", indicates the time-step.

In order to avoid having to resolve the divergence in the force on a shell as it approaches the center, we place a hard inner reflecting sphere at radius $\tilde{r}_{in}$, a tactic also used by Thoul & Weinberg (1995). Clearly, this only an approximation to the full spherical collapse treatment of a collapsing dark matter halo. However, as long as $\tilde{r}_{in}$ is sufficiently smaller than all characteristic length scales of the system, the approximation should not significantly affect collapse dynamics. The relevant length scale of the system is its original size, R_0, and we therefore choose $\tilde{r}_{in} = 0.01$.

The appropriate time scales to consider for choosing the time step, $\widetilde{\Delta t}$, at each iteration are the dynamical time, $\sqrt{\pi^2 r^3/(4Gm)}$, the time it takes for a shell to travel a maximum allowed distance given its velocity, ℓ_{max}/v, and the time it takes for a shell to travel a maximum allowed distance given its acceleration, $\sqrt{\ell_{max}/a}$. The latter two time scales must be considered to ensure that the positions of each shell do not change dramatically across each time-step. The dynamical time scale of each shell is necessary to consider since the force on each shell blows up as it approaches the center. By using a time-step much smaller than a shell's dynamical time, we ensure that the shell does not fall too far a distance over which the force changes appreciably. To time resolve the dynamics of the shells, we therefore choose the time-step at each iteration in the code according to:

$$\widetilde{\Delta t} = \min\{\widetilde{\Delta t}_j^{dyn},\ \widetilde{\Delta t}_j^{v},\ \widetilde{\Delta t}_j^{a},\ \widetilde{\Delta t}_{end}\}. \tag{2.99}$$

Choosing $\ell_{max} = R_0$, and dimensionalizing to the proper units, these time-steps are:

$$\widetilde{\Delta}t_{dyn} = \min_j \left\{ c_{dyn} \sqrt{\frac{\pi^2 (\tilde{r}_j^n)^3 a_0^3}{2\Omega_m [1 + \bar{\delta}_0(R_0)] \tilde{m}_j^n}}, \right\}, \tag{2.100}$$

$$\Delta\tilde{t}_v = \min_j \left\{ c_v \frac{1}{|v_j^n + \epsilon|} \frac{2}{\Omega_m} \right\}, \tag{2.101}$$

and

$$\Delta\tilde{t}_a = \min_j \left\{ c_a \sqrt{\frac{2}{\Omega_m |a_j^{n+1} + \epsilon|}} \right\}. \tag{2.102}$$

Here ϵ is a small number in order to keep $\widetilde{\Delta}t$ from blowing up if the velocities or accelerations are small, and c_{dyn}, c_v and c_a are safety constants. We find that $c_{dyn} = c_v = c_a = 10^{-4}$ provides adequate time resolution. We add one last time-step to ensure that the simulation ends exactly when we wish it to end:

$$\widetilde{\Delta}t_{end} = \tilde{t}_{end} - \tilde{t}^n. \tag{2.103}$$

Since we are interested in the state of the system at the turn-around time of the outermost shell, we stop the simulation at $\tilde{t}_{end} = \tilde{t}_{ta}$, calculated from non-linear theory.

At the end of each simulation, we wish to calculate the non-dimensionalized kinetic energy and binding energies due gravity and dark energy of the system. Given the definitions utilized to non-dimensionalize our code, it is straightforward to show that

$$\mathscr{U}_{ta} = \frac{5}{3} \frac{\mathcal{X}_{ta}}{\mathcal{X}_0} \widetilde{\Delta m} \sum_j \frac{\tilde{m}_j^{n=N}}{\tilde{r}_j^{n=N}}, \tag{2.104}$$

$$\mathscr{K}_{ta} = \frac{5}{12} \Omega_m \mathcal{X}_{ta} \mathcal{X}_0^2 \widetilde{\Delta m} \sum_j \left(\tilde{v}_j^{n=N} \right)^2, \tag{2.105}$$

and

$$\mathscr{U}_{ta}^{\Lambda} = \frac{5}{3} \frac{\mathcal{X}_0^2}{\mathcal{X}_{ta}^2} \widetilde{\Delta m} \sum_j \left(\tilde{r}_j^{n=N} \right)^2. \tag{2.106}$$

Here, $n = N$ refers to the last time step of the calculation.

By taking advantage of Newton's iron shell theorem, we avoid having to gravitationally soften the trajectories of particles that venture too close to each other, as with full, three dimensional simulations. However, Lu et al. (2006) point out that in our strategy, shells experience an unrealistic discontinuity in force when they cross each other. This is due to the discretization of the density field and the fact that under the iron shell theorem, shells only feel the gravitational force of other shells at smaller radii. Indeed, in our simulations we observe a degradation in energy conservation associated with shell crossing events. To alleviate this effect, we try to "soften" the crossings using the same tactic as Lu et al. (2006). We give each shell a small thickness and assume that the total mass of the shell is spread uniformly across its volume. Therefore, when two shells undergo crossing, they gradually overlap and the force on either smoothly changes. We also employ a "shell crossing time scale" when choosing $\widetilde{\Delta t}$ to properly time resolve the crossing event. Unfortunately, we find that this strategy does not significantly improve energy conservation, or the convergence of individual shell trajectories. Specifically, for the steepest initial density profiles we can only obtain reliable convergence with unrealistically high resolution. In this paper, we therefore only show examples for which we are confident that our final results have converged.

In Fig. 2.14, we show example trajectories as well as several other quantities for several shells for a $10^9 \mathrm{M}_\odot h^{-1}$ collapsing at $z_c = 0$. The bottom right panel in the figure shows that energy is very well conserved.

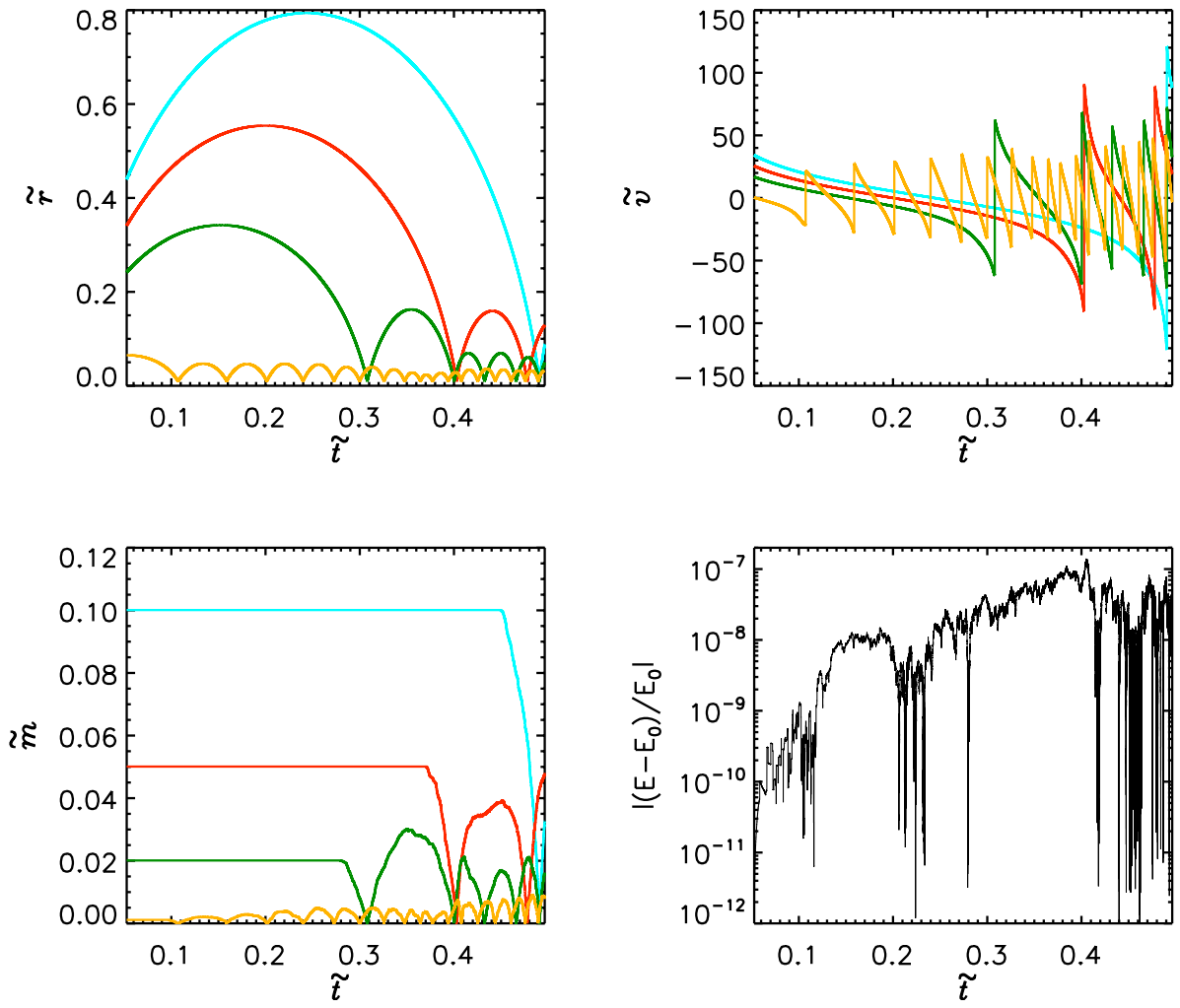

Figure 2.14.—: Example trajectories, velocity and interior mass profiles for several different shells in a $10^9 M_\odot h^{-1}$ mass halo collapsing at $z_c = 0$. We also show the fractional difference in energy as a function of time to illustrate our level of energy conservation.

2.8.2 Initial Conditions

We start our simulations at a time, $\tilde{t}_0$, corresponding to the time when the innermost shell in the simulation has already turned around and is just bouncing off the inner boundary at $\tilde{r}_{in}$. We choose this start time in order to reduce simulation computation time, since it is the latest time at which non-linear, analytic theory is valid. In order to calculate $\tilde{t}_0$, we first calculate the initial normalized position of the innermost shell, $x_{j=0}$. Assuming that no shells cross the first shell between the initial time, t_i, and the simulation start time, t_0, $m_{0,j=0}/M_0 = m_{i,j=0}/M_0$ where $m_{0,j=0}$ ($m_{i,j=0}$) refers to the mass within the innermost shell at time $\tilde{t}_0$ ($\tilde{t}_i$). Since $m_{0,j=0}/M_0 = \widetilde{\Delta m} = 1/N_{shells}$,

$$\frac{1}{N_{shells}} = \frac{(r_{i,j=0})^3 a_0^3}{R_0^3 a_i^3} \frac{\left\{1 + \bar{\delta}_i\left(r_{i,j=0}\right)\right\}}{\left\{1 + \bar{\delta}_0(R_0)\right\}}. \tag{2.107}$$

Using Eqn. 2.94, the fact that $\bar{\delta}_i(r_{i,j=0}) \ll 1$, and simplifying, one can show that:

$$x_{j=0} = N_{shells}^{-1/3}. \tag{2.108}$$

By specifying the halo mass and collapse redshift, we find the initial seed, $\bar{\delta}_i(R_i)/a_i$, and the initial density profile, $\bar{\delta}_i(x)/\bar{\delta}_i(R_i)$ (which we evaluate at $x_{j=0}$), given the formalism presented in App. 2.7. The turn-around radius of the innermost shell, $\chi_{\mathscr{TA}}(x_{j=0})$, is found from Eqn. 3.7 with $\bar{\delta}_i(r_i)/a_i \rightarrow [\bar{\delta}_i(x_{j=0})/\bar{\delta}_i(R_i)][\bar{\delta}_i(R_i)/a_i]$. The start time of our simulation can then be found by evaluating the following integral, calculated from the trajectory of the innermost shell:

$$\tilde{t}_0 = \mathcal{I}\left[0, \chi_{\mathscr{TA}}(x_{j=0}), \left(\frac{\bar{\delta}_i(\chi_{j=0})}{\bar{\delta}_i(R_i)}\right)\left(\frac{\bar{\delta}_i(R_i)}{a_i}\right)\right] + \mathcal{I}\left[\frac{\tilde{r}_{in}}{x_{j=0}}\chi_0, \chi_{\mathscr{TA}}(x_{j=0}), \left(\frac{\bar{\delta}_i(x_{j=0})}{\bar{\delta}_i(R_i)}\right)\left(\frac{\bar{\delta}_i(R_i)}{a_i}\right)\right]. \tag{2.109}$$

The start time can also be found with

$$\tilde{t}_0 = \mathcal{I}\left[0, \chi_0, \left(\frac{\bar{\delta}_i(R_i)}{a_i}\right)\right], \tag{2.110}$$

calculated from the trajectory of the outermost shell. Equations 2.109 and 2.110 form a complete set of equations in $\tilde{t}_0$ and $\mathcal{X}_0$, which we solve for numerically. For a flat universe with a cosmological constant, the corresponding scale factor (necessary to calculate $\bar{\delta}_0(R_0)$) can be found from:

$$a(t) = \left(\frac{\Omega_m}{\Omega_\Lambda}\right)^{1/3} \left[\sinh\left(\frac{3}{2}H_o t\sqrt{\Omega_\Lambda}\right)\right]^{2/3}. \tag{2.111}$$

We initialize the position and velocity of each shell at $\tilde{t}_0$ by using non-linear theory. Similar to Eqn. 2.28, one can show that the mass interior to a position $\tilde{r}_0 \geq \tilde{r}_{in}$ is given by:

$$\tilde{m}_0(\tilde{r}_0) = \widetilde{\Delta m} + 3\int_{\tilde{r}_{in}}^{\tilde{r}_0} x^2(\tilde{r}_0)\frac{dx}{d\tilde{r}_0}(\tilde{r}_0)d\tilde{r}_0, \tag{2.112}$$

where we calculate the x to $\tilde{r}_0$ mapping with non-linear theory from a procedure similar to that as presented in 2.4.2. Once this mass profile is calculated, we place shells at positions, $\tilde{r}_j^{n=0}$, which satisfy the relation $\tilde{m}_0(\tilde{r}_j^{n=0})/\widetilde{\Delta m} = j+1$ with $j = 0, 1, ..., N_s - 1$. To initialize velocity, it is straightforward to show from Eqn. 3.3 with some algebra that the velocity of each shell at t_0 is given by

$$\tilde{v}_0(\tilde{r}_0) = \pm 2\left\{\frac{x^3(\tilde{r}_0)}{\tilde{r}_0\mathcal{X}_0^3\Omega_m} + \frac{\Omega_\Lambda}{\Omega_m^2}\tilde{r}_0^2 - \frac{5}{3}\frac{x^2(\tilde{r}_0)}{\mathcal{X}_0^2\Omega_m}\left(\frac{\bar{\delta}_i[x(\tilde{r}_0)]}{\bar{\delta}_i(R_i)}\right)\left(\frac{\bar{\delta}_i(R_i)}{a_i}\right)\right\}^{1/2}. \tag{2.113}$$

The plus sign is chosen for shells that have yet to turn-around and are traveling outward ($\tilde{t}_0 < \tilde{t}_{\mathscr{TA}}$), and the minus sign is chosen for shells that have already turned around and are traveling inward ($\tilde{t}_0 > \tilde{t}_{\mathscr{TA}}$). We set the velocity of the $j = 0$ shell to $-\tilde{v}(\tilde{r}_{0,j=0})$ since it is just rebounding off the center boundary.

Acknowledgments

We thank Eli Visbal, Mark Vogelsberger and Paul Torrey for helpful conversations. This research was supported in part by NSF grant AST-1312034.

Chapter 3

Analytic Properties of Spherical Collapse in a ΛCDM Cosmology

D. Rubin & A. Loeb, submitted to *Journal of Cosmology and Astroparticle Physics*, 2013

Abstract

The gravitational collapse of a spherically symmetric distribution of matter is an old problem, the dynamics of which have been worked out several decades ago. In this paper, we study several aspects of the problem which have yet to be fully detailed, and which could be useful for the interpretation of numerical simulations or observations. We provide a semi-analytic prescription for calculating the complete non-linear density evolution of isolated, pressureless, matter perturbations in a universe with a cosmological constant and arbitrary curvature. Given an initial over/under-density seed, we utilize the Newtonian spherical collapse model, generalized for any cosmology, to follow

its subsequent evolution. Three distinct regimes are considered: over-densities that will never collapse due to the extra positive energy of the cosmological constant, over-densities that will eventually collapse to form gravitationally bound dark matter halos and under-densities that will expand into tenuous voids. We derive an analytic solution for the critical over-density required to maintain the indefinite expansion of an over-dense region in any cosmology. Important physical properties of halos such as the virial radius, virial temperature, mean over-density at collapse are calculated for several cosmologies. A simple prescription for calculating the density evolution after virialization is presented. We also consider the evolution of voids after shell crossing by implementing a spherically symmetric Lagrangian simulation. An analytic solution for the under-density in a void at the moment shell of crossing is derived for an arbitrary cosmology, which thus far has only been derived under an Einstein de-Sitter cosmology. Finally, by interpreting large scale over/under-densities in a ΛCDM universe as a local change in cosmology we are able to examine the effect of environment on the physical properties of halos at collapse. We show that, regardless of environment, under the spherical collapse model, halos collapsing at the same time will have the same physical properties.

3.1 Introduction

Under the standard ΛCDM model of cosmology, emergent cosmic structure is seeded at an early time from very small density perturbations on top of an homogenous and isotropic background density field. Early on, while the amplitude of the perturbations is still small, their evolution is well described by the linearized theory of fluid flow in an

expanding background. Both Newtonian and relativistic solutions to linear theory have been worked out analytically for some time now (e.g. Lifshitz 1946; Silk 1968; Peebles & Yu 1970; Satō 1971; Weinberg 1971). Eventually, structure grows into the non-linear regime and strongly decouples from the Hubble flow. Much effort has been devoted to understanding the strongly non-linear behavior of matter so that we can explain the formation of the rich array of non-linear structure that we see today.

Our theoretical understanding of non-linear behavior has generally proceeded on two fronts: numerically and analytically. Modern numerical simulations have the ability to probe behavior across a very large dynamic range of scales and have the advantage that very little simplifying assumptions are made. Depending on the scale and sophistication of the simulation, however, numerical simulations can be costly in terms of computation resources and time. Because both time and the density field are discretized in simulations, resolution effects are also a concern. Additionally, simulations are fundamentally limited by our understanding of the physics that we input into them.

Analytic models of non-linear structure formation, on the other hand, are typically quick to calculate, have no resolution limitations and can provide insight into the underlying physics. The main drawback of the analytic approach is that simplifying assumptions must be made in order to keep the problems tractable (e.g. spherical symmetry). Arguably, the most commonly used model for non-linear evolution is the spherical collapse model (Gunn & Gott 1972; Silk & Wilson 1979; Peebles 1980). In the spherical collapse model, matter is assumed to be spherically distributed so that the gravitational force felt by any shell of matter is given only by the mass interior to it. Assuming that the mass interior to a shell under consideration is constant (i.e. no shell crossings), the spherical collapse solution is given in parametric form for an Einstein

de-Sitter universe (E-dS), and is easy to numerically calculate for any other cosmology. Although highly simplified, the model can explain some physical properties of virialized halos, as well as predict their abundance as a function of mass and redshift when worked into the Press-Schechter formalism (Press & Schechter 1974).

Self similar solutions to a shell's trajectory including shell crossings have been found in an E-dS cosmology. The solutions have been found for both the collapse of initially over-dense regions (the so-called "secondary infall models") (Fillmore & Goldreich 1984a; Bertschinger 1985a) and for the expansion of initially under-dense regions (voids) (Fillmore & Goldreich 1984b; Bertschinger 1985b). The secondary infall solutions have been extended to include shell angular momentum (Nusser 2001) as well as external tidal torque (Zukin & Bertschinger 2010).

Additional analytic models include the Zel'dovich approximation (Zel'dovich 1970), for moderately non-linear perturbations, which predicts the existence of dark matter "pancakes." It assumes that the Eulerian position of a particle can be given in terms of its initial Lagrangian position plus a displacement term which is a product of two functions: one of time and one of the initial Lagrangian position. The dynamics of gravitational collapse under ellipsoidal geometry (White & Silk 1979; Bond & Myers 1996) as well as self similar ellipsoidal collapse solutions have also been worked out (Lithwick & Dalal 2011).

By including shell angular momentum, external tidal torque and ellipticity, the self-similar solutions are the most realistic analytic solutions to cosmic structure formation. They include highly non-linear phenomena such as shell crossing and virialization (at least in the case of elliptical self-similar collapse). These solutions,

however, are strictly valid only in an E-dS cosmology since self similarity requires that the background expansion be scale-free, so that the scale factor is a power-law of time. The results of the similarity solutions may therefore not accurately describe the process of structure formation in a ΛCDM cosmology, especially at late cosmic times when the cosmological constant is non-negligible. In this paper, we present a simple and easily calculable analytic prescription to model non-linear structure formation in any cosmology. We apply the spherical collapse model to both expanding and collapsing cosmic structures and provide a simple prescription for dealing with shell crossings and virialization. Additionally, we present exact analytic solutions, valid in an arbitrary cosmology, of quantities important to structure formation, such as the critical seed density required for eventual collapse, the redshift of first shell crossing in a void and the corresponding non-linear and linear under-densities.

In § 3.2 we derive the equations of spherical collapse in an arbitrary cosmology and show how the solution to the equation of motion of a shell can be used to calculate the non-linear over/under-density of an isolated, pressureless, spherical structure as a function of time. In § 3.2.1, we consider over-dense regions that do not collapse due to the addition of positive energy from the cosmological constant and derive an analytic solution of the critical initial over-density required for eventual collapse. We calculate the critical value of the non-linear over-density of an object at a redshift, z, below which the object will never collapse. In § 3.2.2, we consider perturbations above the critical value required for collapse and calculate several important properties of halos at collapse under an arbitrary cosmology. In § 3.2.3, we then consider density perturbations below the critical value (voids) and analytically calculate the redshift of first shell crossing of a void in any cosmology, and the corresponding non-linear under-density. We also perform

this calculation in a flat cosmology, scaling our equations to find the under-density at first shell crossing purely as a function $\Omega_m(z)$, and provide an accurate fitting formula for this calculation. We also examine the dynamics of a spherical voids after shell crossing by implementing a Lagrangian shell code. In § 3.3, we piece together our calculations for each of these three regimes to provide a simple, analytic model of the non-linear over/under-density of a perturbation as a function of redshift and initial perturbation seed in any cosmology. We calculate several useful linear theory quantities in § 3.4, including the linear theory under-density of a void at first shell crossing in any cosmology. As with the non-linear case, we also perform this calculation in a flat cosmology, as a function of $\Omega_m(z)$, and provide an accurate fitting formula. Finally, in § 3.5, we use our results to examine how the physical properties of halos at virialization, as predicted under the spherical collapse model, vary with environment. We do this by interpreting the non-linear over/under-density of a region today as an effective change in cosmology.

3.2 Non-Linear Theory in a General Cosmology

The equation of motion in the Newtonian limit for the proper radius, r, of a shell of dark matter with spherical symmetry and in a universe with a cosmological constant is

$$\frac{d^2r}{dt^2} = H_o^2\Omega_\Lambda r - \frac{GM}{r^2}. \tag{3.1}$$

The parameter H_o is the present day Hubble constant, Ω_Λ is the present day density parameter of the cosmological constant, and M is the total mass interior to r. The first term on the right hand side of this equation is a gravitational force due to the addition of an effective gravitational density from the vacuum, $\rho_{grav} = -2\rho_\Lambda = -3H_o^2\Omega_\Lambda/(4\pi G)$.

Assuming no shell crossings, and integrating once yields a constant with time: the specific energy of the shell

$$\mathscr{E} = \frac{1}{2}\left(\frac{dr}{dt}\right)^2 - \frac{GM}{r} - \frac{1}{2}\Omega_\Lambda H_o^2 r^2. \tag{3.2}$$

Using $\mathscr{E} = \mathscr{E}_i$, and re-expressing this result in terms of a dimensionless parameter, $x \equiv r/[r_i(1+z_i)]$, with r_i the radius at an initial redshift, z_i, leads to the following differential equation in x (Loeb 2006):

$$\frac{1}{H_o^2}\left(\frac{dx}{dt}\right)^2 = \frac{\Omega_m}{x}(1+\bar{\delta}_i) + \Omega_\Lambda x^2 + \Omega_k - \frac{5}{3}\frac{\bar{\delta}_i}{a_i}\Omega_m + \mathcal{O}(a_i). \tag{3.3}$$

The parameter Ω_m is the present day mass energy density and Ω_k is the curvature energy density, $1 - \Omega_m - \Omega_\Lambda$. The factor $(1+\bar{\delta}_i)$ is the density of the perturbation at time a_i in units of the mean density of the universe at a_i. The bar over the delta indicates a volume average over the perturbation, which, under spherical geometry is given by:

$$\bar{\delta}(r) = \frac{3}{r^3}\int_0^r \delta(r')r'^2 dr'. \tag{3.4}$$

In going from eq. (3.2) to eq. (3.3) we have used the the fact that the mass interior to the shell can be re-written as $M = (4/3)\pi r_i^3(1+\bar{\delta}_i)3H_o^2\Omega_m/(8\pi G a_i^3)$, valid until the shell in question undergoes a shell crossing. To solve for $(dr/dt)_i$, we assume that $|\bar{\delta}_i| \ll 1$, so that $\bar{\delta}_i$ is still in the linear regime, and $a_i \ll 1$, so that the peculiar velocity is given by $-H_i r_i \bar{\delta}_i(r_i)/3$ (see eqs. (3.88) and (3.89)). Adding the peculiar velocity to the initial Hubble flow velocity then yields the initial kinetic energy for the shell. Further, we only keep the lowest order terms in a_i when calculating $\mathscr{E}_i$ (noting that in linear theory when $a_i \ll 1$, $\bar{\delta}_i \propto a_i$).

Dropping the factor of $(1+\bar{\delta}_i)$ since we choose an initial time where $|\bar{\delta}_i| \ll 1$, the

solution to eq. (3.3) can be solved by integration:

$$tH_o = \begin{cases} \int_0^{x(t)} dx' \left[1 + \Omega_m \left(\frac{1}{x'} - 1 - \frac{5}{3}\frac{\bar{\delta}_i}{a_i}\right) + \Omega_\Lambda \left(x'^2 - 1\right)\right]^{-1/2} & \text{for } t \leq t_{ta} \\ H_o t_{ta} + \int_{x(t)}^{x_{ta}} dx' \left[1 + \Omega_m \left(\frac{1}{x'} - 1 - \frac{5}{3}\frac{\bar{\delta}_i}{a_i}\right) + \Omega_\Lambda \left(x'^2 - 1\right)\right]^{-1/2} & \text{for } t > t_{ta} \end{cases}, \tag{3.5}$$

where t_{ta} is the turn around time,

$$t_{ta} H_o = \int_0^{x_{ta}} dx' \left[1 + \Omega_m \left(\frac{1}{x'} - 1 - \frac{5}{3}\frac{\bar{\delta}_i}{a_i}\right) + \Omega_\Lambda \left(x'^2 - 1\right)\right]^{-1/2}, \tag{3.6}$$

and x_{ta} is the turn around radius. Note that for flat ($\bar{\delta}_i/a_i = 0$), open trajectories ($\bar{\delta}_i/a_i < 0$), and a subset of closed trajectories ($\bar{\delta}_i/a_i > 0$) with $\bar{\delta}_i/a_i$ less than some critical value, the sphere will not turn around, so that the solution is given by the first line of eq. (3.5).

The turn around radius occurs when $dx/dt = 0$, and from eq. (3.3), this condition leads to the following cubic:

$$\Omega_\Lambda x_{ta}^3 + \left(\Omega_k - \frac{5}{3}\frac{\bar{\delta}_i}{a_i}\Omega_m\right) x_{ta} + \Omega_m = 0. \tag{3.7}$$

As mentioned above, even for a closed trajectory, turn around will never occur for $\bar{\delta}_i/a_i$ less than a critical value since a positive, pure real solution to the cubic will not exist. For a ΛCDM cosmology (see table 3.1), this critical value occurs at $\bar{\delta}_i/a_i \cong 1.58$ (see eq. (3.12)), corresponding to a non-linear mean over density today of about 7.76, below which structure will never collapse (see Sec 3.2.1). For perturbations with $\bar{\delta}_i/a_i$ above the critical value, we provide a closed form solution for x_{ta} in the next section (eq. (3.13)).

The trajectory of a shell in the spherical collapse model is found as a function of time. To examine spherical collapse evolution as a function of redshift, one can convert all times to redshift by integrating the Friedmann equation,

$$H_o t = \int_0^a da' \left[1 + \Omega_m \left(\frac{1}{a'} - 1\right) + \Omega_\Lambda (a'^2 - 1)\right]^{-1/2}, \tag{3.8}$$

where for generality, we have included the so called curvature density.

Once the trajectory x is solved for, the true, non-linear volume averaged density contrast for a dark matter sphere evolving according to the spherical collapse model can be calculated. The volume averaged density contrast is given by $1+\bar{\delta}_{NL} = 3M/(4\pi r^3 \bar{\rho}_m(z))$, where $\bar{\rho}_m$ is the mean matter density of the universe. Assuming no shell crossings one can derive the following equation for $\bar{\delta}_{NL}(z)$:

$$1 + \bar{\delta}_{NL}(z) = x^{-3}(z)(1+z)^{-3}. \tag{3.9}$$

We will show examples of this evolution in §. 3.2.1, 3.2.2 and 3.2.3.

3.2.1 Over-dense, Non-Collapsing Regions

In a cosmology with a cosmological constant, the collapse of a dark matter sphere with $\bar{\delta}_i > 0$ can be prevented indefinitely due to the extra positive energy in the outermost shell contributed by the effective (negative) gravitational density of dark energy at time a_i[1]. The extra initial positive energy results in a critical average over density at time a_i greater than zero required for the sphere to eventually collapse. The value of $\bar{\delta}_i/a_i$ for a general cosmology associated with this critical value, $(\bar{\delta}_i/a_i)_{cr}$ can be found from eq. (3.7). It is the value at which a pure real, positive solution to this cubic no longer

[1]Even in a cosmology without a cosmological constant, curvature can also prevent the collapse of a dark matter sphere with $\bar{\delta}_i > 0$. From eq. (3.7), if $\Omega_\Lambda = 0$, it can be found that the solution to x_{ta} will only be positive when $\bar{\delta}_i/a_i > (3/5)(1/\Omega_m - 1)$. For a matter only universe with positive curvature, this results in a value of $(\bar{\delta}_i/a_i)_{cr}$ greater than zero. For a matter only universe with negative curvature, this results in $(\bar{\delta}_i/a_i)_{cr}$ less than zero, since the collapse is helped by the extra over-density provided by the background.

exists. The relevant solution to eq. (3.7) is:

$$x_{ta} = \frac{1+i\sqrt{3}}{6\Omega_\Lambda}\left[\frac{1}{2}\left(27\Omega_\Lambda^2\Omega_m + \sqrt{-27\Omega_\Lambda^2 b}\right)\right]^{1/3} + \frac{1-i\sqrt{3}}{6\Omega_\Lambda}\left[\frac{1}{2}\left(27\Omega_\Lambda^2\Omega_m - \sqrt{-27\Omega_\Lambda^2 b}\right)\right]^{1/3}, \tag{3.10}$$

with

$$b \equiv -4\Omega_\Lambda\left(\Omega_k - \frac{5}{3}\frac{\bar{\delta}_i}{a_i}\Omega_m\right)^3 - 27\Omega_\Lambda^2\Omega_m^2. \tag{3.11}$$

Eq. (3.10) is the relevant root, because if there are pure real, positive solutions to eq. (3.7), this root always gives the smallest pure real, positive solution (i.e., it corresponds to first turn around). Any pure real, positive solution bigger than this value is spurious since the spherical collapse model fails due to shell crossing before the "second turn around." Examination of eq. (3.10) shows that when $b < 0$, the solution is no longer real[2]. We set eq. (3.11) equal to zero, solve for $(\bar{\delta}_i/a_i)_{cr}$, and take the real result to find:

$$\left(\frac{\bar{\delta}_i}{a_i}\right)_{cr} = \frac{3}{10\Omega_m}\left[2\Omega_k + 3\left(2\Omega_\Lambda\Omega_m^2\right)^{1/3}\right]. \tag{3.12}$$

Perturbations with $\bar{\delta}_i/a_i < (\bar{\delta}_i/a_i)_{cr}$ will never turn around and eventually virialize. For perturbations with $\bar{\delta}_i/a_i$ greater than the critical value, $b > 0$, and the relevant solution to the cubic (eq. (3.10)) can be re-written as:

$$x_{ta} = \sqrt{\frac{c}{3}}\cos\phi - \sqrt{c}\sin\phi, \tag{3.13}$$

with

$$c \equiv \frac{\Omega_m}{\Omega_\Lambda}\left(\frac{5}{3}\frac{\bar{\delta}_i}{a_i} + 1\right) + 1 - \frac{1}{\Omega_\Lambda}, \tag{3.14}$$

and

$$\phi \equiv \frac{1}{3}\arctan\left[\sqrt{\frac{4}{27}\left(\frac{\Omega_\Lambda}{\Omega_m}\right)^2 c^3 - 1}\right]. \tag{3.15}$$

[2]This can be done by expressing the complex numbers in polar coordinates.

Table 3.1:: The various cosmologies that we consider throughout this paper.

	Ω_m	Ω_Λ	Line
E-dS	1	0	dashed black
ΛCDM	0.27	0.73	solid black
CI	0.3	0.1	solid red
CII	0.3	0.4	solid green
CIII	0.3	0.7	solid turquoise
CIV	0.3	1	solid blue
CV	0.3	1.3	solid violet

By plugging $(\bar{\delta}_i/a_i)_{cr}$ into eq. (3.9), we may solve for $\bar{\delta}^{cr}_{NL}(z)$, the critical non-linear over-density of a perturbation at redshift z required for eventual turn-around and collapse. We show $\bar{\delta}^{cr}_{NL}(z)$ as a function of redshift in figure 3.1 for several cosmologies. Since we show examples for these cosmologies repeatedly throughout this paper, we tabulate them in table 3.1 for convenience. We also show the critical non-linear over density today as a function of, Ω_m, the matter density today, for several different values of Ω_Λ.

For comparison with an observable object, the Shapley supercluster, which resides at $z = 0.0388$, is found to have a mean non-linear over density of 0.76 ± 0.17 (Muñoz & Loeb 2008). The supercluster is over-dense, but will never collapse due to the cosmological constant, as we calculate that a non-linear over density of 0.76 at its redshift corresponds to a value of $\bar{\delta}_i/a_i$ of 0.64 (which is $< (\bar{\delta}_i/a_i)_{cr}$). Even though the initial density seed of the Shapley supercluster is well below the critical value required for eventual collapse,

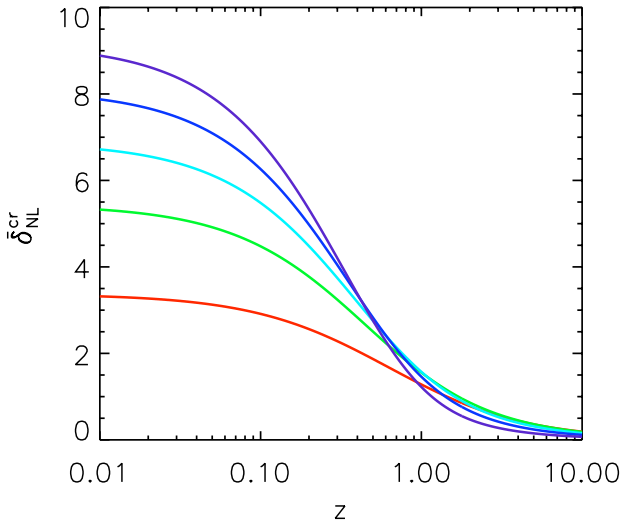

Figure 3.1.—: The critical non-linear over density at redshift z required for the eventual collapse of a dark matter spherical perturbation. The red, green, turquoise, blue and violet lines correspond to the CI, CII, CIII, CIV and CV cosmologies respectively (bottom to top respectively).

it actually represents a rare peak in the cosmic density field. Linearly extrapolating $\bar{\delta}_i/a_i$ to the present day gives a linear theory over density of 0.49. Muñoz & Loeb (2008) compute the linear theory variance today, smoothed on a scale of the size of the Shapely supercluster (50 Eulerian Mpc) to be $\sigma^2 = 0.0529$. Using σ^2 and the over-density value of 0.49, the Shapley supercluster therefore represents about a 2.1σ peak in the cosmic density field (corresponding to the 96 percentile for a gaussian random field).

3.2.2 Halos

For a density perturbation with $\bar{\delta}_i/a_i$ greater than the critical value required for turn around, the perturbation will eventually collapse and virialize, forming a dark matter

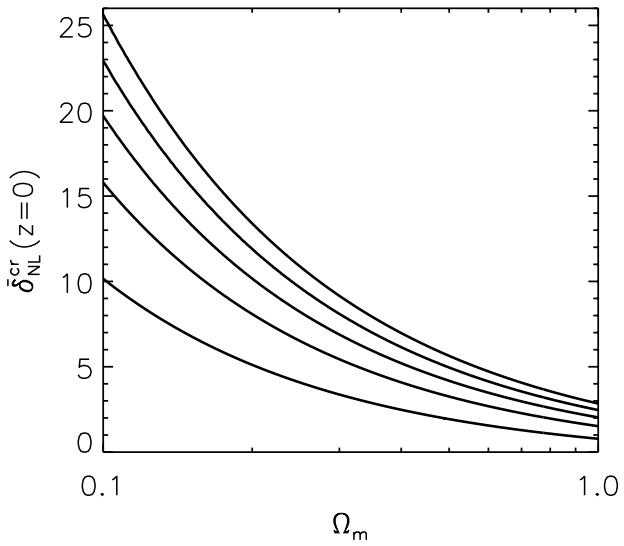

Figure 3.2.—: The critical non-linear over density today as a function of Ω_m for $\Omega_\Lambda = 0.3$, 0.4, 0.7, 1 and 1.3 (bottom to top lines respectively).

halo. It is standard to define the "collapse time" of the sphere as

$$H_o t_c = 2 H_o t_{ta}, \tag{3.16}$$

which is also typically taken to be the time at which the sphere of matter becomes self supporting and virializes. We can solve for the turn around and collapse redshift as a function of the initial seed, $\bar{\delta}_i/a_i$, by calculate t_{ta} as a function of $\bar{\delta}_i/a_i$ with eqs. (3.6) and (3.7). The collapse time can then be calculated with eq. (3.16) and the turn around and collapse times can be converted to corresponding redshifts by plugging them into the Friedmann equation (eq. (3.8)), and numerically solving for the scale factor. We show the results for a ΛCDM cosmology in figure 3.3, along with the results for an E-dS universe. For the latter cosmology, z_{ta} and z_c are given analytically by $z_{ta} = 0.9413\bar{\delta}_i/a_i - 1$ and $z_c = 0.5930\bar{\delta}_i/a_i - 1$ (see for example Loeb & Furlanetto 2013). These relations are found from the standard parametric solutions to the spherical collapse model in and E-dS cosmology by setting the development angle to π and 2π respectively. The time

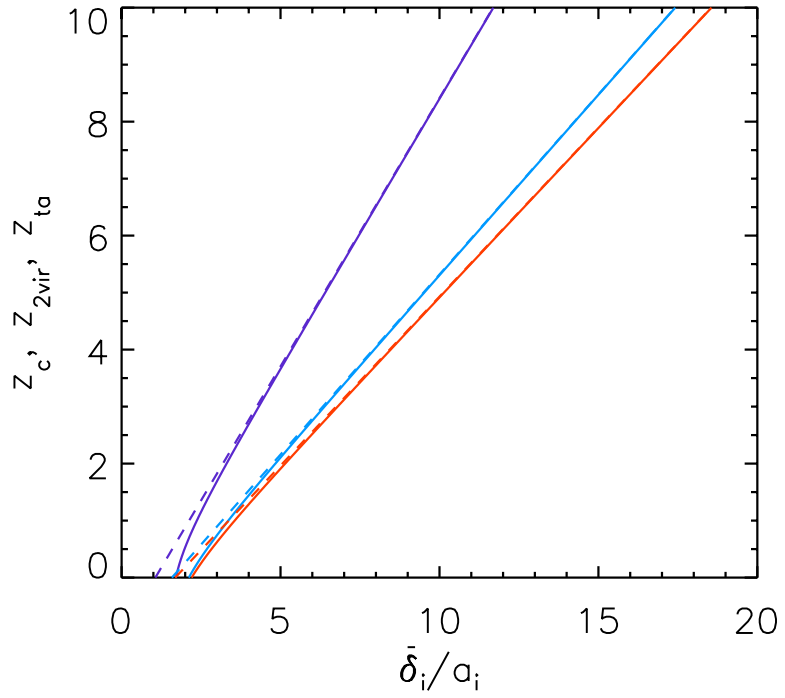

Figure 3.3.—: The turn around (violet lines), collapse (red lines) and z_{2vir} (blue lines) redshifts as a function of $\bar{\delta}_i/a_i$ for a ΛCDM universe (solid lines), and for an E-dS universe (dashed lines).

parametric solution is then converted to redshift with $1+z=(3H_o t/2)^{-2/3}$, valid in an E-dS cosmology. Note that for a flat cosmology with Ω_Λ not necessarily equal to zero, $\bar{\delta}_i/a_i$ as a function of z_c can be conveniently written as a fitting function:

$$\frac{\bar{\delta}_i}{a_i}=\frac{0.674588(1+z_c)}{\Omega_m^{0.9945}(z_c)}\left\{\Omega_m^{4/7}(z_c)+\Omega_\Lambda(z_c)+\left[1+\frac{\Omega_m(z_c)}{2}\right]\left[1+\frac{\Omega_\Lambda(z_c)}{70}\right]\right\}. \qquad (3.17)$$

To derive this function, we have inserted the two fitting functions, eqs. (3.36) (Carroll et al. 1992) and (3.41) (Mo et al. 2010), which describe the linear growth factor and the linear theory over-density at collapse respectively into the linear theory solution (eq. (3.40)) for the density evolution. We have checked this equation against our exact calculations for the ΛCDM cosmology, and have found agreement to about one part in one hundred.

Some time after turn around, the constituent particles of a dark matter sphere will satisfy the virial theorem, and the sphere is said to be virialized. For a top-hat density profile, the value of $\bar{\delta}_i$ is constant for all shells within the sphere, and eqs. (3.6) and (3.7) show that the sphere thus has a well defined turn around time since all shells turn around at the same time. By using the virial theorem, one can solve for the ratio of the virialization radius, r_{vir}, to the turn around radius, r_{ta} (of the outermost shell), which for an E-dS universe is found to be 1/2. In a universe with a non zero cosmological constant, the extra gravitational density due to the cosmological constant contributes to the binding energy of a dark matter sphere (Lahav et al. 1991). Taking this into account in the virial theorem leads to the following cubic in r_{vir}/r_{ta}:

$$4\zeta(\bar{\delta}_i/a_i)\left(\frac{r_{vir}}{r_{ta}}\right)^3 - 2[1+\zeta(\bar{\delta}_i/a_i)]\frac{r_{vir}}{r_{ta}} + 1 = 0, \tag{3.18}$$

where

$$\zeta(\bar{\delta}_i/a_i) \equiv \frac{\Omega_\Lambda}{\Omega_m} x_{ta}^3(\bar{\delta}_i/a_i), \tag{3.19}$$

which incidentally has the same form as eq. (3.7).

The ratio r_{vir}/r_{ta} can be solved for as a function of $\bar{\delta}_i/a_i$ by choosing a value of $\bar{\delta}_i/a_i$, solving for x_{ta} with eq. (3.7) (and thus ζ), then by solving for the smallest positive, pure real root of eq. (3.18). Doing this for a range of $\bar{\delta}_i/a_i$ allows us to solve for r_{vir}/r_{ta} as a function of $\bar{\delta}_i/a_i$, which we show for several cosmologies in figure 3.4. Note that the smallest values of $\bar{\delta}_i/a_i$ in this plot correspond to spheres which will collapse in the future (i.e, $z_c < 0$). This can quickly be seen by for a ΛCDM cosmology (black line) by noting that the smallest values of $\bar{\delta}_i/a_i$ correspond to z_c less than zero as indicated in figure 3.3. As the value of $\bar{\delta}_i/a_i$, increases, the turn around and collapse times take place at higher and higher redshifts, so that the lines for all cosmologies approach the E-ds

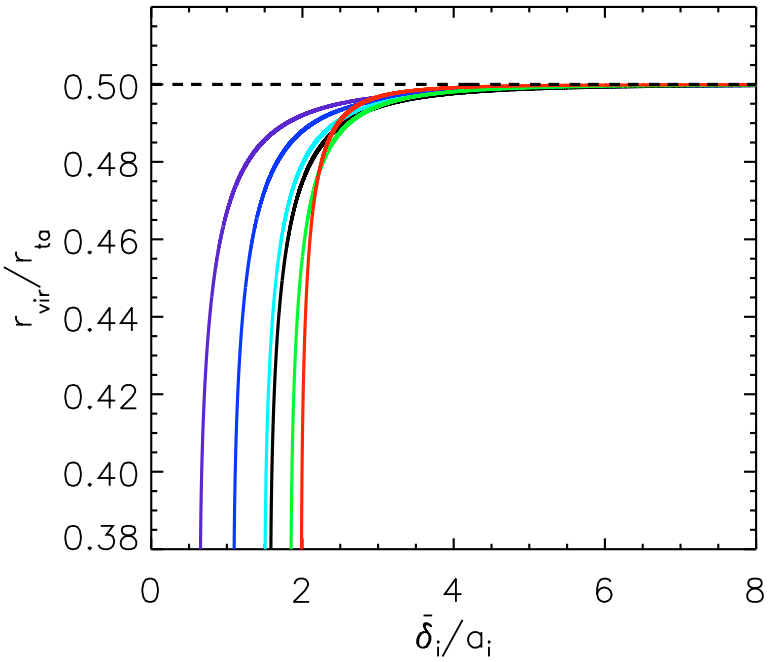

Figure 3.4.—: The ratio of the radius at virialization to the turn around radius for homogenous dark matter spheres. The red, green, turquoise, blue and violet lines correspond to the CI, CII, CIII, CIV and CV cosmologies respectively. The black solid and dashed lines correspond to a ΛCDM and an E-dS universe respectively.

results (dashed line). At the lowest values of $\bar{\delta}_i/a_i$, r_{vir}/r_{ta} quickly tends to a limiting value about 0.37 for all cosmologies, as already noted (but not explained) by Lahav et al. (1991). We derive this value using the formalism presented in the previous section. The reason that r_{vir}/r_{ta} approaches a limiting value is because $\bar{\delta}_i/a_i$ approaches the critical value required for turn around (and thus eventual virialization) for the particular cosmology. The critical value of $\bar{\delta}_i/a_i$ required for collapse corresponds to $b = 0$ in eq. (3.11), and when this is plugged into eq. (3.10), results in $(x_{ta}^{cr})^3 = (1/2)(\Omega_m/\Omega_\Lambda)$, so that $\zeta_{cr} = 1/2$. Notice that the cancellation of Ω_Λ/Ω_m results in a value of ζ_{cr} that is independent of cosmology. Plugging $\zeta = 1/2$ into eq. (3.18), solving, and taking the real

root results in:

$$\left(\frac{r_{vir}}{r_{ta}}\right)_{cr} = \frac{1}{2}(\sqrt{3}-1) \cong 0.366. \tag{3.20}$$

According to the spherical collapse model, a collapsing sphere will have a size x_{vir} at two times: once before turn around, and once after. We denote the redshift at which, according to the spherical collapse model, the collapsing sphere attains the size x_{vir} for the second time as z_{2vir}. We will make use of this quantity later in § 3.3, so we detail its calculation here. This redshift can be calculated as a function of $\bar{\delta}_i/a_i$ by noting that $x_{vir} = x_{ta}r_{vir}/r_{ta}$, where x_{ta} and r_{vir}/r_{ta} are calculated as a function of $(\bar{\delta}_i/a_i)$ as described above. The value of x_{vir} is then plugged into eq. (3.5) to solve for time, which is then converted to redshift with eq. (3.8). For the E-dS case, this occurs when the development angle attains a value of $3\pi/2$, corresponding to: $1 + z_{2vir} = 0.6318\bar{\delta}_i/a_i$. The results for this cosmology, and a ΛCDM cosmology are shown in figure 3.3.

Given the formalism derived thus far, we can solve for the volume averaged density of a halo collapsing at redshift z_c. This quantity is usually expressed in units of the critical density of the universe at the collapse time, denoted as $\Delta_c(z_c)$. For a flat cosmology with a cosmological constant, $\Delta_c(z_c)$ is given by the following fitting formula (Bryan & Norman 1998):

$$\Delta_c(z_c) = 18\pi^2 + 82d - 39d^2, \tag{3.21}$$

with $d \equiv \Omega_m(z_c) - 1$, and

$$\Omega_m(z) = \frac{\Omega_m(1+z)^3}{\Omega_m(1+z)^3 + (1-\Omega_m-\Omega_\Lambda)(1+z)^2 + \Omega_\Lambda}. \tag{3.22}$$

For an E-dS cosmology, $\Delta_c = 18\pi^2$, while for a general cosmology (not necessarily flat), it can be shown that:

$$\Delta_c(z_c) = \left(\frac{r_{vir}}{r_{ta}}\right)^{-3} \frac{a_c^3\Omega_m(z_c)}{x_{ta}^3}, \tag{3.23}$$

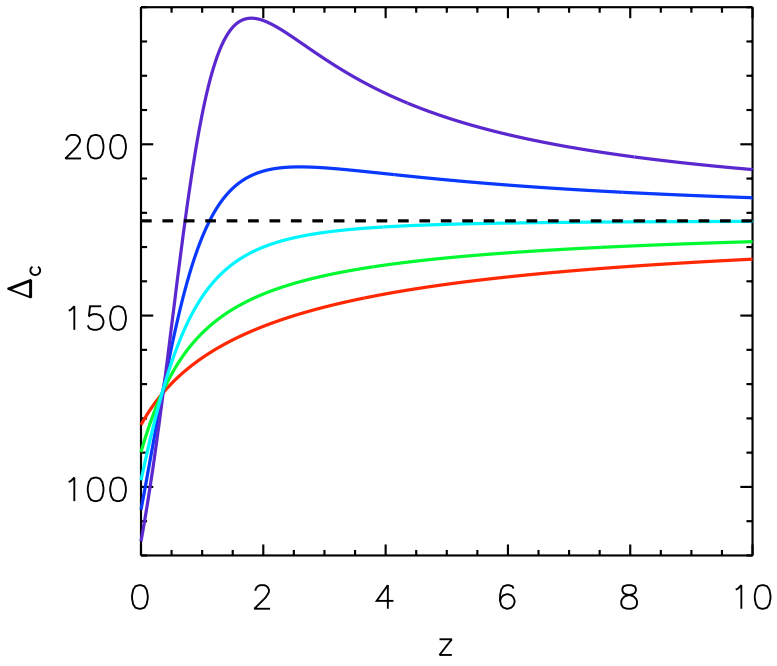

Figure 3.5.—: The average density of a halo at virialization in units of the critical density of the universe at time z given a collapse redshift of z for different cosmologies. The red, green, turquoise, blue and violet lines correspond to the CI, CII, CIII, CIV and CV cosmologies respectively (bottom to top respectively). The dashed black line corresponds to an E-dS cosmology. This figure matches very well with Figure 4 of Lokas & Hoffman (2001).

where we have already described how to derive r_{vir}/r_{ta} and x_{ta} as a function of $\bar{\delta}_i/a_i$, and $\bar{\delta}_i/a_i$ as a function of collapse redshift. We plot $\Delta_c(z_c)$ for different collapse redshifts and cosmologies in figure 3.5. This figure shows that, depending on the collapse redshift and cosmology, Δ_c can be substantially higher or lower than the canonical value of ~ 200. These results match closely to those of Lokas & Hoffman (2001) who perform the same calculation with a different method. We note one small difference in their derivation, which, since their results match well with ours, does not significantly alter the results. When they evaluate the initial specific energy of a shell at a time t_i, they assume no

peculiar velocity, and that the shell velocity is simply given by the Hubble flow (whereas, we, for the sake of realism, do add an initial peculiar velocity).

By noting that, for a halo collapsing at time z, $\Delta_c = \bar{\rho}(z)/\rho_c(z) = (3M/4\pi r_{vir}^3)/\rho_c(z)$, one may derive important physical properties of the halo at virialization (see for example Loeb & Furlanetto 2013). The radius of the halo at virialization is

$$r_{vir} = 0.79\text{kpc } h^{-1}\ M_8^{1/3} \left[\frac{\Omega_m}{\Omega_m(z)}\frac{\Delta_c(z)}{18\pi^2}\right]^{-1/3} \left(\frac{1+z}{10}\right)^{-1}, \tag{3.24}$$

where $M_8 \equiv M/(h^{-1}\ 10^8 M_\odot)$ and $h \equiv H_o/100\text{km s}^{-1}\ \text{Mpc}^{-1}$, with a corresponding circular velocity

$$\begin{aligned} V_c &= \left(\frac{GM}{r_{vir}}\right)^{1/2} \\ &= 23.4\text{km s}^{-1}\ M_8^{1/3} \left[\frac{\Omega_m}{\Omega_m(z)}\frac{\Delta_c(z)}{18\pi^2}\right]^{1/6} \left(\frac{1+z}{10}\right)^{1/2}. \end{aligned} \tag{3.25}$$

The virial temperature, defined by

$$T_{vir} = \frac{\mu m_p V_c^2}{2k_B}, \tag{3.26}$$

is thus given by

$$T_{vir} = 2.0\times 10^4\text{K}\ \left(\frac{\mu}{0.6}\right) M_8^{2/3} \left[\frac{\Omega_m}{\Omega_m(z)}\frac{\Delta_c(z)}{18\pi^2}\right]^{1/3} \left(\frac{1+z}{10}\right), \tag{3.27}$$

where μ is the mean molecular weight in units of the proton mass, m_p, and where k_B is Boltzmann's constant. For a fully ionized primordial gas, $\mu = 0.59$, while for a gas with ionized hydrogen and singly-ionized helium, $\mu = 0.61$. The binding energy of the halo at virialization is also approximately:

$$E_b = \frac{1}{2}\frac{GM^2}{r_{vir}} = 5.45\times 10^{53}\text{erg } h^{-1} M_8^{5/3} \left[\frac{\Omega_m}{\Omega_m(z)}\frac{\Delta_c(z)}{18\pi^2}\right]^{1/3} \left(\frac{1+z}{10}\right). \tag{3.28}$$

We use our calculation of $\Delta_c(z)$ for an arbitrary cosmology to show how these halo properties vary with cosmology. We show r_{vir}, V_c, T_{vir} and E_b as a function of collapse

redshift in figure 3.6 for different cosmologies. The figures show that these properties actually have little dependence on cosmology. Mathematically, this is because the only cosmology dependent term, $\Delta_c(z)/\Omega_m(z)$, in the expressions for r_{vir}, V_c, T_{vir}, and E_b is raised to very small powers. In § 3.5 we use the equations presented here to examine the environmental dependence of these halo properties given a fixed background cosmology. We show that, for halos collapsing at the same time, these properties are independent of environment.

3.2.3 Voids

The early evolution of a void (an extended region in which $\delta < 0$) is well described by the spherical collapse model. However, after a certain amount of time, shells of matter in the void will cross each other. Qualitatively, shell crossing will eventually occur since the average density contrast further out in a void where the perturbation blends into the background is greater than the average density contrast closer to the center. Therefore, according to the spherical collapse model, shells in the former region will expand at a slower rate than shells in the latter region. Eventually, at a redshift, z_{sc}, the inner shells will catch up with the outer shells, and shell crossing will occur. Thereafter, the analytic solution to the spherical collapse model developed in § 3.2 will no longer accurately describe the evolution of the void. This is because the mass interior to a shell (after crossing for that particular shell) is no longer constant in time, which is what we assumed in the solution to eq. (3.1). Exactly when and where in the void shell crossing first occurs depends on the initial density profile.

In Appendix 3.7 we go over the derivation of the redshift at first shell crossing, z_{sc},

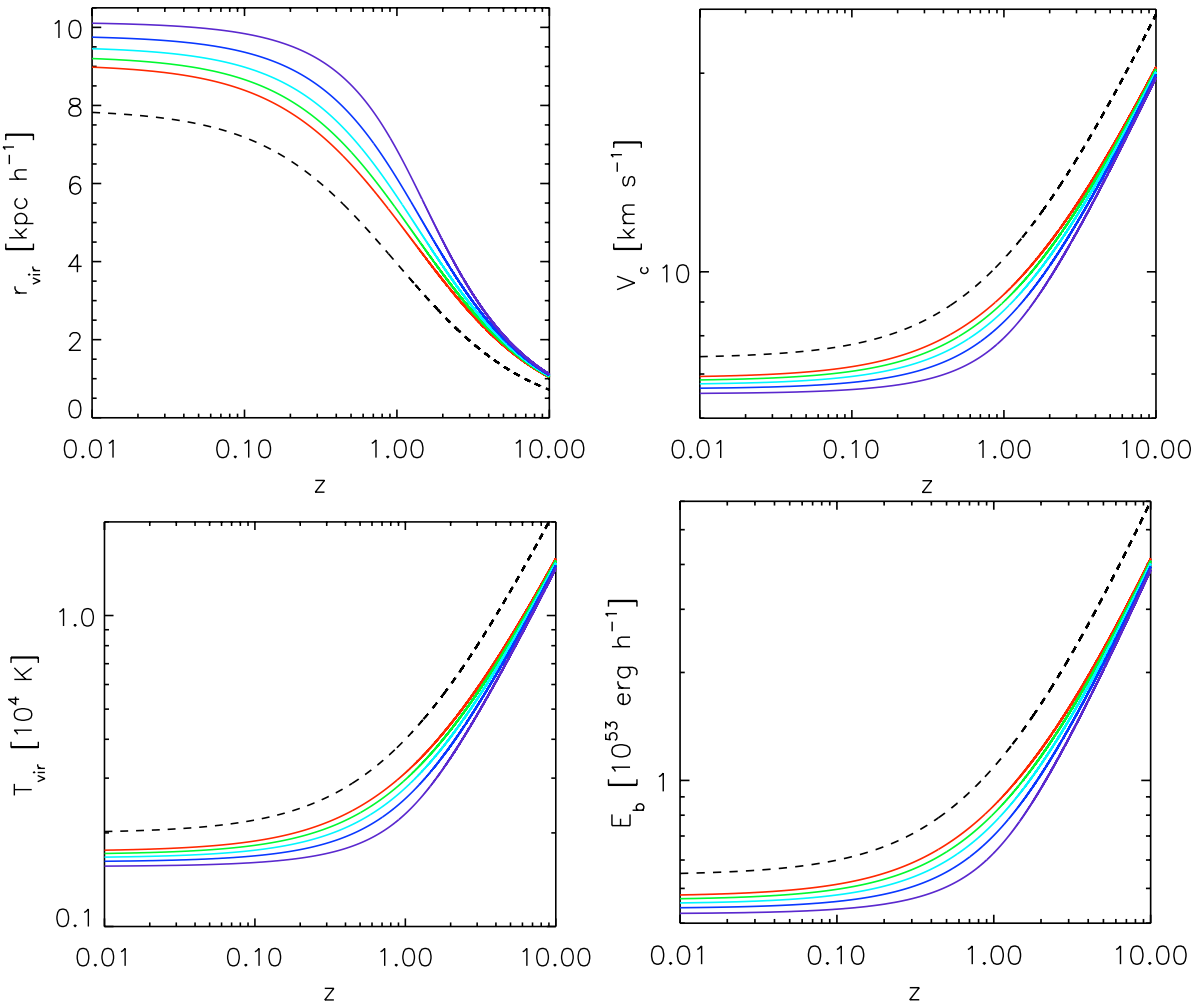

Figure 3.6.—: The virial radius, circular velocity, virial temperature and binding energy of a halo collapsing at z as a function of z for several cosmologies. The red, green, turquoise, blue and violet lines correspond to the CI, CII, CIII, CIV and CV cosmologies respectively (top to respectively in every panel except the r_{vir} panel which is bottom to top respectively). The dashed black line corresponds to an E-dS cosmology. All lines are plotted with a mass $M_8 = 1$.

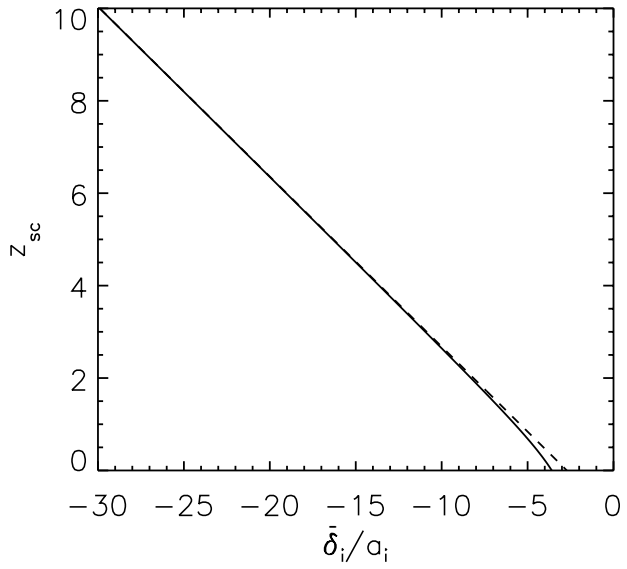

Figure 3.7.—: The redshift at first shell crossing for a void with an initial inverted top hat density profile as a function of $\bar{\delta}_i/a_i$ for a ΛCDM universe (solid line), and for an E-dS universe (dashed line). See figure 3.19 for examples of different cosmologies.

as a function of $\bar{\delta}_i/a_i$, as well as $\bar{\delta}_{NL}(z_{sc})$ and $\bar{\delta}_L(z_{sc})$, the non-linear and linear theory density contrasts at first shell crossing as a function of z_{sc} in an E-dS universe. In Appendix 3.8 we derive $z_{sc}(\bar{\delta}_i/a_i)$, $\bar{\delta}_{NL}(z_{sc})$ and $\bar{\delta}_L(z_{sc})$ for a general cosmology. We show the redshift at first shell crossing as a function of $\bar{\delta}_i/a_i$ for a void in a ΛCDM universe and an E-dS universe in figure 3.7 . The results for the ΛCDM universe only deviate slightly from the E-dS results at low redshift. However, significant deviation is found for other cosmologies (see figure 3.19). We also show the results for $\bar{\delta}_{NL}(z_{sc})$ for several different cosmologies in figure 3.8. Note that all of these calculations depend on the initial density profile of the void. In these figures, we assume an initial inverted top hat density profile, although in deriving our formalism in Appendix 3.7 and 3.8, we leave the formalism general to admit any initial density profile.

Motivated by Bryan & Norman (1998) who found an expression for the over-density

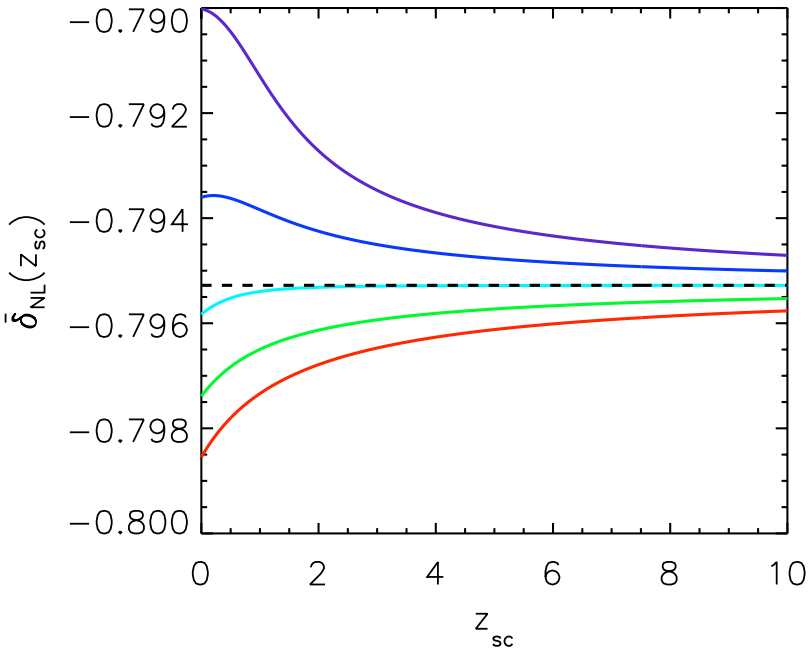

Figure 3.8.—: The non-linear theory under-density of a void with an initial inverted top hat density profile undergoing shell crossing at a redshift z_{sc} for different cosmologies. The red, green, turquoise, blue and violet lines correspond to the CI, CII, CIII, CIV and CV cosmologies respectively (bottom to top respectively). The dashed black line corresponds to an E-dS cosmology.

of a halo at collapse in a flat universe, purely as a function of $\Omega_m(z_c)$ (eq. (3.21)), we seek to find an expression for the under-density of a void in a flat universe (with $\Omega_\Lambda \neq 0$) at first shell crossing as a function of $\Omega_m(z_{sc})$. To do this, we divide eq. (3.3) by Ω_Λ, and replace Ω_m/Ω_Λ with the the relation,

$$\frac{\Omega_m}{\Omega_\Lambda} = \frac{a_{sc}^3}{\Omega_m^{-1}(z_{sc}) - 1}, \tag{3.29}$$

valid for a flat universe. eq. (3.3) is then re-written as

$$\left(\frac{d\hat{x}}{d\hat{t}}\right)^2 = y\hat{x}^{-1} + \hat{x}^2 - \frac{5}{3}y\hat{\delta}_i, \tag{3.30}$$

where we have used the following definitions to eliminate any dependence on a_{sc} or Ω_Λ:

$\hat{x} \equiv x/a_{sc}$, $\hat{t} \equiv tH_o\sqrt{\Omega_\Lambda}$, $\hat{\bar{\delta}}_i \equiv (\bar{\delta}_i/a_i)a_{sc}$. The only dependence is on $\Omega_m(z_{sc})$ through y, where $y \equiv [\Omega_m^{-1}(z_{sc}) - 1]^{-1}$. We also re-write eq. (3.73) with the same definitions:

$$\frac{\hat{\bar{\delta}}_i}{\hat{x}_{sc}} \frac{\partial \hat{x}_{sc}}{\partial \hat{\bar{\delta}}_i} = \frac{1}{\beta}. \tag{3.31}$$

To solve for the under-density at first shell crossing, we use a similar approach as in appendix 3.8. We first choose a value of $\Omega_m(z_{sc})$ and calculate the corresponding cosmic time with the analytic solution of the Friedmann equation for a flat universe:

$$\hat{t}_{sc} = \frac{2}{3} \ln \left[\sqrt{\Omega_m^{-1}(z_{sc}) - 1} + \sqrt{\Omega_m^{-1}(z_{sc})} \right]. \tag{3.32}$$

We then numerically solve for $\hat{x}(\hat{t} = \hat{t}_{sc}, \hat{\bar{\delta}}_i)$, the non-dimensionalized void radius at shell crossing for a given initial under-density, by integrating

$$\hat{t}_{sc} = \int_0^{\hat{x}(\hat{t}=\hat{t}_{sc}, \hat{\bar{\delta}}_i)} d\hat{x} \left[y\hat{x}^{-1} + \hat{x}^2 - \frac{5}{3} y \hat{\bar{\delta}}_i \right]^{-1/2}. \tag{3.33}$$

The initial value of the perturbation, $\hat{\bar{\delta}}_i$, resulting in first shell crossing at time $\hat{t}_{sc}$ is set by the initial shape of the density profile through eq. (3.31), with $\beta = 3$ corresponding to an initially inverted top hat (see appendix 3.8). We therefore insert our calculated $\hat{x}(\hat{t} = \hat{t}_{sc}, \hat{\bar{\delta}}_i)$ function into eq. (3.31) and numerically solve for the value of $\hat{\bar{\delta}}_i$ (and the corresponding $\hat{x}_{sc}$) for which the equation is satisfied. We then choose another value of $\Omega_m(z_{sc})$ and repeat the procedure. In this way, we are able to build up both $\hat{\bar{\delta}}_i$ and $\hat{x}_{sc}$ as functions of $\Omega_m(z_{sc})$. The $\hat{\bar{\delta}}_i$ function is irrelevant for our current purposes, but will be of use in § 3.4.

The non-linear under-density is given by $\bar{\delta}_{NL}^{sc}[\Omega_m(z_{sc})] = \hat{x}_{sc}^{-3}[\Omega_m(z_{sc})] - 1$, found by re-writting eq. (3.9) with $\hat{x}_{sc} = x_{sc}/a_{sc}$. We calculate $\bar{\delta}_{NL}^{sc}$ for $10^{-3} \leq \Omega_m(z_{sc}) \leq 1$ and find that it is well fit by a "broken log" function,

$$\bar{\delta}_{NL}^{sc}[\Omega_m(z_{sc})] = \ln \left\{ A\, \Omega_m^{\lambda}(z_{sc}) \left[1 + \frac{\Omega_m(z_{sc})}{\Omega_m'} \right]^{\kappa} \right\}, \tag{3.34}$$

which has a logarithmic index of λ for $\Omega_m(z_{sc}) \ll \Omega'_m$ and $(\lambda + \kappa)$ for $\Omega_m(z_{sc}) \gg \Omega'_m$. The best-fit parameters are $A = 4.5081 \times 10^{-1}$, $\lambda = 6.2627 \times 10^{-5}$, $\Omega'_m = 3.4044 \times 10^{-2}$ and $\kappa = 4.2016 \times 10^{-4}$, resulting in a better than $10^{-2}\%$ fit across the full range of $\Omega_m(z_{sc})$ that we consider. We note, however, that although $\bar{\delta}^{sc}_{NL}$ increases monotonically with $\Omega_m(z_{sc})$, the variation of $\bar{\delta}^{sc}_{NL}$ is quite slight, so that a value of -0.8 is accurate to within $\sim 1\%$ for any realistic cosmology (e.g. see figure 3.8).

Self similar solutions for the non-linear evolution after shell crossing in an E-dS universe have been derived by Fillmore & Goldreich (1984b); Bertschinger (1985b). For an initially "uncompensated" inverted top hat void (i.e., a void which initially lacks an over-dense ridge at its edge, compensating for the missing mass inside it), the self-similar solution predicts that the radius evolves as $t^{8/9}$, and the mass interior to it grows as $t^{2/3}$. Since, in an E-dS universe, $a \propto t^{2/3}$, the volume averaged density contrast grows as $1 + \bar{\delta}_{NL} \propto (M/r^3)/(a^{-3}) = \text{const}$, so that according to the self similar solution, for $z < z_{sc}$, $\bar{\delta}_{NL}(z|z_{sc}) \approx \bar{\delta}_{NL}(z_{sc})$.

In reality, however, the void takes a finite amount of time to transition to the self-simlar solution. Moreover, the solution is only valid for an E-dS cosmology. To calculate the evolution of a void after shell crossing for an arbitrary cosmology, we therefore employ a spherically symmetric finite difference code which follows the trajectories of each shell in the perturbation (see Appendix 3.9). In figure 3.9, we use this code to plot the non-linear average under-density with (eq. (3.78)) and without (eq. (3.9)) fixing for shell crossing (solid and dotted lines respectively) at the edge of an initial inverted top-hat for various cosmologies. The solutions are identical before shell crossing, but differ markedly after. After shell crossing, the true density contrast (solid lines) begins to increase. This is due to two conspiring effects: 1) the mass interior to

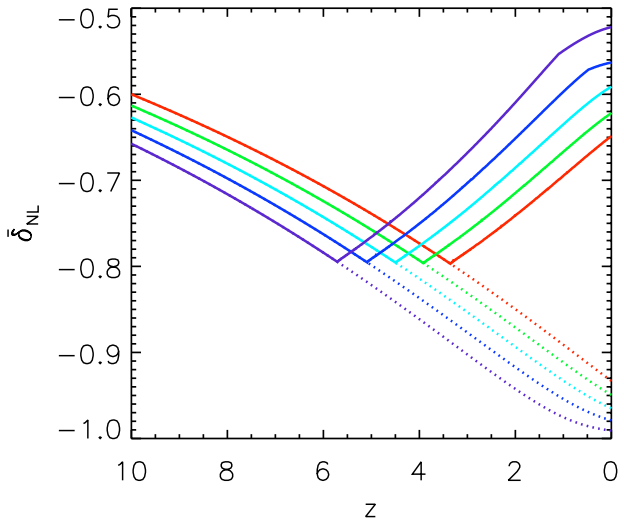

Figure 3.9.—: The evolution of the volume averaged non-linear density contrast within the edge of a void with an initial inverted top-hat density profile. Solid lines include the effects of shell crossing (see Appendix 3.9), and dotted lines do not (see § 3.2). The red, green, turquoise, blue and violet lines correspond to the CI, CII, CIII, CIV and CV cosmologies respectively (top to bottom respectively at $z = 10$). All lines have an initial seed, $\bar{\delta}_i/a_i = -15$.

the edge grows as shells from the outside flow into it, and 2) the expansion of the edge slows as the inward force increases due to the increasing amount of interior mass. We verify with a simulation in and E-dS cosmology, in which shell crossing occurs at a high redshift, that the monotonic increase in $\bar{\delta}_{NL}(z)$ eventually flattens, and transitions into the $\bar{\delta}_{NL} = \text{const}$, self-similar solution (see figure 3.22). Similar flattening can already start to be seen in the solid lines in figure 3.9. We also note that the discontinuity seen at first shell crossing is indeed physical, and is due to the fact that the mass interior to the edge of the void as a function of time has a discontinuity since constant up until the exact moment of shell crossing.

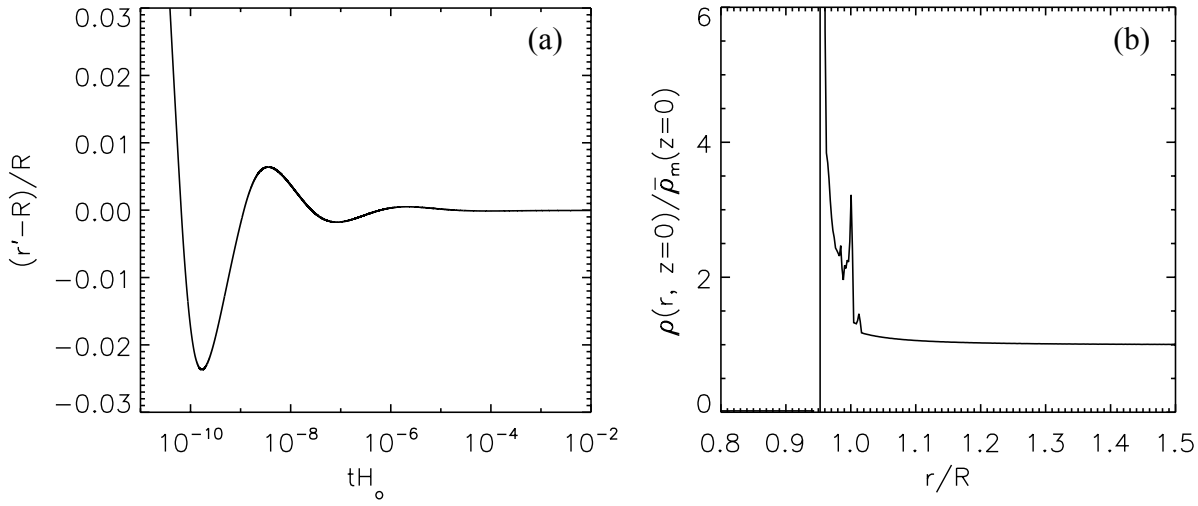

Figure 3.10.—: (a) The position of a shell, r', relative to the edge of the void, R in units of R. We set up the initial conditions such that shell crossing occurs very early, so that several periods of oscillation can be seen. (b) The radial density profile at $z = 0$ for a void with first shell crossing around a redshift of 10, in units of the mean matter density of the universe. The radial position is in units of the edge of the void, R. The cosmology for both panels is the CII cosmology.

We observe that the voids in our non-zero Ω_k and Ω_Λ cosmology simulations share several features with voids in an E-dS cosmology as calculated analytically from the self-similar solution. In figure 3.10a, we plot the position of a shell (r'), initially just outside of the edge of the void, relative to the position of the edge of the void (R) in units of R in a CII cosmology. The figure shows that a shell at r' oscillates about the edge of the void, with the amplitude of oscillation dampening in time. This damped, oscillatory motion was also noted in voids in the self-similar E-dS solution by Fillmore & Goldreich (1984b) (see their figure 3) and Bertschinger (1985b) (see there figure 8). The voids in our simulations also induce the formation of caustics, just as calculated in the previous two references (their figures 4 and 9 respectively). In figure 3.10b we plot the

measured density profile at $z = 0$ in units of the mean matter density of the universe (as given by eq. (3.91)) for a void in a CII cosmology, with first shell crossing around $z = 10$. The radial position is plotted in units of the position of the edge of the void. The density profile displays several distinct caustic features, with the density approaching the mean density of the universe far away from the void. Note that since we calculate the derivative of mass with respect to r by averaging over bins, the heights of the caustics (which are formally infinite) are truncated, and fine grained features are suppressed.

3.3 Model for the Full Run of the Evolution of Density Perturbations

In this section we bring together our treatment of over-dense non-collapsing regions, voids and halos to provide a simple model for the full non-linear evolution of a pressureless density perturbation. We will provide prescriptions for taking into account several highly non-linear effects, such as virialization and shell crossing. We keep our model general to allow for any cosmology and initial perturbation seed.

Once a halo virializes, its density remains roughly constant, while the background density of the universe declines as a^3. Therefore, to calculate $\bar{\delta}_{NL}(z|z_c)$ (the non-linear over-density given a collapse redshift $z_c \geq z$), we must fix the average density of the halo ($\bar{\rho}$) to its density at z_c. Given that $\Delta_c(z_c) = \bar{\rho}(z_c)/\rho_c(z_c)$, it is easy to show that that the formula for the non-linear volume averaged over-density for an object collapsing at $z_c \geq z$ as a function of z is:

$$\bar{\delta}_{NL}(z|z_c) = \frac{\Delta_c(z_c)}{\Omega_m(z_c)} \left(\frac{a}{a_c}\right)^3 - 1 = \left(\frac{r_{vir}}{r_{ta}}\right)^{-3} x_{ta}^{-3} a^3 - 1, \tag{3.35}$$

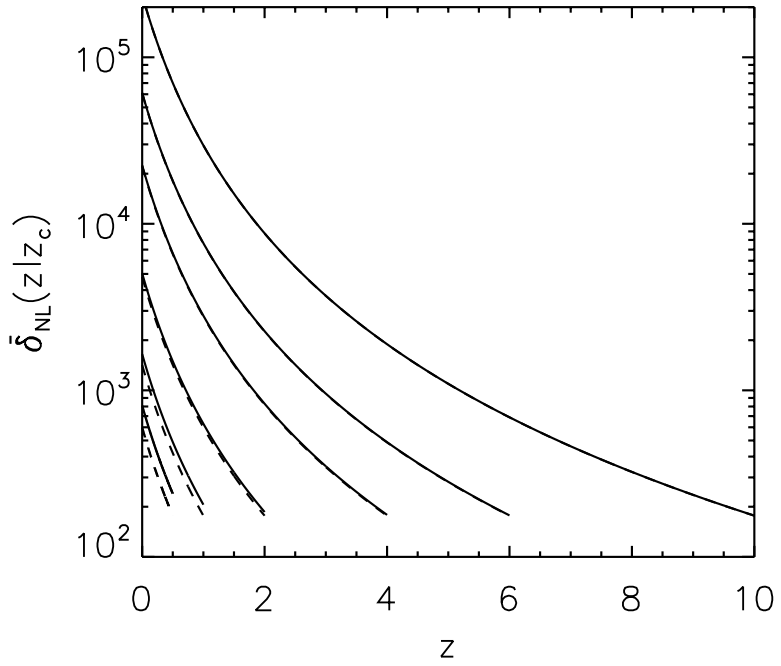

Figure 3.11.—: The average over-density of a virialized object as a function of redshift given a virialization redshift $z_c \geq z$. The different set of lines are for $z_c = 0.5$, 1, 2, 4, 6 and 10, with the solid lines showing the results for a ΛCDM universe, and the dashed lines showing the results for an E-dS universe. Note that by $z_c = 4$, the results for the two different cosmologies converge, and the lines in the figure become indistinguishable.

with the E-dS case reducing to $\bar{\delta}_{NL}(z|z_c) = 18\pi^2(a/a_c)^3 - 1$. We have already shown how to calculate r_{vir}/r_{ta} as well as x_{ta} for an arbitrary cosmology as a function of collapse redshift in § 3.2. We show $\bar{\delta}_{NL}(z|z_c)$ for a ΛCDM universe, as well as for an E-dS universe in figure 3.11 for different values of z_c.

In our model, we take the non-linear evolution of a collapsing over-dense dark matter sphere to be given by eq. (3.9) (before z_c) and (3.35) (after z_c). However, since the virial radius is roughly half the turn around radius (see § 3.2.2), if we use the spherical collapse model (eq. (3.9)) to evolve $\bar{\delta}_{NL}$ all the way until z_c, there will be a period of time after

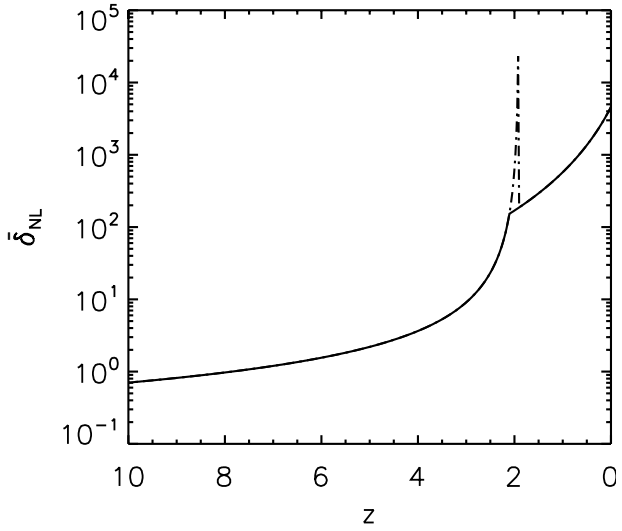

Figure 3.12.—: The evolution in redshift of the non-linear density contrast for a top-hat with $\bar{\delta}_i/a_i = 5$ in a ΛCDM cosmology. We show the evolution with (solid line) and without (dashed-dotted line) the fix we employ for the failure of the spherical collapse model due to virialization.

turn around when the radius of the sphere will be much smaller than r_{vir}. This means that the density of the sphere will be much greater than its density when virialized. This is an artifact due to the failure of the spherical collapse model some time after turn around. In reality, some time after turn-around, the object will no longer accurately be described by spherical collapse as it starts to virialize due to slight deviations from perfect spherical symmetry. To fix this unphysical spike in density, we stop evolving the radius of the sphere at a time z_{2vir}, as defined and solved for in § 3.2.2. That is, we calculate the evolution of the over-density with eq. (3.35) for $z < z_{2vir}$ (i.e. $z_c \rightarrow z_{2vir}$ in this equation). We show an example of $\bar{\delta}_{NL}$ as a function of z for an object that will virialize in figure 3.12, with and without this fix. The sudden spike in density for a time $z_c < z < z_{2vir}$ is clearly noticeable.

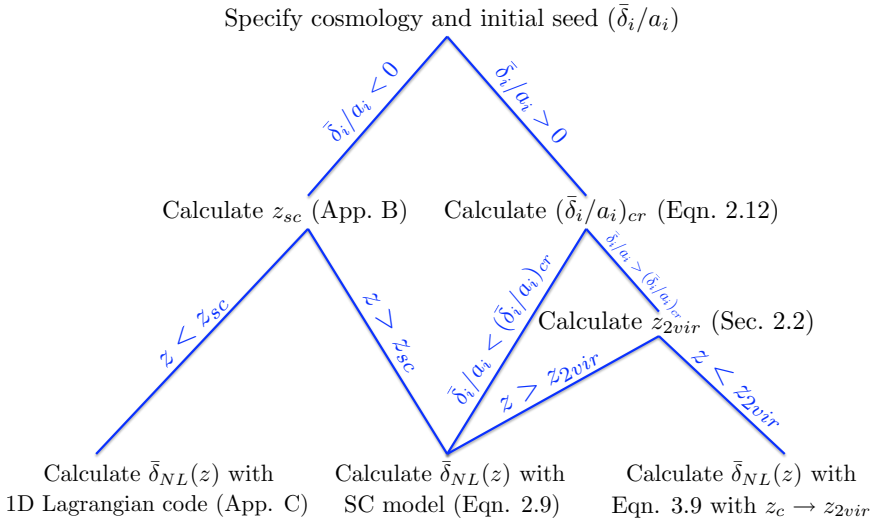

Figure 3.13.—: The decision tree corresponding to our simple analytic model for calculating the non-linear evolution of a pressureless density perturbation.

We now put together all of the formalism thus derived to present a simple analytic model for the full non-linear evolution of an over/under-density perturbation. We show a decision tree for our model in figure 3.13. Once the cosmology and initial seed $(\bar{\delta}_i/a_i)$ is specified, if $\bar{\delta}_i/a_i < 0$, the perturbation eventually turns into a rarified void. To determine the non-linear density at a redshift z, we must first determine if the void has already undergone shell crossing by calculating z_{sc} (§ 3.8 and figure 3.19). If shell crossing has already occurred, then we use eq. (3.78) and the spherically symmetric Lagrangian code presented in appendix 3.9 to calculate $\bar{\delta}_{NL}(z)$. If shell crossing has not yet occurred, then the evolution is described by spherical collapse, and we calculate $\bar{\delta}_{NL}(z)$ with eq. (3.9) using the spherical collapse equations in § 3.2. If the seed $\bar{\delta}_i/a_i > 0$ then we must determine if it is greater than $(\bar{\delta}_i/a_i)_{cr}$ (eq. (3.12)) and will collapse, or whether it is smaller and will expand forever. If the value of the seed is less than that required for eventual collapse, we calculate $\bar{\delta}_{NL}(z)$ with the spherical collapse model. If it is greater than we must determine the second redshift at which the perturbation reaches

its virial size, z_{2vir}, where the procedure for calculating z_{2vir} is outlined in § 3.2.2. If z is before z_{2vir}, then $\bar{\delta}_{NL}(z)$ is determined by the spherical collapse model, otherwise the perturbation is close to virialization and we use eq. (3.35).

In figure 3.14 we show results of our model for the evolution of the non-linear density contrast as a function of the initial seed perturbation, at different redshifts and for different cosmologies. The figure shows the density contrast in units of the mean density of the universe, $\bar{\delta} + 1$, which, following convention, we label $\bar{\Delta}$. The three different prescriptions for determining $\bar{\delta}_{NL}(z)$ are clearly visible: the 1D shell code at the lowest values of $\bar{\delta}_i/a_i$, eq. (3.35) at the highest values and the spherical collapse model in between. All lines have the solution $\bar{\Delta}_{NL}(\bar{\delta}_i/a_i = 0) = 1$ since an initial seed perturbation equal to zero corresponds to the mean density of the universe, which evolves according to the Hubble flow. Note that since we are showing the volume averaged density contrast, there are regions within the perturbation which can be significantly more or less dense than as shown by the lines. For example, at the lowest values of $\bar{\delta}_i/a_i$ after shell crossing, figure 3.10b shows that voids have regions with highly dense thin shells, and an interior with a density that is virtually zero. At the highest values of $\bar{\delta}_i/a_i$, after virialization, the halo density profile is roughly given by the NFW profile, which is highly dense at the center. However, in the regime in which the evolution is described by spherical collapse, for an initial top-hat perturbation, the density everywhere in the perturbation is given exactly by the curves shown. This is because, in the spherical collapse regime, $\bar{\delta}_{NL}$ is given by $x^{-3}(1+z)^{-3} - 1$ (eq. (3.9)). If the initial perturbation is a top-hat, then for $r < R$ (where R is the edge of the top-hat) x has no space dependence (i.e., the trajectories, when scaled to x are self-similar). Therefore, for $r < R$, $\bar{\delta}_{NL}$ is itself a top-hat that is scaled up or down in time. Since the volume averaged density is constant

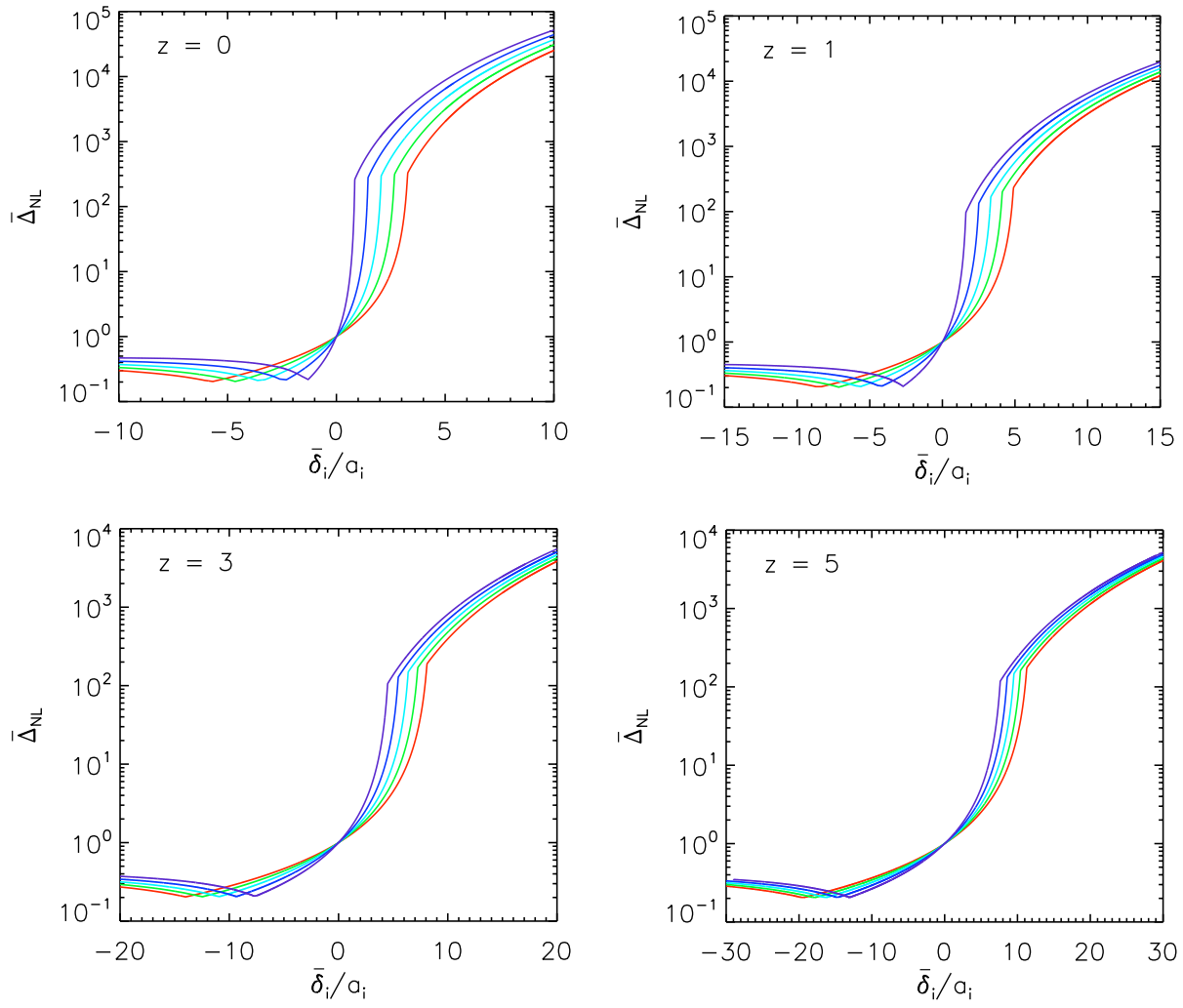

Figure 3.14.—: The full run of the evolution of the volume averaged non-linear density (in units of the mean density of the universe) for an initial top-hat perturbation as a function of initial seed for different cosmologies. Each panel corresponds to a different redshift. The red, green, turquoise, blue and violet lines correspond to the CI, CII, CIII, CIV and CV cosmologies respectively (bottom to top respectively at the highest values of $\bar{\delta}_i/a_i$).

in space, then the local density, δ_{NL}, must everywhere within R be equal to $\bar{\delta}_{NL}$.

3.4 Linear Perturbation Theory

The linear theory evolution of density perturbations is also useful as it is widely used in statistical calculations such as the excursion set formalism. We now briefly go over linear theory in an arbitrary cosmology, and use the theory to calculate some valuable linear theory properties of pressureless density perturbations. In linear theory, the growing mode solution quickly dominates, and the evolution of an over-density evolves proportionally to the growth factor, $D(z)$. For a flat cosmology, Carroll et al. (1992) find that D is well approximated (to within $\sim 2\%$ for $\Omega_m > 0.1$) by the following fitting function:

$$\mathcal{D}(z) = \frac{5}{2}\Omega_m(z)\left\{\Omega_m^{4/7}(z) - \Omega_\Lambda(z) + \left[1 + \frac{\Omega_m(z)}{2}\right]\left[1 + \frac{\Omega_\Lambda(z)}{70}\right]\right\}^{-1}, \tag{3.36}$$

with $\mathcal{D} \equiv D/a$,

$$\Omega_m(z) = \frac{\Omega_m(1+z)^3}{\Omega_m(1+z)^3 + \Omega_\Lambda}, \tag{3.37}$$

and

$$\Omega_\Lambda(z) = \frac{\Omega_\Lambda}{\Omega_m(1+z)^3 + \Omega_\Lambda}. \tag{3.38}$$

Eq. (3.36) is normalized to equal unity in the matter dominated era when $\Omega_m(z) \to 1$.

In a general cosmology, the growth factor must be solved by an integral:

$$\mathcal{D} = \frac{5\Omega_m}{2a^2}\left[1 + \Omega_m\left(\frac{1}{a} - 1\right) + \Omega_\Lambda(a^2 - 1)\right]^{1/2}\int_0^a \left[1 + \Omega_m\left(\frac{1}{a'} - 1\right) + \Omega_\Lambda(a'^2 - 1)\right]^{-3/2} da'. \tag{3.39}$$

For a_i sufficiently small enough, the linear theory over-density is therefore given by

$$\delta_L(z) = a\mathcal{D}(z)\frac{\delta_i}{a_i}. \tag{3.40}$$

A useful quantity used to calculate the mass function of halos is the linear theory over-density of a perturbation at the halo collapse time, δ_c. For an E-dS universe, this can be shown to be 1.68647, while for a flat cosmology with $\Omega_\Lambda \neq 0$, δ_c is a function of collapse redshift, and is well fit by the following fitting function (Mo et al. 2010):

$$\delta_c(z_c) = 1.686[\Omega_m(z_c)]^{0.0055}. \tag{3.41}$$

We calculate $\delta_c(z_c)$ for a general cosmology by first calculating $z_c(\bar{\delta}_i/a_i)$ as outlined in § 3.2.2. We then calculate $\mathcal{D}(a = a_c)$ with eq. (3.39) and $\delta_c(z_c)$ with eq. (3.40). We show examples of $\delta_c(z_c)$ for various cosmologies in figure 3.15. This figure matches very well with figure 3 of Lokas & Hoffman (2001) who perform the same calculation with a different method. They expand the solutions to the equations of motion of the perturbation and the universe at early times and then invert the series to find an expression for δ_i/a_i as a function of collapse redshift. To complete the calculation, they must then numerically solve for the initial perturbation as a function of collapse redshift in much the same way that we do. We prefer our method of solving for $\delta_c(z_c)$ as we believe its derivation and actual computation is more straightforward.

We also calculate $\bar{\delta}_L(z_{sc})$, the linear theory under-density of a void at first shell crossing. This quantity has been used to calculate void statistics, such as the void size distribution (e.g. Sheth & van de Weygaert 2004). Since $\bar{\delta}_L(z_{sc})$ for a general cosmology has not yet been calculated, these calculations have used the $\bar{\delta}_L(z_{sc})$ value for an E-dS cosmology, -2.72. (see appendix 3.7). We calculate $\bar{\delta}_L(z_{sc})$ for a general cosmology by first calculating $z_{sc}(\bar{\delta}_i/a_i)$ as outlined in appendix 3.8. The quantities, $\mathcal{D}(a = a_{sc})$ and $\bar{\delta}_L(z_{sc})$ are then calculated with eqs. (3.39) and (3.40) respectively. We note that since z_{sc} is no longer linear with $\bar{\delta}_i/a_i$, as with δ_c, $\bar{\delta}_L(z_{sc})$ is no longer constant with redshift.

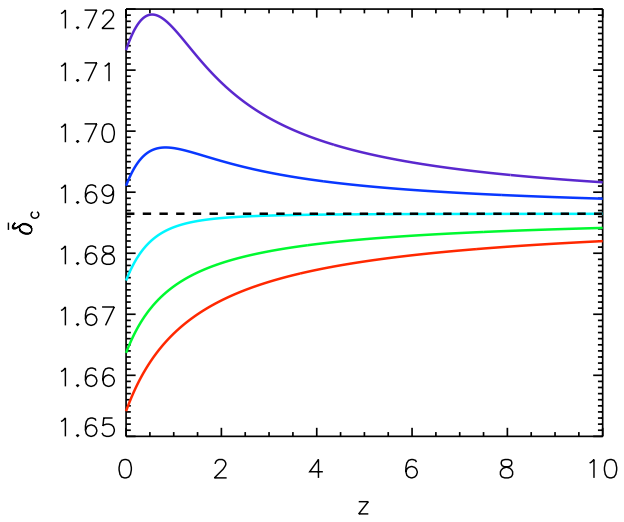

Figure 3.15.—: The linear theory over-density at collapse given a collapse redshift z. The red, green, turquoise, blue and violet lines correspond to the CI, CII, CIII, CIV and CV cosmologies respectively (bottom to top respectively). The dashed black line corresponds to an E-dS cosmology. This figure matches very well with Figure 3 of Lokas & Hoffman (2001).

We show the linear theory under-density at first shell crossing as a function of first shell crossing redshift for several cosmologies in figure 3.16.

As we did in non-linear theory, we calculate the linear theory under-density of a void at first shell crossing in a flat universe (with $\Omega_\Lambda \neq 0$) as a function of $\Omega_m(z_{sc})$. To do this, we re-write eq. (3.40) as $\bar{\delta}_L^{sc} = \mathcal{D}[\Omega_m(z_{sc})]\hat{\bar{\delta}}_i[\Omega_m(z_{sc})]$, where $\hat{\bar{\delta}}_i$ ($\equiv \bar{\delta}_i a_{sc}/a_i$) is the initial seed resulting in first shell crossing at $\Omega_m(z_{sc})$ for a specific initial density profile. In § 3.2.3, we have already explained how to calculate $\hat{\bar{\delta}}_i$ as a function of $\Omega_m(z_{sc})$ for an initial inverted top hat profile in a flat universe. To calculate $\mathcal{D}$ as a function of $\Omega_m(z_{sc})$ in a flat universe, we insert eq. (3.29) into eq. (3.39) to eliminate dependence on Ω_m and

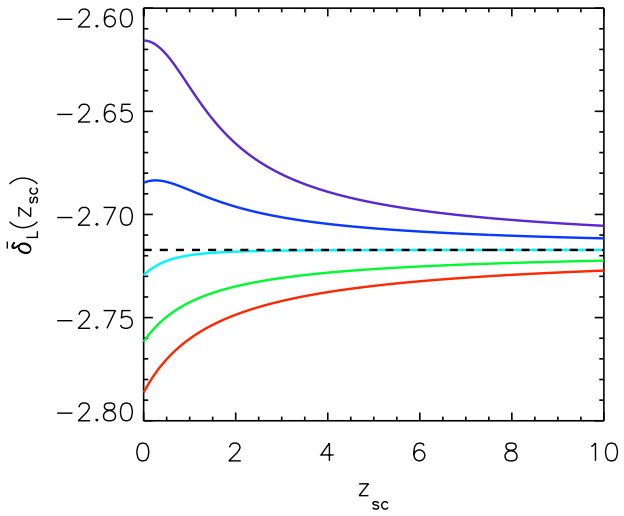

Figure 3.16.—: The linear theory under-density of a void with an initial inverted top hat density profile undergoing first shell crossing at a redshift z_{sc} for different cosmologies. The red, green, turquoise, blue and violet lines correspond to the CI, CII, CIII, CIV and CV cosmologies respectively (bottom to top respectively). The dashed black line corresponds to an E-dS cosmology.

Ω_Λ and find that

$$\mathcal{D} = \frac{5}{2} y \sqrt{y+1} \int_0^1 \left[y\hat{a}^{-1} + \hat{a}^2 \right]^{-3/2} d\hat{a}, \tag{3.42}$$

where $\hat{a} \equiv a'/a_{sc}$ and where y is a function of $\Omega_m(z_{sc})$ and has already been defined in § 3.2.3.

We calculate $\bar{\delta}_L^{sc}[\Omega_m(z_{sc})]$ for $10^{-3} \leq \Omega_m \leq 1$ and find that is well fit by the same fitting function as in the non-linear theory case:

$$\bar{\delta}_L^{sc}\left[\Omega_m(z_{sc})\right] = \ln\left\{ A_L\, \Omega_m^{\lambda_L}(z_{sc}) \left[1 + \frac{\Omega_m(z_{sc})}{\Omega'_{m,L}} \right]^{\kappa_L} \right\}. \tag{3.43}$$

Our best-fit parameters are $A_L = 6.396 \times 10^{-2}$, $\lambda_L = 1.438 \times 10^{-3}$, $\Omega'_{m,L} = 3.071 \times 10^{-2}$ and $\kappa_L = 9.220 \times 10^{-3}$ resulting in a better than $10^{-2}\%$ fit across the full range of $\Omega_m(z_{sc})$ considered. Although $\bar{\delta}_L^{sc}$ increases monotonically with $\Omega_m(z_{sc})$, considering the

small values of the logarithmic slopes, λ_L and κ_L, it has a fairly weak dependence on cosmology, so that the E-dS value of ≈ -2.7 is accurate to within a few percent for any flat cosmology.

3.5 Environmental Dependence

The formation of structure in environments with large-scale over/under-densities is important to consider, since in reality, the universe is not perfectly smooth on large scales. For example, by considering regions with large scale over-densities, the excursion set formalism has been used to model the clustering of halos, quantified by a halo bias factor, b (Mo & White 1996). By considering the spherical collapse of dark matter, we now investigate how the physical properties of halos (e.g., virial radius, temperature) depend on environment. We do this by identifying the overall over/under-density in a region, $\mathcal{R}$, as a change in cosmology, and use the spherical collapse formalism for that particular cosmology as developed in § 3.2. We will show that, regardless of environment, for halos collapsing at the same time, their physical properties are the same, but that they formed from different fluctuation amplitudes in the initial cosmic density field.

3.5.1 The Cosmology of $\mathcal{R}$

We parameterize the over/under-density in $\mathcal{R}$ by $\bar{\delta}^o_{\mathcal{R}}$, the present-day, non-linear, volume averaged density with respect to the mean matter density of the universe today:

$$\bar{\delta}^o_{\mathcal{R}} = \frac{\bar{\rho}^o_{\mathcal{R}}}{\bar{\rho}_o} - 1. \tag{3.44}$$

Under Birkhoff's theorem, this region evolves according to its own cosmology, with it's expansion is governed by its own Friedmann equation,

$$H_{\mathcal{R}}^2 = H_{o,\mathcal{R}}^2(\Omega_m^{\mathcal{R}} a_{\mathcal{R}}^{-3} + \Omega_\Lambda^{\mathcal{R}} + \Omega_k^{\mathcal{R}} a_{\mathcal{R}}^{-2}). \tag{3.45}$$

We now solve for the non-dimensionalized energy densities of $\mathcal{R}$ as a function of $\bar{\delta}_{\mathcal{R}}^o$. From eq. (3.44), it can be seen that

$$\bar{\rho}_{\mathcal{R}}^o = \bar{\rho}_o(1 + \bar{\delta}_{\mathcal{R}}^o) = \frac{3H_o^2}{8\pi G}\Omega_m(1 + \bar{\delta}_{\mathcal{R}}^o), \tag{3.46}$$

from which it follows that

$$\Omega_m^{\mathcal{R}} = \frac{\bar{\rho}_{\mathcal{R}}^o}{\rho_c^{\mathcal{R}}} = \left(\frac{H_{o,\mathcal{R}}}{H_o}\right)^{-2} \Omega_m(1 + \bar{\delta}_{\mathcal{R}}^o). \tag{3.47}$$

Since $\mathcal{R}$ is pervaded by the same amount of dark energy as the background universe,

$$\Omega_\Lambda^{\mathcal{R}} = \frac{\rho_\Lambda^o}{\rho_c^{\mathcal{R}}} = \left(\frac{H_{o,\mathcal{R}}}{H_o}\right)^{-2} \Omega_\Lambda. \tag{3.48}$$

Using the previous two equations, the non-dimensionalized curvature energy density is

$$\begin{aligned} \Omega_k^{\mathcal{R}} &= 1 - \Omega_m^{\mathcal{R}} - \Omega_\Lambda^{\mathcal{R}} \\ &= 1 - \left(\frac{H_{o,\mathcal{R}}}{H_o}\right)^{-2} \left[\Omega_m(1 + \bar{\delta}_{\mathcal{R}}^o) + \Omega_\Lambda\right], \end{aligned} \tag{3.49}$$

which reduces to $1 - (H_{o,\mathcal{R}}/H_o)^{-2}(1 + \Omega_m \bar{\delta}_{\mathcal{R}}^o)$ if the background universe is flat. All that is left to do to completely specify the cosmology of $\mathcal{R}$ is to solve for the ratio $H_{o,\mathcal{R}}/H_o$ in terms of $\bar{\delta}_{\mathcal{R}}^o$. We do this by integrating the Friedmann equation for the background and the Friedmann equation for $\mathcal{R}$ (eq. (3.45)) to the present day, and matching the times. The age of the universe is

$$t_o H_o = \int_0^1 \frac{da}{\sqrt{\Omega_m(a^{-1} - 1) + \Omega_\Lambda(a^2 - 1) + 1}}, \tag{3.50}$$

which for $(\Omega_m, \Omega_\Lambda) = (0.27, 0.73)$ equals about 0.99268687. Integrating eq. (3.45) to the present day, and rearranging, it can be shown that:

$$t_o H_o = \int_0^1 \frac{da_{\mathcal{R}}}{\sqrt{\Omega_m(1+\bar{\delta}^o_{\mathcal{R}})(a_{\mathcal{R}}^{-1}-1) + \Omega_\Lambda(a_{\mathcal{R}}^2-1) + \left(\frac{H_{o,\mathcal{R}}}{H_o}\right)^2}}. \tag{3.51}$$

By setting $t_o H_o$ to the value previously quoted, we may numerically solve this equation for $H_{o,\mathcal{R}}/H_o$ as a function $\bar{\delta}^o_{\mathcal{R}}$. We then this insert this function into eqs. (3.47) - (3.49) to solve for the cosmology of $\mathcal{R}$.

In figure 3.17 we plot the present-day Hubble parameter and the cosmological energy densities of $\mathcal{R}$ as a function $\bar{\delta}^o_{\mathcal{R}}$, where the background cosmology has $(\Omega_m, \Omega_\Lambda) = (0.27, 0.73)$. To show the curvature of $\mathcal{R}$, we plot $\Omega^{\mathcal{R}}_m + \Omega^{\mathcal{R}}_\Lambda$ instead of $\Omega^{\mathcal{R}}_k$ since the y-axis is logarithmic and since $\Omega^{\mathcal{R}}_k$ goes negative. The figure shows that when $\bar{\delta}^o_{\mathcal{R}} < 0$ (> 0), $\mathcal{R}$ behaves as an open (closed) universe, while when $\bar{\delta}^o_{\mathcal{R}} = 0$, $\mathcal{R}$ behaves as the background universe with $H_{o,\mathcal{R}}/H_o = 1$, $\Omega^{\mathcal{R}}_m = \Omega_m$, $\Omega^{\mathcal{R}}_\Lambda = \Omega_\Lambda$.

3.5.2 Halos in $\mathcal{R}$

In this section we consider the effect of environment on the collapse of halos by applying the change of cosmology in $\mathcal{R}$ to the spherical collapse model. We start by deriving a useful relationship between a_i and $a_{i,\mathcal{R}}$. We solve for $t_i H_o$ by integrating both eqs. (3.50) and (3.51) till a_i and $a_{i,\mathcal{R}}$ respectively. Setting both expressions equal to each other, and expanding the integrands, we have

$$\int_0^{a_i} \left[\sqrt{\frac{a'}{\Omega_m}} + \mathcal{O}\left(a'^{3/2}\right)\right] da' = \int_0^{a_{i,\mathcal{R}}} \left[\sqrt{\frac{a'_{\mathcal{R}}}{\Omega_m(1+\bar{\delta}^o_{\mathcal{R}})}} + \mathcal{O}\left(a'^{3/2}_{\mathcal{R}}\right)\right] da'_{\mathcal{R}}, \tag{3.52}$$

so that

$$a_{i,\mathcal{R}} \cong a_i(1+\bar{\delta}^o_{\mathcal{R}})^{1/3}. \tag{3.53}$$

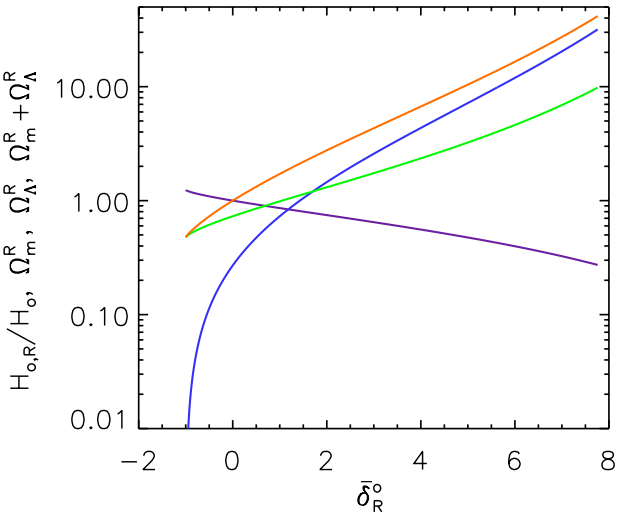

Figure 3.17.—: The cosmological parameters of $\mathcal{R}$ as a function of the present-day under/over-density of $\mathcal{R}$, where the background universe has $(\Omega_m,\ \Omega_\Lambda) = (0.27,\ 0.73)$. The purple, green, blue and orange lines (bottom to top respectively at the highest $\bar{\delta}_{\mathcal{R}}^o$) correspond to $H_{o,\mathcal{R}}/H_o$, $\Omega_\Lambda^{\mathcal{R}}$, $\Omega_m^{\mathcal{R}}$ and $\Omega_m^{\mathcal{R}} + \Omega_\Lambda^{\mathcal{R}}$ respectively.

Using this expression, we may write the non-dimensionalized turn around radius in $\mathcal{R}$ as

$$x_{ta}^{\mathcal{R}} = \frac{r_{ta}^{\mathcal{R}} a_{i,\mathcal{R}}}{r_i} = \frac{r_{ta}^{\mathcal{R}} a_i (1+\bar{\delta}_{\mathcal{R}}^o)}{r_i}. \tag{3.54}$$

Several important physical properties of a halo at collapse are given by eqs. (3.24)-(3.28). We may re-express these equations for the cosmology appropriate to $\mathcal{R}$ by re-writing any cosmology dependent variables. For example, for a halo collapsing in $\mathcal{R}$ at a time corresponding to z

$$r_{vir}^{\mathcal{R}}(z) \propto \left[\frac{\Omega_m^{\mathcal{R}}}{\Omega_m^{\mathcal{R}}(z)}\Delta_c^{\mathcal{R}}(z)\right]^{-1/3} \left(\frac{H_{o,\mathcal{R}}}{H_o}\right)^{-2/3}, \tag{3.55}$$

where we have left out terms without any cosmological dependance. By re-writing $\Delta_c^{\mathcal{R}}(z)$ with $(r_{vir}/r_{ta})_{\mathcal{R}}^{-3} a\Omega_m^{\mathcal{R}}(z)/(x_{ta}^{\mathcal{R}})^3$ (see eq. (3.23)), $x_{ta}^{\mathcal{R}}$ with eq. (3.54) and $\Omega_m^{\mathcal{R}}$ with

eq. (3.47), we find

$$r_{vir}^{\mathcal{R}}(z) \propto \Omega_m^{-1/3} \chi_{ta}{}^{\mathcal{R}} \left(\frac{r_{vir}}{r_{ta}}\right)_{\mathcal{R}}, \tag{3.56}$$

where $\chi_{ta}{}^{\mathcal{R}} \equiv r_{ta}^{\mathcal{R}} a_i / r_i$. The other expression for the physical properties at collapse (V_c, T_{vir} and E_b) can similarly be written in terms of Ω_m, $\chi_{ta}{}^{\mathcal{R}}$ and $(r_{vir}/r_{ta})_{\mathcal{R}}$. We now show that both $\chi_{ta}{}^{\mathcal{R}}$ and $(r_{vir}/r_{ta})_{\mathcal{R}}$ are independent of the cosmology in $\mathcal{R}$, so that for all halos collapsing at z, their physical are given by the mean cosmology of the universe.

The ratio $(r_{vir}/r_{ta})_{\mathcal{R}}$ is found by solving eq. (3.18), where the only comsological dependence in this equation is through, ζ. For $\mathcal{R}$, ζ, is given by

$$\zeta = \frac{\Omega_\Lambda^{\mathcal{R}}}{\Omega_m^{\mathcal{R}}} \left(\frac{r_{ta}^{\mathcal{R}} a_{i,\mathcal{R}}}{r_i}\right)^3 = \frac{\Omega_\Lambda}{\Omega_m} \left(\chi_{ta}{}^{\mathcal{R}}\right)^3, \tag{3.57}$$

where, in the second equality, we have used eqs. (3.47), (3.48) and (3.53). Therefore, if $\chi_{ta}{}^{\mathcal{R}}$ is independent of cosmology, so too is $(r_{vir}/r_{ta})_{\mathcal{R}}$.

To solve for the dynamics of a collapsing halo in $\mathcal{R}$, we make the following substitutions in the equation of motion for spherical collapse: $H_o \to H_{o,\mathcal{R}}$, $a_i \to a_{i,\mathcal{R}}$, $\Omega_m \to \Omega_m^{\mathcal{R}}$, $\Omega_\Lambda \to \Omega_\Lambda^{\mathcal{R}}$, $\Omega_k \to \Omega_k^{\mathcal{R}}$ and $\bar{\delta}_i \to \bar{\delta}_i^{\mathcal{R}}$ (where $\bar{\delta}_i^{\mathcal{R}} = \rho_{\mathcal{R}}(i)/\bar{\rho}_{\mathcal{R}}(i) - 1$, with $\rho_{\mathcal{R}}(i)$ the initial density of the region in $\mathcal{R}$, and $\bar{\rho}_{\mathcal{R}}(i)$ the initial mean density of $\mathcal{R}$). Since $\bar{\rho}_{\mathcal{R}}(i) = 3H_o^2\Omega_m(1+\bar{\delta}_{\mathcal{R}}^o)/[8\pi G a_i^3(1+\bar{\delta}_{\mathcal{R}}^o)] = \bar{\rho}(i)$, where $\bar{\rho}(i)$ is the initial mean density of the universe, $\bar{\delta}_i^{\mathcal{R}} = \rho_{\mathcal{R}}(i)/\bar{\rho}(i) - 1$. The parameters $\Omega_m^{\mathcal{R}}$, $\Omega_\Lambda^{\mathcal{R}}$ and $a_i^{\mathcal{R}}$ are then re-written with eqs. (3.47), (3.48) and (3.53), respectively, to find:

$$t_c H_o = 2 \int_0^{\chi_{ta}{}^{\mathcal{R}}} \left\{ \Omega_\Lambda x'^2 + \left[\frac{\Omega_k^{\mathcal{R}}}{(1+\bar{\delta}_{\mathcal{R}}^o)^{2/3}} \left(\frac{H_{o,\mathcal{R}}}{H_o}\right)^2 - \frac{5}{3}\frac{\bar{\delta}_i^{\mathcal{R}}}{a_i}\Omega_m \right] + \frac{\Omega_m}{x'} \right\}^{-1/2} dx', \tag{3.58}$$

with

$$\Omega_\Lambda \left(\chi_{ta}{}^{\mathcal{R}}\right)^3 + \left[\frac{\Omega_k^{\mathcal{R}}}{(1+\bar{\delta}_{\mathcal{R}}^o)^{2/3}} \left(\frac{H_{o,\mathcal{R}}}{H_o}\right)^2 - \frac{5}{3}\frac{\bar{\delta}_i^{\mathcal{R}}}{a_i}\Omega_m \right] \chi_{ta}{}^{\mathcal{R}} + \Omega_m = 0. \tag{3.59}$$

By fixing a halo collapse time, $t_c H_o$, regardless of the cosmology of $\mathcal{R}$, the right hand side of eq. (3.58) must also be fixed (i.e. the integrand and upper limit of integration must be fixed). This occurs when the term in the brackets in the previous two equation is a constant with respect to the cosmology of $\mathcal{R}$, so that

$$\frac{\Omega_k^{\mathcal{R}}}{(1+\bar{\delta}_{\mathcal{R}}^o)^{2/3}}\left(\frac{H_{o,\mathcal{R}}}{H_o}\right)^2 - \frac{5}{3}\frac{\bar{\delta}_i^{\mathcal{R}}}{a_i}\Omega_m = \Omega_k - \frac{5}{3}\frac{\bar{\delta}_i}{a_i}\Omega_m. \tag{3.60}$$

Therefore, for halos collapsing at the same time, ${\chi_{ta}}^{\mathcal{R}}$ and $(r_{vir}/r_{ta})_{\mathcal{R}}$ are constant, and the physical properties $r_{vir}(z)$, $V_c(z)$, $T_{vir}(z)$ and $E_b(z)$ are given by considering the mean cosmology of the universe.

Eq. (3.60) shows that even though the physical properties of halos collapsing at the same time but in different environments are identical, they start from different initial seed perturbations. Rearranging the previous equation, we find a linear relation between the amplitude of the initial seed of a halo collapsing in $\mathcal{R}$ and a halo collapsing at the same time outside of $\mathcal{R}$

$$\frac{\bar{\delta}_i^{\mathcal{R}}}{a_i} = \frac{\bar{\delta}_i}{a_i} - \frac{3}{5\Omega_m}\left[\Omega_k - \frac{\Omega_k^{\mathcal{R}}}{(1+\bar{\delta}_{\mathcal{R}}^o)^{2/3}}\left(\frac{H_{o,\mathcal{R}}}{H_o}\right)^2\right]. \tag{3.61}$$

We show several examples of this relationship in figure 3.18. The fact that halos collapsing in an over/under-dense region start from different initial perturbations in the cosmic density field will have an effect on the halo statistics of that region. For example, the excursion set formalism has been used to determine the halo mass function in environments with large scale bias (Mo & White 1996).

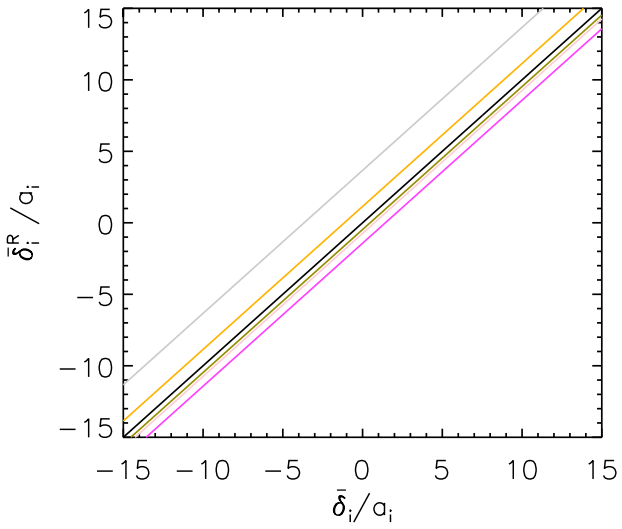

Figure 3.18.—: The relationship between the initial seed perturbation for halos collapsing in $\mathcal{R}$ and the initial seed for halos collapsing at the same time under the mean cosmology of the universe. The magenta, pink, green, black, orange and silver lines (bottom to top respectively) correspond to $\bar{\delta}_{\mathcal{R}}^o$ = 5, 1, 0.5, 0, -0.5 and -0.8 respectively.

3.6 Conclusions

We have developed the equations of motion for spherical collapse in an arbitrary cosmology, and have used them to examine the non-linear evolution of isolated, pressureless cosmic structures. We considered evolution in three distinct regimes:

1. *Over-dense ($\bar{\delta} > 0$), but non-collapsing regions*

   These are regions which have a matter density greater than that of the background but below a critical value required for eventual turn-around. Even though these regions are over-dense, turn-around (and thus collapse) is halted indefinitely due to the extra positive energy contributed by dark energy. We have derived the critical initial seed value $(\bar{\delta}_i/a_i)_{cr}$ required for eventual collapse (eq. (3.12)), and in the

same section provided a closed form formula for the turn around radius of a sphere with $(\bar{\delta}_i/a_i) > (\bar{\delta}_i/a_i)_{cr}$ in an arbitrary cosmology (eq. (3.13)). We calculated the non-linear over-density required for eventual collapse as a function of redshift (figure 3.1) and applied the results to the Shapley supercuster.

2. *Halos*

   We identify halos as spherical perturbations with $(\bar{\delta}_i/a_i) > (\bar{\delta}_i/a_i)_{cr}$, so that the perturbation will eventually collapse and virialize. Using the virial theorem in conjunction with the spherical collapse model, we calculated the ratio of the virialization radius to the turn-around radius in an any cosmology (figure 3.4) This then allowed us to calculate several interesting physical properties of halos at collapse in an arbitrary cosmology: the mean over-density (figure 3.5), virial radius, circular velocity, virial temperature and binding energy (figure 3.6). The first of these properties is highly dependent on cosmology (and therefore redshift), while the others have a very weak dependence on cosmology.

3. *Voids*

   Voids are extended, under-dense regions, which continually expand to become very tenuous. A void will eventually undergo shell crossing, at which point the spherical collapse model is no longer valid. We presented the derivation for the redshift of first shell crossing, and the corresponding non-linear and linear under-densities in an E-dS universe in appendix 3.7 In appendix 3.8, we detailed how to perform the same calculation in an arbitrary cosmology and show the results in figures 3.7, 3.8 and 3.16 (we also verified these analytic results by comparing against the redshift at first crossing as calculated in our 1 dimensional numerical simulation, as

presented in 3.19). Since this calculation is most useful in a ΛCDM cosmology, we re-wrote our equations for a flat universe, and scaled them so that the only variable was $\Omega_m(z_{sc})$. We then calculated the non-linear and linear under-densities at first shell crossing as a function of $\Omega_m(z_{sc})$ and provided very accurate fitting functions for $\bar{\delta}^{sc}_{NL}[\Omega_m(z_{sc})]$ (eq. (3.34)) and $\bar{\delta}^{sc}_{L}[\Omega_m(z_{sc})]$ (eq. (3.43)). We note that, in a flat cosmology, both of these quantities vary little with redshift, and are therefore are well approximated by the E-dS values.

We also considered the qualitative behavior of voids in an arbitrary cosmology after shell crossing by implementing our 1-dimensional Lagrangian shell code. We found features of voids similar to those exhibited in the E-dS self similar solutions, such as caustics and oscillations of shells around the edge (figure 3.10). We also found that after shell crossing, the average non-linear under-density of a void increases significantly due to the accumulation of mass within the void, and the slowing of its edge (figure 3.9).

We pieced together our calculations from each regime to come up with an easy-to-calculate, semi-analytic prescription for the evolution of the non-linear density of a perturbation. The model is summarized in figure 3.13, and examples of the non-linear density evolution are presented in figure 3.14. We also went over linear perturbation theory in an arbitrary cosmology, and calculated the linear theory over-density at collapse time for halos and the linear theory under-density at first shell crossing in voids in an arbitrary cosmology (figures 3.15 and 3.16).

We used our results of spherical collapse in an arbitrary cosmology to examine the environmental dependence of halo properties on large scale over/under-densities.

We accomplished this by considering the large-scale over/under-density as an effective change in cosmology by invoking Birkhoff's theorem and calculating the effective cosmological parameters for the region as a function of the mean non-linear over-density today (figure 3.17). We used these cosmological parameters in our equations for spherical collapse to show that the physical properties of a halo at collapse are actually independent of environment for halos collapsing at the same time. The only difference is the amplitude of the initial seed from which the halo was formed.

3.7 Appendix A: Void Shell Crossing in an E-dS Universe

For a void in an E-dS Universe with an initial volume averaged density profile of $\bar{\delta}_i(r_i)$, each shell within the void evolves according to the parametric solution:

$$r = \frac{r_i}{2a_i}\left(\frac{5}{3}\frac{|\bar{\delta}_i(r_i)|}{a_i}\right)^{-1}[\cosh\eta - 1], \tag{3.62}$$

and

$$t = \frac{1}{2H_o}\left(\frac{5}{3}\frac{|\bar{\delta}_i(r_i)|}{a_i}\right)^{-3/2}[\sinh\eta - \eta]. \tag{3.63}$$

To calculate when shell crossing within the void occurs, we consider two shells initially separated by a small distance, Δr_i. If Δr_i is sufficiently small enough, the separation between these two shells as a function of time is $\Delta r = (dr/dr_i)(t)\Delta r_i$, which according to eq. (3.62) is

$$\Delta r = \Delta r_i \frac{3}{10}\frac{d}{dr_i}\left\{\frac{r_i}{|\bar{\delta}_i(r_i)|}\cosh\eta[\bar{\delta}_i(r_i)] - \frac{r_i}{|\bar{\delta}_i(r_i)|}\right\}. \tag{3.64}$$

Evaluating the derivative, and noting from eq. (3.63) that

$$\frac{d\eta}{d\delta_i} = |\bar{\delta}_i|^{-1} \frac{3}{2} \frac{\sinh\eta - \eta}{\cosh\eta - 1}, \tag{3.65}$$

we end up with

$$\Delta r = \Delta r_i \frac{3}{10} \frac{\cosh\eta - 1}{|\bar{\delta}_i|} \left\{ 1 - \frac{d\ln|\bar{\delta}_i|}{d\ln r_i} \left[1 - \frac{3}{2} \frac{\sinh\eta(\sinh\eta - \eta)}{(\cosh\eta - 1)^2} \right] \right\}. \tag{3.66}$$

For simplicity, we consider a power law initial volume averaged density profile:

$$\bar{\delta}_i \propto r_i^{-\beta}. \tag{3.67}$$

By setting the separation distance, Δr, to 0, we can solve for η_{sc}, the value of η when two initially adjacent shells cross each other, leading to the following transcendental equation (Blumenthal et al. 1992; Sheth & van de Weygaert 2004):

$$\frac{\sinh\eta_{sc}(\sinh\eta_{sc} - \eta_{sc})}{(\cosh\eta_{sc} - 1)^2} = \frac{2}{3} \frac{1+\beta}{\beta}, \tag{3.68}$$

Once a value of β is supplied this equation must be solved numerically. This expression has no solution for $\beta < 2$, and therefore shell crossing does not occur in voids with shallow power law initial density profiles. If $\beta(r_i)$, however, shell crossing will occur in the void where $\beta > 2$. These shells may then make their way to shells which initially started with $\beta < 2$, so that crossing can occur for the $\beta < 2$ shells.

For a top hat initial density profile, $\beta = 3$ beyond the edge of the top hat (see eq. (3.86)), and the solution to eq. (3.68) is $\eta_{sc} = 3.4875$. We can now solve for the shell crossing redshift, z_{sc}, for a top hat void by noting that in an E-dS universe $1 + z = (3H_o t/2)^{-2/3}$ and by plugging in eq. (3.63):

$$\begin{aligned} 1 + z_{sc} &= \frac{5}{3} \left(\frac{4}{3} \right)^{2/3} (\sinh\eta_{sc} - \eta_{sc})^{-2/3} \frac{|\bar{\delta}_i|}{a_i} \\ &= 0.3680 \frac{|\bar{\delta}_i|}{a_i} \quad \text{(inverted top hat)}. \end{aligned} \tag{3.69}$$

Since in an E-dS universe, the linear theory under-density evolves according to $\bar{\delta}_L = a\bar{\delta}_i/a_i$ (see eq. (3.40)), we use the previous equation and find that the linear theory average under density at shell crossing is

$$\begin{aligned}\bar{\delta}_L(z_{sc}) &= -\frac{3}{5}\left[\frac{3}{4}\left(\sinh\eta_{sc} - \eta_{sc}\right)\right]^{2/3} \\ &= -2.7172 \quad \text{(inverted top hat)}.\end{aligned} \tag{3.70}$$

We can also calculate the non-linear theory average under density at shell crossing with eq. (3.9) by using eq. (3.62) to solve for $x^{-3}(z_{sc})$ and eq. (3.69) to solve for $(1+z_{sc})^{-3}$:

$$\begin{aligned}\bar{\delta}_{NL}(z_{sc}) &= \frac{9}{2}\frac{(\sinh\eta_{sc} - \eta_{sc})^2}{(\cosh\eta_{sc} - 1)^3} - 1 \\ &= -0.7953 \quad \text{(inverted top hat)}.\end{aligned} \tag{3.71}$$

Note that our value of η_{sc}, (and therefore our values of $\bar{\delta}_L(z_{sc})$ and $\bar{\delta}_{NL}(z_{sc})$) is different than that as calculated by Sheth & van de Weygaert (2004), who calculated $\eta_{sc} = 3.53$ (and $\bar{\delta}_L(z_{sc}) = -2.8059$ and $\bar{\delta}_{NL}(z_{sc}) = -0.8018$). We attribute this discrepancy to the fact that the authors did not numerically solve eq. (3.68) accurately.

3.8 Appendix B: Void Shell Crossing in a General Cosmology

To calculate when shell crossing occurs between two initially adjacent shells in a void in an arbitrary cosmology, we begin by calculating Δr $(= (dr/dr_i)(t)\Delta r_i)$ given that our definition of x is ra_i/r_i. In this case, the separation between two shells as a function of redshift is:

$$\Delta r = \frac{\Delta r_i}{a_i}\frac{d}{dr_i}\left\{x[z, \bar{\delta}_i(r_i)/a_i]r_i\right\} = \frac{\Delta r_i}{a_i}\left[\frac{\partial x}{\partial(\ln|\bar{\delta}_i|/a_i)}\frac{d\ln|\bar{\delta}_i|}{d\ln r_i} + x\right]. \tag{3.72}$$

By setting this equal to 0, and using eq. (3.67) we find the following condition for shell crossing:

$$\frac{\partial \ln[x(z_{sc}, \bar{\delta}_i/a_i)]}{\partial(\ln|\bar{\delta}_i|/a_i)} = \frac{1}{\beta}. \tag{3.73}$$

As in the E-dS case, there will be values of β which cannot satisfy the above equation, so that shell crossing between two initially adjacent shells is precluded. These values will depend on the cosmology under consideration. Using this equation, we numerically solve for $z_{sc}(\delta_i/a_i)$ for an initial top hat ($\beta = 3$) in the following manner: we first choose a value for z_{sc}, and then calculate x at that particular z_{sc} as a function of $\bar{\delta}_i/a_i$ using eq. (3.5), and eq. (3.8) (to convert time to redshift). We then find the value of $\bar{\delta}_i/a_i$ for that z_{sc} which satisfies eq. (3.73) by numerically taking the derivative. We repeat this procedure for many values of z_{sc} to build up z_{sc} as a function of $\bar{\delta}_i/a_i$. We compare the results of this calculation in a ΛCDM universe to the E-dS results in figure 3.7, and we calculate the shell crossing redshifts for several other cosmologies in figure 3.19.

Given our solution for $z_{sc}(\bar{\delta}_i/a_i)$, we may calculate $\bar{\delta}_L(z_{sc})$ for any cosmology using eq. (3.39) (or eq. (3.36) for a flat cosmology). We may also calculate $\bar{\delta}_{NL}(z_{sc})$ by calculating $x(z_{sc})$ with eqs. (3.5) and (3.8) with a $\bar{\delta}_i/a_i$ value as given by $z_{sc}(\bar{\delta}_i/a_i)$. The nonlinear average under density at shell crossing can then be calculated with eq. (3.9). We show examples for different cosmologies of the linear under density at shell crossing in figure 3.16, and the non-linear under density at shell crossing in figure 3.8. The figures show that for a flat cosmology, the values of $\bar{\delta}_L(z_{sc})$ and $\bar{\delta}_{NL}(z_{sc})$ are very well approximated by the E-dS results (-2.7172 and -0.7953 respectively), while the values for open and closed cosmologies can show more marked differences.

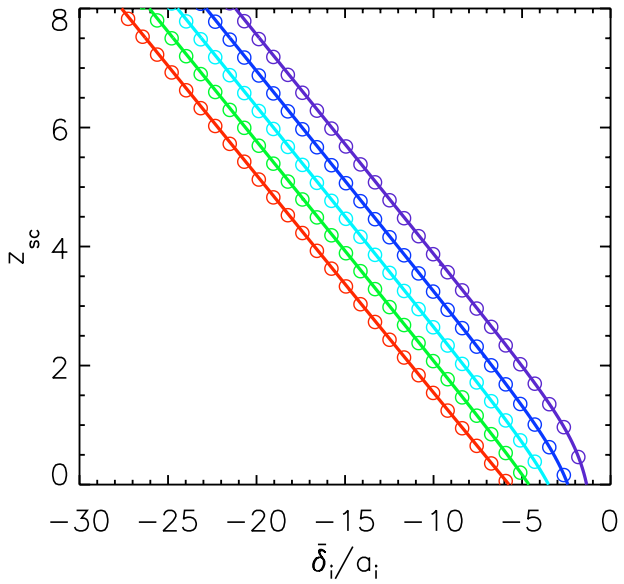

Figure 3.19.—: The shell crossing redshift as a function of $\bar{\delta}_i/a_i$ for voids residing in universes with various cosmologies. The red, green, turquoise, blue and violet lines and points correspond to the CI, CII, CIII, CIV and CV cosmologies respectively (bottom to top respectively). Lines are calculated from analytic theory (eq. (3.73)), and the circle points are calculated from our numerical simulation (see Appendix 3.9). The figure shows that our analytic theory matches our numerical results quite well.

3.9 Appendix C: Void Evolution After Shell Crossing

3.9.1 1-D Simulations

The previous two appendices have shown that spherical cosmological voids undergo shell crossing after an initial period of expansion governed by the spherical collapse model with the mass interior to each shell constant. After shell crossing, the dynamics of each shell is no longer given by eq. (3.3). We follow the evolution of voids after shell crossing by integrating the equations of motion for $N = 5 \times 10^4$ shells with a second order-accurate

Lagrangian finite difference scheme, similar to the codes of Thoul & Weinberg (1995) and Lu et al. (2006). We implement the "drift-kick-drift" leap-frog algorithm in which 1) particles drift for a half time step at at velocity v^n, 2) particles velocities are kicked for a full time step, and 3) particles drift for another half time step at the new velocity, v^{n+1}. The update equations for this scheme are [3]:

$$r_j^{n+1/2} = r_j^n + \frac{1}{2} v_j^n \Delta t^n, \tag{3.74}$$

$$v_j^{n+1} = v_j^n + a_j^{n+1/2} \Delta t^n, \tag{3.75}$$

and

$$r_j^{n+1} = r_j^{n+1/2} + \frac{1}{2} v_j^{n+1} \Delta t^n. \tag{3.76}$$

In this simulation, we work with time, position, mass, velocity and energy normalized to the following units:

$$\begin{aligned} \tilde{t} &= \frac{t}{1/H_o}, \\ \tilde{r} &= \frac{r}{R_i}, \\ \tilde{m} &= \frac{m}{M_i}, \\ \tilde{v} &= \frac{v}{R_i H_o \Omega_m / 2} \\ \tilde{E} &= \frac{E}{M_i R_i^2 H_o^2 \Omega_m / 2}, \end{aligned} \tag{3.77}$$

where R_i is the initial radius at the edge of the initial top-hat perturbation, and M_i is the mass within this radius. When shell crossing is included, the evolution of the volume

[3] In the following equations, the "n" superscripts refers to the time step, and "j" subscripts refer to the shell number.

averaged non-linear density contrast for the edge of the top-hat is given by:

$$1 + \bar{\delta}_{NL}(z) = \frac{\tilde{m}(\tilde{r}, z)}{\tilde{r}^3} \left(\frac{a}{a_i} \right)^3 . \tag{3.78}$$

In the limit of no shell crossings ($\tilde{m} = 1$) and this equation reduces to eq. (3.9).

Including a force due to the cosmological constant, the acceleration of each particle at time t is:

$$a = \frac{-Gm(r,t)}{r^2} + H_o^2 \Omega_\Lambda r, \tag{3.79}$$

Using the units adopted for this calculation, the update equations must then be re-written according to:

$$\Delta\tilde{v} = \frac{-\tilde{m}(\tilde{r})}{\tilde{r}^2 a_i^3} \Delta\tilde{t}(1 + \bar{\delta}_i) + 2\frac{\Omega_\Lambda}{\Omega_m} \tilde{r} \Delta\tilde{t} + O(\Delta\tilde{t}^2), \tag{3.80}$$

and

$$\Delta\tilde{r} = \tilde{v}\Delta\tilde{t}\frac{\Omega_m}{2} + O(\Delta\tilde{t}^2). \tag{3.81}$$

The relevant timescales for this calculation are the dynamical time and ℓ_{char}/v_j^n, the time it takes for a particle to travel a characteristic distance, where we choose ℓ_{char} to be some fraction the particle's current distance from the origin. The time step at each iteration is therefore taken to be $\Delta\tilde{t}^n = \min\{\Delta\tilde{t}^n_{dyn}, \Delta\tilde{t}^n_{char}\}$, with

$$\Delta\tilde{t}^n_{dyn} = \min_j \left\{ c_{dyn} \sqrt{\frac{\pi^2 (\tilde{r}_j^n)^3 2 a_i^3}{4\Omega_m (1 + \bar{\delta}_i) \tilde{m}_j^n (\tilde{r}_j^n)}} \right\}, \tag{3.82}$$

and

$$\Delta\tilde{t}^n_{cour} = \min_j \left\{ c_{char} \left| \frac{\tilde{r}_j^n}{\tilde{v}_j^n + \epsilon} \right| \frac{2}{\Omega_m} \right\}. \tag{3.83}$$

Here, c_{dyn} and c_{char} are safety constants and ϵ is a very small number to avoid an infinity if shell velocities become very small. Unlike Thoul & Weinberg (1995), we do not need to implement an inner boundary condition since we are considering the expansion of voids,

so that no shells in our simulations become appreciably close to the origin. The total energy of the system at each time step is given by:

$$\tilde{E}^n = \Delta\tilde{m} \sum_j \left[\frac{1}{2}\tilde{v}_j^{n2}\frac{\Omega_m}{2} - \frac{\tilde{m}_j^n(1+\bar{\delta}_i)}{\tilde{r}_j^n a_i^3} - \frac{\Omega_\Lambda}{\Omega_m}\tilde{r}_j^{n2} \right], \tag{3.84}$$

where $\Delta\tilde{m}$ is the mass of a shell ($= 1/N$), and where the first, second and third terms in the brackets represents the kinetic, gravitational potential and potential due to the cosmological constant respectively.

3.9.2 Initial Conditions

To initialize the position for each run, we adopt an initial top-hat perturbation,

$$\delta_i(\tilde{r}_i) = \begin{cases} \bar{\delta}_i & \text{for } \tilde{r}_i \leq 1 \\ \\ 0 & \text{for } \tilde{r}_i > 1 \end{cases}, \tag{3.85}$$

which gives

$$\bar{\delta}_i(\tilde{r}_i) = \begin{cases} \bar{\delta}_i & \text{for } \tilde{r}_i \leq 1 \\ \\ \bar{\delta}_i \tilde{r}_i^{-3} & \text{for } \tilde{r}_i > 1 \end{cases}. \tag{3.86}$$

We place shells of equal mass (and infinitesimal thickness) at appropriate positions to replicate the $\tilde{m}(\tilde{r}_i)$ profile for this density profile,

$$\tilde{m}(\tilde{r}_i) = \tilde{r}_i^3 \left[\frac{1+\bar{\delta}_i(\tilde{r}_i)}{1+\bar{\delta}_i} \right], \tag{3.87}$$

out to a radius $\tilde{r}_{max}$. To avoid boundary effects, which might be an issue for times much later than shell crossing, we check for convergence of our results when integrated to $z = 0$. We find that for the values of $\bar{\delta}_i/a_i$ we consider (about -40 to 0), which control the shell crossing time, the results our well converged by $\tilde{r}_{max} = 5$.

In linear theory, the velocity of each shell is given by

$$v_i(r_i) = H_i r_i \left[1 - f(a_i)\frac{\bar{\delta}_i(r_i)}{3}\right], \tag{3.88}$$

where the second term in the brackets is the peculiar velocity term, and where

$$\begin{aligned} f(a) &\equiv \frac{d\ln D}{d\ln a} \\ &= \frac{\Omega_m\left(1-\frac{3}{2a}\right)+\Omega_\Lambda - 1}{1+\Omega_m\left(\frac{1}{a}-1\right)+\Omega_\Lambda\left(a^2-1\right)} + \frac{a\left[1+\Omega_m\left(\frac{1}{a}-1\right)+\Omega_\Lambda(a^2-1)\right]^{-3/2}}{\int_0^a\left[1+\Omega_m\left(\frac{1}{a'}-1\right)+\Omega_\Lambda(a'^2-1)\right]^{-3/2}da'}. \end{aligned} \tag{3.89}$$

Notice that in the limit that $a \to 0$, $f \to 1$ and $H_i \to \Omega_m^{1/2} a_i^{-3/2}$, which is what we used to calculate the initial peculiar velocity in eq. (3.3). We find in our simulations, however, that the shell trajectories are extremely sensitive to initial conditions, so that accurate simulations with these initial conditions would need to start at unmanageably small values of a_i. We therefore initialize velocities with the full eq. (3.88) expression, which when normalized to the proper units gives:

$$\tilde{v}_i(\tilde{r}_i) = \tilde{r}_i\sqrt{\Omega_m a_i^{-3} + \Omega_\Lambda + (1-\Omega_m-\Omega_\Lambda)a_i^{-2}}\left[1 - f(a_i)\frac{\bar{\delta}_i(\tilde{r}_i)}{3}\right]\frac{2}{\Omega_m}. \tag{3.90}$$

Eq. (3.5) shows that the evolution of a shell at r_i, with perturbation $\bar{\delta}_i(r_i)$, at time a_i is fully determined by the ratio $\bar{\delta}_i(r_i)/a_i$. To compute the evolution of voids with different values of this ratio, we set $\bar{\delta}_i = -10^{-4}$ and vary a_i to attain the desired ratio, typically giving a_i of order 10^{-6}.

3.9.3 Tests

We perform several tests of our code to make sure that it is functioning properly. A first basic test is to set $\bar{\delta}_i(\tilde{r}_i) = 0$ everywhere, let the shells evolve, and then measure

the radial density profile in units of the Hubble flow matter density. If the code is functioning properly, then this ratio should be unity at all radii. The Eulerian density profile can be obtained from the measured $m(r)$ profile with $\rho = 1/(4\pi r^2)dm/dr$, which when normalized to the Hubble flow and properly dimensionalized is:

$$\frac{\rho(\tilde{r}, z)}{\bar{\rho}_m(z)} = \frac{1}{3\tilde{r}^2}\frac{d\tilde{m}}{d\tilde{r}}\left(\frac{a}{a_i}\right)^3. \tag{3.91}$$

We find that for all the cosmologies we consider, at $z = 0$, this ratio is, to a very high degree, unity at all radii if we set our time step safety constants to $c_{dyn} = c_{char} = 10^{-4}$, and if we do not start the simulation at times early than $a_i \sim 10^{-6}$. The latter stipulation is due to the fact that energy conservation is harder to attain if the simulation is running for longer amounts of time.

Another simple test is to make sure that the time of first shell crossing agrees with the analytic results presented in the previous appendix. We measure the first shell crossing redshift for simulations of different $\bar{\delta}_i/a_i$ values in various cosmologies and plot the results in figure 3.19 (colored circles). The figure shows that the measured values of z_{sc} match the analytic results very well.

We can also test whether our simulations agree with the analytic solution, eq. (3.5) (which assumes no shell crossing), before shell crossing occurs. We show the trajectories of the edge of an initial inverted top-hat in figure 3.20 for two cosmologies (different panels) and several values of $\bar{\delta}_i/a_i$ (different sets of lines in each panel). The thick grey lines are calculated from eq. (3.5), while the thin black lines are measured from our simulations, with the solid portion of the line representing the trajectory before shell crossing and the dashed after. The figure shows that our numerical solution is identical to the analytic solution before shell crossing occurs. Deviations only occur some time

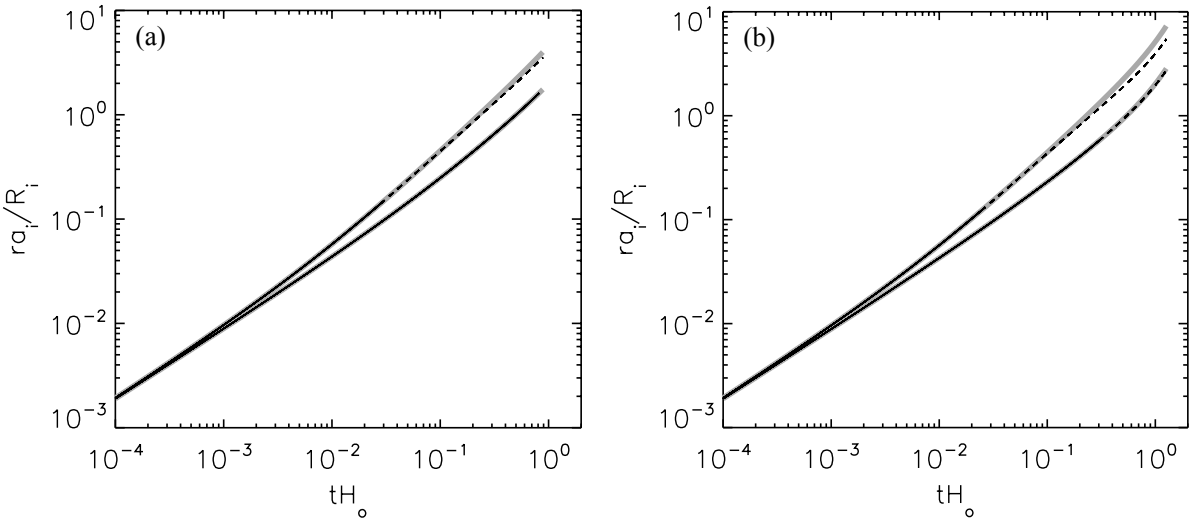

Figure 3.20.—: Trajectories of the edge of an initial inverted top-hat density profile in the CII (a) and CV (b) cosmologies. The thick grey lines are the analytic results which assume no shell crossings, (eq. (3.5)). The thin black lines are the results from the numerical simulation presented in this appendix, which *do* take shell crossing into account. The solid portion of each line is the trajectory before shell crossing, while the dashed is after. In both panels, the upper set of lines was calculated with $\bar{\delta}_i/a_i = -35$, while the lower set was calculated with $\bar{\delta}_i/a_i = -5$.

after shell crossing, when the edge of the top-hat has had time to react to the change in the amount of its interior mass. After shell crossing, the edge grows more slowly than as predicted by analytic theory since the amount of mass interior to it has increased, so that it experiences a greater inward force.

We note that energy is well conserved in our simulations. In figure 3.21, we show the change in the total energy (i.e., eq. (3.84)) relative to the total initial energy as a function of time for the runs in figure 3.20b. Our simulations conserve energy to typically about one part in one thousand.

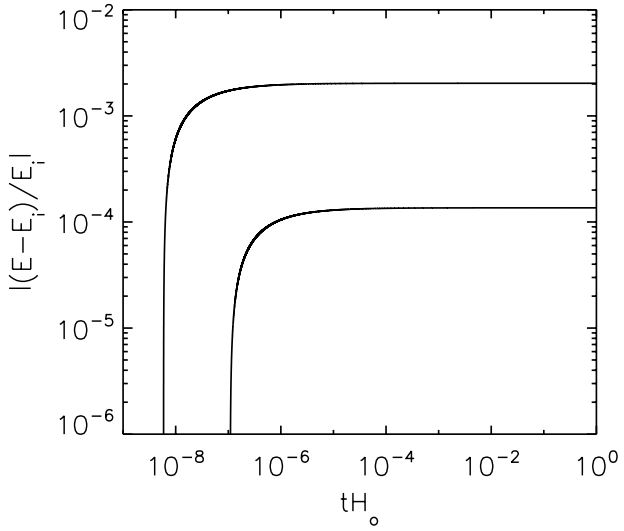

Figure 3.21.—: The fractional change in energy as a function of time for the two runs presented in figure 3.20b.

As a final test, we make sure that, in an E-dS cosmology, long after shell crossing when the mass swept up by the edge of the void dominates the initial mass (i.e., $\tilde{m}[\tilde{R}(\tilde{t})] \gg 1$), our simulation transitions to the self-similar solution. We run an E-dS simulation up to the present time with $z_{sc} = 100$ (i.e., with $\bar{\delta}_i/a_i = -(1+100)/0.3680$ according to eq. (3.69)), and compare the results with the self similar solution for the edge of a void ($r \propto t^{8/9}$ and $m \propto t^{2/3}$) in figures 3.22a and b. In figure 3.22a, we show the trajectory as predicted analytically from eq. (3.3) (thick grey line), from our simulation (thin black line, where the solid portion is the trajectory before shell crossing, and the dotted portion is after), and from the self similar solution (thin grey line). The transition of the numerical results from the analytic to the self similar solution is clearly noticeable after shell crossing. In figure 3.22b we plot the mass interior to the edge of the void as measured from our simulation, and as predicted by the self similar solution. Before shell crossing occurs, $\tilde{m}[\tilde{R}(\tilde{t})] = 1$, while long after shell crossing, $\tilde{m}[\tilde{R}(\tilde{t})]$ transitions to the

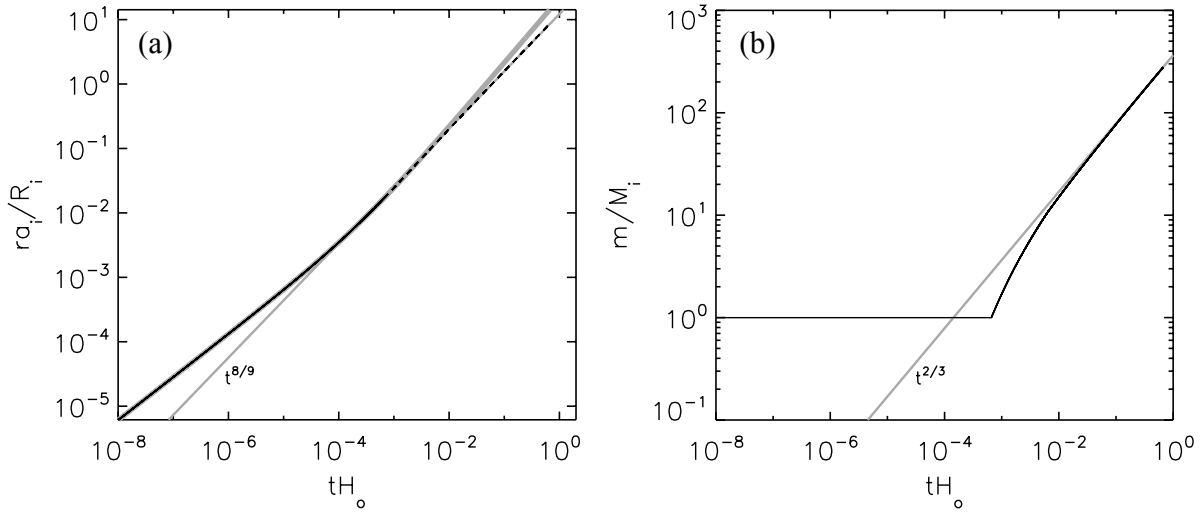

Figure 3.22.—: The trajectory (a) of, and interior mass (b) to the edge of an initial inverted top hat void in an E-dS cosmology, which shell crosses at $z_{sc} = 100$. The thick grey, thin black and thin grey lines correspond to the results of the analytic solution (eq. (3.3)), the simulation, and the self similar solution respectively. The solid portion of the thin black line in (a) is the trajectory before shell crossing, while the dashed line is after shell crossing.

$m \propto t^{2/3}$ self-similar solution.

Acknowledgments

This work was supported in part by NSF grant AST-0907890 and NASA grants NNX08ALY3G and NNA09DB30A.

Chapter 4

Constraining the Stellar Mass Function in the Galactic Center Via Mass Loss from Stellar Collisions

D. Rubin & A. Loeb, *Advances in Astronomy*, Vol. 2011, ID 174105, 2011

Abstract

The dense concentration of stars and high velocity dispersions in the Galactic center imply that stellar collisions frequently occur. Stellar collisions could therefore result in significant mass loss rates. We calculate the amount of stellar mass lost due to indirect and direct stellar collisions and find its dependence on the present-day mass function of stars. We find that the total mass loss rate in the Galactic center due to stellar collisions is sensitive to the present-day mass function adopted. We use the observed diffuse X-ray

luminosity in the Galactic center to preclude any present-day mass functions that result in mass loss rates $> 10^{-5}\mathrm{M}_{\odot}\mathrm{yr}^{-1}$ in the vicinity of $\sim 1''$. For present-day mass functions of the form, $dN/dM \propto M^{-\alpha}$, we constrain the present-day mass function to have a minimum stellar mass $\lesssim 7\mathrm{M}_{\odot}$ and a power law slope $\gtrsim 1.25$. We also use this result to constrain the initial mass function in the Galactic center by considering different star formation scenarios.

4.1 Introduction

The dense stellar core at the Galactic center has a radius of $\sim 0.15 - 0.4$pc, a stellar density $> 10^{6}\mathrm{M}_{\odot}\mathrm{pc}^{-3}$ (Genzel et al. 1996; Eckart et al. 1993; Genzel et al. 2003; Schödel et al. 2007) high velocity dispersions ($\geq 100\mathrm{km\,s}^{-1}$), and Sgr A*, the central supermassive black hole with a mass $\approx 4 \times 10^{6} M_{\odot}$ (Eckart et al. 2002; Schödel et al. 2002, 2003; Ghez et al. 2003, 2008). Due to the extreme number densities and velocities, stellar collisions are believed to play an important role in shaping the stellar structure around the Galactic center, and in disrupting the evolution of its stars (Frank & Rees 1976). Genzel et al. (1996) found a paucity of the brightest giants in the galactic center, and proposed that collisions with main sequence (MS) stars could be the culprit. This hypothesis was found to be plausible by Alexander (1999). Other investigations of collisions between giants and MS, white dwarf and neutron stars (Bailey & Davies 1999) and collisions between giants and binary MS and neutron stars (Davies et al. 1998) could not account for the dearth of observed giants. The contradictory results were resolved by Dale et al. (2009), who concluded that the lack of the faintest giants (but not the brightest giants) could be explained by collisions between giants and stellar mass black

holes. Significant mass loss in the giants' envelopes after a collision would prevent the giants from becoming bright enough to be observed.

The above studies concentrated on collisions involving particular stellar species with particular stellar masses. To examine the cumulative effect of collisions amongst an entire ensemble of a stellar species with a spectrum of masses, one must specify the present-day stellar mass function (PDMF) for that species. The PDMF gives the current number of stars per unit stellar mass up to a normalization constant. Given a certain star formation history, the PDMF can be used to determine the initial mass function of stars (IMF), the mass function with which the stars were born. There is currently no consensus as to whether the IMF in the Galactic center deviates from the canonical IMF (Bastian et al. 2010).

First described by Salpeter more than 50 years ago (Salpeter 1955), the canonical IMF is an empirical function which has been found to be universal (Kroupa 2001), with the Galactic center as perhaps the sole exception. Maness et al. (2007) found that models with a top-heavy IMF were most consistent with observations of the central parsec of the Galaxy. Paumard et al. (2006), and subsequently Bartko et al. (2010) found observational evidence for a flat IMF for the young OB-stars in the Galactic center. On the other hand, Löckmann et al. (2010) concluded that models of constant star formation with a canonical IMF could explain observations of the Galactic center.

In this work we use calculated mass loss rates due to stellar collisions as a method to constrain the PDMF for main sequence stars in the Galactic center. We construct a simple model to estimate the actual mass loss rate in the Galactic center based on observed diffuse X-ray emission. PDMFs that predict mass loss rates from stellar

collisions greater than the observed rate are precluded. This method allows us to place conservative constraints on the PDMF, because we do not include the contribution to the mass loss rate from stellar winds from massive evolved stars (Baganoff et al. 2003). Specifically, this method allows us to place a lower limit on the power-law slope and an upper limit on the minimum stellar mass of the PDMF in the Galactic center (see § 4.5). Inclusion of the mass loss rate from stellar winds (or other sources) could further constrain the PDMF of the Galactic center.

The work presented in this paper has implications for the fueling of active galactic nuclei (AGNs). To trigger an AGN, a significant amount of matter must be funneled onto the supermassive black hole in a galactic nucleus. The most common way of channelling gas is through galaxy mergers, which has been studied for quite some time (eg: Toomre & Toomre (1972); Gunn (1979); Hernquist & Mihos (1995)). Even without mergers, AGN can be fed by several processes from stellar residents in a galactic center. The tidal disruption of a star which passes too close to the supermassive black hole can strip mass off the star. Additionally, it is known that a significant amount of gas is ejected into the Galactic center due to stellar winds from massive, evolved stars (Baganoff et al. 2003; Najarro et al. 1997; Quataert 2004). Another potential source for the fueling of AGN could be from unbound stellar material, ejected in a stellar collision. Since the easiest place to look for such an event (due to its proximity) is the Galactic center, in this paper we theoretically investigate stellar collisions in this environment. By calculating the cumulative mass loss rate from stellar collisions in the Galactic center, we place constraints on the fueling of Sgr A* due to this mechanism.

We present novel, analytical models to calculate the amount of stellar mass lost due to stellar collisions between main sequence stars in § 4.2 through § 4.2.3. In § 4.3 we

develop the formalism for calculating collision rates in the Galactic center. We utilize our calculations of the mass loss per collision, and the collision rate as a function of Galactic radius to find the radial profile of the mass loss rate in § 4.4. Since the amount of mass lost is dependent on the masses of the colliding stars, the mass loss rate in the Galactic center is sensitive to the underlying PDMF. By comparing our calculations to mass loss rates obtained from the diffuse X-ray luminosity measured by *Chandra*, in § 4.5 we constrain the PDMF of the Galactic center. We derive analytic solutions of the PDMF as a function of an adopted IMF for different star formation scenarios, which allows us to place constraints on the IMF in §6. In § 7, we estimate the contribution to the mass loss rate from collisions involving red giant (RG) stars.

4.2 Condition for Mass loss

Throughout this paper we refer to the star that loses material as the perturbed star, and the star that causes material to be lost as the perturber star. Quantities with the subscript or superscript "pd" or "pr" refer to the perturbed star and perturber star respectively. [1] We work in units where mass is measured in the mass of the perturbed star, M_{pd}, distance in the radius of the perturbed star, r_{pd}, velocity in the escape velocity of the perturbed star, v_{esc}^{pd} ($= \sqrt{2GM_{pd}/r_{pd}}$), and time in r_{pd}/v_{esc}^{pd}. We denote normalization by these quantities (or the appropriate combination of these quantities)

[1]Note that for any particular collision, it is arbitrary which star we consider the perturber star, and which star the perturbed star. Both stars will lose mass due to the presence of the other, so in order to calculate the total mass loss, we interchange the labels (pd↔pr), and repeat the calculation.

with a tilde:

$$\begin{aligned} \tilde{M} &\equiv M/M_{pd} \\ \tilde{r} &\equiv r/r_{pd} \\ \tilde{v} &\equiv v/v_{esc}^{pd} \\ \tilde{t} &\equiv t/\frac{r_{pd}}{v_{esc}^{pd}}. \end{aligned} \tag{4.1}$$

We refer to collisions in which $b > r_{pd} + r_{pr}$ as "indirect" collisions, and collisions in which $b \leq r_{pd} + r_{pr}$ as "direct" collisions. The impact parameter, b, is the distance of closest approach measured from the centers of both stars.

We consider the condition for mass loss at a position, $\tilde{r}$, within the perturbed star to be that the kick velocity due to the encounter at $\tilde{r}$ exceeds the escape velocity of the perturber star at $\tilde{r}$, $\Delta\tilde{v}(\tilde{r}) \geq \tilde{v}_{esc}(\tilde{r})$. The escape velocity as a function of position within the perturbed star can be found from the initial kinetic and potential energies of a test particle at position $\tilde{r}$,

$$\begin{aligned} \tilde{v}_{esc}(\tilde{r}) &= \sqrt{-\int_{\tilde{r}}^{\infty} \frac{\tilde{M}_{int}(\tilde{r}')}{\tilde{r}'^2} d\tilde{r}'} \\ &= \sqrt{\frac{\tilde{M}_{int}(\tilde{r})}{\tilde{r}} + 4\pi \int_{\tilde{r}}^{1} \tilde{\rho}(\tilde{r}')\tilde{r}' d\tilde{r}'} \end{aligned} \tag{4.2}$$

where $\tilde{M}_{int}$ is the mass interior at position $\tilde{r}'$ and $\tilde{\rho}$ is the density profile of the star.

4.2.1 Mass Loss due to Indirect Collisions

To calculate the mass lost due to an indirect collision, we first calculate the kick velocity given to the perturbed star as a function of position within the star. We work under the

impulse approximation (Spitzer 1958), valid under the condition that the encounter time is much shorter than the characteristic crossing time of a constituent of the perturbed system.

Given a mass distribution for the perturbed system, ρ_{pd} and a potential for the perturber system, Φ, the kick velocity after an encounter under the impulse approximation is given by Binney & Tremaine (2008):

$$\Delta\vec{v}(\vec{r}) = -\int_{-\infty}^{\infty} \left[\vec{\nabla}\Phi(\vec{r},t) - \frac{1}{M_{pd}} \int \rho_{pd}(\vec{r'},t)\vec{\nabla}\Phi(\vec{r'},t)\, d^3r' \right] dt.$$

Equation (4.3) can be simplified by expanding the gradient of the potential in a Taylor series, resulting in

$$\Delta\vec{v}\,(\vec{r}) = \frac{2GM_{pr}}{b^2 v_{rel}} \begin{pmatrix} -x \\ y \\ 0 \end{pmatrix} + O\left(\overline{r^2}\right). \tag{4.3}$$

The expansion is valid under the "distant tide" approximation which is satisfied when $r_{pd} \ll b$. The parameter v_{rel} is the relative speed between the stars ($v_{rel} \equiv |\vec{v}_{pd} - \vec{v}_{pr}|$). We are interested in the magnitude of equation (4.3), which when normalized to the units that we have adopted for this paper is

$$\Delta\tilde{v}(\tilde{x},\tilde{y}) \cong \gamma\sqrt{\tilde{x}^2 + \tilde{y}^2}, \tag{4.4}$$

where

$$\gamma \equiv \frac{\tilde{M}_{pr}}{\tilde{b}^2\tilde{v}_{rel}}. \tag{4.5}$$

To solve for the mass lost per encounter as a function of γ, we consider a star within a cubic array, where the star contains $\sim 3 \times 10^6$ cubic elements. As a function of γ we

compare the kick velocity in each element to the escape velocity for that element, and consider the mass within the element to be lost to the star if the velocities satisfy the condition given in § 4.2. We note that by $\sim 10^5$ elements, the results converge to within about 2%, and we are therefore confident that $\sim 3 \times 10^6$ provides adequate resolution.

To calculate the amount of mass in each element, the density profile for the perturbed star must be specified. As with several previous studies on mass loss due to stellar collisions (Benz & Hills 1987, 1992; Lai et al. 1993; Rauch 1999) we utilize polytropic stellar profiles. Polytropic profiles are easy to calculate, and yield reliable results for stars of certain masses. Polytropic profiles of polytropic index $n = 1.5$ describe the density structure of fully convective stars, and therefore very well describe MS stars with $M_\star \lesssim 0.3\mathrm{M}_\odot$ (nearly fully convective) and MS stars with $M_\star \gtrsim 10\mathrm{M}_\odot$ (convective cores). MS stars with $M_\star \gtrsim 1\mathrm{M}_\odot$ have radiative envelopes, and are therefore well described by $n = 3$. For n for stars with masses of $0.3 - 1\mathrm{M}_\odot$ and $5 - 10\mathrm{M}_\odot$, we linearly interpolate between $n = 1.5$ and 3. We discuss the uncertainties introduced by this approach in § 4.4. Note that this approach is biased towards zero-age main sequence stars, since as stars evolve, they are less adequately described by polytropic profiles.

We plot the fraction of mass lost from the perturbed star per event, Δ, as a function of γ in Fig. 4.1 for several polytropic indeces. The lines are third order polynomial fits to our results, in the range of $0.98 \leq \gamma \leq 5$. We list the coefficients of the polynomial fits in Table 4.1. For each density profile, no mass is lost up until γ of about 0.98, and thereafter the mass loss increases monotonically. The increasing trend is due to the fact that larger perturber masses and smaller impact parameters result in an increased potential felt by the perturbed star. Smaller velocities also cause more mass to be lost, as this increases the "interaction time" between the perturber and perturbed stars.

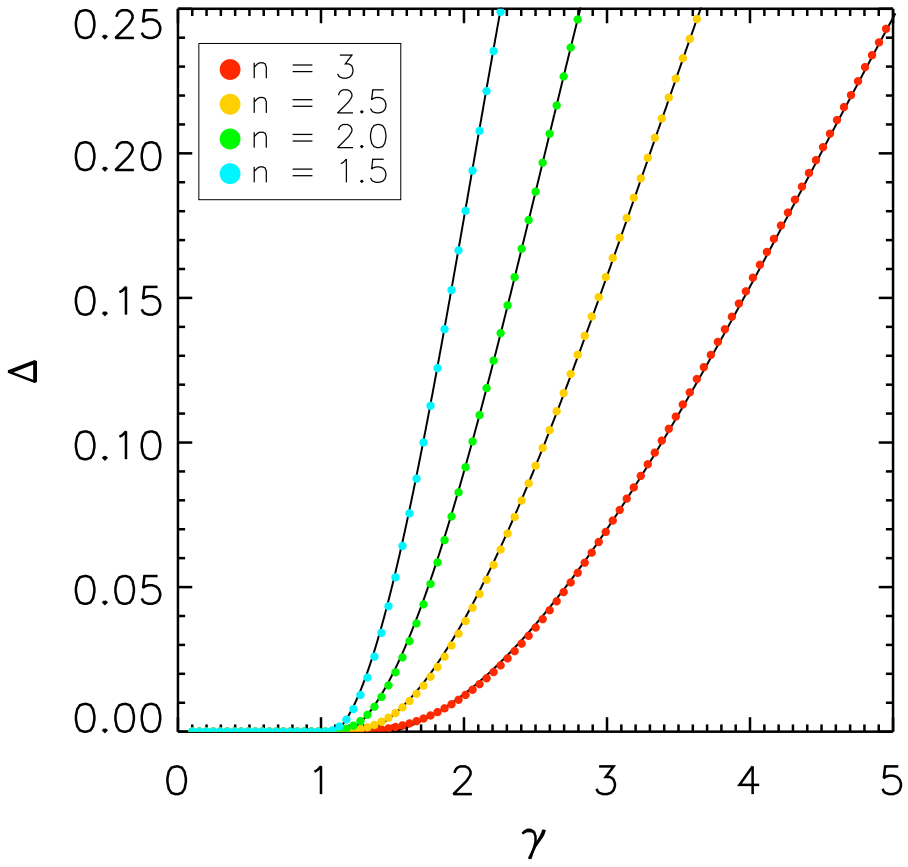

Figure 4.1.—: The fraction of mass lost per collision as a function of γ for several polytropic indeces. The lines are third order polynomial fits, whose coefficients are given in Table 4.1.

The location of the mass loss within the perturbed star for fixed γ depends upon the polytropic index, since the escape velocity within the star is dependent upon the density profile, as indicated by equation. (4.2). In Fig. 4.2, we illustrate where mass will be lost in the perturbed star by plotting contours of the kick velocity ($\Delta\tilde{v}(\tilde{r})$) due to the encounter normalized to $\tilde{v}_{esc}^{pd}(\tilde{r})$ for $n = 1.5$ and $n = 3$ (top and bottom row respectively). We show two different cases: a slightly perturbing encounter with $\gamma = 1.2$ in the first column, and a severely perturbing encounter with $\gamma = 1.6$ in the second column. The grey region underneath shows where mass is still left after the encounter, since $\Delta\tilde{v}/\tilde{v}_{esc}^{pd}(\tilde{r})$

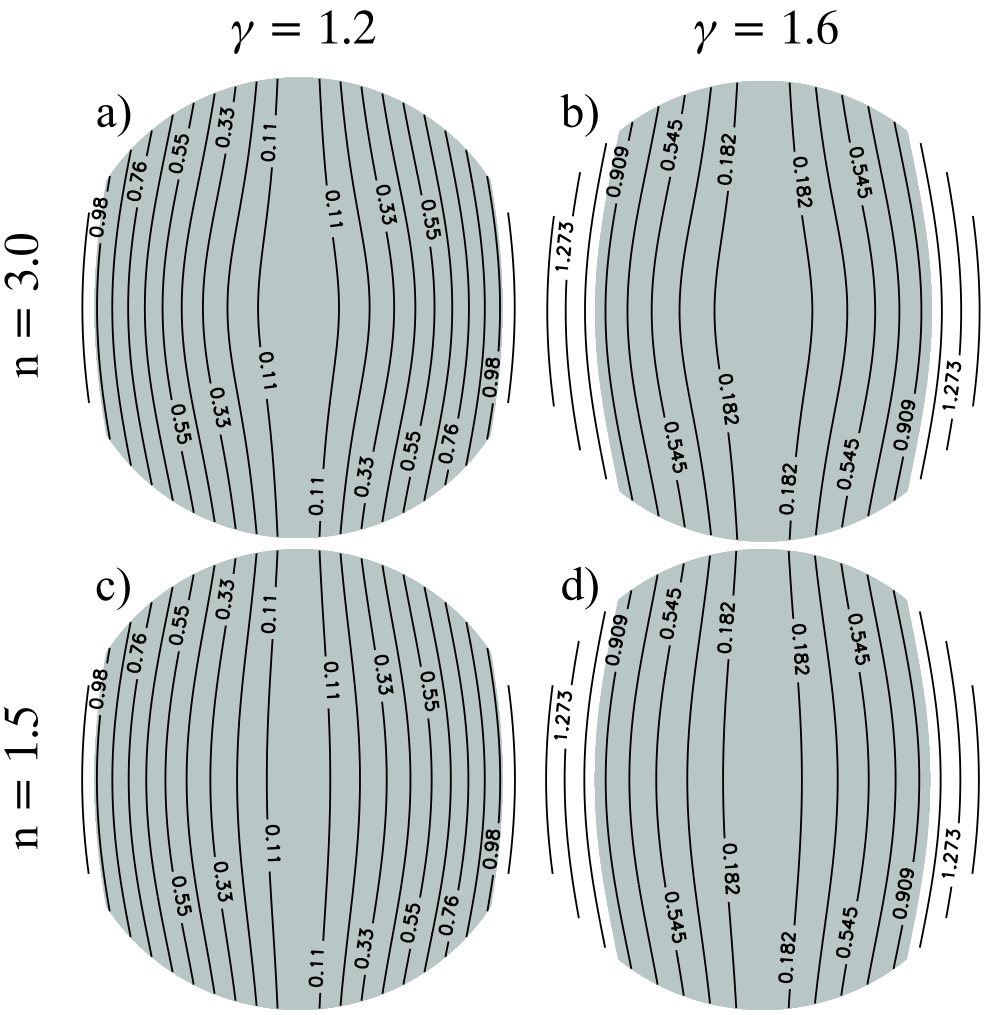

Figure 4.2.—: Slices through the perturbed star along the plane parallel to the perturber star's trajectory. The first column (panels a) and c)) correspond to encounters with $\gamma = 1.2$, and the second column (panels b) and d)) correspond to $\gamma = 1.6$. The first row (panels a) and b)) have $n = 3$, and the second row (panels c) and d)) have $n = 1.5$. The contours are the kick velocity within the star due to the encounter normalized to the escape velocity (as a function of $\tilde{r}$). The outline of the grey region underneath has $\Delta\tilde{v}/\tilde{v}^{pd}_{esc}(\tilde{r}) = 1$, so that the grey region represents the location of where mass is still left after the event.

Table 4.1:: Coefficients of polynomial fits for $\Delta(\gamma)$ with varying polytropic indeces

n	a_0	a_1	a_2	a_3
1.5	0.395	-0.865	0.559	-0.091
2.0	0.210	-0.424	0.246	-0.032
2.5	0.105	-0.197	0.102	-0.101
3.0	0.051	-0.088	0.040	-0.003

within this region is < 1. The $\gamma = 1.6$ encounter results in bigger kick velocities, and so we see that the mass loss penetrates farther into the star. We note that the shape and magnitude of the contours for both polytropic indeces at fixed γ converge at large radii. This is due to the fact that regardless of the polytropic index used, $\tilde{v}_{esc}^{pd}$ converges to the same value at large radii when the second term in equation (4.2) becomes negligible. Even though the location of where mass is lost is similar for different polytropic stars at the same value of γ, the amount of the mass lost is substantially different (as shown in Fig. 4.1), due to the different density profiles.

4.2.2 Validity of Approach for Indirect Collisions

The impulse approximation is valid provided that the time over which the encounter takes place, t_{enc}, is much shorter than the time it takes to cross the perturbed system, t_{cross}. To estimate when our calculations break down, we approximate t_{enc} as b/v_{rel}, and t_{cross} as t_s, the time it takes for a sound wave to cross an object that is in hydrostatic

equilibrium:

$$t_{cross} \sim t_s \sim \frac{1}{\sqrt{G\bar{\rho}_{pd}}} \sim \frac{1}{\sqrt{GM_{pd}/r_{pd}^3}}. \tag{4.6}$$

These approximations lead to the condition that

$$\tilde{v}_{rel}^{-1}\tilde{b} \ll 1. \tag{4.7}$$

Aguilar & White (1985) find that for a large range of collisions, the impulse approximations remains remarkably valid, even when t_{enc} is almost as long as t_{cross}. We therefore assume that the impulse approximation holds until the left hand side of equation (4.7) is ~ 1. Our calculation of Δ as a function of γ should therefore be valid for $\gamma \lesssim \gamma_{valid}$, where $\gamma_{valid} \equiv \tilde{M}_{pr}/\tilde{b}^3$. We plot contours of $\log(\gamma_{valid})$ in the M_{pr}/M_{pd} - b/r_{pd} parameter space in Fig. 4.3, where both the x and y axes span ranges relevant to our calculations. The shaded grey area in the figure is the region of the parameter space where the impulse approximation predicts non-zero mass loss due to the encounter. The figure shows that γ_{valid} is smaller for low M_{pr} to M_{pd} ratios at high impact parameters. In fact, most of the right side of the parameter space has γ_{valid} less than 0.98 (where below this value, the impulse approximation predicts no mass lost).

In our calculations, when, for any particular set of M_{pr}/M_{pd} and b/r_{pd}, $\gamma > \gamma_{valid}$, we adopt $\Delta(\gamma > \gamma_{valid}) = \Delta(\gamma = \gamma_{valid})$. This approach represents a lower limit on the amount of mass loss that we calculate, since mass loss should increase with increasing γ. We find, however, that if we set $\Delta(\gamma > \gamma_{valid}) = 1$ (which represents the absolute upper limit in the amount of mass lost) the change in our final results is negligible at small Galactic radii. At large radii, where the mass loss from indirect collisions dominates (see § 4.4), the results change by at most a fact of ~ 2.

Equation (4.3) was derived under the assumption that the impact parameter is much

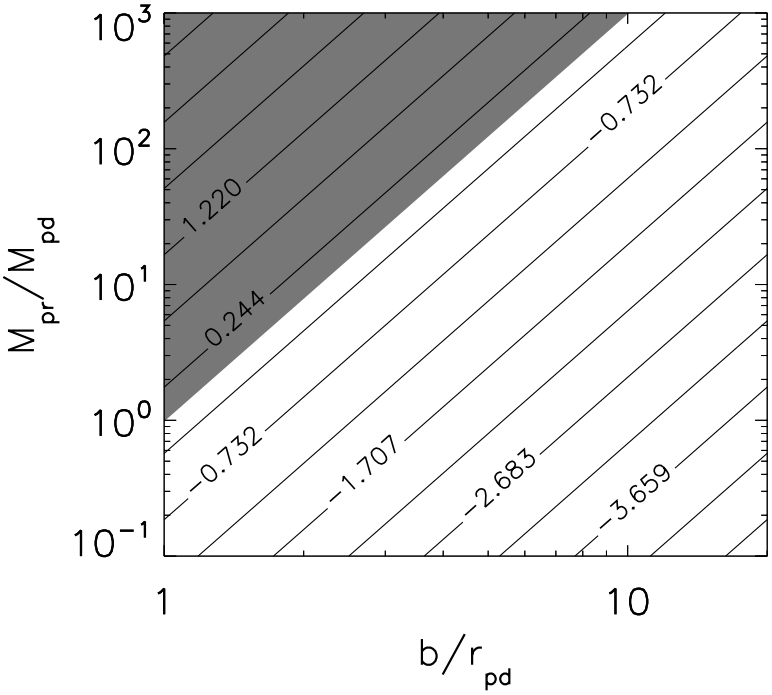

Figure 4.3.—: Contours of $\log(\gamma_{valid})$ in the M_{pr}/M_{pd} - b/r_{pd} parameter space, where γ_{valid} is defined in § 4.2. The shaded grey area indicates where the impulse approximation predicts non-zero mass loss

.

bigger than both r_{pd} and r_{pr}. Since Δv scales as b^{-2}, the equation predicts that most mass loss occurs for small impact parameters. However, given the assumption that was used to derive the equation, the regime of small impact parameters is precisely where equation. (4.3) breaks down. Numerical simulations (Aguilar & White 1985; Gnedin et al. 1999) show that for a variety of perturber mass distributions, the energy input into the perturbed system is well described by equation (4.3) for $b \gtrsim 5r_h$, where r_h is the half mass radius of the perturber system. For an $n = 3$ polytropic star, $5r_h = 1.4r_\star$. Since for indirect collisions, $b/r_{pd} = 1 + r_{pr}/r_{pd} + d/r_{pd}$ (where d is the distance between the surface of both stars), there is only a small region in our calculations, $0 \leq d/r_{pd} \lesssim (0.4 - r_{pr}/r_{pd})$,

for which equation (4.3) may give unreliable results.

4.2.3 Mass Loss due to Direct Collisions

A number of papers over the past few decades have addressed the outcomes of stellar collisions where the two stars come so close to each other that not only gravitational, but also hydrodynamic forces must be accounted for. Early studies used one or two dimensional low resolution hydrodynamic simulations (e.g. Mathis 1967; De Young 1968). Modern studies typically utilize smooth particle hydrodynamics with various stellar models, mass-radius relations, and varying degrees of particle resolution (Benz & Hills 1987, 1992; Lai et al. 1993; Rauch 1999). A detailed review of the literature can be found in this area can be found in Freitag & Benz (2005).

We approach the problem of direct collisions in a highly simplified, analytic manner without hydrodynamic considerations, and find that for determining the amount of mass lost, our method compares well to the complex hydrodynamic simulations. As a first order model, we approximate the encounter as two colliding disks, by projecting the mass of both stars on a plane perpendicular to the trajectory of the perturber star. The problem of calculating mass loss then becomes easier to handle, as it is two dimensional. We also assume that mass loss can only occur in the geometrical area of intersection of the two stars.

We find the kick velocity as a function of position in the area of intersection by conserving momenta, and by assuming that all of the momentum in the perturber star in each area element was transfered to the corresponding area element in the perturbed star. Working in the frame of the perturbed star, and with a polar coordinate system at

its center (so that $r = \sqrt{x^2 + y^2}$), we find

$$\Delta\tilde{v}(\tilde{r}) = \frac{\tilde{\Sigma}_{pr}(\tilde{r})\tilde{v}_{rel}}{\tilde{\Sigma}_{pd}(\tilde{r})}. \tag{4.8}$$

The parameters Σ_{pr} and Σ_{pd} represent the surface density of the perturber and perturbed stars respectively ($\Sigma \equiv \int \rho dz$).

To find the region of intersection, we need to know the impact parameter, and the radii of both stars. To obtain the stellar radii as a function of mass, we use the mass-radius relation calculated by Kippenhahn & Weigert (1994) for a MS star with $Z = Z_{\odot}$, $X_H = 0.685$, and $X_{He} = 0.294$ from a stellar evolution model, where X represents the mass fraction. We fit a polynomial to their Fig. 22.2, and extrapolate on the high and low mass ends so that we have a mass-radius relation that spans from about 0.01 to 150$M_{\odot}$. We compare our mass-radius relation to those used in other studies of direc stellar collisions in Fig. 4.4. Rauch (1999), Lai et al. (1993) and Benz & Hills (1992) all adopted power laws with power law indices of 1.0, 0.8, 0.85 respectively (thin lines). Freitag & Benz (2005) (dotted line) use main sequence stellar evolution codes to obtain a mass-radius relation for masses $> 0.4M_{\odot}$, and a polytropic mass-radius relation of $n = 1.5$ for masses $< 0.4M_{\odot}$.

Our simple model for calculating mass loss due to direct stellar collisions compares surprisingly well to full blown smooth particle hydrodynamic simulations. We borrow plots of the fractional amount of mass lost as a function of impact parameter for specific relative velocities and stellar masses from Freitag & Benz (2005) (Figs. 4.5 and 4.6). They show their own work, the best calculations of mass loss due to stellar collisions to date. For comparison, and to show how the calculations have evolved over the years, the

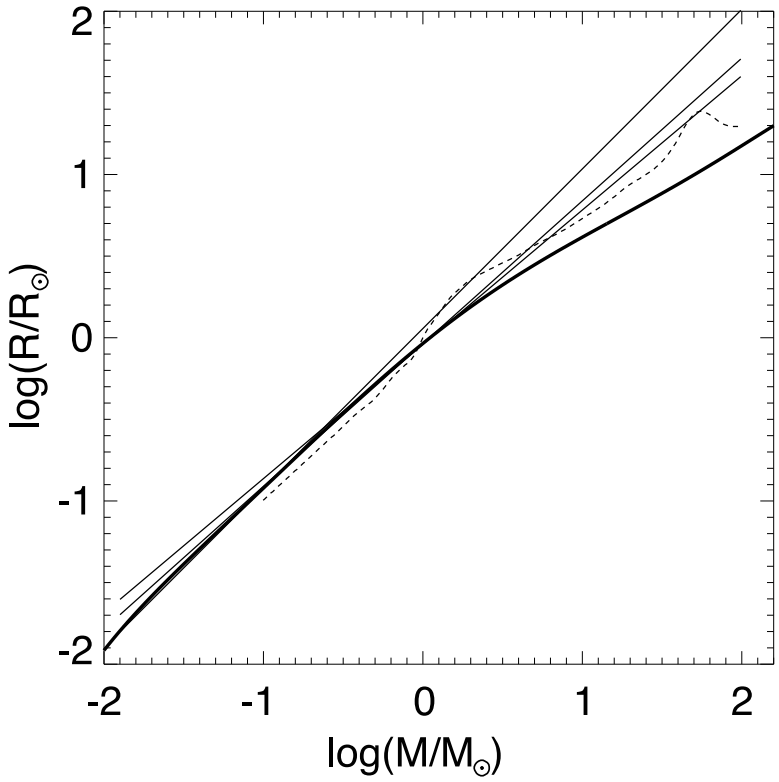

Figure 4.4.—: Mass-radius relations used in studies of calculating mass loss from stars due to stellar collisions. The thin lines are power-law relations of power-law index 1.0, 0.8, and 0.85 used by Rauch (1999), Lai et al. (1993) and Benz & Hills (1992) respectively. The dotted line is the relation used by Freitag & Benz (2005), and the thick line is the relation used in this work.

results from older studies are also shown. Our own results are plotted (dashed-dotted black lines) over these previous studies. We make sure to show results spanning a wide range of stellar masses and relative velocities. Note that these plots show the fractional amount of mass lost from both stars normalized to the initial masses of both stars, and that the impact parameter is normalized to the sum of both stellar radii. Our results show the same qualitative trends seen in the Freitag & Benz (2005) curves, even replicating several "bumps" seen in their curves (see the two bottom panels of Fig. 4.6).

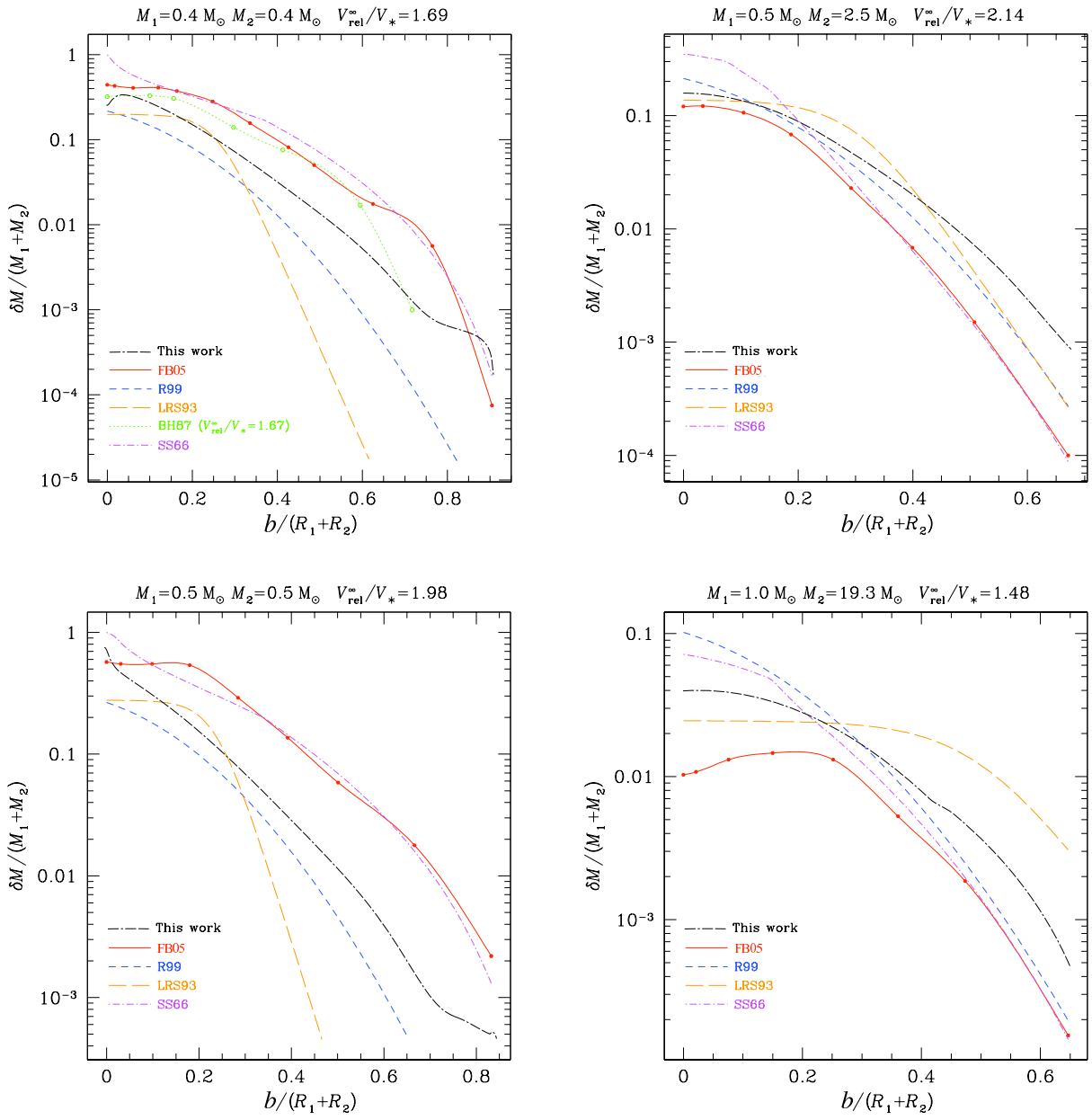

Figure 4.5.—: The calculated fractional amount of mass lost as a function of impact parameter from several works. Our results are the black dashed-dotted lines. The acronyms FB05, R99, LRS93, BH87, and SS66 refer to Freitag & Benz (2005), Rauch (1999), Lai et al. (1993), Benz & Hills (1987) and Spitzer & Saslaw (1966) respectively. The figures are adopted from Freitag & Benz (2005).

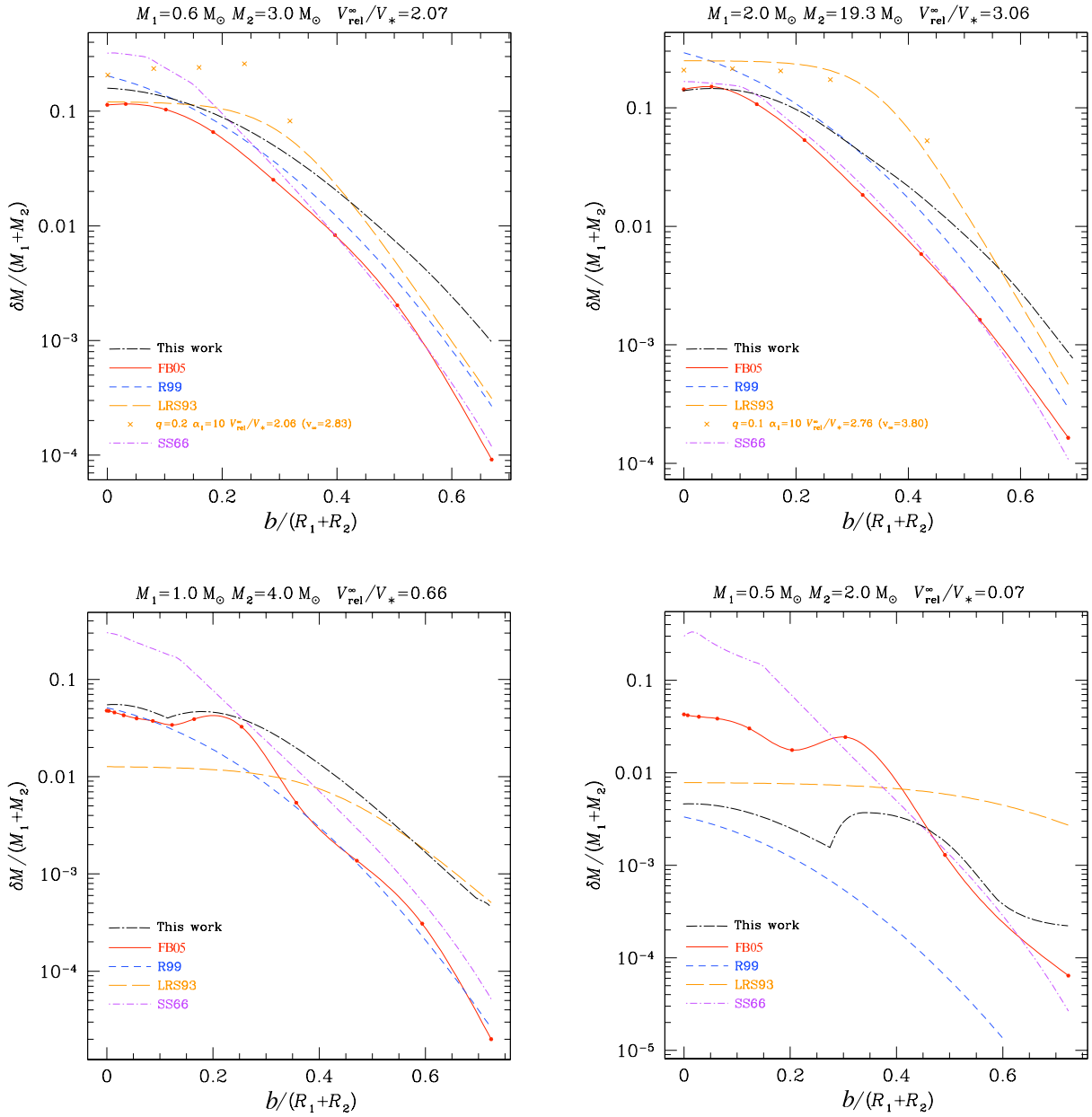

Figure 4.6.—: The calculated fractional amount of mass lost as a function of impact parameter from several works. Our results are the black dashed-dotted lines. The figures are adopted from Freitag & Benz (2005).

As compared to the Freitag & Benz (2005) results, for any specific set stellar masses, relative velocity and impact parameter, our calculations sometimes over or under-predict the amount of mass lost by of a factor of a few to at most a factor of 10. We discuss the error introduced into our main calculations by this discrepancy at the end of §4.5.

4.3 Stellar Collision Rates in the Galactic Center

To calculate mass loss rates in the Galactic center, we will need to find the collision rates as a function of the perturber and perturbed star masses, impact parameter, and relative velocity. Additionally, the collision rate will be a function of distance from the Galactic center, since the stellar densities and relative velocities vary with this distance. In this section, we first present the Galactic density profile that we use, and we then derive the differential collision rate as a function of these parameters.

We adopt the stellar density profile of Schödel et al. (2007), one of the best measurements of the density profile within the Galactic center to date. Using stellar counts from high resolution images of the galactic center, they find that the density profile is well approximated by a broken power law. Moreover, they use measured velocity dispersions to constrain the amount of enclosed stellar mass as a function of galactic radius, r_{gal}. Using their density profile, and velocity dispersion measurements, they find that

$$\bar{\rho}(r_{gal}) = \begin{cases} 2.8 \pm 1.3 \times 10^6 M_\odot pc^{-3} \left(\frac{r_{gal}}{0.22pc}\right)^{-1.2} & \text{for } r_{gal} \leq 0.22\ pc \\ 2.8 \pm 1.3 \times 10^6 M_\odot pc^{-3} \left(\frac{r_{gal}}{0.22pc}\right)^{-1.75} & \text{for } r_{gal} > 0.22\ pc \end{cases} . \quad (4.9)$$

Their average density can be converted into a local density, $\rho(r_{gal})$, by considering the

definition of $\bar{\rho}$,

$$\bar{\rho}(r_{gal}) \equiv \frac{\int_0^{r_{gal}} 4\pi r'^2_{gal} \rho(r'_{gal}) dr'_{gal}}{4/3\pi r^3_{gal}}, \tag{4.10}$$

from which we derive:

$$\rho(r_{gal}) = \bar{\rho}(r_{gal}) + \frac{r_{gal}}{3} \frac{d\bar{\rho}(r_{gal})}{dr_{gal}}. \tag{4.11}$$

We use equations (4.9) and (4.11), to find $\rho(r)$, and plot the result in Fig. 4.7. We "smoothed" the unphysical discontinuity in ρ arising from the kink of the broken power law fit by fitting a polynomial to equation (4.9).

The differential collision rate, $d\Gamma$, between two species, "1" and "2" at impact parameter b characterized by distribution functions f_1 and f_2, and moving with relative velocity $|\vec{v}_1 - \vec{v}_2|$ in a spherically symmetric system is

$$d\Gamma = f_1(r_{gal}, \vec{v}_1)\, d^3v_1 f_2(r_{gal}, \vec{v}_2)\, d^3v_2 |\vec{v}_1 - \vec{v}_2| 2\pi b\, db\, 4\pi r^2_{gal} dr_{gal}. \tag{4.12}$$

For simplicity, we adopt Maxwellian distributions,

$$f_{1,2}(r_{gal}, \vec{v}_{1,2}) = \frac{n_{1,2}(r_{gal})}{(2\pi\sigma^2)^{3/2}} e^{-v^2_{1,2}/2\sigma^2}, \tag{4.13}$$

where we find the velocity dispersion, σ, from the Jean's equations. Assuming an isotropic velocity dispersion, a spherical distribution of stars, and a power-law density profile with power-law slope β, $\rho \propto r_{gal}^{-\beta}$, the Jean's equations lead to $\sigma^2 = \frac{GM_{\rm SMBH}}{r_{gal}(1+\beta)}$, where $M_{SMBH} = 4 \times 10^6 \mathrm{M}_\odot$. From Fig. 4.7, it is evident that β is a function of r_{gal}, but for simplicity, we adopt an averaged value of β, $\beta = 1.3$. Note that we have also assumed that the enclosed mass at position r_{gal} is dominated by the SMBH. This assumptions is valid out till $\sim 1pc$, which is also the point where our impulse approximation starts to break down.

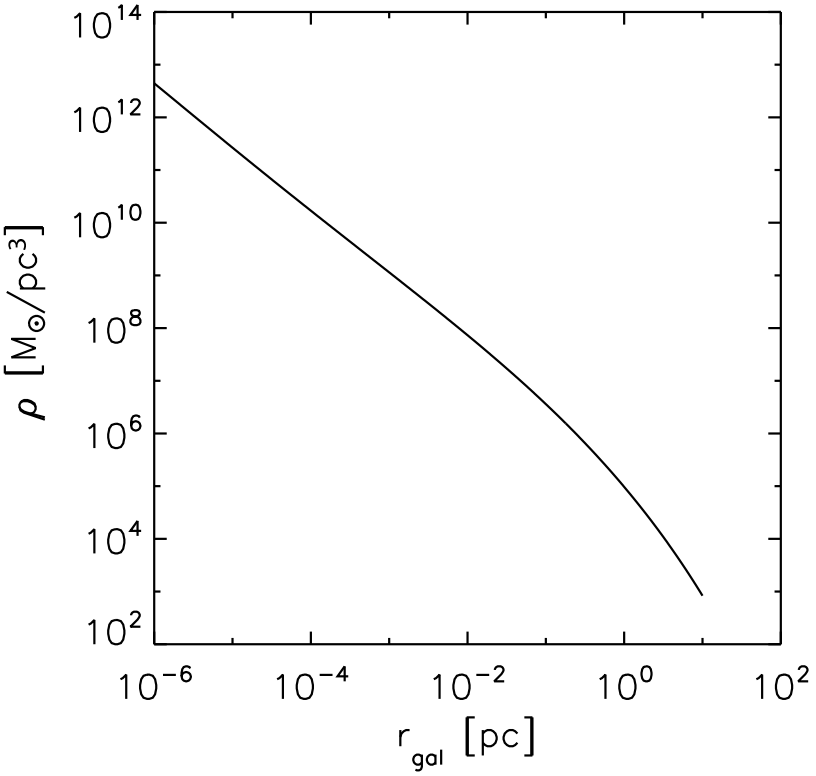

Figure 4.7.—: The stellar density profile that we adopt, based on the average density profile of Schödel et al. (2007).

A change of variables allows one to integrate out 3 of the velocity dimensions, and to write the expression in terms of v_{rel} (see Binney & Tremaine 2008). We can also take into account the fact that both species have a distribution of masses by introducing, $\xi_{1,2}$, the PDMF, which gives the number density of stars per mass bin ($\xi \equiv dn/dM$). We adopt a power law PDMF,

$$\xi \propto M^{-\alpha}, \tag{4.14}$$

that runs from some minimum mass, M_{min} to a maximum mass M_{max}. Since most initial mass functions are parameterized with a power law, the present-day mass function might be modified from a power law due to the effects of collisions and stellar evolution. Although the actual PDMF might have deviations from a power law, adopting a power

law provides us with a quick and simple way to parameterize the PDMF. Taking all of this into account, and assuming that the relative velocities are isotropic, we arrive at the final non-dimensionalized expression for the differential collision rate:

$$d\tilde{\Gamma} = 4\pi^{3/2}\tilde{\sigma}^{-3}e^{-\tilde{v}_{rel}^2/4\tilde{\sigma}^2}\tilde{v}_{rel}^3\tilde{K}^2\tilde{M}_1^{-\alpha}\tilde{M}_2^{-\alpha}\tilde{r}_{gal}^2\tilde{b}\,d\tilde{b}\,d\tilde{r}_{gal}\,d\tilde{v}_{rel}\,d\tilde{M}_1\,d\tilde{M}_2. \tag{4.15}$$

The tildes denote normalization by the proper combination of M_2, r_2, and v_{esc}^2. The parameter K is the normalization constant for ξ, which can be solved for by using the density profile of Fig. 4.7 and the following expression:

$$\rho = \int_{M_{min}}^{M_{max}} \frac{dn}{dM} M dM = K(r_{gal}) \int_{M_{min}}^{M_{max}} M^{1-\alpha} dM = K(r_{gal}) \frac{M_{max}^{2-\alpha} - M_{min}^{2-\alpha}}{2-\alpha}. \tag{4.16}$$

Since the expression for K, which controls the total number of stars, has no time dependence, our expression for the PDMF assumes a constant star formation rate in the Galactic center.

Our calculations involve the computation of multidimensional integrals over a two dimensional parameter space (see §4.4). Therefore, for the ease of calculation, we ignore the enhancement of the collision rate due to the effects of gravitational focusing. This results in a conservative estimate of the collision rate. As two projectiles collide with each other, their mutual gravitational attraction pulls them together, resulting in an enhancement of the cross section:

$$S \rightarrow S\left(1 + \frac{2G(M_1+M_2)}{bv_{rel}^2}\right). \tag{4.17}$$

We discuss the uncertainties in our final results due to ignoring gravitational focusing at the end of §4.5.

To illustrate the frequency of collisions in the Galactic center, we integrate equation. (4.15) over v_{rel}, M_1 and M_2 assuming a Salpeter-like mass function ($\alpha = 2.35$,

$M_{min} = 0.1M_{\odot}$ and $M_{max} = 125M_{\odot}$) to obtain $d\Gamma/(dlnr_{gal}db)$ as a function of r_{gal} (Fig. 4.8a)[2]. We plot $d\Gamma/(dlnr_{gal}db)$ for several different impact parameter values. We calculate $d\Gamma/(dlnr_{gal}db)$ with and without the effect of gravitational focusing (solid and dashed lines respectively). The latter is obtained by multiplying equation (4.15) by the gravitational focusing enhancement term before the integration. As expected, gravitational focusing is negligible at small Galactic radii since typical stellar encounters involve high relative velocities. As the typical relative velocities decrease with increasing Galactic radius, the enhancement to the collision rate from gravitational focusing becomes important. The figure also shows that gravitational focusing becomes less important with increasing impact parameter since the gravitational attraction between the stars is weaker. Fig. 4.8b shows the cumulative differential collision rate (integrated over r_{gal}) per impact parameter as a function of r_{gal}. Again, we plot the results with and without gravitational focusing and for the same impact parameters.

4.4 Mass Loss Rates in the Galaxy

To calculate the mass loss rate from stars due to collisions within the Galactic center, we multiply equation (4.15) by the fraction of mass lost per collision, $\Delta(\gamma)$, and compute the multi-dimensional integral. We calculate the total mass loss rate from both the

[2]This figure, and subsequent figures in this paper with r_{gal} as the independent variable start from $r_{gal} = 10^{-6}$pc. This value of r_{gal} corresponds to the tidal radius for a $1M_{\odot}$ star associated with a $4 \times 10^{6}M_{\odot}$ SMBH. Although stars of different masses will have slightly different tidal radii, the main conclusions of our paper are based off of distances in r_{gal} of order 0.1pc (see §4.5), well above the tidal radius for any particular star.

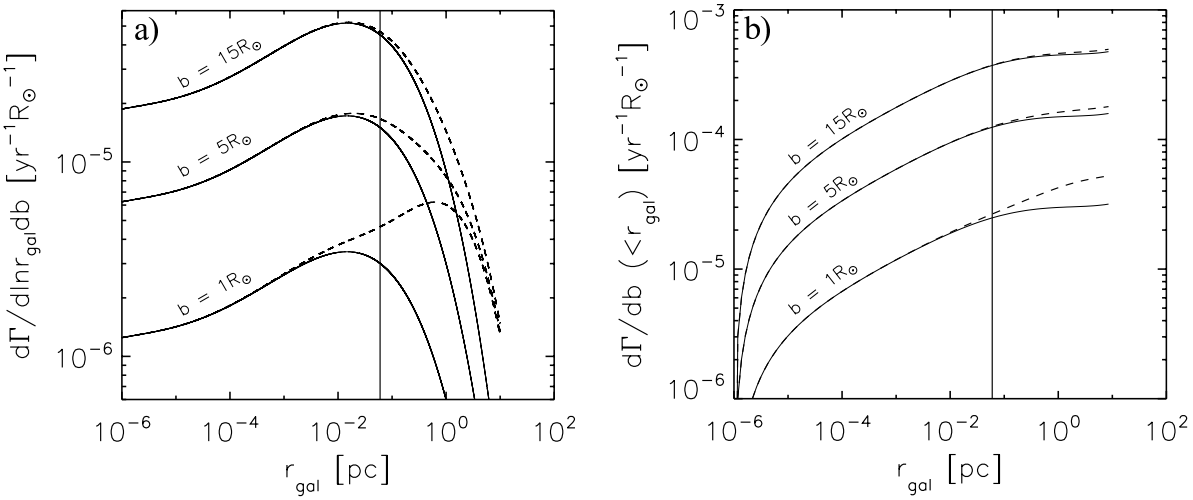

Figure 4.8.—: a) The differential collision rate per logarithmic Galactic radius per impact parameter as a function of Galactic radius for several different impact parameters. The solid (dashed) lines were calculated ignoring (including) gravitational focusing. The curves were made by made by integrating equation (4.15) (with and without the gravitational focusing term) assuming Salpeter values. b) The cumulative differential collision rate (integrated over r_{gal}) per impact parameter with and without gravitational focusing for the same impact parameter values. a and b) The vertical line in each panel is placed at $r_{gal} = 0.06$pc, the upper bound in our integration across r_{gal} as performed in §4.5.

perturbed and perturber stars by simply interchanging the "pr" and "pd" labels and re-performing the calculation.

We first compute the differential mass loss rate for indirect collisions. The mass loss per collision is given by:

$$\Delta(\gamma) = \begin{cases} 0 & for \quad \gamma < 0.98 \\ polynomial & for \quad 0.98 \leq \gamma \leq \gamma_{valid} \\ \Delta(\gamma_{valid}) & for \quad \gamma > \gamma_{valid} \end{cases} . \tag{4.18}$$

The coefficients for the polynomial depend on the polytopic index of the perturbed star (and thus on its mass) and are taken from Table 4.1. We multiply equation (4.18) and equation (4.15) and simplify the integration. In principle, b should go to ∞, but we cut off the integral at $\tilde{b}_{max} = 20$ as we find that the results converge well before this point. The velocity integral is also cut off at $\tilde{v}_{max}$ due to the fact that $\Delta(\gamma)$ becomes zero below $\gamma = 0.98$. This cut-off corresponds to $\tilde{v}_{max} = \frac{(\tilde{M}_{pr})_{max}}{0.98\tilde{b}^2_{min}}$. We may safely throw away the exponential as $\tilde{v}^2_{max} \ll \tilde{\sigma}^2(\tilde{r}_{gal})$ for the range of $\tilde{r}_{gal}$ that we consider. Thus, the integral that we evaluate is:

$$\left(\frac{d\tilde{M}}{dln\tilde{r}_{gal}}\right)_{pd} \cong 4\pi^{3/2}\tilde{\sigma}^{-3}\tilde{r}^3_{gal}\tilde{K}^2 \int_{\tilde{M}_{min}}^{\tilde{M}_{max}} \int_{\tilde{M}_{min}}^{\tilde{M}_{max}} \int_0^{\tilde{v}_{max}} \int_{1+\tilde{r}_{pr}}^{\tilde{b}_{max}} \tilde{b}\tilde{v}^3_{rel}\Delta_{pd}(\gamma)\tilde{M}^{-\alpha}_{pr}\tilde{M}^{-\alpha}_{pd}d\tilde{b}d\tilde{M}_{pr} \times d\tilde{M}_{pd}d\tilde{v}_{rel}. \tag{4.19}$$

For direct collisions, $\Delta(\tilde{b}, \tilde{M}_{pr}, \tilde{M}_{pd}, \tilde{v}_{rel})$ is calculated given the prescription in Sec. 4.2.3. To evaluate the multidimensional integral, we make the approximation of evaluating Δ_{pd} at $\tilde{v}_{rel} = 2\tilde{\sigma}$. The factor of Δ_{pd} thus comes out of the $\tilde{v}_{rel}$ integral, so that

the $\tilde{v}_{rel}$ integral can be performed analytically:

$$\left(\frac{d\tilde{\dot{M}}}{dln\tilde{r}_{gal}}\right)_{pd} \cong 32\pi^{3/2}\tilde{\sigma}\tilde{r}_{gal}^{3}\tilde{K}^{2}\int_{\tilde{M}_{min}}^{\tilde{M}_{max}}\int_{\tilde{M}_{min}}^{\tilde{M}_{max}}\int_{0}^{1+\tilde{r}_{pr}}\tilde{b}\Delta_{pd}(\tilde{b},\tilde{M}_{pr},\tilde{M}_{pd},\tilde{v}_{rel}=2\tilde{\sigma}(\tilde{r}_{gal}))$$
$$\times\tilde{M}_{pr}^{-\alpha}\tilde{M}_{pd}^{-\alpha}d\tilde{b}d\tilde{M}_{pr}d\tilde{M}_{pd}. \quad (4.20)$$

We evaluate the remaining integrals numerically.

Once values for α, M_{min} and M_{max} are specified, equations (4.19) and (4.20) can be integrated to obtain the mass loss rate as a function of Galactic radius. To show how the mass loss rate profiles vary with M_{min}, M_{max} and α, we plot $d\dot{M}/dlnr_{gal}$ for direct collisions in Fig. 4.9 and vary these parameters. In the figure, we have evaluated M_{min} at 0.05, 0.5 and 5M$_\odot$, M_{max} at 75, 100, 125M$_\odot$ and α from 1.00 to 2.5 in equal increments. The parameter M_{min} increases vertically from the bottom panel to the top, M_{max} increases horizontally from the left panel to the right, and in each panel α increases from the bottom to the top. We have indicated a Salpeter-like mass function ($\alpha = 2.29$, $M_{min} = 0.5M_\odot$ and $M_{max} = 125M_\odot$) with the dashed line. Mass loss is extensive and approximately constant until about r_{gal} of 10^{-2}pc and then drops dramatically. This drop reflects that fact that collisions are less frequent at larger radii since star densities and relative velocities drop. The amount of mass lost for any direct collision also decreases with galactic radius since Δ decreases with decreasing relative velocities. Note that the profiles are approximately constant as a function of M_{max}, so that the choice of M_{min} determines the extent of the mass loss rate.

In Fig. 4.10 we show the contributions to $d\dot{M}/dlnr_{gal}$ from both direct and indirect collisions for M_{min}=0.2M$_\odot$, M_{max}=100M$_\odot$ and $\alpha = 1.2$. We find that at small radii the mass loss rate is dominated by direct collisions, and at large radii it is dominated by indirect collisions. Mass loss due to indirect collisions is suppressed in the Galactic

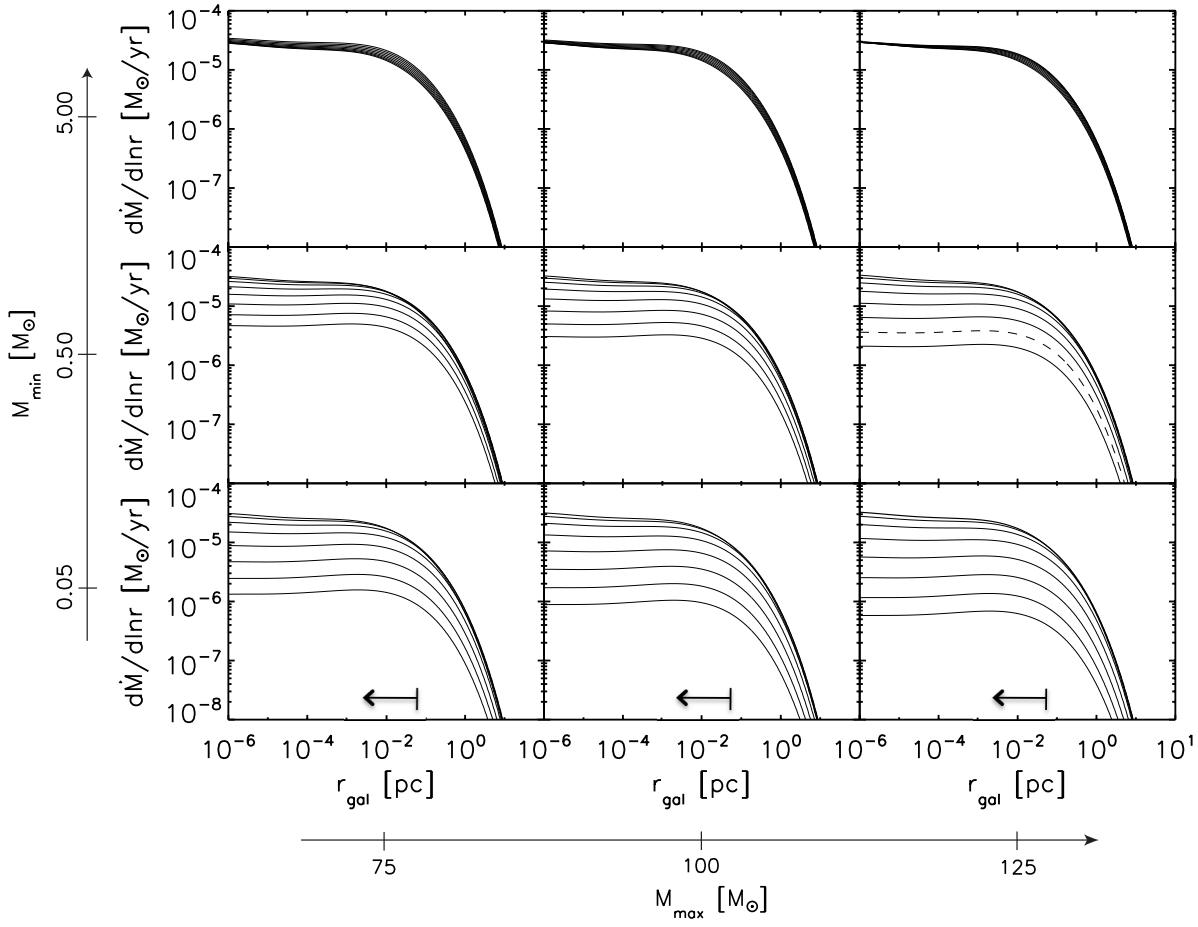

Figure 4.9.—: Mass loss rates as a function of Galactic radius due to direct collisions for various parameters of M_{min} M_{max}, and α. The parameter M_{min} varies in each panel from bottom to top, and M_{max} varies from left to right. The power law slope, α varies within each panel from 1.00 (top line) to 2.5 (bottom line) in equal increments of 0.188. The dashed line corresponds to a Salpeter-like mass function values ($M_{min} = 0.5\mathrm{M}_{\odot}$, $M_{max} = 125\mathrm{M}_{\odot}$, $\alpha = 2.29$). The arrows indicate the range in the diffuse X-ray observations ($r_{gal} < 1.5''$) which we use to constrain the PDMF (see §4.5).

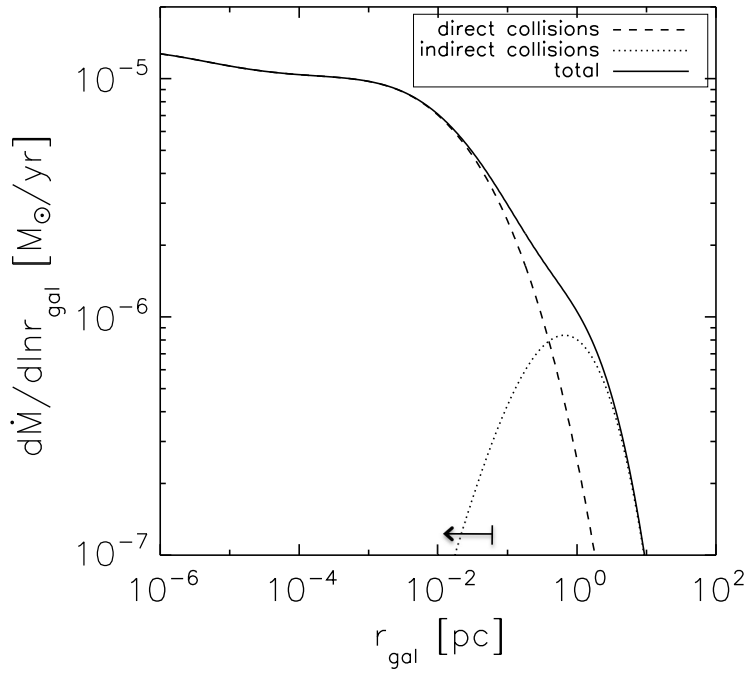

Figure 4.10.—: Mass loss rates due to direct and indirect stellar collisions within the Galactic center for M_{min}=0.2M$_\odot$, M_{max} = 100M$_\odot$ and $\alpha = 1.2$. The arrow indicates the range in the diffuse X-ray observations ($r_{gal} < 1.5''$) which we use to constrain the PDMF (see §4.5).

center, due to the very fast relative stellar velocities. Even though the high velocities (and high densities) in the Galactic center make collisions more frequent, under the impulse approximation, when velocities are very fast, mass loss is minimized.

To illustrate which mass stars contribute the most to the total mass loss rate, we plot $d\dot{M}/dlnM_{pd}$ as a function of M_{pd} in Fig. 4.11 for several different PDMFs. The range of integration we choose for r_{gal} is from 0 to 0.06pc (see §4.5). We choose M_{min} to be 0.05, 0.5 and 5M$_\odot$(left to right in the figure), and we use a constant M_{max} of 125M$_\odot$. In each panel, we vary α from 1.5 to 2.5 in equal increments. The figure shows that for $M_{min} = 0.05$M$_\odot$, changing α has little effect on what mass stars contribute the most to

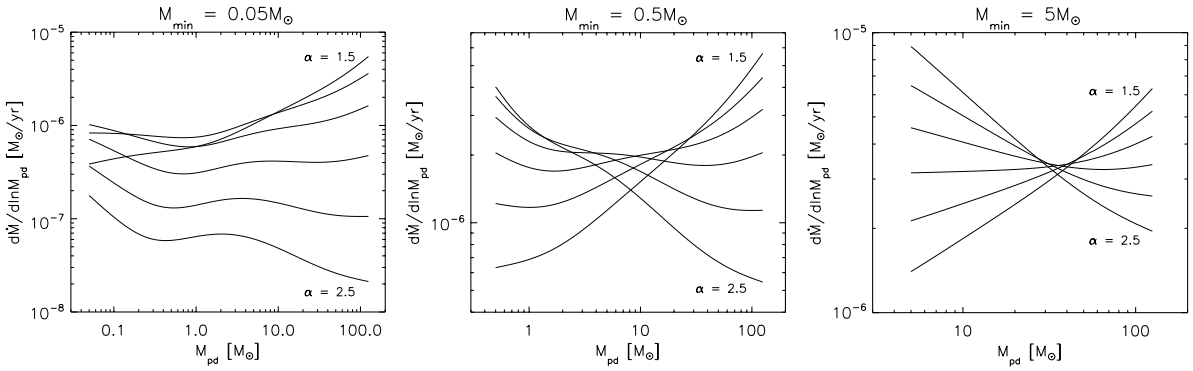

Figure 4.11.—: The amount of mass loss per logarithmic mass interval of the perturbed star as a function of the perturbed star's mass. Each line was calculated with a different PDMF. The titles in each panel indicate the value of M_{min} used for that panel. In each panel, α goes from 1.5 to 2.5 in even increments of 0.167, and for each line $M_{max} = 125M_{\odot}$.

the mass loss rate (although, the total mass loss rate is decreased with increasing α). For the $M_{min} = 0.5\mathrm{M}_{\odot}$ and $5\mathrm{M}_{\odot}$ cases, increasing α results in lower mass stars contributing more to the mass loss rate. This trend makes sense, since PDMF profiles with higher values of α have fractionally more lower mass stars.

To test how our interpolation between the $n = 1.5$ and 3 polytropic indeces affects the main results of this paper, we consider two extreme cases. The first case we consider has $n = 1.5$ for $M_{\star} < 1M_{\odot}$ and $M_{\star} > 5M_{\odot}$, and $n = 3$ for $1M_{\odot} \leq M_{\star} \leq 5M_{\odot}$. This approach has $n = 1.5$ for much of the mass spectrum, and should result in the highest mass loss rates since (as is evident from Fig. 4.1) collisions with the perturbed star having $n = 1.5$ result in the most mass lost. This is due to the fact that for $n = 1.5$ stars, the mass is less centrally concentrated, and more mass can therefore escape at large radii which receive a stronger velocity kick. The second case we consider has $n = 1.5$ for $M_{\star} < 0.3M_{\odot}$ and $M_{\star} > 10M_{\odot}$, and $n = 3$ for $0.3M_{\odot} \leq M_{\star} \leq 10M_{\odot}$. This case

should result in the smallest mass loss rates, since it has $n = 1.5$ for a smaller fraction of the mass spectrum. Since different mass functions have different fractions of the total mass in the neighborhood of $1M_{\odot}$ (where we expect the least mass loss per collision since $n = 3$), we test the two cases for several different mass functions. We find that differences in $d\dot{M}/dlnr_{gal}(r_{gal})$ for both cases are relatively minor, differing at most by $\sim 10\%$ depending on the mass function that we use.

4.5 Constraining the Mass Function in the Galactic Center

It is known through diffuse X-ray observations from *Chandra*, that the central supermassive black hole in the Galactic center is surrounded by gas donated from stellar winds (e.g. Baganoff et al. 2003). The diffuse X-ray luminosity is due to Bremsstrahlung emission from unbound material supplied at a rate of $\sim 10^{-3}\mathrm{M}_{\odot}\mathrm{yr}^{-1}$ (Najarro et al. 1997). This unbound material has been studied theoretically by Quataert (2004), who solved the equations of hydrodynamics (under spherical symmetry) to follow how the gas is accreted onto Sgr A*. Quataert (2004) finds that his model agrees with the level of diffuse diffuse X-ray emission measured by *Chandra*, and predicts an inflow of mass at $r_{gal} \sim 1''$ at a rate of $\sim 10^{-5}\mathrm{M}_{\odot}\mathrm{yr}^{-1}$.

Using the the 2-10keV luminosity as measured by *Chandra* (Baganoff et al. 2003), we estimate the total mass loss rate at a radius of $r_{gal} \sim 1.5''$ (0.06pc). We use the word "total" to indicate the mass loss rate integrated over Galactic radius. By using this total mass loss rate as an upper limit, we will be able to constrain the PDMF in the Galactic

center by precluding any PDMFs with total mass loss rates greater than this value. We will do this by integrating our calculated mass loss rate profiles (e.g., Figs. 4.9 and 4.10) over r_{gal}.

Unbound material at a radius r_{gal} has a dynamical timescale of

$$t_{dyn}(r_{gal}) \sim \frac{r_{gal}}{v_{char}(r_{gal})} \approx 1.1 \times 10^4 \mathrm{yrs} \left(\frac{r_{gal}}{\mathrm{pc}} \right)^{1.5}, \tag{4.21}$$

where the characteristic velocity at radius r_{gal}, $v_{char}(r_{gal})$, is taken as the velocity dispersion as given in § 4.3. The electron density at radius r_{gal} may therefore be estimated by:

$$\begin{aligned} n_e(r_{gal}) \sim n_p(r_{gal}) &\sim \frac{\dot{M} t_{dyn}(r_{gal})}{\frac{4}{3}\pi r_{gal}^3 m_p} \\ &= 1.1 \times 10^5 \mathrm{cm}^{-3} \left(\frac{\dot{M}}{\mathrm{M}_\odot \mathrm{yr}^{-1}} \right) \left(\frac{r_{gal}}{\mathrm{pc}} \right)^{-1.5}, \end{aligned} \tag{4.22}$$

where m_p is the proton mass.

For thermal Bremsstrahlung emission, the volume emissivity ($dE/dVdtd\nu$) is (Rybicki & Lightman 1979)

$$\epsilon_\nu^{ff} = 6.8 \times 10^{-38} \mathrm{erg\,s^{-1}cm^{-3}Hz^{-1}} \left(\frac{n_e}{\mathrm{cm}^{-3}} \right)^2 \left(\frac{T}{\mathrm{K}} \right)^{-1/2} e^{-h\nu/k_B T} \bar{g}_{ff}, \tag{4.23}$$

where we set $\bar{g}_{ff} = 1$. The luminosity in the 2-10keV band, L_{2-10}, can be found substituting equation (4.22) into equation (4.23) and integrating the volume emissivity over volume (assuming spherical symmetry) and frequency:

$$L_{2-10} \sim 6.7 \times 10^{43} \mathrm{erg\,s^{-1}} \left(\frac{\dot{M}}{\mathrm{M}_\odot \mathrm{yr}^{-1}} \right)^2 \int_{r_{min}}^{0.06} \left(\frac{r}{\mathrm{pc}} \right)^{-1} d\left(\frac{r}{\mathrm{pc}} \right) \int_2^{10} e^{-h\nu/\mathrm{keV}} d\left(\frac{h\nu}{\mathrm{keV}} \right). \tag{4.24}$$

We have assumed a constant temperature of 1keV. A constant value of 1keV should suffice for an order of magnitude estimate as Baganoff et al. (2003) find that the gas temperature varies from approximately 1.9 to 1.3keV from $r_{gal} = 1.5$ to 10" (assuming an optically thin plasma model). Quataert (2004)'s model also predicts that the temperature varies from about 2.5 to 1keV from $r_{gal} = 0.3$ to 10". By plugging the value of L_{2-10} within 1.5" ($2.4 \times 10^{33}\mathrm{erg\,s^{-1}}$) as measured by Baganoff et al. (2003) into equation (4.24) , we find $\dot{M} \sim 10^{-5} M_{\odot} yr^{-1}$. This value is consistent with the mass inflow rate at $\sim 1''$ calculated by Quataert (2004). For clarification, we again note that even though our value agrees with Quataert (2004), the underlying physical processes associated with both models are quite different. The model of Quataert (2004) takes the source of unbound material to be due to mass ejected by stellar winds, whereas our model uses mass ejected from stellar encounters.

Our results are not sensitive to the choice of the lower limit in the integral across r_{gal}. The lower limit should be at most a few hundreths of pcs to at least $\sim 10^{-6}$pc. The former value is the tidal radius for the SMBH at the Galactic center for a $1\mathrm{M}_{\odot}$ star. Unbound material due to stellar collisions or from stellar wind should not exist at smaller radii since there are very few stars there to produce it. The value of the integral thus ranges from about unity to a few tens. Since $\dot{M}$ depends upon the square root of this value, the exact value of r_{min} only affects our calculation at the level of a factor of a few, and we thus take the square root of the integral to be unity.

Having established that $\dot{M} \sim 10^{-5}\mathrm{M}_{\odot}\mathrm{yr}^{-1}$ in the vicinity of $1.5''$, we now calculate the expected mass loss rates due to stellar collisions for different PDMFs. The value of

$\dot{M}$ that contributes to the 2-10keV flux is given by:

$$\dot{M} = \int_0^{0.06\mathrm{pc}} \frac{d\dot{M}}{d^3 r_{gal}} \zeta(r_{ral}) d^3 r_{gal}, \tag{4.25}$$

where we have shown how to calculate the mass loss rate profiles, $d\dot{M}/d^3 r_{gal}$ in the previous section. We account for the fact that not all of the emission from the unbound gas contributes to the 2-10keV band with $\zeta(r_{gal})$, defined as the fraction of flux from gas at radius r_{gal} with $2\mathrm{keV} \leq h\nu \leq 10\mathrm{keV}$:

$$\zeta(r_{gal}) \equiv \frac{\int_{resu2keV}^{10keV} \epsilon_\nu^{ff} d\nu}{\int_0^\infty \epsilon_\nu^{ff} d\nu} = e^{-2keV/k_B T(r_{gal})} - e^{-10keV/k_B T(r_{gal})}. \tag{4.26}$$

Since the gas at each radius is at a slightly different temperature, and since ζ is exponentially sensitive to the temperature, we must estimate $T(r_{gal})$. We do this by setting the thermal energy of the unbound material equal to the kinetic energy at a radius r_{gal}, and find that

$$k_B T(r_{gal}) \approx m_p \sigma^2(r_{gal}) = 7.8 \times 10^{-2}\mathrm{keV} \left(\frac{r_{gal}}{pc}\right)^{-1}. \tag{4.27}$$

We plot equation (4.26) in Fig. 4.12. The value of ζ goes to zero at the highest and smallest radii since, for the former, the gas is cool and emits most of its radiation redward of 2keV, and for the latter, the gas is hot and emits mostly blueward of 10keV. Thus, even though the integral in equation (4.25) extends to $r_{gal} = 0$, the contribution to $\dot{M}$ is suppressed exponentially at the smallest radii.

Since, by equations (4.19) and (4.20), $\dot{M}$ depends on the parameters of the PDMF, we now constrain these parameters by limiting the allowed mass loss rate from stellar collisions calculated via equation (4.25) at $10^{-5}\mathrm{M}_\odot\mathrm{yr}^{-1}$. We consider changes in M_{min} and α, and keep M_{max} set at $125\mathrm{M}_\odot$ since (as seen in Fig. 4.9) $\dot{M}$ is approximately independent of M_{max}.

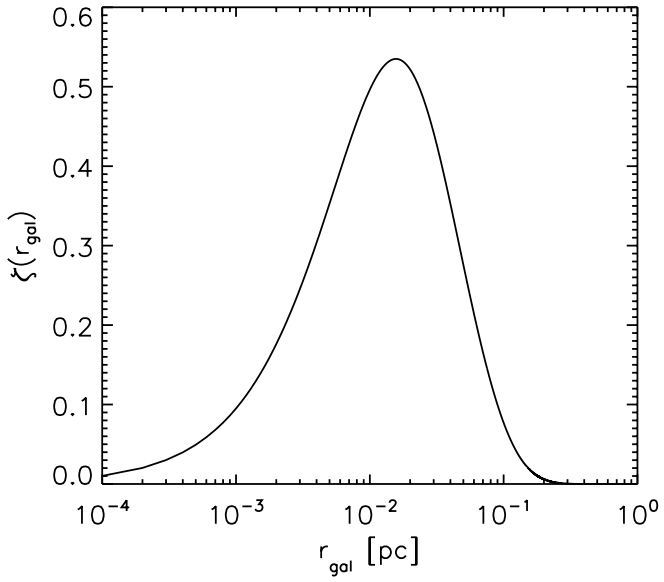

Figure 4.12.—: The fraction of flux emitted from unbound material at radius r_{gal} that contributes to the 2-10keV band.

We sample the $M_{min} - \alpha$ parameter space and use equation (4.25) to compute the total mass loss rate, the results of which are shown in Fig. 4.13. The contours represent the calculated $\dot{M}$ values, where the solid contours are on a logarithmic scale, and where they are limited from above at a value of $\dot{M} = 10^{-5}\mathrm{M}_{\odot}\mathrm{yr}^{-1}$. The figure shows that PDMFs with flat to canonical-like profiles are allowed. Very top-heavy profiles ($\alpha \lesssim 1.25$) are not allowed, as they predict too high of a mass loss rate. Mass functions with $M_{min} \gtrsim 7\mathrm{M}_{\odot}$ are also not allowed. These results are consistent with measurements of the Arches star cluster, a young cluster located about 25pc from the Galactic center. Recent measurements (Kim et al. 2006; Stolte et al. 2005; Figer et al. 1999) probing stellar masses down to about $1\mathrm{M}_{\odot}$ show that the cluster has a flat PDMF, with α in the range of about 1.2 to 1.9 (depending on the location within the cluster).

Since $\dot{M}$ is a much stronger function of α than of M_{min} it is difficult for us to place

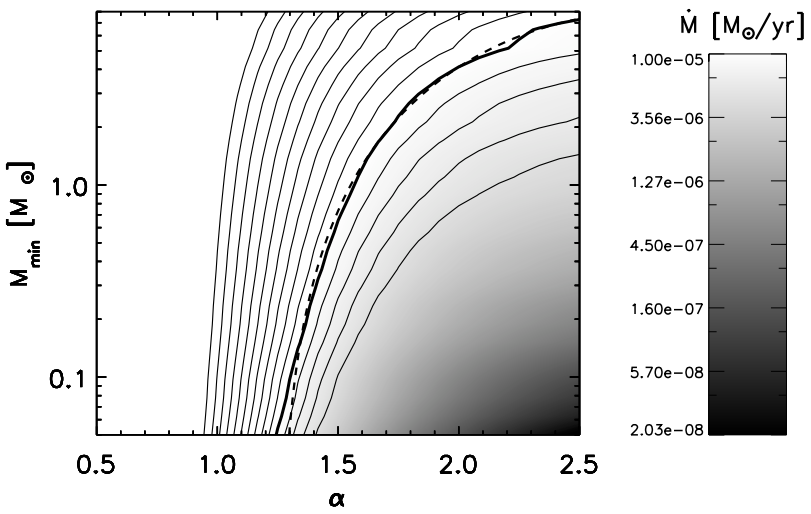

Figure 4.13.—: The total mass loss rate contributing the 2-10keV flux (calculated from equation (4.25)) as a function of M_{min} and α. The solid contours are on a logarithmic scale, and are limited from above at $10^{-5}\mathrm{M}_{\odot}\mathrm{yr}^{-1}$. The line contours are on a linear scale, and are separated by intervals of $1.5 \times 10^{-6}\mathrm{M}_{\odot}\mathrm{yr}^{-1}$. The thick line denotes the $1 \times 10^{-5}\mathrm{M}_{\odot}\mathrm{yr}^{-1}$contour. The dashed line is a 3rd order polynomial fit which represents the absolute allowed upper limit of M_{min} as a function of α. The coefficients of this polynomial are 21.71, -42.37, 25.33 and -4.27 for a_0 to a_3 respectively.

tight constraints on the allowed range of M_{min}. Fig. 4.13 shows that we can, however, place a constraint on the allowed upper limit of M_{min}, since very high values of M_{min} result in mass loss rates $> 10^{-5}\mathrm{M}_{\odot}\mathrm{yr}^{-1}$. For $\alpha > 1.25$, we fit a 3rd degree polynomial (the dashed line in Fig. 4.13) to the $\dot{M} = 10^{-5}\mathrm{M}_{\odot}\mathrm{yr}^{-1}$ contour. This fit analytically expresses the upper limit of M_{min} as a function of α. We provide the coefficients of this fit in the caption of Fig. 4.13.

The small difference between the solid and dashed lines at $r_{gal} = 0.06$pc in Fig. 4.8b suggests that, even for stellar encounters involving small impact parameters, our

integration does not miss many collisions by ignoring gravitational focusing. To estimate the contribution to the total mass loss rate in Fig. 4.13 from gravitational focusing, we take δM_{typ}, the typical amount of mass lost per collision, to be simply a function of b. This avoids the multi-dimensional integrations involved in equations (4.19 and 4.20), since for these equations Δ_{pd} is a function of b, M_{pr}, M_{pd}, and $v_{rel}(r_{gal})$. For simplicity, we choose $\delta M_{typ}(b)$ to decrease linearly from $2\mathrm{M}_{\odot}$ (we assume that both stars are completely destroyed) at $b = 0$ to 0 at $b = b_0$. We find b_0 by noting from Fig. 4.1 that for all values of the polytropic index, the amount of mass loss for an indirect collision goes to zero at around $\gamma = 0.98$. By recalling the definition of γ (equation (4.5)), we solve for b_0 at $\gamma = 0.98$ by setting $\tilde{M}_{pr} = 1$, and taking $v_{rel} \sim 2\sigma(r_{gal} = 0.06\mathrm{pc})$. By calculating $d\Gamma/db$ $(< r_{gal})$ (for Salpeter values) evaluated at 0.06pc across a range of b, and multiplying by $\delta M_{typ}(b)$, we are able to estimate $d\dot{M}/db$. We do this for $d\Gamma/db$ $(< r_{gal})$ with and without gravitational focusing, and integrate across b. Subtracting the two numbers results in our estimate of the contribution to the total mass loss rate due to gravitational focusing: $2.3 \times 10^{-7}\mathrm{M}_{\odot}$. This is about twice the mass loss rate from Fig. 4.13 evaluated at Salpeter values. We perform the same calculation across the M_{min} - α parameter space, and find that gravitational focusing contributes a factor of at most ~ 2.5 to the total mass loss rate.

An underestimate of a factor of 2.5 slightly affects the region of parameter space that we are able to rule out, as shown by the line contours in Fig. 4.13. The $4 \times 10^{-6}\mathrm{M}_{\odot}\mathrm{yr}^{-1}$ contour (2.5 times less than the 10^{-5} contour) shows that the region of the parameter space that is ruled out is $M_{min} \gtrsim 1.4\mathrm{M}_{\odot}$ and $\alpha \lesssim 1.4$.

4.6 Implications for the IMF

We now place constraints on the IMF in the Galactic center with a simple analytical approach that connects the IMF to the PDMF, and with the results of the previous section. The mass function as a function of time is described by a partial differential equation that takes into account the birth rate and death rate of stars:

$$\frac{\partial \xi(M,t)}{\partial t} = R_B(t)\Phi(M) - \xi \frac{1}{\tau_\star(M)}, \tag{4.28}$$

where $R_B(t)$ is the birth rate density of stars ($dN_B/(dtd^3r_{gal})$), $\Phi(M)$ is the initial mass function normalized such that $\int \Phi(M)dM = 1$, and $\tau_\star(M)$ is the main sequence lifetime of stars as a function of stellar mass. For the initial mass function, we take a power law,

$$\Phi = M^{-\gamma}, \tag{4.29}$$

and for $\tau_\star(M)$ we use the expression given by Mo et al. (2010)

$$\tau_\star(M) = \frac{2.5 \times 10^3 + 6.7 \times 10^2 M^{2.5} + M^{4.5}}{3.3 \times 10^{-2} M^{1.5} + 3.5 \times 10^{-1} M^{4.5}} \mathrm{Myr}, \tag{4.30}$$

valid for $0.08\mathrm{M}_\odot < M < 100\mathrm{M}_\odot$ and for solar-type metallicity.

In the following paragraphs, we consider different star formation history scenarios. For each scenario, we will need to know $R_B(\tau_{MW})$, the star formation rate density in the Galactic center at the age of the Milky Way (which we take to be 13Gyr). A rough estimate of this value is given by the number density of young stars in the Galactic center divided by their age: $R_B(\tau_{MW}) \sim \bar{\rho}(r)\eta/(\langle\tau\rangle\langle M\rangle)$. Here $\langle\tau\rangle$ and $\langle M\rangle$ are the average age and average mass of the young stars in the Galactic center, which we take to be ~ 10Myr and $\sim 10\mathrm{M}_\odot$ respectively. The parameter η is the fraction of stars with

masses above $10M_\odot$, which for reasonable mass functions is $\sim 0.1\%$. For self-consistency, we use $\bar{\rho}$ evaluated at 0.06pc (which from equation (4.9) is $\sim 10^7 M_\odot pc^{-3}$), since this was the radius at which we used to constrain the present-day mass function. These values result in $R_B(\tau_{MW}) \sim 10^{-4} pc^{-3} yr^{-1}$.

For the simple case of a constant star formation rate, $R_B(t) = R_B(\tau_{MW})$, and the solution to equation (4.28) with the boundary condition that $\xi(M, t = 0) = \Phi(M) n_{tot}(t = 0)$, evaluated at the current age of the Milky-way is:

$$\xi(M, t = \tau_{MW}) = \Phi(M) e^{-\tau_{MW}/\tau_\star(M)} \left[R_B(\tau_{MW}) \tau_\star(M) e^{\tau_{MW}/\tau_\star(M)} - R_B(\tau_{MW}) \tau_\star(M) + n_{tot}(0) \right] \tag{4.31}$$

We evaluate the solution at the age of the Milky-way (yielding the PDMF) because want to compare with our constraints on the PDMF as found in the previous section. To solve for $n_{tot}(0)$, we use the known mean density of the Galactic center today at 0.06pc, $\bar{\rho}(\tau_{MW}, r = 0.06pc)$, insert equation (4.31) into the following expression:

$$\bar{\rho}(\tau_{MW}, r = 0.06pc) = \int \xi(M, t = \tau_{MW}) M dM, \tag{4.32}$$

and solve for $n_{tot}(0)$.

We solve for $\xi(M, \tau_{MW})$ for a range of different IMF power-law slopes, γ, and fit a power-law to the solution, with a power-law slope α. We plot the IMF power-law slope as a function of the calculated PDMF power-law slope for constant star formation in Fig. 4.14a. We have constrained the PDMF in the previous section to have $\alpha \gtrsim 1.25$, indicated in the figure by the vertical line. The figure therefore shows that for the case of constant star formation, the IMF power-law slope, γ, must be $\gtrsim 0.9$.

For the general case of a star formation rate that varies with time, $R_B(t) \neq R_B(\tau_{MW})$, and the solution to equation (4.28) with the same boundary condition and evaluated at

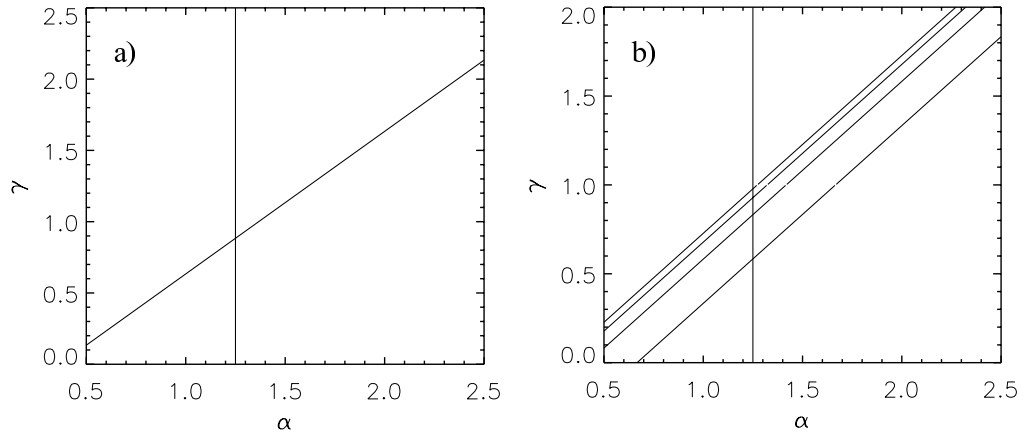

Figure 4.14.—: a) The IMF power-law slope as a function of the PDMF power-law slope for the case of constant star formation. b) The same except for exponentially decreasing star formation with τ_{exp} = 3, 5, 7, 9Gyr (bottom to top line respectively).

τ_{MW} is:

$$\xi(M, t = \tau_{MW}) = \Phi(M) e^{-\tau_{MW}/\tau_\star(M)} \left[\int_0^{\tau_{MW}} R_B(t') e^{t'/\tau_\star(M)} dt' + n_{tot}(0) \right]. \qquad (4.33)$$

For an exponentially decreasing star formation history, the star formation rate is given by:

$$R_B(t) = R_B(\tau_{MW}) e^{-(t-\tau_{MW})/\tau_{exp}}. \qquad (4.34)$$

Given this star formation history, we solve for $\xi(M, \tau_{MW})$ (by solving for $n_{tot}(0)$ with equation (4.32)) for τ_{exp} =3, 5, 7 and 9Gyr. We fit power-laws to the resulting PDMFs, and show the results in Fig. 4.14b. The figure shows that smaller values of τ_{exp} result in larger values of α for any given γ. The trend can be explained by the fact that since a smaller value of τ_{exp} results in a steeper R_B profile, and that all profiles must converge to $R_B(\tau_{MW})$ at the present-time, R_B profiles with smaller values of τ_{exp} have had overall more star formation in the past. More overall star formation means that the present-day mass function is comprised of fractionally more lower-mass stars since the IMF favors

lower-mass stars. The constant build-up of lower-mass stars results in a steeper PDMF, so that for any given γ, α should be larger. The figure shows that for exponentially decreasing star formation γ must be $\gtrsim$ 0.6, 0.8, 0.9 and 1.0 for τ_{exp} = 3, 5, 7, and 9Gyr respectively.

The final case we consider is episodic star formation, where each episode lasts for a duration Δt, where the ending and beginning of each episode is separated by a time, T, and where the magnitude of each episode is $R_B(\tau_{MW})$. For such a star formation history, the solution to equation (4.33) is:

$$\xi(M, t = \tau_{MW}) = \Phi(M) e^{-\tau_{MW}/\tau_\star(M)} \left\{ R_B(\tau_{MW}) \tau_\star(M) \sum_{n=0}^{n_{max}} \left[e^{[(n+1)\Delta t + nT]/\tau_\star(M)} \right. \right. \tag{4.35}$$

$$\left. \left. - e^{n(\Delta t + T)/\tau_\star(M)} \right] + n_{tot}(0) \right\}, \tag{4.36}$$

where $n_{max} = \text{floor}\{(\tau_{MW} - \Delta t)/(T + \Delta t)\}$, and where we again solve for $n_{tot}(0)$ with equation (4.32). We consider 9 cases with Δt and $T = 10^6$, 10^7, and 10^8yrs, and show the results in Fig. 4.15. In each panel the lowest line is $\Delta t = 10^8$yrs and the highest line is $\Delta t = 10^6$yrs. For $T = 10^6$yrs, $\gamma \gtrsim 0.8$ and 0.5 for $\Delta t = 10^6$ and 10^7yrs respectively, while the $\Delta t = 10^8$yrs case results in constraints on γ that are too low to be realistic. For $T = 10^7$yrs, $\gamma \gtrsim 0.5$ and 0.4 for $\Delta t = 10^6$ and 10^7yrs respectively, while again, the $\Delta t = 10^8$yrs case results in unrealistic constraints. Finally, for the $T = 10^8$yrs, $\gamma \gtrsim 0.5$ for $\Delta t = 10^6$, while the $\Delta t = 10^7$ and 10^8yrs case result in unrealistic constraints. We test if when the last star formation episode occurs (relative to the present day) affects our solution of $\xi(M, \tau_{MW})$ by varying the start time of the star formation episodes. By varying the start time and testing all the combinations of Δt and T that we consider, we find that the lines in Fig. 4.15 vary by at most about 5%, so that the main trends in the

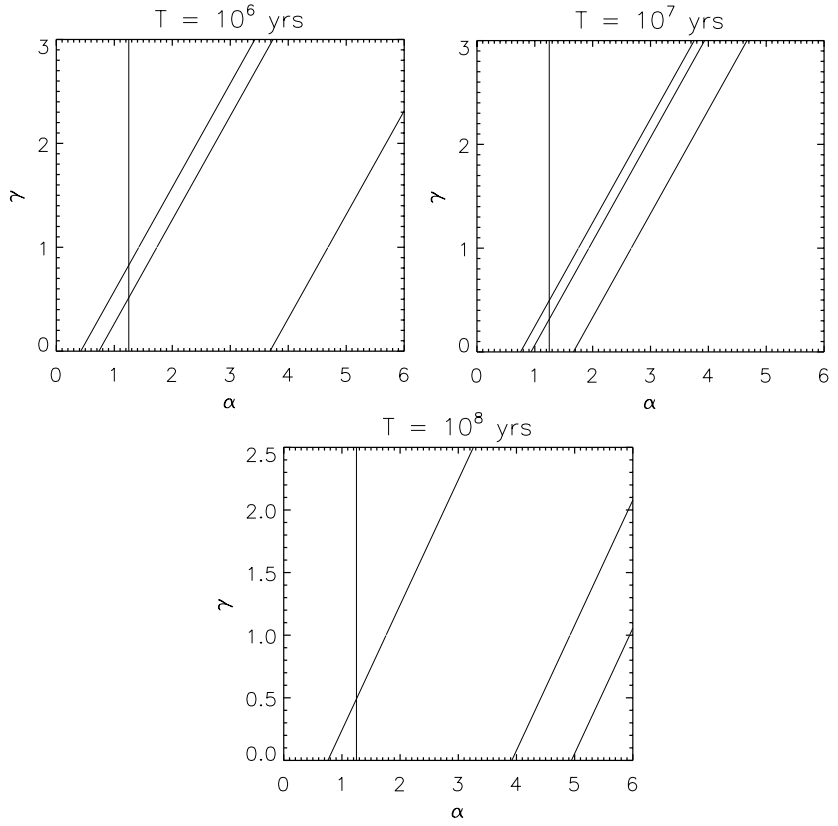

Figure 4.15.—: The IMF power-law slope as a function of the PDMF power-law slope for the case of episodic star formation. In each panel the lowest line is $\Delta t = 10^8$yrs and the highest line is $\Delta t = 10^6$yrs.

figure are unaffected.

4.7 Contribution from red giants

Spectroscopic observations have revealed that the central parsec of the Galaxy harbors a significant population of giant stars (Paumard et al. 2006; Maness et al. 2007). Due to their large radii (and hence large cross sections), it is possible that they could play an important part in the mass loss rate due to collisions in the Galactic center.

In assessing their contribution to the mass loss rate, care must be taken when deriving the collision rates, because their radii, r_{RG}, are strong functions of time, t. Dale et al. (2009) have already calculated the probability, $P(r_{gal})$, for a red giant (RG) in the Galactic center to undergo collisions with main sequence impactors. They have taken into account that $r_{RG}(t)$ by integrating the collision probability over the time that the star resides on the RG branch. We use their results to estimate the mass loss rate due to RG - MS star collisions.

To find the number density of RGs in the Galactic center, we weight the total stellar density by the fraction of time the star spends on the RG branch:

$$n_{RG}(r_{gal}) \sim n_{\star}(r_{gal})\frac{\tau_{RG}}{\tau_{\star}}. \tag{4.37}$$

This approximation should be valid given a star formation history that is approximately constant when averaged over time periods of order τ_{RG}. The number of collisions per unit time suffered by any one red giant, $\dot{P}(r_{gal})$, should of order the collision rate averaged over the lifetime of the RG, and is given by

$$\dot{P}(r_{gal}) \sim \left\langle \dot{P}(r_{gal}) \right\rangle_t = \frac{P(r_{gal})}{\tau_{RG}}. \tag{4.38}$$

If we define δM to be the typical amount of mass lost in the collision, then the mass loss rate is

$$\frac{d\dot{M}}{dlnr_{gal}} = 4\pi r_{gal}^3 \frac{d\dot{M}}{d^3 r_{gal}} \sim 4\pi r_{gal}^3 n_{RG}(r_{gal})\frac{P(r_{gal})}{\tau_{RG}}\delta M. \tag{4.39}$$

To calculate an upper limit for the contribution of RG - MS star collisions to the mass loss rate, we assume all RG and MS stars have masses of $1M_{\odot}$, and that the entire RG is destroyed in the collision. Collisions involving $1M_{\odot}$ RGs yield an upper limit, because there is not an appreciable amount of RGs with masses less than $\sim 1M_{\odot}$ due to

their MS lifetimes being greater than the age of the Galaxy. For RGs with masses greater than $1M_\odot$, the amount they contribute to the mass loss rate is a competition between their lifetimes and radii. Red giant lifetimes decrease with mass (thereby decreasing the time they have to collide) and their radii increase with mass (thereby increasing the cross section). In their Fig. 3, Dale et al. (2009) clearly show that the number of collisions decreases with increasing RG mass, indicating that the brevity of their lifetime wins over their large sizes. One solar mass MS impactors should yield approximately an upper limit to the mass loss rate, since $\sim 1M_\odot$ MS stars are the most common for the PDMFs under consideration.

Since we assume that the entire RG is destroyed in the collision $\delta M = 1M_\odot$. For the case that all impactors are $1M_\odot$ MS stars, we calculate $n_{RG}(r_{gal})$ from equation (4.37) by noting that $n_\star(r_{gal}) = \rho_\star(r_{gal})/(1M_\odot)$. For self-consistency, we must truncate $P(r_{gal})$ at 1 for all $P(r_{gal}) > 1$ since we are considering the case where one collision destroys the entire star. We plot equation (4.39) for this calculation in Fig. 4.16. The discontinuity is due to our truncating $P(r_{gal})$ at 1. The figure shows that the mass loss rate for RG-MS star collisions never exceeds $10^{-5}M_\odot yr^{-1}$, well below typical $d\dot{M}/dlnr_{gal}$ for values for MS - MS collisions (see Figs. 4.9 and 4.10). Moreover, in their hydrodynamic simulations, Dale et al. (2009) note that in a typical RG - MS star collision, at most $\sim 10\%$ of the RG envelope is lost to the RG. We therefore conclude that the contribution of RGs to the total mass loss rate in the central parsec of the Galaxy is negligible.

The figure shows that by $r_{gal} = 0.06$pc, the mass loss rate for RG-MS star collisions is at most about $10^{-6}M_\odot yr^{-1}$. It is thus possible that for MS-MS collisions, values of M_{min} and α that results in total mass loss rates just below $10^{-5}M_\odot yr^{-1}$ could be pushed past this threshold with the addition of mass loss due to RG collisions. However,

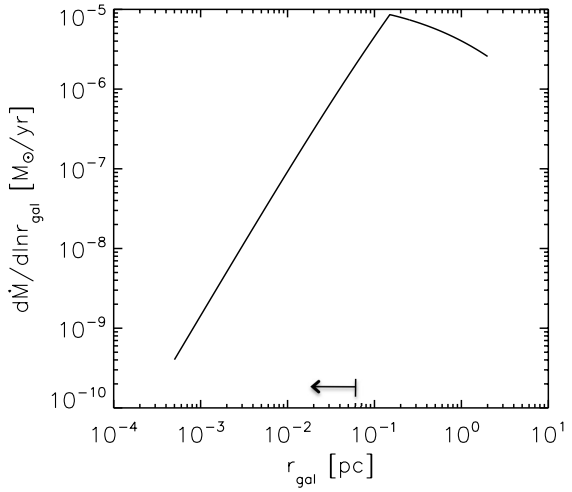

Figure 4.16.—: An upper limit to the mass loss rate due to collisions between RG and MS stars. The arrow indicates the range in the diffuse X-ray observations ($r_{gal} < 1.5''$)which we use to constrain the PDMF (see §4.5).

we believe that this is unlikely for two reasons. The inclusion of the factor, ζ, when calculating the total mass loss rate (see equation (4.25)) will reduce the mass loss by at least a factor of 0.6 (see Fig. 4.12). Also, as noted by the hydrodynamic simulations of Dale et al. (2009), for a typical RG - MS star collision, at most $\sim 10\%$ of the RG envelope is lost to the RG. This will reduce $d\dot{M}/dlnr_{gal}$ for RG-MS collisions by another factor of 10.

4.8 Conclusions

We have have derived novel, analytical methods for calculating the amount of mass loss from indirect and direct stellar collisions in the Galactic center. Our methods compares very well to hydrodynamic simulations, and do not require costly amounts of computation time. We have also computed the total mass loss rate in the Galactic

center due to stellar collisions. Mass loss from direct collisions dominates at Galactic radii below ~ 0.1pc, and thereafter indirect collisions dominate the total mass loss rate. Since the amount of stellar material lost in the collision depends upon the masses of the colliding stars, the total mass loss rate depends upon the PDMF. We find that the calculated mass loss rate is sensitive to the PDMF used, and can therefore be used to constrain the PDMF in the Galactic center. As summarized by Fig. 4.13, our calculations rule out $\alpha \lesssim 1.25$ and $M_{\rm min} \gtrsim 7{\rm M}_{\odot}$ in the $M_{min} - \alpha$ parameter space. Finally, we have used our constraints on the PDMF in the Galactic center to constrain the IMF to have a power-law slope $\gtrsim 0.4$ to 0.9 depending on the star formation history of the Galactic center.

Acknowledgments

This work was supported in part by the National Science Foundation Graduate Research Fellowship, NSF grant AST-0907890 and NASA grants NNX08AL43G and NNA09DB30A.

Chapter 5

The Kinetic Sunyaev-Zel'dovich Effect from the Diffuse Gas in the Local Group

D. Rubin & A. Loeb, *Journal of Cosmology and Astroparticle Physics*, Issue 01, ID 051, 2014

Abstract

Since the Local Group (LG) of galaxies moves with a bulk velocity with respect to the cosmic microwave background radiation (CMB), free electrons in its gaseous halo should imprint large-scale non-primordial temperature shifts in the CMB via the kinetic Sunyaev-Zel'dovich (kSZ) effect. By modeling the distribution of gas in the LG halo and using its inferred velocity with respect to the CMB, we calculate the resulting kSZ

signal from the diffuse LG medium. We find that it is dominated by a hot spot $\sim 10^{\circ}$ in size in the direction of M31, where the optical depth of free electrons is the greatest. By performing a correlation analysis, we find no statistical evidence that the kSZ signal from model of the LG halo is embedded in the CMB temperature map measured by the Planck satellite. We constrain the amount of mass in the LG halo by limiting the kSZ temperature shift around the hot spot to be smaller than the observed temperature shift in the Planck map. We find the tightest constraints for models where the halo mass is highly concentrated, with the mass limited to roughly $2.5 - 5 \times 10^{12} \mathrm{M}_{\odot}$, but note that halos with such high concentrations are rare.

5.1 Introduction

The kinetic Sunyaev-Zel'dovich effect occurs when cosmic microwave background photons scatter off free electrons with bulk velocities relative to the cosmic rest frame (Sunyaev & Zeldovich 1980; Hogan 1992). The CMB temperature shift associated with the kSZ effect depends upon the distribution of free electrons along the line of sight and their radial velocities relative to the CMB, and is given by:

$$\frac{\Delta T}{T} = -\frac{\sigma_T}{c} \int_{\ell os} v_{\ell os} n_e d\ell. \tag{5.1}$$

In this equation, σ_T is the Thomson cross section, c is the speed of light, v_{los} is the line-of-sight velocity, n_e is the electron number density and ℓ is the position variable along the line-of-sight. Unlike the thermal SZ effect, the kSZ effect only induces a temperature shift, and does not alter the spectral shape of the CMB signal. It is thus particularly difficult to remove kSZ contaminates from measurements of the primordial temperature fluctuations of the CMB.

Since measuring the power spectrum of the CMB temperature fluctuations is now a precision science, it is therefore worth the effort to understand foreground contaminants which induce even relatively small temperature shifts. One such contaminant, which can produce temperature shifts of order a few μK (Birnboim & Loeb 2009; Peiris & Smith 2010; Hajian et al. 2007), is the kSZ shift due to free electrons in the local universe. Additionally, these temperature shifts may help explain well known anomalies in the CMB sky maps. Large scale anomalies such as the observed hemispherical asymmetry (Planck Collaboration et al. 2013b; Eriksen et al. 2004) in the power spectrum amplitude are contrary to the expected statistical isotropy of the CMB signal. Without resorting to exotic physics (and barring observation or analysis issues), one potential explanation is the kSZ effect from local sources, which, because of their proximity, produce large scale temperature shifts on the sky.

The kSZ effect due to free electrons in the local universe has been studied by several groups. The expected kSZ signal from the Milky Way (MW) halo, inflowing filaments and high velocity clouds within the halo has been calculated in by Birnboim & Loeb (2009). A cross correlation analysis with the WMAP5 data, however, showed no significant correlation. The kSZ signal from the MW halo has also been considered by Peiris & Smith (2010), but in the context of attempting to explain the large scale anomalies in the CMB data. Using different statistical metrics, they found that the kSZ signal from the halo could explain the observed anomalies, but only if the column density of free electrons is at least an order of magnitude larger than indicated by observations. The kSZ signal from the MW itself has also been calculated by Hajian et al. (2007) by using the electron distribution inferred from pulsar dispersion measurements. Both the kSZ and thermal SZ signals from local superclusters were calculated by Dolag et al.

(2005). They simulated the local distribution of gas by using hydrodynamical simulations with the initial conditions constrained to reproduce prominent structures in the local universe. They found that it could be possible to extract and estimate of the SZ signal at the largest scales from Planck's measurement of the CMB.

In this paper, we consider the kSZ effect from another local source: the diffuse intragroup medium associated with the Local Group (LG) of galaxies. Although it has been difficult to detect observationally (Maloney & Bland-Hawthorn 1999), a gaseous halo surrounding groups of galaxies is predicted theoretically. In particular, the mass of the LG medium ($\sim 10^{12}\mathrm{M}_{\odot}$) is expected to be a substantial fraction of the total mass of the LG (Cox & Loeb 2008). Assuming that the fraction of baryons in the LG medium follows the cosmic mean (about 17%), the baryonic mass in the LG medium should therefore be $\sim 10^{11}\mathrm{M}_{\odot}$. For comparison, after subtracting the total baryonic mass in stars and gas in the Galaxy, the diffuse baryonic mass of the MW halo is about $5\times10^{10}\mathrm{M}_{\odot}$ (Birnboim & Loeb 2009; Peiris & Smith 2010). Since the total mass in diffuse gas in the LG medium is several times larger than that of the MW halo, it is possible that the kSZ temperature shift from the LG medium could be several times larger, or $\sim 10\mu$K. Indeed, the thermal SZ effect due to the diffuse LG medium was considered by Suto et al. (1996) and it was found that the temperature shift from the quadrupole term could be a considerable contaminant to the CMB.

The outline of this paper is as follows. In §2, we present our model for the distribution of gas in the LG halo. Using this model, we derive the formalism to actually calculate the kSZ signal in §3. In §4, we present the sky maps and power spectra from the kSZ signal due to the LG medium. In the same section we describe our correlation analysis of the kSZ maps with the Planck satellite map to test if the kSZ signal is

embedded in the measured CMB temperature fluctuations. In §5 we compare the kSZ maps in order to the Planck map to limit the amount of mass in the LG halo. We conclude in §6 and discuss how our results might change by using more realistic models of the gas distribution in the LG.

5.2 Physical Model of the Diffuse Local Group Medium

In order to compute the kSZ temperature shift due to free electrons in the LG halo, we require a model of the baryonic content in the diffuse LG medium. Several groups have modeled the distribution of mass in the LG medium in order to set the gravitational potential for various studies, such as simulating the collision between the MW and M31 (Cox & Loeb 2008) and calculating the trajectories of hypervelocity stars (Sherwin et al. 2008). The LG medium was also modeled by Suto et al. (1996) to calculate the thermal SZ effect, and we follow their general approach by modeling the LG halo as a virialized sphere whose center coincides with the center of mass position of the galaxies in the LG. The virial radius of the sphere, R_{vir}, can be calculated once the halo mass and virialization redshift are set. An illustration of our model of the LG medium is shown in Fig. 5.1. Since the total mass in galaxies in the LG is dominated by the MW and M31, we only consider these two galaxies in determining the center of mass position of the LG galaxies. The center of the virialized sphere will therefore be at a point on the line that passes through the centers of the MW and M31.

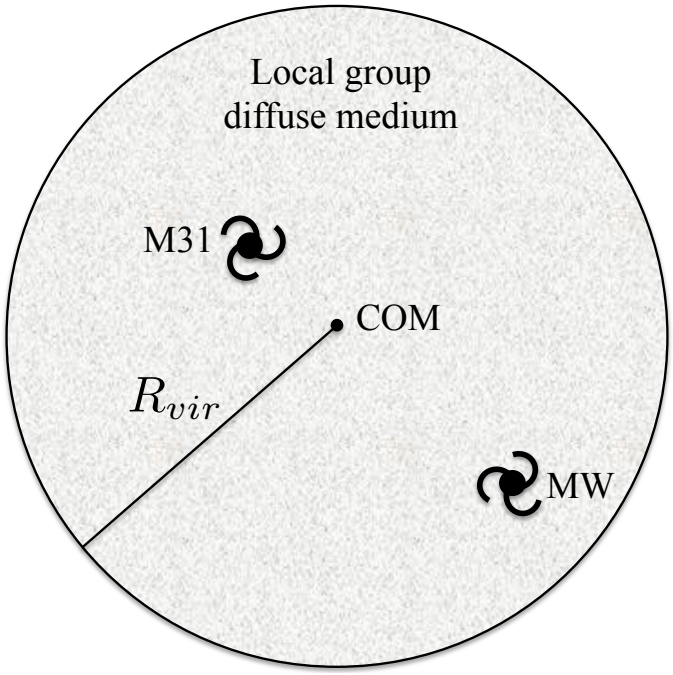

Figure 5.1.—: An illustration of our model for the distribution of mass in the LG medium.

We adopt an NFW profile (Navarro et al. 1996),

$$\rho(R) = \frac{\rho_o}{\frac{R}{R_{vir}}\left(1 + c\frac{R}{R_{vir}}\right)^2}, \tag{5.2}$$

as the density profile of the LG halo, where R is the radial distance from the halo center. The quantity, c, is the so-called concentration parameter, and ρ_o is a normalization constant which can be re-expressed in terms of the virial mass by integrating the density profile out to the virial radius:

$$\rho_o = \frac{M_{vir}c^2}{4\pi R_{vir}^3\left[\ln(1+c) - \frac{c}{1+c}\right]}. \tag{5.3}$$

Once a halo's mass and virialization redshift are specified, its virial radius can be found from

$$R_{vir} \cong 1.5\text{kpc}\left[\frac{\Omega_m}{\Omega_m(z_{vir})}\frac{\Delta_c(z_{vir})}{18\pi^2}\right]^{-1/3}\left(\frac{M_{vir}}{10^8 M_\odot}\right)^{-1/3}\left(\frac{1+z_{vir}}{10}\right)^{-1}, \tag{5.4}$$

where the pre-factor of 1.5 was calculated using $h = 0.7$ (the Hubble constant in units of 100km/s/Mpc), and where $\Delta_c(z_{vir})$ is the mean density at collapse in units of the critical density of the universe at collapse. This quantity is typically found from the spherical collapse model, and for a flat universe with a cosmological constant is well fit by

$$\Delta_c = 18\pi^2 + 82d - 39d^2, \tag{5.5}$$

with $d \equiv \Omega_m(z_{vir}) - 1$ (Loeb & Furlanetto 2013).

Although there have been several studies to determine the total mass of the LG group (van der Marel & Guhathakurta 2008; Li & White 2008; van der Marel et al. 2012), the exact amount of mass within the LG medium is still uncertain. We therefore parameterize M_{vir} as

$$M_{vir} = \eta(m_{mw} + m_{M31}), \tag{5.6}$$

with η as a free variable. As in Cox & Loeb (2008) and Sherwin et al. (2008) we take $m_{M31} = 1.6 \times 10^{12}\mathrm{M}_\odot$ and $m_{MW} = 10^{12}\mathrm{M}_\odot$, consistent with a range of observations and simulations (see van der Marel et al. 2012, for a review on the literature of the masses of the MW and M31). If the amount of mass in the LG medium is is equal to the combined mass of the MW and M31 (as assumed by Cox & Loeb 2008), $\eta = 2$, and assuming that the LG has virialized only recently ($z_{vir} = 0$) we find that $R_{vir} = 402.6$kpc and $\rho_o = 6.27 \times 10^4 \mathrm{M}_\odot\mathrm{kpc}^{-3}$. These values were calculated with $c = 4$, a typical concentration parameter for recently formed halos (Zhao et al. 2009).

To model the density profile of the diffuse gas in the halo, we assume that the distribution of baryons follows the dark matter and that the fraction of baryons to dark matter in the LG medium is the same as the cosmic average, $f_b \equiv \Omega_b/(\Omega_b + \Omega_{DM}) \cong 0.15$. In this case, the density profile of the baryons is found by multiplying Eqn. 5.2 by the

fraction, f_b:

$$\rho_b(R) = \frac{f_b \rho_o}{\frac{R}{R_{vir}}\left(1 + c\frac{R}{R_{vir}}\right)^2} \tag{5.7}$$

With our model for the baryonic density profile set, and with all the quantities in this model (ρ_o, R_{vir}, M_{vir}) found from the expressions provided above, we may now determine the number density profile of free electrons for use in calculating the kSZ temperature shift. Assuming that the relative fraction of hydrogen to helium in the LG is primordial,

$$n_H \approx 12 n_{He}, \tag{5.8}$$

and that the mass from heavier elements is negligible, the baryon mass density is given by

$$\rho_b = m_p n_H + 4 m_p n_{He}. \tag{5.9}$$

In the above equation we have used the highly accurate approximation that the mass of a neutron is equal to the mass of a proton. Since the gas temperature in the LG halo is $\sim 10^6 - 10^7$K, hydrogen and helium are fully ionized so that

$$n_e = n_H + 2 n_{He}. \tag{5.10}$$

Using the previous three equations, we find that the free electron density profile in the diffuse LG medium is given by

$$n_e(R) \cong 0.88 \left[\frac{\rho_b(R)}{m_p}\right]. \tag{5.11}$$

5.3 Calculating the kSZ Signal

In order to calculate the kSZ temperature shift due to the diffuse LG medium, we must integrate the free electron density along a particular line of sight (parameterized by

$\hat{\mathbf{r}}(\theta, \phi)$) from our observation point near the Sun. However, since the free electron density is expressed as a function of radial distance away from the center of mass origin, R, we must convert a given radial distance from the Sun, r, (for a particular $\hat{\mathbf{r}}$ direction) to a value of R. In this section we go over the geometry needed to accomplish this, but leave lengthy derivations for the Appendix.

To derive the geometric conversion, we define several cartesian coordinate systems shown in Fig. 5.2. We place a coordinate system, denoted by (X, Y, Z), at the center of mass position and orient the axes such that its Y axis points directly toward the Galactic center. Another coordinate system, denoted by ($\mathscr{x}'$, $\mathscr{y}'$, $\mathscr{z}'$) is placed at the Galactic center and we orient its axes to be in the same direction as the center of mass system. We set the $\mathscr{x}'$ axis to be in the Galactic plane. We define a heliocentric coordinate system, denoted by (x, y, z), in the usual way by placing the origin at the sun and orienting the x and y axes in the Galactic plane with the x axis pointing toward the Galactic center. This coordinate system is commonly called the Galactic coordinate system. We also place a coordinate system at the Galactic center whose axes, denoted by ($\mathscr{x}$, $\mathscr{y}$, $\mathscr{z}$), are oriented in the same way as the heliocentric system (a Galactocentric Galactic coordinate system). To aide the reader for the equations in the rest of this paper, the notation associated with each coordinate system is shown in Table 5.1. From Fig. 5.2, it can be seen that any position vector in the Galactic coordinate system can be expressed in the center of mass system by a translation to the Galactocentric frame, a rotation to the "primed" frame and another translation to the center of mass frame. In Appendix 5.8 we perform these operations to express R as a function of r, θ and ϕ, and in Appendix 5.7, we derive the rotation matrix between the primed and Galactocentric frames.

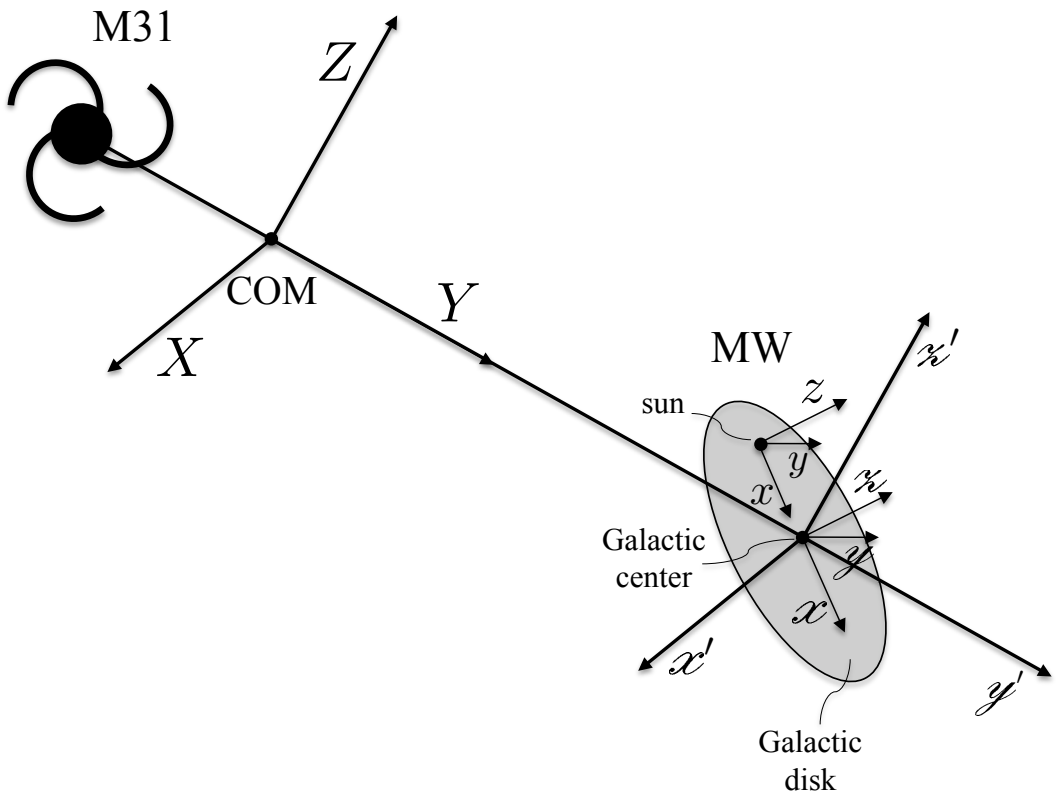

Figure 5.2.—: The coordinate systems used to convert from the heliocentric to center of mass frames.

To perform these operations, we also require several observed quantities. We take the distance from the sun to the Galactic center to be $d_\odot = 8.3$kpc, consistent with Gillessen et al. (2009); McMillan (2011). To find the direction to the center of mass, we use the position vector of M31 (in the Galactocentric coordinate system) given by van der Marel et al. (2012),

$$\boldsymbol{r}_{M31} = (-378.9, 612.7, -283.1)\text{kpc}, \tag{5.12}$$

so that the distance from the Galactic center to M31 is

$$d_{M31} = |\boldsymbol{r}_{M31}| = 774.0\text{kpc}. \tag{5.13}$$

Since we ignore the contributions from dwarf satellites in calculating the center of mass

Table 5.1:: Coordinate system notation in the Local Group

coordinate system	notation
heliocentric frame	$(x, y, z, r, \theta, \phi)$[a]
Galactocentric frame	$(\mathscr{x}, \mathscr{y}, \mathscr{z}, \mathscr{r})$
primed frame	$(\mathscr{x}', \mathscr{y}', \mathscr{z}', \mathscr{r}')$
center of mass frame	(X, Y, Z, R)

[a]For the derivations presented in this paper we only require angular variables for the heliocentric frame.

position of the LG galaxies, the distance from the Galactic center to the center of mass is

$$d_{com} = d_{M31}\left(\frac{m_{M31}}{m_{M31}+m_{mw}}\right) = 476.3\text{kpc}. \tag{5.14}$$

The center of mass position vector expressed in the Galactocentric frame is therefore the distance, d_{com}, times a unit vector in the direction of $M31$:

$$\begin{aligned}\boldsymbol{\mathscr{r}}_{com} &= d_{com}\left(\frac{\boldsymbol{\mathscr{r}}_{M31}}{d_{M31}}\right)\\ &= (-233.2, 377.0, -174.2)\text{kpc}.\end{aligned} \tag{5.15}$$

Having defined the relevant geometry to calculate $R(r, \theta, \phi)$, we may now calculate the kSZ temperature shift from the LG medium. To do this, we re-write Eqn. 5.1 as

$$\frac{\Delta T}{T}(\theta, \phi) = -\frac{1}{c}\left(\mathbf{v}_{LG-CMB}\cdot\hat{\mathbf{r}}\right)\tau(\theta, \phi), \tag{5.16}$$

where $\hat{\mathbf{r}} = \hat{\mathbf{r}}(\theta, \phi) = (\sin\theta\cos\phi, \sin\theta\sin\phi, \cos\theta)$, so that

$$\mathbf{v}_{LG-CMB}\cdot\hat{\mathbf{r}} = v^x_{LG-CMB}\sin\theta\cos\phi + v^y_{LG-CMB}\sin\theta\sin\phi + v^z_{LG-CMB}\cos\theta, \tag{5.17}$$

and where τ is the optical depth along the line of sight. From Loeb & Narayan (2008), the velocity of the local group with respect to the CMB in the heliocentric frame is

$$\mathbf{v}_{LG-CMB} = (-1.8, -537.2, 293.2)\mathrm{km\,s^{-1}}. \tag{5.18}$$

Since we are not situated at the center of mass origin, the optical depth depends on the particular line of sight. By using Eqn. 5.34 in Appendix 5.8 to re-write R in terms of the heliocentric variables r, θ and ϕ, the optical depth is given by integrating the density along the heliocentric radial direction:

$$\tau\left(\theta,\phi\right) = \sigma_T \int_0^{r_{vir}(\theta,\phi)} n_e \left(\sqrt{r^2 + d_\odot^2 - 2d_\odot r \sin\theta\cos\phi + d_{com}^2 + 2d_{com}\mathscr{y}'(r,\theta,\phi)}\right) dr. \tag{5.19}$$

The $\mathscr{y}'$ value at a particular set of (r, θ, ϕ) is given in Eqn. 5.35. The integration runs till the edge of the virial sphere, at a distance $r_{vir}(\theta,\phi)$ away from the Sun. This is found for a particular line of sight by evaluating Eqn. 5.36 at $R = R_{vir}$,

$$r_{vir}(\theta,\phi) \equiv r(\theta,\phi,R=R_{vir}) = -B(\theta,\phi) + \sqrt{B^2(\theta,\phi) + C(R_{vir})}, \tag{5.20}$$

where the functions B and C are defined in Eqns. 5.37 and 5.38.

5.4 The kSZ Signal Due to the Diffuse Local Group Medium and its Correlation with the CMB

Using the methodology described in the previous section, we calculate the expected kSZ signal from the diffuse medium associated with the local group. We choose a fiducial model of $\eta = 2$ and $c = 4$ and show a Mollweide projection in Galactic coordinates of

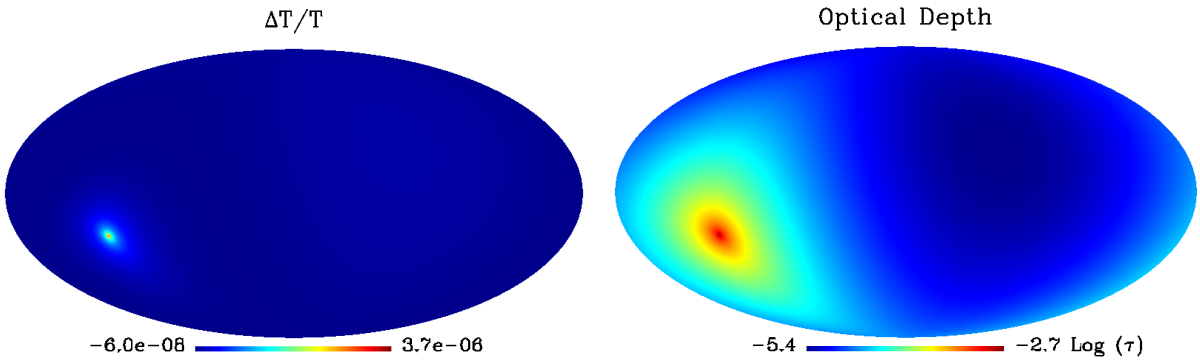

Figure 5.3.—: Sky maps of the $\Delta T/T$ kSZ signal (monopole and dipole subtracted) and the optical depth from the diffuse LG medium for our fiducial model with $c = 4$ and $\eta = 2$.

the fractional temperature shift in the first panel of Fig. 5.3. We have subtracted the monopole and dipole components of the map. We use the HEALPix pixelization scheme (Górski et al. 2005) with Nside $= 2^9$. In the second panel we show a map of the optical depth calculated with Eqn. 5.19. The figure shows that the temperature shift due to the gaseous halo of the local group is dominated by a hot spot several degrees in size. The spot is in the direction of M31 and is due to the fact that in our model the center of mass position is in the direction of M31. From Fig. 5.1 it is evident that not only does this direction correspond to the greatest path length through the medium, but it also passes directly through the center where the density is the highest. This results in the greatest optical depth along that line of sight. The scale shows that the temperature shift can be order several μK, which exceeds the detectability threshold of the CMB map measured by Planck.

We show the angular power spectrum of the kSZ signal for several values of c in Fig. 5.4. The figure shows that most of the power comes from large scales (low

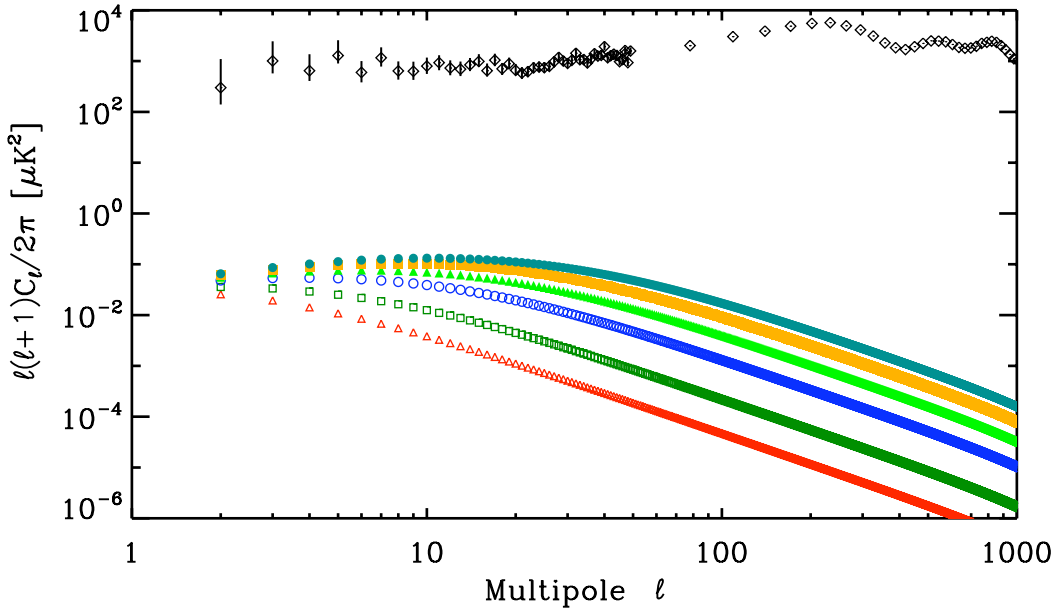

Figure 5.4.—: The angular power spectrum of our kSZ sky maps calculated with $c = 2$, 4, 8, 12, 16 and 20 (red open triangles, green open squares, blue open circles, light-green filled triangles, orange filled squares and teal filled circles respectively). The black open diamonds correspond to the angular power spectrum of the CMB temperature fluctuations as measured by Planck (Planck collaboration et al. 2013).

ℓ) consistent with the fact that the map is dominated by a large hot spot. At the smallest scales (highest values of ℓ), the amount of power has a clear dependence on c, with the highest values resulting in the greatest power. We also show the measured power spectrum of CMB temperature fluctuations from Planck (Planck collaboration et al. 2013). At the largest scales, the power from the temperature shift induced by the kSZ effect from the LG halo can be as much 0.01% that of the primordial CMB temperature fluctuations. This, of course, depends on value of η used, which in this figure is $\eta = 2$. Since the overall amplitude of the kSZ temperature shift is proportional to η ($\Delta T \propto n_e \propto \rho_o \propto M_{vir} \propto \eta$, as quickly verified from the equations presented above),

the lines in this figure scale as η^2, and thus have a strong dependence on η. However, as described in § 5.2 a reasonable estimate of the amount of gas in the LG diffuse medium limits η to be close to unity.

In order to test whether the kSZ signal from the diffuse LG medium is embedded in the CMB map measured by Planck, we perform the following correlation analysis. We first rebin the (background/foreground subtracted) CMB temperature shift map from Planck from its original size of Nside = 2^{11} to Nside = 2^7 in order to keep the analysis computationally manageable. The mask is also rebinned to Nside = 2^7, and all pixels with a value less than 1 are set to 0. We then calculate the kSZ map from our fiducial model with the same Nside and subtract the monopole and dipole components. We compute the correlation at zero separation between the two maps (excluding bad pixels as indicated by the rebinned mask), ξ , with $\xi \equiv \langle \delta_{CMB} \delta_{kSZ} \rangle$. Here, $\delta_{CMB} \equiv (T_{CMB} - T_o)/T_o = \Delta_{CMB}/T_o$, where Δ_{CMB} is the rebinned Planck map, and where $T_o = 2.7255K$ and $\delta_{kSZ} \equiv (\Delta T/T - \overline{\Delta T/T})/\overline{\Delta T/T}$. Given this definition of ξ, if no correlation exists between the two maps, then $\xi = 0$. To test the significance of this correlation value, we adopt a Monte Carlo approach where we make mock CMB maps from a given power spectrum and calculate the same correlation (again excluding the same bad pixels), but using the mock CMB maps instead of the Planck data. We use the power spectrum calculated by CAMB using the best fit cosmological parameters from Planck (Planck Collaboration et al. 2013a). To generate random realizations from the power spectrum, we use the HEALPix IDL procedure isynfast.pro, with a FWHM beamsize of 5 arcminutes (the beamsize of the Planck data Planck Collaboration et al. 2013b). We calculate ξ for 10,000 realizations and show the results as a probability distribution in Fig. 5.5. In this figure, the vertical line indicates the value of ξ calculated

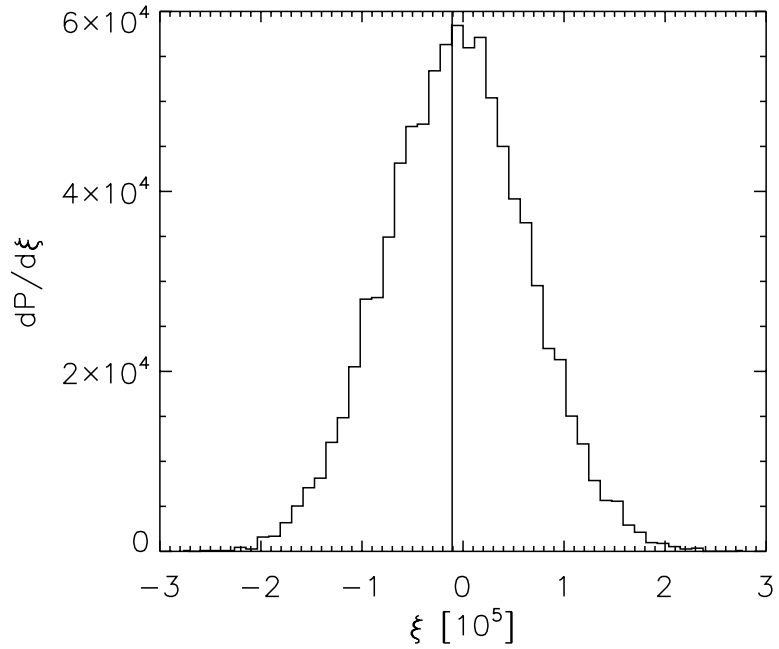

Figure 5.5.—: The distribution of ξ generated from random realizations of the CMB power spectrum. The vertical line gives the correlation from the temperature map measured by Planck.

from the original Planck map. Not only is the value of the correlation calculated with the original Planck map slightly negative (anti-correlated), but it is clear from the figure that the standard deviation of ξ is many times bigger than than this value. It is therefore impossible to tell whether this slightly negative correlation is due to the actual kSZ effect or a chance realization of the primordial CMB signal, and we find no statistical evidence to suggest that the kSZ signal from the LG medium is embedded in the Planck map. In order to test for possible resolution dependence, we have performed the same analysis for several values of Nside and have come to the same conclusion.

5.5 Limiting the Baryonic Mass in the Local Group Medium

Since the kSZ temperature shift due to the diffuse LG medium is concentrated in a hot spot in the direction of M31, we can place an upper limit on the amount of allowed mass in the LG medium. This is done by ruling out halo masses which result in temperatures around the hot spot which are greater than what is actually observed in the CMB data. To do this, we first make contour levels from our fiducial map extending from the brightest pixel in the hot spot to about the size of the hot spot. We then calculate the average temperature shift within each of these contours for both the kSZ map and the Planck map. We exclude bad pixels as indicated by the (rebinned) mask. This is shown in Fig. 5.6, where have plotted the average temperature shift within a contour versus the contour level for both the kSZ signal for several values of η (solid lines) and the Planck map (dashed line). The horizontal axis is plotted from the highest contour to lowest contour which corresponds to the center of the hot spot at the origin. The amplitude of the kSZ lines scale as η, since, as mentioned in the previous section, the kSZ shift is proportional to η. The highest line, with $\eta \approx 11$, is clearly not allowed since it results in a temperature shift greater than observed. We note that the maximum allowed value of η depends slightly on the size of the maps used. We use Nside $= 2^7$ since this results in the tightest constraint on η. Since η represents the mass of the LG medium plus the masses of M31 and the MW in units of $m_{M31} + m_{MW}$, the total amount of allowed mass in the medium is $(\eta_{max} - 1)(m_{M31} + m_{MW}) \approx 10(m_{M31} + m_{MW})$.

Since the concentration parameter is a free parameter in our model, we repeat the same calculation for different values of c to obtain the maximum allowed mass in the

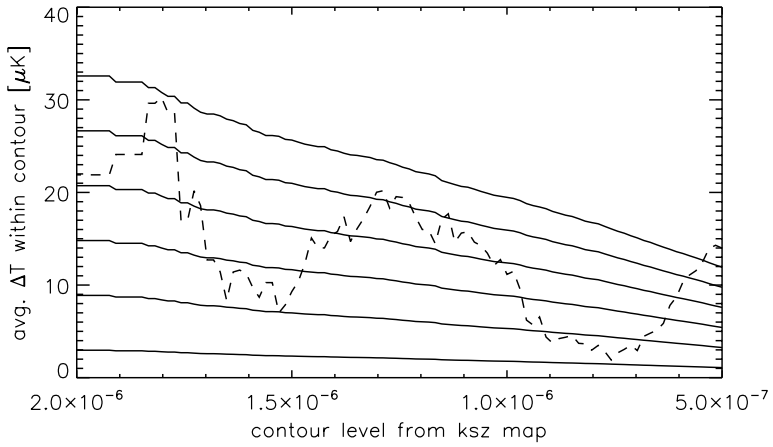

Figure 5.6.—: The average temperature shift within a contour level plotted as a function of the contour level. The levels, constructed from our fiducial kSZ map, are centered on the hot spot and extend out to about the size of the hot spot. The dashed line denotes the average temperature shift from the Planck map, while the solid lines denote the average temperature shift from our kSZ maps for different values of η. The solid lines extend from $\eta = 1$ (lowest line) to $\eta = 11$ (highest line) in steps of 2.

LG medium as a function of c. We show in the results in Fig. 5.7. The shaded part of the figure denotes the region not allowed by our analysis. By comparison, the so-called "timing argument" estimates the amount of mass in the LG to be about $5 \times 10^{12} \mathrm{M}_{\odot}$ (Li & White 2008). (See also Partridge et al. 2013, who include the dynamical effects of dark energy in the timing argument.) The smallest values of c result in upper mass limits much greater than the timing argument estimate, while the largest ($c \gtrsim 15$) result in mass limits roughly consistent with it.

It has been found from numerical simulations that there exists a reasonably tight correlation between the concentration of a halo and its mass (where the halo mass is identified at a certain redshift) (e.g. Bullock et al. 2001; Eke et al. 2001; Macciò et al.

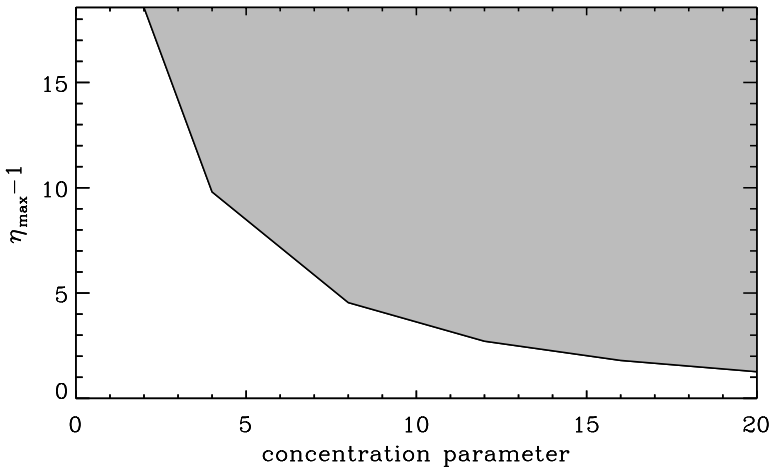

Figure 5.7.—: The maximum amount of allowed mass in the LG halo (in units of $m_{M31} + m_{MW}$) as a function of the concentration parameter assumed for the LG halo profile. The shaded region of the plot denotes values of $\eta_{max} - 1$ not allowed by our analysis.

2008; Zhao et al. 2009; Prada et al. 2012). For a given redshift and halo mass, there is, of course, a spread in the concentration parameters measured. For example, by analyzing the halos in the GIF2 simulation, Giocoli et al. (2012) find that, at $z = 0$, for a halo mass roughly equal to that of the LG (a few $\times 10^{12} M_\odot$) the third quartile of the distribution corresponds to $c \approx 12$ (see their figure 9). Using the Millennium Simulation, for the same mass and redshift, Neto et al. (2007) find a slightly lower value of $c \approx 10$ for the third quartile. Disregarding complexities such as whether to consider all halos or only relaxed halos, in general it is found that, at a given mass and redshift, the distribution in c is well fit by a lognormal function with variance $\sigma_{\log c} \cong 0.12 \pm 0.2$ (Bullock et al. 2001; Wechsler et al. 2002; Dolag et al. 2004; Neto et al. 2007). Depending on which fitting formula one uses to calculate the mean value of $\log(c)$ for a halo with a mass equal to that of the LG at $z = 0$, the $3\sigma_{\log c}$ value away from the mean corresponds to roughly $c \approx 15 - 20$. It is therefore improbable that the concentration parameter of the

LG is greater than 20, and we therefore truncate the x-axis of Fig. 5.7 at this value. We do note, however, that even though we obtain the tightest constraints on η_{max} for the highest values of c in this figure, even these values of c can be quite rare.

5.6 Discussion and Conclusions

We have modeled the distribution of baryonic mass in the LG medium to calculate the column density of free electrons along a particular line of sight. Our model assumes that the mass in the halo is distributed as an NFW profile, that the baryons trace the dark matter and that the ratio of baryons to dark matter follows the cosmic average. We have calculated sky maps of the possible kSZ signal due to the gaseous halo surrounding the LG, and have found that the it is concentrated in a hot spot several degrees in size in the direction of M31. The maximal temperature shift is $\sim 10\mu$K, several times bigger than the kSZ effect due to the MW and MW halo. The kSZ signal, however, is still far sub-dominant to the primordial CMB temperature fluctuations as seen from its power spectrum. Using random realizations of the CMB fluctuations, we found that the correlation of our kSZ signal with the Planck map is statistically insignificant. By ruling out halo masses resulting in temperature shifts around the kSZ hot spot greater than observed, we were able to place an upper limit on the amount of mass in the LG medium. We found that for the largest concentration parameters used to model the density profile of the LG medium, the amount of allowed mass is the most tightly constrained. For the largest values of c, the mass in the halo is constrained to be about $\eta_{max} - 1 \approx 1 - 2$ (see Fig. 5.7), corresponding to roughly $2.5 - 5 \times 10^{12}\mathrm{M}_{\odot}$ (where we have multiplied $(\eta_{max} - 1)$ by $(m_{M31} + m_{MW})$ to convert to halo mass). However, we again note that it

is very rare for halos at $z = 0$ with a mass comparable to that of the LG to have such large concentration parameters.

Our model of the diffuse LG medium assumes a spherically symmetric density profile centered on the center of mass position of M31 and the MW. In reality, the distribution of gas will not have perfect spherical symmetry, will have small-scale spatial inhomogeneities and will have a center of mass position that might not coincide with the center of mass position of the LG galaxies. It is possible that a more realistic model of the distribution of gas in the LG halo may change the significance of the correlation between the kSZ signal and the Planck map. The upper limit on the amount of mass in the LG halo inferred from our kSZ sky maps could change as well. However, as discussed below, it is difficult to make a more realistic model of the diffuse gas in the LG halo since the actual distribution of gas is relatively unconstrained.

Small-scale spatial inhomogeneities would lead to more textured kSZ sky maps and could significantly increase the power spectrum at larger values of ℓ. Indeed small-scale inhomogeneities have been included in studies of the kSZ signal due to the MW halo (Birnboim & Loeb 2009) and local superclusters (Dolag et al. 2005). The former study included a prescription for including high velocity clouds and infalling filaments of gas in their model of the gaseous halo of the MW. These structures are seen clearly in their kSZ sky maps as small-scale inhomogeneities in the kSZ signal. The inclusion of these features drastically enhances the angular power spectrum of the kSZ signal at $\ell \gtrsim 10$, compared to the case where only a smooth, gas density profile is included. Still, at the highest multipoles, the kSZ power spectrum is subdominant to the WMAP5 primordial power spectrum by several orders of magnitude. The latter study calculated the kSZ signal from hydrodynamic simulations, constrained to reproduce prominent observed

structure in the local universe. Small-scale inhomogeneities in the simulation lead to a roughly monotonic increase with ℓ in their measured kSZ power spectrum. This is in contrast to our kSZ power spectrum, which shows a monotonic decrease with ℓ (Fig. 5.4). Again, even at the highest values of ℓ, their power spectra are subdominant to the primordial CMB spectrum. We therefore do not expect the inclusion of small-scale gaseous structure in our model of the diffuse gas in the LG to significantly enhance the kSZ power spectrum (compared to the primordial signal). It is also not probable that the inclusion of small scale structure will lead to a significant correlation with the CMB signal measured by Planck, as this is highly dependent on precisely how this structure is distributed on the sky. Indeed, the distribution of small-scale structure in the LG is relatively unconstrained, and it would therefore be difficult to even devise a prescription for the inclusion of gaseous inhomogeneities.

Numerical simulations have shown that dark matter halos are in general not spherically symmetric, but are instead better approximated as ellipsoidal. An ellipsoidal geometry, however, is more difficult to model as it has more free parameters (the ratio of the length of the axes as well as the orientation) which may not be well constrained. One study actually has considered the kSZ signal due to an ellipsoidal gaseous halo associated with the MW (Peiris & Smith 2010). The authors of this study used axis ratios proposed by Law et al. (2009) in order to explain the observed properties of the Sagittarius dwarf spheroidal and considered several orientations. Their main results, however, were not qualitatively different than as compared to a spherical geometry. Any ellipsoidal model of the LG would be relatively unconstrained since the axis ratios and orientation for a triaxial model of LG halo are not well known.

More complex models of the gaseous halo of the LG which could include small-scale

inhomogeneities and triaxiality would have to cover a large parameter space since the actual distribution of gas in the LG halo is not well known. We have therefore taken the simplest approach by modeling the gaseous halo with spherical symmetry. This should reproduce the main features of the kSZ signal, specifically the presence of a large hot spot in the direction of M31.

5.7 Appendix A: Rotating Between the Galactocentric and Primed Frames

The Galactocentric (x, y, z) and primed (x', y', z') frames share the same origin, but their axes are rotated relative to each other (see Fig. 5.2). In this section, we derive the rotation matrices for transforming a position vector from one frame to the other. This can be done by solving a coupled set of non-linear equations to solve for the Euler angles for the proper rotation matrix. We, however, prefer to solve for the rotation matrix by hand, and present that derivation.

By definition, the $\hat{\boldsymbol{y}}'$ unit vector points in the direction opposite M31, so that $\hat{\boldsymbol{y}}'$ can be written down immediately by normalizing the opposite of Eqn. 5.12, $\hat{\boldsymbol{y}}' = -\boldsymbol{r}_{M31}/d_{M31}$, resulting in

$$\hat{\boldsymbol{y}}' = 0.4895\hat{\boldsymbol{x}} - 0.7916\hat{\boldsymbol{y}} + 0.3658\hat{\boldsymbol{z}}. \tag{5.21}$$

We are now free to orient the x' axis in which ever direction we please, so long as $\hat{\boldsymbol{y}}'$ and $\hat{\boldsymbol{x}}'$ are orthonormal. For convenience, we choose to keep the x' axis in the Galactic plane. In this case, $\hat{\boldsymbol{x}}'$ is written out as a linear combination of the $\hat{\boldsymbol{x}}$ and $\hat{\boldsymbol{y}}$ unit vectors: $\hat{\boldsymbol{x}}' = A\hat{\boldsymbol{x}} + B\hat{\boldsymbol{y}}$. We solve for the coefficients A and B by noting that due to

orthonormality $0.4895A - 0.7916B = 0$ (since $\hat{\boldsymbol{y}}' \cdot \hat{\boldsymbol{x}}' = 0$) and that $A^2 + B^2 = 1$. Solving these equations results in $B = \pm 0.5260$ and $A = \pm 0.8505$. The 2 solutions are due to the fact that there are 2 unit vectors in the galactic plane, exactly opposite each other, which are orthonormal to $\hat{\boldsymbol{y}}'$. The solution we choose will determine the direction of the $\hat{\boldsymbol{x}}'$ unit vector, since its direction is restricted by requiring a right handed coordinate system. We choose the minus solution as this results in a $\hat{\boldsymbol{x}}'$ unit vector which points away from the galactic plane in the same direction as the $\hat{\boldsymbol{x}}$ unit vector:

$$\hat{\boldsymbol{x}}' = -0.8505\hat{\boldsymbol{x}} - 0.5260\hat{\boldsymbol{y}}. \tag{5.22}$$

We solve for $\hat{\boldsymbol{x}}'$ by noting that in a right handed coordinate system, $\hat{\boldsymbol{x}}' = \hat{\boldsymbol{x}}' \times \hat{\boldsymbol{y}}'$, so that

$$\begin{aligned} \hat{\boldsymbol{x}}' &= \begin{vmatrix} \hat{\boldsymbol{x}} & \hat{\boldsymbol{y}} & \hat{\boldsymbol{z}} \\ -0.8505 & -0.5260 & 0 \\ 0.4895 & -0.7916 & 0.3658 \end{vmatrix} \\ &= -0.1924\hat{\boldsymbol{x}} + 0.3111\hat{\boldsymbol{y}} + 0.9307\hat{\boldsymbol{z}}. \end{aligned} \tag{5.23}$$

Indeed, since the $\hat{\boldsymbol{z}}$ compnent is positive, $\hat{\boldsymbol{x}}'$ sticks above the galactic plane, as a consequence of us choosing the minus root solution of the $\hat{\boldsymbol{x}}'$ unit vector.

A position vector can be expressed in the primed basis as $x'\hat{\boldsymbol{x}}' + y'\hat{\boldsymbol{y}}' + z'\hat{\boldsymbol{x}}'$ or in the Galactocentric basis as as $x\hat{\boldsymbol{x}} + y\hat{\boldsymbol{y}} + z\hat{\boldsymbol{x}}$. By equating the two expressions, replacing the primed unit vectors in the former expression with Eqns. 5.21 - 5.23, and

grouping together terms of like unit vectors, one can find that:

$$\begin{cases} x = -0.8505x' + 0.4895y' - 0.1924z' \\ y = -0.5260x' - 0.7916y' + 0.3111z' \\ z = 0.3658y' + 0.9307z'. \end{cases} \tag{5.24}$$

This set of equations may be written in matrix form so that the rotation of a vector in the primed frame to the Galactocentric frame is given by the matrix operation

$$\boldsymbol{r} = \mathscr{R}'\boldsymbol{r}', \tag{5.25}$$

where the rotation matrix, $\mathscr{R}'$, is

$$\mathscr{R}' = \begin{bmatrix} -0.8505 & 0.4895 & -0.1924 \\ -0.5260 & -0.7916 & 0.3111 \\ 0 & 0.3658 & 0.9307 \end{bmatrix}. \tag{5.26}$$

The rotation of a position vector in the Galactocentric frame to the primed frame is given as

$$\boldsymbol{r}' = \mathscr{R}\boldsymbol{r}, \tag{5.27}$$

where, in this case, the rotation matrix $\mathscr{R}$ is the inverse of $\mathscr{R}'$ (which, for a rotation matrix, is simply its transpose):

$$\mathscr{R} = \begin{bmatrix} \mathscr{R}_{11} & \mathscr{R}_{12} & \mathscr{R}_{13} \\ \mathscr{R}_{21} & \mathscr{R}_{22} & \mathscr{R}_{23} \\ \mathscr{R}_{31} & \mathscr{R}_{32} & \mathscr{R}_{33} \end{bmatrix} = \begin{bmatrix} -0.8505 & -0.5260 & 0 \\ 0.4895 & -0.7916 & 0.3658 \\ -0.1924 & 0.3111 & 0.9307 \end{bmatrix}. \tag{5.28}$$

5.8 Appendix B: Converting Heliocentric Position to Center of Mass Position

To calculate the kSZ temperature shift due to the diffuse LG medium we choose a line of sight and integrate over r. Since the free electron density, however, is a function of the center of mass distance R, we must find a geometric relation between R and a heliocentric position (r, θ, ϕ). From Fig. 5.2, it can be seen that to convert a position vector in the heliocentric frame to the center of mass frame we must (1) translate the vector a distance $d_\odot$ to the Galactic center, (2) rotate this vector into the primed coordinate frame, and (3) translate this vector a distance d_{com} to the center of mass origin.

Starting with the most general expression for a position vector expressed in the heliocentric frame, $\mathbf{r} = (x, y, z)$, the above sequence of transformations can be written mathematically as:

$$\begin{aligned} \boldsymbol{r} &= (x, y, z) \\ &= (x - d_\odot, y, z), \end{aligned} \tag{5.29}$$

$$\begin{aligned} \boldsymbol{r}' &= (x', y', z') \\ &= \mathcal{R}\boldsymbol{r} \\ &= (x\mathcal{R}_{11} + y\mathcal{R}_{12}, x\mathcal{R}_{21} + y\mathcal{R}_{22} + z\mathcal{R}_{23}, x\mathcal{R}_{31} + y\mathcal{R}_{32} + z\mathcal{R}_{33}), \end{aligned} \tag{5.30}$$

and

$$\begin{aligned} \mathbf{R} &= (X, Y, Z) \\ &= (x', y' + d_{com}, z'). \end{aligned} \tag{5.31}$$

From the previous equation the magnitude of $\mathbf{R}$ is

$$R = \sqrt{\mathscr{r}'^2 + d_{com}^2 + 2d_{com}\mathscr{y}'}, \tag{5.32}$$

where $\mathscr{r}'^2$ may be re-written in heliocentric variables by noting that $\mathscr{r}' = \mathscr{r}$ (since they share the same origin):

$$\mathscr{r}'^2 = \mathscr{r}^2 = (x - d_\odot)^2 + y^2 + z^2 = r^2 + d_\odot^2 - 2d_\odot x. \tag{5.33}$$

Plugging this into the previous equation and replacing x, y, z with $r\sin\theta\cos\phi$, $r\sin\theta\sin\phi$ and $r\cos\theta$ respectively, we find an expression for R as a function of r, θ and ϕ,

$$R = \sqrt{r^2 + d_\odot^2 - 2d_\odot r\sin\theta\cos\phi + d_{com}^2 + 2d_{com}\mathscr{y}'(r,\theta,\phi)}. \tag{5.34}$$

The function $\mathscr{y}'(r,\theta,\phi)$ is found from Eqns. 5.29 and 5.30 and is given as

$$\begin{aligned}\mathscr{y}' &= (x - d_\odot)\mathscr{R}_{21} + y\mathscr{R}_{22} + z\mathscr{R}_{23} \\ &= (r\sin\theta\cos\phi - d_\odot)\mathscr{R}_{21} + r\sin\theta\sin\phi\mathscr{R}_{22} + r\cos\theta\mathscr{R}_{23}.\end{aligned} \tag{5.35}$$

Eqn. 5.34 can be inverted to solve for r in terms of R for a certain line of sight, yielding a quadratic, which when solved, results in,

$$r(\theta,\phi,R) = -B(\theta,\phi) + \sqrt{B^2(\theta,\phi) + C(R)}, \tag{5.36}$$

where the following definitions have been employed:

$$B(\theta,\phi) \equiv d_{com}\mathscr{R}_{23}\cos\theta + \sin\theta[\cos\phi(d_{com}\mathscr{R}_{21} - d_\odot) + d_{com}\mathscr{R}_{22}\sin\phi] \tag{5.37}$$

and

$$C(R) \equiv R^2 - d_{com}^2 - d_\odot^2 + 2d_{com}d_\odot\mathscr{R}_{21}. \tag{5.38}$$

Acknowledgments

We thank Douglas Finkbeiner and Maxim Lavrentovich for helpful conversations. This research was supported in part by NSF grant AST-1312034.

Chapter 6

Conclusion

This thesis has presented a theoretical treatment of aspects of dark matter halos and has limited several properties of the baryons in these systems through observation. The first half of the thesis, Chapters 1 and 2, was concerned with analytic calculations of the structure of spherically symmetric distributions of dark matter. In the second half of the thesis, Chapters 3 and 4, we computed the expected observed signal from baryons within dark matter halos as a function of several free parameters, and limited those parameters using observational data.

In Chapter 2, we calculate the non-linear over-density, Δ_c, of dark matter halos at virialization using realistic density profiles. Using these profiles significantly complicates calculating the kinetic and potential energies at turn-around as the trajectories of the shells within the collapsing halo are no longer self-similar (as compared to the standard top-hat calculation). However, using the equations of spherical collapse, we derive the formalism to calculate these energies for an E-dS cosmology as well as for a cosmology with matter, dark energy and possible curvature. We find that Δ_c can be reduced by as

much as a factor of ~ 10 in a ΛCDM universe. This might have a considerable affect on the halo mass function measured from numerical simulations when the spherical over-density algorithm is used to identify halos. We attempt to quantify this effect by using fitting functions from Watson et al. (2013). Future studies, however, could investigate this more rigorously by utilizing our improved values of Δ_c to identify halos in actual numerical simulations. It is important to fully explore any refinements to the halo mass function measured from simulations since the success of any particular analytic model of the halo mass function is typically based off of its agreement with simulations.

In Chapter 3 we utilize the spherical collapse model to calculate several novel properties of spherically symmetric dark matter halos and voids. We also present several new analytic solutions pertaining to these systems, such as the turn-around radius of a collapsing halo and the critical initial seed below which a spherically symmetric perturbation will never collapse (where both were calculated in cosmologies with matter, dark energy and possible curvature). The new calculations presented in this chapter can be applied to a variety of problems regarding dark matter structure. For example, in Sec. 3.2.1, we use our results to theoretically show that the Shapley supercluster is supported against gravitational collapse due to the cosmological constant. As another example, our fitting formula for the linear theory under-density of a void at shell crossing (Eqn. 3.43) in a ΛCDM cosmology, $\bar{\delta}_L(z_{sc})$, can be used to derive a more accurate "void mass function" from the excursion set formalism (Sheth & van de Weygaert 2004). As with the halo mass function, the void mass function requires a linear theory density which defines a void, and this is typically taken to be $\bar{\delta}_L(z_{sc})$. Thus far, the void mass function has only been calculated with the E-dS value of $\bar{\delta}_L(z_{sc})$, since up till now, the linear theory under-density at shell crossing has only been derived for an E-dS cosmology.

Chapter 4 presents a novel method for constraining the IMF of stars in the Galactic center. We derive a semi-analytic model to calculate the mass lost in a direct and indirect stellar collision. By computing the collision rate, we are able to calculate the mass loss rate due to stellar collisions in the Galactic center as a function of the PDMF of stars. We construct a simple analytic model for the total x-ray luminosity emitted by the gas ejected due to the collisions. We are able to constrain the PDMF of stars by limiting the x-ray luminosity to be less than what is observed. By considering several star formation histories, we are able to constrain the IMF of stars in the Galactic center. Our constraints suggest a top-heavy to a canonical (Salpeter) IMF. However, given the variation in findings regarding the shape of the IMF in the Galactic center, more work in this area is required to fully test the supposed universality of the Salpeter IMF.

In Chapter 5, we model the distribution of gas associated with the LG halo and compute its expected kSZ signal. By performing a correlation analysis with the CMB temperature map measured by Planck, we find no statistically significant evidence that the kSZ effect from the LG halo contaminates the Planck map. Since the kSZ temperature shift from the LG results in a pronounced hot spot in the direction of M31, we are able to constrain the amount of mass in the LG halo by requiring the temperature shift in this direction to be less than what is observed. Although we find a null correlation with the CMB temperature map, it is important to undertake further investigations into local foreground contaminants (whether from the kSZ effect, or other effects such as the tSZ effect or the Integrated Sachs-Wolfe effect) since the observed large-scale anomalies in the CMB map, if primordial, have significant implications in the physics of the early universe.

References

Aguilar, L. A., & White, S. D. M. 1985, ApJ, 295, 374

Alexander, T. 1999, ApJ, 527, 835

Angulo, R. E., Springel, V., White, S. D. M., Jenkins, A., Baugh, C. M., & Frenk, C. S. 2012, MNRAS, 426, 2046

Baganoff, F. K., et al. 2003, ApJ, 591, 891

Bailey, V. C., & Davies, M. B. 1999, MNRAS, 308, 257

Bardeen, J. M., Bond, J. R., Kaiser, N., & Szalay, A. S. 1986, ApJ, 304, 15

Bartko, H., et al. 2010, ApJ, 708, 834

Bastian, N., Covey, K. R., & Meyer, M. R. 2010, ARA&A, 48, 339

Benz, W., & Hills, J. G. 1987, ApJ, 323, 614

—. 1992, ApJ, 389, 546

Bertschinger, E. 1985a, ApJS, 58, 39

—. 1985b, ApJS, 58, 1

Binney, J., & Tremaine, S. 2008, Galactic Dynamics: Second Edition (Princeton University Press)

Birnboim, Y., & Loeb, A. 2009, JCAP, 6, 8

Blumenthal, G. R., da Costa, L. N., Goldwirth, D. S., Lecar, M., & Piran, T. 1992, ApJ, 388, 234

Bond, J. R., Cole, S., Efstathiou, G., & Kaiser, N. 1991, ApJ, 379, 440

Bond, J. R., & Myers, S. T. 1996, ApJS, 103, 1

Bryan, G. L., & Norman, M. L. 1998, ApJ, 495, 80

Bullock, J. S., Kolatt, T. S., Sigad, Y., Somerville, R. S., Kravtsov, A. V., Klypin, A. A., Primack, J. R., & Dekel, A. 2001, MNRAS, 321, 559

Carroll, S. M., Press, W. H., & Turner, E. L. 1992, ARA&A, 30, 499

Cox, T. J., & Loeb, A. 2008, MNRAS, 386, 461

Crocce, M., Fosalba, P., Castander, F. J., & Gaztañaga, E. 2010, MNRAS, 403, 1353

Cupani, G., Mezzetti, M., & Mardirossian, F. 2008, MNRAS, 390, 645

—. 2011, MNRAS, 417, 2554

Dale, J. E., Davies, M. B., Church, R. P., & Freitag, M. 2009, MNRAS, 393, 1016

Davies, M. B., Blackwell, R., Bailey, V. C., & Sigurdsson, S. 1998, MNRAS, 301, 745

Davis, M., Efstathiou, G., Frenk, C. S., & White, S. D. M. 1985, ApJ, 292, 371

De Young, D. S. 1968, ApJ, 153, 633

Dolag, K., Bartelmann, M., Perrotta, F., Baccigalupi, C., Moscardini, L., Meneghetti, M., & Tormen, G. 2004, A&A, 416, 853

Dolag, K., Hansen, F. K., Roncarelli, M., & Moscardini, L. 2005, MNRAS, 363, 29

Eckart, A., Genzel, R., Hofmann, R., Sams, B. J., & Tacconi-Garman, L. E. 1993, ApJ, 407, L77

Eckart, A., Genzel, R., Ott, T., & Schödel, R. 2002, MNRAS, 331, 917

Eisenstein, D. J., & Loeb, A. 1995, ApJ, 439, 520

Eke, V. R., Cole, S., & Frenk, C. S. 1996, MNRAS, 282, 263

Eke, V. R., Navarro, J. F., & Steinmetz, M. 2001, ApJ, 554, 114

Eriksen, H. K., Hansen, F. K., Banday, A. J., Górski, K. M., & Lilje, P. B. 2004, ApJ, 605, 14

Figer, D. F., Kim, S. S., Morris, M., Serabyn, E., Rich, R. M., & McLean, I. S. 1999, ApJ, 525, 750

Fillmore, J. A., & Goldreich, P. 1984a, ApJ, 281, 1

—. 1984b, ApJ, 281, 9

Frank, J., & Rees, M. J. 1976, MNRAS, 176, 633

Freitag, M., & Benz, W. 2005, MNRAS, 358, 1133

Genzel, R., Thatte, N., Krabbe, A., Kroker, H., & Tacconi-Garman, L. E. 1996, ApJ, 472, 153

Genzel, R., et al. 2003, ApJ, 594, 812

Ghez, A. M., et al. 2003, ApJ, 586, L127

—. 2008, ApJ, 689, 1044

Gillessen, S., Eisenhauer, F., Trippe, S., Alexander, T., Genzel, R., Martins, F., & Ott, T. 2009, ApJ, 692, 1075

Giocoli, C., Tormen, G., & Sheth, R. K. 2012, MNRAS, 422, 185

Gnedin, O. Y., Hernquist, L., & Ostriker, J. P. 1999, ApJ, 514, 109

Górski, K. M., Hivon, E., Banday, A. J., Wandelt, B. D., Hansen, F. K., Reinecke, M., & Bartelmann, M. 2005, ApJ, 622, 759

Gunn, J. E. 1979, Feeding the monster - Gas discs in elliptical galaxies, ed. C. Hazard & S. Mitton, 213–225

Gunn, J. E., & Gott, III, J. R. 1972, ApJ, 176, 1

Hajian, A., Hernández-Monteagudo, C., Jimenez, R., Spergel, D., & Verde, L. 2007, ApJ, 671, 1079

Hernquist, L., & Mihos, J. C. 1995, ApJ, 448, 41

Hogan, C. J. 1992, ApJ, 398, L77

Jenkins, A., Frenk, C. S., White, S. D. M., Colberg, J. M., Cole, S., Evrard, A. E., Couchman, H. M. P., & Yoshida, N. 2001, MNRAS, 321, 372

Kim, S. S., Figer, D. F., Kudritzki, R. P., & Najarro, F. 2006, ApJ, 653, L113

Kippenhahn, R., & Weigert, A. 1994, Stellar Structure and Evolution

Komatsu, E., et al. 2011, ApJS, 192, 18

Kroupa, P. 2001, MNRAS, 322, 231

Lacey, C., & Cole, S. 1993, MNRAS, 262, 627

—. 1994, MNRAS, 271, 676

Lahav, O., Lilje, P. B., Primack, J. R., & Rees, M. J. 1991, MNRAS, 251, 128

Lai, D., Rasio, F. A., & Shapiro, S. L. 1993, ApJ, 412, 593

Law, D. R., Majewski, S. R., & Johnston, K. V. 2009, ApJ, 703, L67

Li, Y.-S., & White, S. D. M. 2008, MNRAS, 384, 1459

Lifshitz, E. M. 1946, J. Phys. (USSR), 10, 116

Lilje, P. B., & Lahav, O. 1991, ApJ, 374, 29

Lithwick, Y., & Dalal, N. 2011, ApJ, 734, 100

Löckmann, U., Baumgardt, H., & Kroupa, P. 2010, MNRAS, 402, 519

Loeb, A. 2006, ArXiv Astrophysics e-prints

Loeb, A., & Furlanetto, S. 2013, The First Galaxies in the Universe

Loeb, A., & Narayan, R. 2008, MNRAS, 386, 2221

Lokas, E. L., & Hoffman, Y. 2001, ArXiv Astrophysics e-prints

Lu, Y., & Mo, H. J. 2007, MNRAS, 377, 617

Lu, Y., Mo, H. J., Katz, N., & Weinberg, M. D. 2006, MNRAS, 368, 1931

Macciò, A. V., Dutton, A. A., & van den Bosch, F. C. 2008, MNRAS, 391, 1940

Maloney, P. R., & Bland-Hawthorn, J. 1999, ApJ, 522, L81

Maness, H., et al. 2007, ApJ, 669, 1024

Mathis, J. S. 1967, ApJ, 147, 1050

McMillan, P. J. 2011, MNRAS, 414, 2446

Mo, H., van den Bosch, F. C., & White, S. 2010, Galaxy Formation and Evolution

Mo, H. J., & White, S. D. M. 1996, MNRAS, 282, 347

Muñoz, J. A., & Loeb, A. 2008, MNRAS, 391, 1341

Najarro, F., Krabbe, A., Genzel, R., Lutz, D., Kudritzki, R. P., & Hillier, D. J. 1997, A&A, 325, 700

Navarro, J. F., Frenk, C. S., & White, S. D. M. 1996, ApJ, 462, 563

Neto, A. F., et al. 2007, MNRAS, 381, 1450

Nusser, A. 2001, MNRAS, 325, 1397

Partridge, C., Lahav, O., & Hoffman, Y. 2013, MNRAS, 436, L45

Paumard, T., et al. 2006, ApJ, 643, 1011

Peebles, P. J. E. 1980, The large-scale structure of the universe

Peebles, P. J. E., & Yu, J. T. 1970, ApJ, 162, 815

Peiris, H. V., & Smith, T. L. 2010, Phys. Rev. D, 81, 123517

Planck collaboration et al. 2013, ArXiv e-prints

Planck Collaboration et al. 2013a, ArXiv e-prints

—. 2013b, ArXiv e-prints

Prada, F., Klypin, A. A., Cuesta, A. J., Betancort-Rijo, J. E., & Primack, J. 2012, MNRAS, 423, 3018

Press, W. H., & Schechter, P. 1974, ApJ, 187, 425

Quataert, E. 2004, ApJ, 613, 322

Rauch, K. P. 1999, ApJ, 514, 725

Reed, D. S., Bower, R., Frenk, C. S., Jenkins, A., & Theuns, T. 2007, MNRAS, 374, 2

Rubin, D., & Loeb, A. 2013a, submitted to JCAP

—. 2013b, submitted to JCAP

Rybicki, G. B., & Lightman, A. P. 1979, Radiative processes in astrophysics

Salpeter, E. E. 1955, ApJ, 121, 161

Satō, H. 1971, Progress of Theoretical Physics, 45, 370

Schödel, R., Ott, T., Genzel, R., Eckart, A., Mouawad, N., & Alexander, T. 2003, ApJ, 596, 1015

Schödel, R., et al. 2002, Nature, 419, 694

—. 2007, A&A, 469, 125

Sherwin, B. D., Loeb, A., & O'Leary, R. M. 2008, MNRAS, 386, 1179

Sheth, R. K., Mo, H. J., & Tormen, G. 2001, MNRAS, 323, 1

Sheth, R. K., & Tormen, G. 1999, MNRAS, 308, 119

—. 2002, MNRAS, 329, 61

Sheth, R. K., & van de Weygaert, R. 2004, MNRAS, 350, 517

Silk, J. 1968, ApJ, 151, 459

Silk, J., & Wilson, M. L. 1979, ApJ, 228, 641

Spitzer, Jr., L. 1958, ApJ, 127, 17

Spitzer, Jr., L., & Saslaw, W. C. 1966, ApJ, 143, 400

Springel, V., et al. 2005, Nature, 435, 629

Stolte, A., Brandner, W., Grebel, E. K., Lenzen, R., & Lagrange, A.-M. 2005, ApJ, 628, L113

Sunyaev, R. A., & Zeldovich, I. B. 1980, ARA&A, 18, 537

Suto, Y., Makishima, K., Ishisaki, Y., & Ogasaka, Y. 1996, ApJ, 461, L33

Thoul, A. A., & Weinberg, D. H. 1995, ApJ, 442, 480

Tinker, J., Kravtsov, A. V., Klypin, A., Abazajian, K., Warren, M., Yepes, G., Gottlöber, S., & Holz, D. E. 2008, ApJ, 688, 709

Toomre, A., & Toomre, J. 1972, ApJ, 178, 623

Tseliakhovich, D., & Hirata, C. 2010, Phys. Rev. D, 82, 083520

van der Marel, R. P., Fardal, M., Besla, G., Beaton, R. L., Sohn, S. T., Anderson, J., Brown, T., & Guhathakurta, P. 2012, ApJ, 753, 8

van der Marel, R. P., & Guhathakurta, P. 2008, ApJ, 678, 187

Warren, M. S., Abazajian, K., Holz, D. E., & Teodoro, L. 2006, ApJ, 646, 881

Watson, W. A., Iliev, I. T., D'Aloisio, A., Knebe, A., Shapiro, P. R., & Yepes, G. 2013, MNRAS, 433, 1230

Wechsler, R. H., Bullock, J. S., Primack, J. R., Kravtsov, A. V., & Dekel, A. 2002, ApJ, 568, 52

Weinberg, S. 1971, ApJ, 168, 175

White, S. D. M., & Silk, J. 1979, ApJ, 231, 1

Zel'dovich, Y. B. 1970, A&A, 5, 84

Zhao, D. H., Jing, Y. P., Mo, H. J., & Börner, G. 2009, ApJ, 707, 354

Zukin, P., & Bertschinger, E. 2010, Phys. Rev. D, 82, 104044